Spatio-Temporal Response of a Compliant-Wall, Turbulent Boundary Layer System to Dynamic Roughness Forcing

Thesis by
David Pham Huynh

In Partial Fulfillment of the Requirements for the
Degree of
Doctorate Of Philosophy in Aeronautics

Caltech

CALIFORNIA INSTITUTE OF TECHNOLOGY
Pasadena, California

2019
Defended April 15, 2019

ACKNOWLEDGEMENTS

Support for this work by AFOSR under grant #FA 9550-16-1-0361 and ONR under N00014-17-1-2960 is gratefully acknowledged. I also want to acknowledge the support of the Foster and Coco Stanback STEM Fellowship for my graduate studies.

It's impossible to understate how much support, guidance, and love I have received these past six years. Over the course of my life, I've realized that I care far more about the people I'm with than the thing I'm doing, and I have been incredibly blessed to be with incredible people. They have made this journey so much more than just the pursuit of a PhD. I have more of a crowd to thank than I ever could, but here's my honest effort.

I want to thank my thesis committee: Professors Dale Pullin, Mory Gharib, and Guruswami (Ravi) Ravichandran. I appreciate them lending their time and expertise through classes, Tuesday Talks, and personal interactions.

I want to thank Professor Beverley McKeon for being an incredible adviser, mentor, advocate, and role model. I can say without hesitation that it was not a fervent love for turbulence or resolvent analysis that drew me to the McKeon group. I asked to join because from my first meeting with Beverley on my visit day, I felt that she genuinely valued the graduate experience of her students. For me, she has always struck a delicate balance between providing guidance when I start to feel aimless and stepping back for me to find my path forward. She has shown amazing leadership in our group, our department, and our community, and I can only hope to emulate the model she has set. For these reasons and many more, I could not have asked for a better adviser.

Beverley also has a knack for finding good seconds-in-command, and I want to thank Jamie Meighen-Sei and Denise Ruiz for being wonderful people and incredible group administrative assistants. Jamie has always been a source of positivity and helped me so much in adjusting to being a part of the research group. I still struggle to understand how she handled my onslaught of McMaster orders while managing everything else on her plate. And when Jamie moved into her role with CAST, Denise stepped in and added our group to death-defying juggling act with a smile. Both of these women have been wonderful to work with and I'm very grateful for their support and friendship.

Steve Anderson from LaVision has been an invaluable source of DaVis and PIV knowledge and dramatically reduced the time it took to gain proficiency with the techniques. Professor Sergio Pellegrino and his students (my classmates) Maria Sakovsky and Yuchen Wei graciously allowed and taught me to use their group's Instron machine for the material characterization of my compliant gelatin surface. The folks in the GALCIT machine shop, Stephanie Rider, Matt Zargarian, Ali Kiani, and Joe Haggerty, have all been patient, instructive, and kind through the hectic bursts of machining during the fabrication of the experiments. Christine Ramirez, Peggy Blue, and Dimity Nelson have been wonderful GALCIT staff and made navigating the administrative side of graduate life much more pleasant and much less stressful. I am extremely grateful to all of these people.

I have several people to thank for the three years I was funded by the Foster and Coco Stanback STEM Fellowship, while I served as a graduate mentor in the Caltech-Base 11 STEM outreach program. I am indebted to Foster and Coco Stanback for establishing the fellowship with our department. Ravi and Beverley have served as the GALCIT leaders supporting the program, instilling it with tremendous value and working hard to secure funding so that it may continue. Beverley also brought the program to my attention and encouraged me to apply, for which I am so grateful. Dimity and Jamie worked incredibly hard to build up the structure and logistics of hosting the program, and it could not have been executed without them. I had the great fortune to work with several other dedicated graduate mentors: Cong Wang, Arnold Deffo, Brian Schmidt, Ryan Song, Akshay Sridhar, and Joel Lawson. On the other side of this collaboration, the Base 11 team were some of the most inspiring and big-dreaming people I've ever met. Working with Landon and Michelle Taylor, Ingrid Ellerbe, Christine Byrd, and the rest of Base 11 has been formative in ways I could not have imagined. And at the heart of this experience were the amazing community college students who participated in the program. Each one came in with unique goals and background, but all brought with them such motivation and eagerness to learn. It was an opportunity for me to play the supporting character in the narrative of someone else's journey, and it gave me a perspective that I could not have experienced otherwise. It's difficult to put into words how much I've grown as a teacher, student, mentor, and person from my time with these students, and it's a part of my graduate career that I would not trade for anything. So I want to sincerely thank everyone who was a part of making this program happen.

I'm quite certain that I will never again find the kind of work environment I've enjoyed in the McKeon group. I owe that to the graduate students who came before me: Jonathan Morgan, Kevin Rosenberg, Sean Symon, Tess Saxton-Fox, Subbu Duvvuri, Esteban Hufstedler, and Reeve Dunne; to the students who have joined since: Ryan McMullen, Simon Toedtli, Maysam Shamai, Morgan Hooper, and Ben Barthel; to the many postdocs with whom I've overlapped: Mitul Luhar, Rashad Moarref, Scott Dawson, Angeliki Laskari, Arslan Ahmed, and Jane Bae; and of course to the lifeblood of the group: Beverley, Jamie, and Denise. Not only have I learned from literally each one of them, but being surrounded by such intelligent, driven, and generally amazing people has pushed me to improve myself well beyond what I thought was possible. Everyone in this group wants to support each other and success for one is success for all. And for every bit that this group is wonderful to work with, they are equally fun to party with. From genuinely ridiculous group lunch conversations to less-than-sober karaoke nights together, being a member of this graduate school family has been a joy. I thank everyone who has been a part of it.

I can't imagine having gotten through these past several years without the amazing friends I've made along the way. Many of these friendships forged in the white-hot core that was First Year, and lasted well beyond Quals: Arturo Mateos, Nathan Martin, Jason and Susie Schlup, Noah Braun, Ryan McMullen, Cong, Akshay, Ilana Gat, Stevan Van Heerdan, the Kirchdoerfers (Trent, Yuka, Takato, and Masato), Ian Brownstein, and Kristy Schlueter-Kuck. I have especially fond memories of the game nights with my wife, Arturo, Nathan, Jason, Susie, and Noah, where we never had a dull evening pushing our friendships to the brink. Outside of my Caltech bubble, my wife's wonderfully quirky friends, Sau and Mike Murphy, became my wonderfully quirky friends, and they have been a source of never-ending adventure for us. I am thankful to all the people who have given me their friendship and made life outside of school fun-filled.

I want to thank my family, my mom, my dad, my sister, Amanda, and my brother, Benji, for everything they've done for me. My parents have been my role models since I can remember. I learned through their example to take care of those you love and to treat others thoughtfully and with respect. They were involved in my education and my childhood, encouraging and enabling me to take advantage of all my opportunities. As I've grown, they've trusted me to navigate my life which has allowed me to develop trust in myself, while always being at the ready to help if I need it. Though they may not fully recognize it, my sister and brother have been a huge part of my development as a person. I learned so much in empathy, responsibility, and my own personal flaws through being their brother. I can't imagine my childhood without them, and I hope to continue growing up alongside them. My family is a fundamental part of who I am today and why I had the opportunity and capability to pursue this degree. I have always been and will always be thankful to them.

Literally, figuratively, emotionally, and in all other ways, I could not have done this without my amazing wife, Nikky. She has seen me at my highest high, my lowest low, and everything in the middle, and through it all she has been my rock to lean on. Since we moved out to California, she has carved her own footholds and built many wonderful friendships, while managing not only her own work stress, but also some of mine. During my late nights at the lab, she would stay up to make sure I was safe, make sure I ate, and make sure I slept (some). Through my rollercoaster of anxieties, she has always known what to say and what to do to help bring me back to center. And when the days are good, Nikky makes them better. Being with friends, traveling, cooking, chores, and TV-watching are all made brighter when we do them together. I have grown unimaginably being with her, and we're about to take another incomprehensible leap as we welcome our baby boy into the world in May. Nikky has been a constant source of support, encouragement, motivation, relief, and love in this entire process. I'll never be able to thank her enough, but I'll gladly spend the rest of our lives trying.

ABSTRACT

This thesis investigates the interaction between an elastic compliant surface and a turbulent boundary layer exposed to dynamic roughness forcing. The goals are to explore a unique perspective of this fluid-structural problem through narrow-band forcing, and to further develop the understanding of dynamic roughness. Water tunnel experiments are designed with flow and surface measurements, both phase-locked to the roughness actuation. This enables a phase-averaged analysis, which leverages the deterministic input to isolate the temporally correlated components of the flow and surface response. Identifying the directly interacting velocity and deformation modes allows the complex, fluid-structural system to be studied in a more tractable, input-output manner.

The first experiment is conducted with a smooth-wall turbulent boundary layer forced by dynamic roughness, and contributes to the knowledge of this type of forcing through structure-resolved particle image velocimetry. This allows for the streamwise-spatial nature and the wall-normal velocity component (v) of the roughness-forced flow to be explored, which had not been previously studied. A spatial amplitude modulation is observed in the synthetic structure and investigated directly through the spatial spectra. Through a parametric study and an empirical fit, the forcing frequency may now be selected to target a particular streamwise length scale.

The second experiment implements a gelatin sample subject to an unforced turbulent boundary layer. The surface response is characterized and serves as a base case with which to identify the roughness-forced component of the deformations. This naturally leads to the third experiment, where the full compliant-wall, dynamic-roughness-forced turbulent boundary layer system is considered. The surface response to the synthetic flow structure is confirmed, which sets the stage for a comparison between the smooth-wall and compliant-wall data to study the effect of the compliant surface.

The smooth/compliant comparison is guided by a resolvent analysis, which predicts a virtual wall feature in the v velocity mode for the elastic material under consideration. Using this prediction to inform a conditional average, the virtual wall is revealed in the experimental data. Thus, the action of the elastic surface is interpreted as opposing the v velocity near the wall, in a manner similar to wall-jet opposition control.

Previous experimental studies of viscoelastic compliant surfaces have demonstrated the potential for turbulent drag reduction, though either indirectly via the turbulence intensities or with relatively high skin friction measurement error. A common observation in these studies was the importance of the interaction between the surface and the coherent structures in the flow. To that end, this study has isolated and modeled the behavior of the fluid-structural system with a single spatio-temporal scale generated by dynamic roughness forcing. The results provide a physical interpretation of the effect of an elastic surface on turbulent boundary layer flow structures and informs the ongoing development of a reduced-order modeling tool in the resolvent analysis.

PUBLISHED CONTENT AND CONTRIBUTIONS

D. Huynh and B. McKeon (submitted). Characterization of the spatio-temporal response of a turbulent boundary layer to dynamic roughness. *Flow, Turbulence and Combustion*.

David Huynh performed the experiments, analyzed the results, created the figures, and was the primary author of the paper.

TABLE OF CONTENTS

LIST OF ILLUSTRATIONS

Number *Page*

LIST OF TABLES

Chapter 1

INTRODUCTION

Turbulent flow is a ubiquitous and visually beautiful phenomenon, and has been a focus of fluid mechanics research for over a century. It is present at an impressive range of scales, from stirred coffee cups to planetary atmospheres and stellar dynamics, and is unrelentingly pervasive in many engineering applications. Turbulence is the ‘high’ setting on nature’s blender, mixing mass, momentum, and heat with marked efficiency. Inside the combustor of an aircraft engine, this enhanced mixing boosts fuel efficiency, while just outside on the wing, the same phenomenon massively increases drag. In both cases, understanding the behavior of the flow is critical to designing faster, quieter, and more efficient transport. As expected of such a long-lived subject of research, the field of turbulence has evolved from its primarily experimental and analytical roots to incorporate recent computational capabilities, such as highly-resolved direct numerical simulations (DNS) and numerical reduced-order models. It will no doubt require the efforts of a three-pronged approach to develop tools and technologies to understand, modify, and control the effects of turbulence.

This thesis investigates the longstanding topic of compliant surfaces interacting with a turbulent boundary layer, with the unique input-output perspective enabled by the novel experimental tool that is dynamic roughness. This chapter provides a brief overview of turbulent boundary layers and compliant surfaces, motivates the input-output viewpoint, and outlines the approach taken in this work.

1.1 Description of turbulent boundary layer flows

Incompressible and viscous fluid flows are governed by the incompressible Navier-Stokes and continuity equations:

$$\frac{\partial \grave{\mathbf{U}}}{\partial \grave{t}} + \grave{\mathbf{U}} \cdot \grave{\nabla} \grave{\mathbf{U}} = -\frac{1}{\rho} \nabla \grave{p} + \nu \grave{\nabla}^2 \grave{\mathbf{U}} \tag{1.1}$$

$$\grave{\nabla} \cdot \grave{\mathbf{U}} = 0\,, \tag{1.2}$$

where $\mathbf{U}$ is the flow velocity (vector), p is pressure, ρ is the fluid density, and ν the fluid kinematic viscosity. ∇, $\nabla \cdot$, and ∇^2 represent the gradient, divergence, and

Laplacian operators, respectively. The grave accent, $\grave{(\cdot)}$, indicates a dimensional quantity.

Wall-bounded shear flows are differentiated from free-shear flows by the presence of boundaries in the domain, typically rigid walls, which introduce a geometric length scale to the problem. In internal shear flows like in a pipe or channel, the flow is bounded on all/both sides and the geometric length scale is the radius (r) or channel half-height (h), respectively. External wall-bounded shear flows do not have a fully encapsulating geometries. One such flow of common interest is a boundary layer, which has a single flat wall and introduces length scales like the boundary layer thickness (δ) and momentum thickness (θ), defined in the next section, which evolve in the primary direction fo the flow. Another effect of the presence of the wall(s) is an inhomogeneity in the direction perpendicular to the boundary, caused by friction dragging to the fluid to zero relative velocity at the wall. This is known as the no-slip boundary condition, and for viscous fluids, it causes a shear-stress gradient to penetrate into the flow. The coordinate system that will be used here for three-dimensional, wall-bounded shear flows is x aligned to the dominant flow direction ('streamwise'), y aligned to the outward-pointing normal from the wall ('wall-normal'), and z aligned to the right-hand consistent perpendicular direction ('spanwise'), with t being time. In equations 1.1 and 1.2, $\mathbf{U}$ and p are functions of x, y, z, and t.

Equations 1.1 and 1.2 can be non-dimensionalized using characteristic length, velocity, and pressure scales, L_s, U_s, and ρU_s^2, respectively, yielding:

$$\frac{\partial \mathbf{U}}{\partial t} + \mathbf{U} \cdot \nabla \mathbf{U} = -\nabla p + \frac{1}{Re} \nabla^2 \mathbf{U} \tag{1.3}$$

$$\nabla \cdot \mathbf{U} = 0 \,, \tag{1.4}$$

where Re is the well-known Reynolds number, $Re = \frac{U_s L_s}{\nu}$. The length scale is often chosen based on a feature of the flow geometry, such as the boundary layer thickness or momentum thickness for a boundary layer flow. Choosing the velocity scale to represent the condition away from the boundary, i.e. the freestream velocity (U_∞) for a boundary layer, the Reynolds number, $Re_\infty = \frac{U_\infty \delta}{\nu}$ can be interpreted as a ratio of inertial to viscous forces. The same procedure and interpretation can be made for pipe and channel flows as well. For sufficiently high Reynolds number, these flows become turbulent, a chaotic flow state characterized by instantaneously fluctuating flow fields and enhanced mass, momentum, and thermal mixing, leading to, among other things, increased skin friction drag. Several texts have been written discussing the details of these flows, e.g. [49, 53, 57, 58]. Here, a brief overview of relevant observations of turbulent boundary layer flows will be provided.

1.1.1 Mean flow properties

Though chaotic in nature, canonical turbulent flows have been found to have robust mean characteristics. Thus, the velocity field of such a flow is often separated into a mean and fluctuating component using the Reynolds decomposition:

$$U = \overline{U} + u\,, \tag{1.5}$$

where $\overline{U}$ is the temporal mean velocity (or simply mean velocity), and u is the fluctuation about the mean. The temporal mean operation, denoted by $\overline{(\cdot)}$, is estimated by an ensemble average by invoking the assumption of ergodicity of the flow. For fully developed internal shear flows or boundary layer flows under the locally-parallel-flow assumption, only the streamwise component of the mean velocity is considered, as the other components are very small or zero by the geometry, and this component is a function of only y, i.e. $\overline{U} = \overline{U}(y)$.

In turbulent boundary layer flows, the wall-normal profile of the mean velocity has been observed to contain two sets of dynamically relevant scales, defining two regions of the flow where each scaling holds. In the ‘outer’ region farther from the wall, the flow is dominated by the inertial terms in Navier-Stokes and the relevant length and velocity scales are the boundary layer thickness (δ) and freestream velocity (U_∞), respectively. U_∞ is the streamwise velocity of the flow far from the wall, where the shear-stress gradient is zero. δ is defined as the y location at which the mean profile attains 99% of the freestream value. As the choice of 99% is somewhat arbitrary, an alternative or accompanying integral length scale that is often used is the momentum thickness, θ, defined for an incompressible (uniform density) flow as:

$$\theta = \int_0^\infty \frac{\overline{U}(y)}{U_\infty}\left(1 - \frac{\overline{U}(y)}{U_\infty}\right) dy\,, \tag{1.6}$$

which is related to the reduction in the time rate transfer of momentum due to the presence of the boundary layer versus an equivalent inviscid flow, matching the freestream velocities and mass flow rates. θ defines the corresponding momentum thickness Reynolds number, $Re_\theta = \frac{U_\infty \theta}{\nu}$, which is a frequently used parameter when comparing turbulent boundary layer data.

In the ‘inner’ region very near the wall, the viscous terms dominate and the relevant scaling quantities are the kinematic viscosity (ν) and the mean shear stress at the wall,

$\tau_w = \rho\nu \left.\frac{\partial \overline{U}}{\partial y}\right|_0$. These quantities are used to define the friction velocity, $u_\tau = \sqrt{\frac{\tau_w}{\rho}}$, which in turn is used to define a viscous length scale, $\delta_\nu = \frac{\nu}{u_\tau}$. Scaling using u_τ and δ_ν is commonly referred to as inner scaling, and inner scaled quantities are typically denoted by the superscript +. The friction Reynolds number is correspondingly defined as $Re_\tau = \frac{u_\tau \delta}{\nu} = \frac{\delta}{\delta_\nu} = \delta^+$, and can be thought of as the scale separation between the outer and inner length scales. Under inner scaling, the mean velocity profile has been found to collapse near the wall for a wide range of Re_τ and different wall-bounded geometries [49].

Pope (2001) [49] defines the outer region of the flow to be $y^+ \gtrsim 50$ and the inner region $y/\delta \lesssim 0.1$. Thus, with sufficient scale separation (i.e. sufficiently high Re_τ), there is a region of overlap where both inner and outer scalings hold. This overlap leads to the famous result of a logarithmic region within the mean profile, the so-called ‘log law’:

$$\overline{U}^+ = \frac{1}{\kappa}\log y^+ + B\,, \tag{1.7}$$

where B is a constant and κ is the Kármán constant. Pope (2001) [49] defines the wall-normal range where the log law holds to be $30\delta_\nu < y < 0.3\delta$. Among other consequences, the log law allows experimentalists to estimate the value of u_τ by fitting equation 1.7 to mean velocity data, a process known as the Clauser chart method [15].

A brief mention of critical layers is given here, with a more thorough discussion provided in Maslowe (1986) [44] and Schmid & Henningson (2001) [54]. Critical layers are a key idea in classical stability analysis of parallel shear flows, and are located at the wall-normal height, y_{CL}, at which the wave speed, c, of a given traveling wave matches the base flow profile, i.e. $U_{\mathrm{base}}(y_{\mathrm{CL}}) = c$. These concepts have found utility in fully turbulent flows as well; for example, McKeon & Sharma (2010) [45] found critical-layer-type behavior in their resolvent-based investigation of a turbulent pipe flow. For a turbulent flow, the critical layer is based off the turbulent mean profile, i.e. $\overline{U}(y_{\mathrm{CL}}) = c$. y_{CL} underpins the mode shape structure for many traveling wave perturbations, as will be seen in later chapters.

1.1.2 Coherent flow structures

In addition to robust statistical characteristics, many researchers have observed recurrent structural flow features in instantaneous data of turbulent boundary layer flows. These ‘coherent structures’, so called because of their spatio-temporal coherence, are thought to play key dynamical roles in the behavior and self-sustaining nature of turbulence. Coherent structures are often broadly categorized as small-scale motions, corresponding to near-wall cycle (NWC) features with size $\mathcal{O}(\delta)$, and large-scale and very-large-scale motions (LSMs and VLSMs, respectively), associated with turbulent bulges and organization of bulges, $\mathcal{O}(2-3\delta)$ and $\mathcal{O}(10\delta)$ respectively [1]. The near-wall cycle is characterized by streamwise velocity streaks and quasi-streamwise vortices appearing near the wall, and is believed to play a critical role in the self-sustaining nature of turbulence. LSMs are associated with turbulent bulges and thought to be made of organized packets of hairpin vortices. At high enough Reynolds numbers, these packets are believed to further streamwise align into superstructures deemed VLSMs, centered in the logarithmic region of the flow [1]. LSMs and VLSMs are considered dynamically relevant, as they carry a significant portion of the turbulent kinetic energy and Reynolds shear stress [24].

Though localized in different regions of the flow and often at vastly different scales, several studies have found the behavior of these large- and small-scale motions to be correlated. In particular, the studies of Hutchins & Marusic (2007) [28] and Ganapathisubramani et al. (2012) [22] have suggested that large-scale motions act to modulate the amplitude and frequency of the small scales. In these studies, the amplitude of the small-scales was found to be positively correlated with the value of the large-scale near the wall and negatively correlated away from the wall. The observed frequency modulation was restricted to the near-wall region, where the frequency corresponding to the peak in small-scale activity was found to increase with increasing value of the large-scale.

The idea of coherent structures is very enticing from a flow modeling perspective, as it may allow for critical flow features to be described and predicted without requiring huge amounts of information. Several advances in understanding are still necessary to fulfill that potential, but coherent structures continue to play a central role in the field of turbulence.

1.2 Compliant surfaces

As mentioned at the beginning of this chapter, there are many practical incentives to develop control mechanisms in turbulent flows to achieve performance goals, one example being reduction of turbulent skin-friction drag. Many potential control schemes have been explored, one of which is the compliant surface. A compliant surface is one that deforms under and modifies the surrounding flow, and in its simplest implementation offers a passive and cost-effective means of flow control.

A thorough review of the literature and history is given in Gad el Hak (2002) [21], with a brief overview provided here.

The seminal publications by Kramer (1957, 1960) [37–39] were inspired his observation of wave-like ripples forming on the skin of dolphins as they swam. Kramer hypothesized that, like the dolphins, one could reduce the frictional drag on a ship by applying a compliant coating to its hull, tuned to damp Tollmien-Schlichting (T-S) instabilities and delay transition to turbulence. He created flexible rubber coatings that were filled with silicone oil or other viscous fluids, and applied the coatings to a model that he then towed behind a motor boat in Long Beach Harbor, California. Kramer reported drag reduction in excess of 50% with these coatings, a result which quickly drew the attention of many researchers. Several follow-up studies failed to replicate Kramer's drag reduction findings, leading to a good deal of controversy to surround the quickly booming field of compliant coatings. It is now appreciated that experimental investigations concerning drag reduction via compliant surfaces require extremely well controlled conditions. Many factors such as freestream turbulence and slight geometrical surface defects can adversely affect the drag outcome, and are likely a large part of the inconsistent results in the early literature. Though there was a large body of skeptics, the numerical and analytical studies by Carpenter [5, 6] and Carpenter & Garrad [7] and the experiments of Gaster [23] suggested that a Kramer-type surface could indeed delay transition and yield significant drag reduction. Carpenter et al. (2000) [8] suggested that an optimized coating may in fact play an important role in the efficient swimming of dolphins by maintaining laminar flow along their skin, as envisioned by Kramer.

Much of the early compliant coating work centered around reducing skin friction drag by delaying the onset of turbulence. The problem of reducing drag in an already turbulent flow was understandably much more challenging. However, some experimental studies have found encouraging results. Lee et al. (1993) [40] performed water tunnel experiments of a turbulent boundary layer with a single-layer viscoelastic compliant surface and found that the low-speed streaks associated with the near-wall cycle had an increased spanwise spacing and elongated spatial coherence over the smooth-wall case. In addition, the authors observed a reduction in streamwise turbulence intensity and Reynolds shear stress, suggesting a possible interruption of the self-sustaining turbulence cycle. In the water tunnel experiments of Choi et al. (1997) [9], drag reduction on a slender body of revolution with a single-layer viscoelastic coating was reported, with a maximum drag reduction of

7%. However, the strain-gauge skin friction measurement error was estimated to be as high as ±4%, and so this drag reduction should be interpreted cautiously. A common observation of these experimental studies was the importance of the interaction between the surface and the coherent structures in the flow. A recent experimental effort has been made by Zhang et al. (2015, 2017) [63, 64], who leveraged modern flow and surface measurement techniques. The authors studied a relatively stiff polydimethylsiloxane (PDMS) wall in a turbulent channel flow, using tomographic-PIV and Mach-Zehnder interferometry to obtain the 3D flow field and 2D surface deformation field. This work was able to categorize classes of surface deformation waves and propose potential scalings for these classes.

As computational capabilities have grown in recent decades, several DNS studies have been performed on turbulent channel flows with compliant walls and reported somewhat less optimistic results than experiments. Xu et al. (2003) [62] simulated a turbulent channel flow with a compliant wall modeled as a spring-supoprted plate and found little change to the turbulent skin friction. In the work of Fukagata et al. (2008) [17], an anisotropic compliant wall led to 8% maximum drag reduction rate; however, the drag was found to increase as the computational domain was increased. Kim & Choi (2014) [36] parametrically studied the effect of stiffness of the compliant walls and observed that stiff materials led to minimal changes in the skin-friction drag and coherent structures, while soft materials led to significant drag increase due to resonant surface behavior.

Clearly the daunting parameter space, difficulty in measuring skin-friction drag, and resource-intensive nature of simulations and experiments make the question of turbulent drag reduction via rationally-designed compliant surfaces incredibly challenging, and one that will likely require the advent of new and refined reduced-order modeling tools.

1.3 Input-output analysis

The current work aims to take a different approach to other experimental studies of compliant surfaces in turbulent boundary layer flows. Rather than consider the material response to the broad spatio-temporal spectrum typical of turbulence, this work attempts to study the response to a single, externally-forced flow structure in an otherwise turbulent flow. This input-output type analysis intends to reduce the complexity of the problem and provide a fundamental framework with which to build up to the full flow. Such an approach is motivated by the dynamical significance of coherent structures in canonical and compliant-wall turbulent flows. In this work, the novel technique of dynamic roughness is employed to force the flow structure. This analysis also leverages the resolvent framework of McKeon & Sharma (2010) [45] to guide the interpretation of the experimental results. Both of these methodologies are discussed in the following sections.

1.3.1 Overview of dynamic roughness

Jacobi & McKeon (2011) [33] studied a turbulent boundary layer subject to a short, static strip of two-dimensional roughness elements in a wind tunnel. Through hot-wire anemometry and particle image velocimetry (PIV) measurements, they observed that the spatially impulsive roughness patch had a prolonged imprint on the downstream flow in the form of two internal layers that developed from the roughness. Each layer corresponded to the changes in the boundary condition over the roughness, going smooth-to-rough and then rough-to-smooth. The signature of the internal layers was readily observed in the flow statistics, with the mean profile exhibiting a deficit (most notably for $y/\delta \lesssim 0.3$) and the streamwise turbulence intensity showing a distinct hump (centered at $y = 0.08\delta$) over the smooth-wall case. Jacobi & McKeon (2011) drew comparison with a previous study [2] and interpreted the hump in turbulence intensity as a stress bore, or local region of increased shear stress, introduced by the roughness that propagated away from the wall. Indeed, as the flow recovered downstream, the hump in turbulence intensity drifted away from the wall, consistent with the stress bore analogy, and allowed the wall-normal growth rate of the internal layers to be estimated by a power-law fit. Though the signature of the roughness decayed in the streamwise direction, it persisted and remained discernible over the 10δ measurement domain.

Building on these finding, Jacobi & McKeon (2011) [32] considered the same roughness element and imparted a temporal oscillation using a crank-shaft assembly and DC motor. They then studied the flow response to the now dynamic roughness. They were able to decompose the flow response into spatially small-scale and large-scale components, with the former congruent with the static effects of the previous study, and the latter associated with an organized wave introduced by the roughness dynamics. The large-scale, dynamic effects were found to permeate the mean and higher-order statistics, and took on critical-layer-type velocity mode shapes. These effects persisted for 20δ from the roughness, highlighting the potential impact of a relatively small, local control mechanism on the downstream life of the flow.

Later, Duvvuri & McKeon (2015) [14] performed wind tunnel experiments with hot-wire measurements, using a similar dynamic roughness setup to study the interaction between the roughness-forced, synthetic large scale and the triadically consistent small scales. Rather than a strip of two-dimensional elements, Duvvuri & McKeon (2015) used a single two-dimensional rib and actuated with reduced amplitude versus Jacobi & McKeon (2011) [32], so as to not modify the mean profile as substantially. The authors reported a streamwise wavelength of the synthetic structure on the order of 15δ, comparable to the scale of VLSMs in high-Reynolds number flows. They calculated the correlation coefficient between the synthetic large scale and the envelope of the triadically coupled small scales, and found that triadic envelope was nearly perfectly in-phase with the synthetic mode near the wall, and jumped near the critical layer to be almost exactly out-of-phase. This was interpreted as a phase organization by the synthetic large scale, acting to modulate the amplitude of the small scales. This is analogous to the observation of Hutchins & Marusic (2007) [28] discussed in Section 1.1.2, and demonstrates the utility of studying the interactions in turbulent flows through the lens of an externally-introduced synthetic scale.

Dynamic roughness offers a tractable means to investigate flow structure dynamics and interactions, as well as provides a basis from which to understand and evaluate other types of flow control schemes, as discussed in McKeon, Jacobi, & Duvvuri (2018) [46].

1.3.2 Resolvent framework

Dynamic roughness forcing introduces a dominant synthetic scale into a turbulent flow. This lends itself to a reduced-order-modeling framework, with the synthetic scale serving as a deterministic input, and the velocity/surface response interpreted as the output. Such input-output frameworks have been explored in previous studies. In the turbulent channel flow experiments of Hussain & Reynolds (1970, 1972) [26, 27], spanwise-constant dynamic disturbances were generated by vibrating ribbons located near the wall. The authors attempted to model the downstream behavior of the disturbances by the laminar Orr-Sommerfeld equations, augmented with various closure schemes to model the effect of the Reynolds stresses. Jovanović & Bamieh (2001) [35] studied the linearized NSEs for a laminar channel flow. The authors considered a spatio-temporally impulsive external forcing (representative of transitional 'turbulent spots') that mapped to the velocity response through the linearized resolvent operator. Hwang & Cossu (2010) [30] also explored the resolvent operator, but with respect to the turbulent mean profile instead of the linearized base flow. They use an eddy viscosity term to model the effect of the Reynolds stresses to circumvent the closure problem.

In this work, the modeling framework considered is the resolvent operator-based formulation put forward by McKeon & Sharma (2010) [45]. In this method, the Navier-Stokes equations for a turbulent flow are recast into an input-output form, with the nonlinear term explicitly retained and acting to force the velocity through the linear dynamics captured in the resolvent operator. The turbulent mean profile is assumed known (via experiments, simulations, or models) and is incorporated into the resolvent operator, serving as the only data input for the analysis. The resolvent operator is discretized and a singular value decomposition (SVD) is performed to identify the operator's singular response and forcing modes, and the corresponding singular values. McKeon & Sharma (2010) [45] found that this operator is low rank for a range of physically relevant wavenumber vectors, which allows for a rank-1 approximation to be made, significantly reducing the computational cost of the analysis. This rank-1 model has been found to approximate key statistical ([47]) and structural ([42, 45, 46, 55]) features of the flow. What's more, the analysis was extended by Luhar et al. (2015) [43] to consider a compliant-wall boundary condition and compared favorably to DNS studies [17, 36, 62]. Thus, it is used as a lens through which to view the results of the compliant surface experiments. Greater detail on the precise formulation will be provided in Chapter 7.

1.4 Approach

In the present work, a dynamic roughness element is used to force a flat plate turbulent boundary layer and study the interaction between the roughness-forced synthetic mode and an embedded compliant surface. Rather than aim for a particular performance goal such as turbulent drag reduction, this work seeks a well-characterized input and measurable and attributable output to contribute to a fundamental framework, with an ultimate view to extend to fully complex flows and surfaces. This work provides an experimental demonstration of the efficacy of the compliant-wall resolvent framework, as it is used to predict subtle modifications to the synthetic velocity structures. In addition to the compliant surface study, this work seeks to contribute to the understanding dynamic roughness by performing spatially resolved measurements and exploring the relevant parameter space.

Chapter 2 describes the design, apparatus, and methodology developed for these experiments. This work was done in a water tunnel, which has two significant benefits for this type of study. First, the higher density of water enables flow-driven surface deformations more readily. As discussed in Gad el Hak (2002) [21], there have been some studies with favorable results of compliant surfaces in air flows, but the higher fluid-to-surface mass ratio of water allows much more practical surfaces to be designed and tested. The second advantage of water is the inherently longer timescales, which grant access to higher non-dimensional frequencies and thus shorter streamwise structures than previous studies [14, 32]. This allows for a more streamwise-resolved picture of the synthetic scale to be developed. This chapter also discusses gelatin as the selected compliant material and a simple characterization of its properties. Flow measurements were made with two-dimensional particle image velocimetry (2D-PIV) and surface measurements made through stereo digital image correlation (stereo-DIC). Stereo-DIC is not a common measurement technique for compliant surface studies due to the difficulty in creating and maintaining a reliable speckle pattern on the surface, particularly in a submerged environment. A speckle generation method has been developed that overcomes these challenges. These measurement techniques and processes are also discussed in the chapter.

Chapter 3 provides a characterization of the flat plate facility in the water tunnel, as it was newly developed for this study. Typical flow statistics are compared to DNS [60, 61] to ensure a canonical flow base case.

Chapter 4 presents the data from the smooth-wall, dynamic-roughness-forced (SW-DRF) studies, with the dynamic roughness actuated sinusoidally from the flat plate in a similar manner to previous work [14, 32]. The signature of the synthetic mode on the flow statistics is discussed and found to agree closely with the internal layer-structures of Jacobi & McKeon (2011) [33]. The velocity field is triple decomposed following Hussain & Reynolds (1970) [26], and the synthetic mode identified through phase-averaging of the data. Spanwise-spaced 2D-PIV planes are acquired to provide insight on any three-dimensionality of the flow. The temporal Fourier mode corresponding to the roughness forcing frequency is extracted and used to characterize the streamwise wavenumber of the synthetic mode. A full streamwise-temporal Fourier decomposition is employed and the spatial nature of the synthetic mode is explored in a manner not previously done.

Chapter 5 discusses the stereo-DIC measurements made on the compliant-wall without the dynamic roughness forcing (CW-unforced). This ‘unforced’ response is characterized in order to determine whether the ‘forced’ surface response is attributable to the synthetic mode from the roughness, or an amplification of a naturally occurring response. A number of deformation features are observed and characterized.

Chapter 6 follows with the stereo-DIC measurements of the compliant-wall, dynamic-roughness-forced (CW-DRF) study. Comparison of the CW-unforced and CW-DRF DIC data provide confidence that an identifiable portion of the surface response is due to interaction with the synthetic mode. The PIV data are processed in a parallel manner to the SW-DRF studies, in preparation to compare the spatio-temporal Fourier modes and investigate the effect of the compliant-wall.

Chapter 7 outlines the compliant-wall resolvent framework used to guide the analysis of the experimental data through prediction of flow features, namely a virtual wall. The experimental mode shapes are then examined, with some favorable comparisons with the resolvent predictions, but the anticipated virtual wall is not distinguishable. An additional conditional averaging approach is taken, which does reveal aspects of the virtual wall in the mode shapes. This suggests that the elastic, gelatin surface is acting to oppose the wall-normal velocity near the wall, in a manner similar to the wall jets of opposition control.

Chapter 8 closes the thesis with concluding remarks and potential future work.

Chapter 2

EXPERIMENTAL DESIGN

The study of a gelatin surface interacting with a dynamic-roughness-forced flow was developed as three separate sets of experiments of increasing complexity. First, a flat-plate boundary layer facility was constructed and tested. Next, the dynamic roughness apparatus was designed and implemented. Finally, the fabrication and molding process for the gelatin surface were developed. All flow measurements were made through 2D particle image velocimetry (2D-PIV) and surface deformation measurements were primarily made through stereo digital image correlation (stereo-DIC). Preliminary surface deformation measurements were made with a Keyence laser displacement sensor as a qualitative diagnostic tool, but were not used in the analysis and will only be mentioned briefly when relevant. Details of each experimental stage, the 2D-PIV and stereo-DIC measurements, and phase-locking process are presented in this chapter.

2.1 Flat-plate boundary layer facility

All the experiments were done in the NOAH water tunnel in GALCIT. The test section of the tunnel is 1500 mm long, 460 mm deep, and 460 mm wide, with Plexiglas side walls and bottom. The tunnel freestream velocity calibration is

$$U_\infty(f_p) = 1.62 f_p - 0.677\,,$$

where U_∞ is the tunnel freestream velocity in cm/s and f_p is the pump frequency in Hz. For all experiments, the pump was operated at 18.94 Hz for an unobstructed freestream velocity of 30 cm/s.

The flat plate facility was designed as a series of acrylic plates sections, as shown in the SolidWorks drawing in Figure 2.1. Measurements were performed on the underside of the plate to avoid free-surface effects and to have the dynamic roughness actuator to above the water. Accordingly, the positive coordinate directions used are streamwise (x) aligned with the tunnel's downstream, wall-normal (y) aligned with the outward-pointing normal of the plate underside, and spanwise (z) along the test section's width (right-hand consistent), as illustrated in Figure 2.1. Dimensions of experimental components will be provided in streamwise, wall-normal, and spanwise order unless otherwise specified. The full plate dimensions are 1280 mm long (excluding the trailing-edge flap), 32 mm thick, and 440 mm wide, nearly spanning the length and width of the tunnel test section. The leading-edge and middle sections are each 603 mm long, and the trailing-edge section is 178 mm long (excluding the flap), with a 50.5 mm overlap between each section. The leading-edge section has an elliptical edge with semi-major and semi-minor axes of 63.5 mm and 31.8 mm, respectively. Acrylic plates were selected to minimize laser reflections off the plate surface and reduce weight. The modular plate design allowed the middle section to be refitted per the needs of the current experiment. Large pockets were cut out of the leading and middle sections to reduce weight. The joins between the plates use screws and spring washers in tandem to adjust the transition from one plate to the next to be smooth within ~25 um, as confirmed by a dial indicator. The trailing-edge flap angle was set to about 30° to bias the leading-edge stagnation point to the underside of the plate, as confirmed through dye visualization.

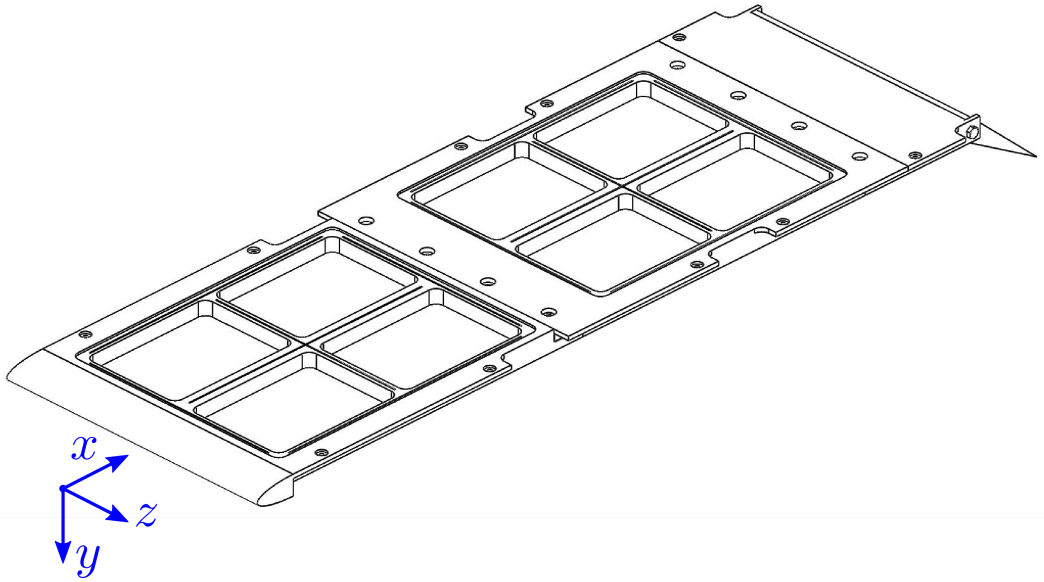

Figure 2.1: Model of the full acrylic plate assembly, with leading-edge, middle, and trailing-edge sections.

The plate was submerged 230 mm under the free surface (about half the water depth) with an aluminum 80/20 frame, supported by the rails on top of the tunnel side walls. The sides of the plate were sealed to the tunnel walls using latex tubing running the length of the apparatus to minimize any flow between the top and bottom of the plate.

Measurements were made over the middle plate section, where the freestream velocity ranged between 33.4 and 36.4 cm/s. As mentioned, the flow fields were measured using 2D-PIV. Data were acquired for an unmodified, flat-plate boundary layer to ensure a canonical flow base case. These data will be presented in Chapter 3.

2.2 Dynamic roughness apparatus

A dynamic roughness element was used to force the turbulent boundary layer in a similar manner to Duvvuri et al. [14]. The roughness element is two-dimensional (spanwise-constant), consisting of a thin rib, 1.5 mm wide, 6.2 mm tall, and 304 mm long (70% of the plate's width), protruding from a rectangular body, with a 13 mm diameter set screw shaft coupler attached, and is shown in Figure 2.2. Pockets were cut into the roughness body to reduce the dynamic load on the actuator. The entire roughness element is made of aluminum that was hard anodized to prevent corrosion. The time-varying roughness height will be denoted by $h(t)$, where $h = 0$ indicates that the top of the rib is flush with the plate and $h > 0$ indicates that the rib is protruding into the flow. The actuation condition of the roughness height is parameterized by the motion amplitude, either peak-to-peak or rms, $h_{\mathrm{p-p}}$ or h_{rms}, respectively, and the motion frequency, either ordinary or angular, f_{f} or ω_{f}, respectively, where the subscript 'f' indicates 'forcing'.

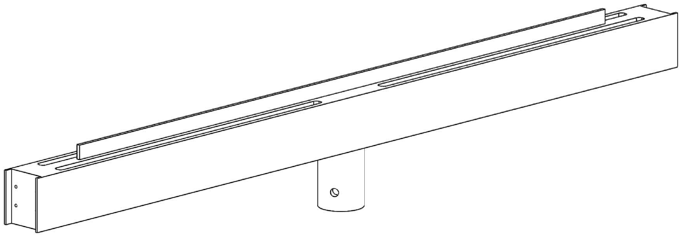

Figure 2.2: Model of the roughness element.

A middle plate section was designed with a cavity and through-slot to accept the roughness element, as shown in Figure 2.3. The slot is located 626 mm downstream of the leading edge, with dimensions 2.2 mm wide, 3.2 mm deep, and 307 mm long, to provide tight clearance when the roughness was inserted and aligned, as illustrated in Figure 2.4. The clearance was made as small as possible to minimize flow through the slot, while still allowing a feasible alignment process. This flow was tested by injecting dye through the slot and actuating the rib with the water tunnel off. A Stokes-like flow was observed, where a small amount of dye was dragged out as the rib extended, and pulled back in as the rib retracted, confirming that there was no jet-like flow through the slot. For all experiments involving dynamic roughness, the origin of the coordinate system is located on the underside of the plate, at the downstream-edge, spanwise-center of the slot, as illustrated in Figures 2.3 and 2.4.

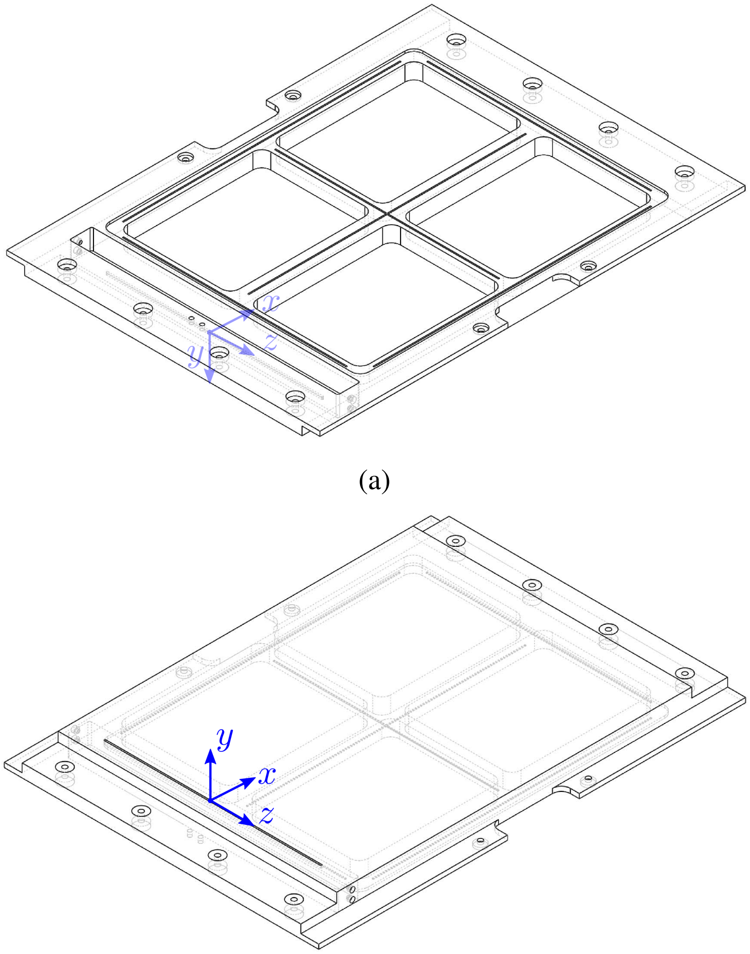

(a)

(b)

Figure 2.3: Model of the plate section for smooth-wall, dynamic roughness experiments: (a) top view, (b) bottom view. Coordinate system and origin illustrated.

A Bose ElectroForce LM1 linear motor was used to actuate the roughness element. Among other capabilities, this motor is able to execute a singly periodic displacement with amplitude precision of ~1 um and frequency accuracy of ~0.1 mHz, using built-in optical encoders to construct a compensating transfer function between the control signal and motor shaft displacement. The motor's encoders also serve as a time-resolved, high-resolution roughness displacement measurement. The motor was suspended above the test section (motor shaft pointed downward), and connected to the roughness element via a 13 mm diameter, 457 mm long shaft and set screw coupler, as shown in Figure 2.5.

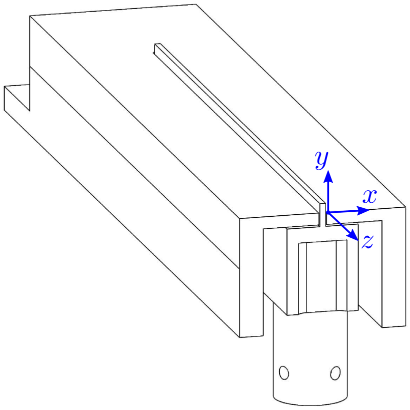

Figure 2.4: A cross-sectional view of the roughness element and slot alignment.

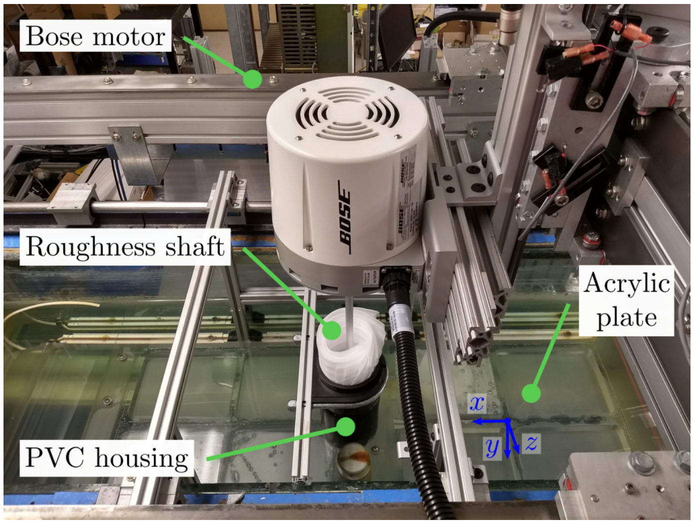

Figure 2.5: Photo of the smooth-wall, dynamic roughness experimental setup. The roughness element is connected to the Bose motor, which is mounted to the motorized gantry frame. A PVC-pipe housing is placed around the roughness shaft to shield the element from the flow.

The motor-roughness system was mounted to a motorized gantry frame in the NOAH lab, also shown in Figure 2.5. The gantry frame uses stepper motors to enable sub-mm translation along three axes. Initially, a shaft bearing was mounted to the plate and used to align the roughness shaft to slot. The slight contact between the shaft and bearing appeared to slightly distort the displacement waveform through amplified harmonic content. More pressingly, this contact transferred the motor's actuation to direct vibrations in the plate, which was later found to excite significant response in the gelatin sample.

Thus, to best isolate vibrations from the plate, the shaft bearing was removed and the roughness element was ‘freely’ suspended in the tunnel. The gantry frame was used to establish and maintain alignment between the roughness and the slot in the plate section. To minimize fluid loading and preserve the displacement waveform, the roughness shaft was encased on the non-measurement side by a cylindrical housing, as seen in Figure 2.5. This provided a local region of quiescent flow during operation and noticeably improved the motor’s performance. Thin aluminum plates were machined to cover the plate inset and roughness body, in order to reduce any cavity flow. The result of the specialized equipment, design choices, and careful alignment processes was a precise, repeatable, pure-tone displacement signal, as illustrated by the encoder signal in Figure 2.6. The signal, h_{norm}, has been mean subtracted and normalized to have unit amplitude, and was acquired with the water tunnel running. The time trace in Figure 2.6a is predominantly a single-frequency sinusoid, and the power spectrum in Figure 2.6b confirms and quantifies this, indicating that the next harmonic peak is more than three orders of magnitude smaller than the fundamental frequency. These data are for an actuation with $h_{\mathrm{p-p}} = 2.5$ mm and $f_{\mathrm{f}} = 5$ Hz, which had the greatest and still minute distortion. Better results are obtained for other actuation conditions, with some having a spectral peak separation greater than a factor of 10^4. Such ideal actuation signals were key enablers for the unique, spectrally-targeted analysis in this work.

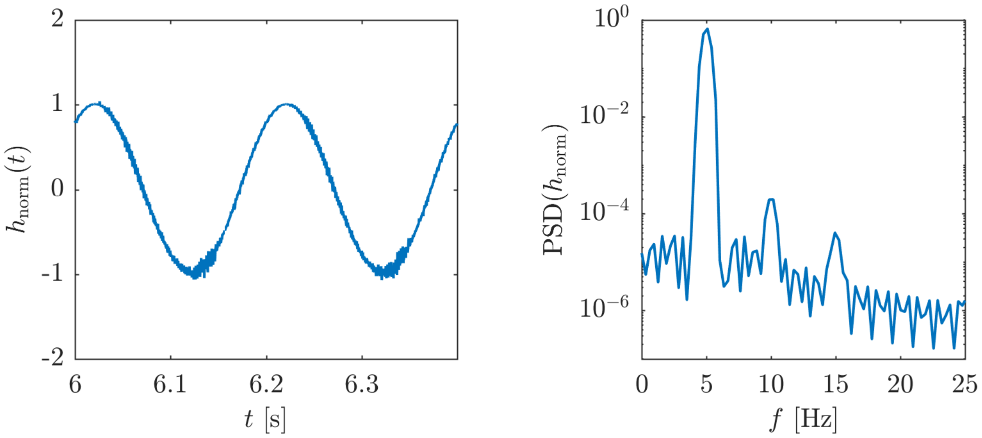

(a) (b)

Figure 2.6: Encoder signal of the motor/roughness element displacement: (a) time signal, (b) power spectrum. The signal is single-frequency to good approximation.

2.3 Gelatin surface

Naturally, the first step in designing the compliant surface portion of this study was determining a suitable material. As previously emphasized, the goal of this work was not to achieve a particular performance metric (e.g. drag reduction), but rather to elicit and study a measurable surface response to the synthetic structure generated by the dynamic roughness. To that end, it was key that the material be able to be made sufficiently soft, to promote detectable deformations. Anticipating an iterative design process for the fabrication and molding of the compliant sample, it was desirable that the material be inexpensive and simple to manufacture. Lastly, a linearly elastic material was ideal to facilitate the modeling of the surface's behavior.

Gad el Hak (1987) [20] mentions three 'easy-to-make' materials: plastisol gel, gelatin, and polydimethylsiloxane (PDMS). PDMS is a commonly studied and well-documented material, used in many works [14, 63]. However, a solidified gelatin-water mixture is able to be made the softest, the least expensive, and known to behave linear elastically for small deformations [12]. Thus, gelatin was selected as the material for study.

As mentioned, the process of fabricating the gelatin samples is fairly simple. Briefly, boiling water is added to (Knox, unflavored) gelatin powder, the two are mixed thoroughly and allowed to cool, and the mixture is poured into a mold. The full procedure took care to minimize bubbles and gelatin clumps, and is outlined in Appendix A. A gelatin-water ratio of 4:100 was used in this study, which is near the minimum ratio for which a cohesive solid still forms.

To characterize the elastic properties, compression tests were performed with an Instron 5500, on 25.4×25.4 cm^2 cylindrical gelatin samples. Though cylindrical molds were used in fabrication, the samples tended to 'slump' due to their softness. A photo of the test setup is provided in Figure 2.7. A plastic plate was affixed to the compressing arm to ensure full and flat contact with the sample's top face. The sample displacement was measured optically using an EIR LE-01 laser extensometer, which uses a high-speed scanning laser and a CCD camera to measure the distance between strips of reflective tape. The extensometer has a measurement range of 8-80 mm, resolution of 1 um, repeatability of ±1 um, and a scan rate of 100 scans/s [50]. In these tests, the reflective strips were placed on side of the compressing plastic plate and the metal base supporting the sample. Tests were performed at displacement rates of 5 and 10 mm/min, with identical results. Thus rate-dependent, viscoelastic effects were deemed negligible. Four samples were fabricated and each

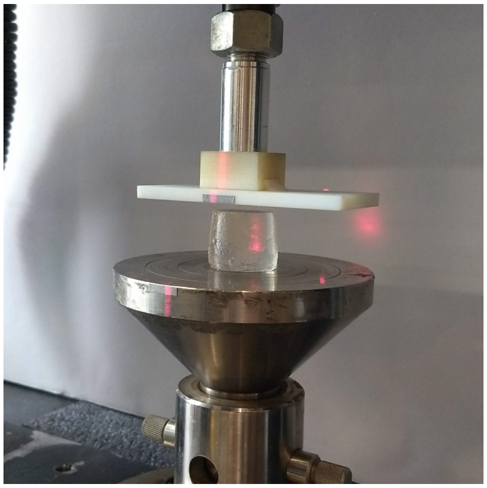

Figure 2.7: Compression test setup

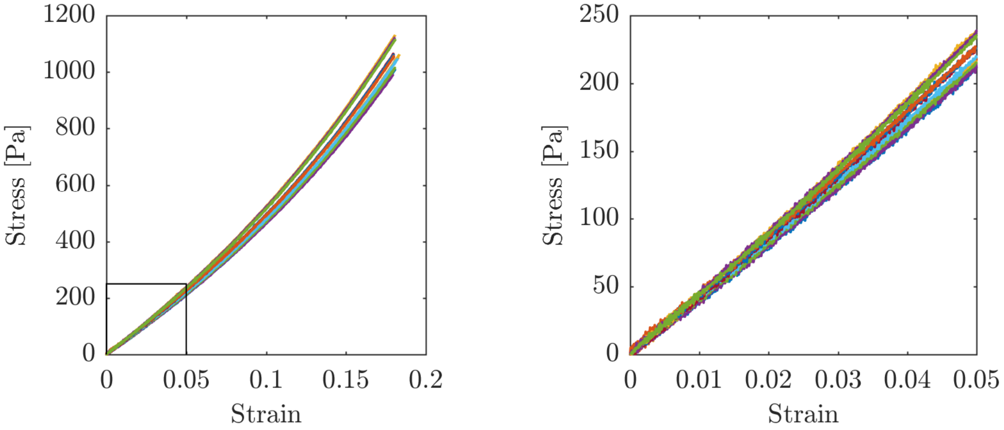

(a)

(b)

Figure 2.8: Stress-strain curves from the compression tests.

was tested three times consecutively at a displacement rate of 10 mm/min and a total displacement of 5 mm. Force and displacement time signals were recorded and used to calculate stress-strain curves, as shown in Figure 2.8. The data reflect a linearly elastic behavior for small strains (Figure 2.8b), which were expected for the flow-driven deformations. From the slopes of these curves, the average Young's modulus, E, was calculated to be 4.5 kPa, with a standard deviation of 0.2 kPa, which was consistent with values reported by Gad el Hak (1986) [19]. This is extremely compliant; for comparison, the PDMS studied by Zhang et al. [63] had a Young's modulus of ~1 MPa. It is noted that while these simple compression tests may not have been as accurate as other methods, e.g. tensile tests, they were suitable for an estimate of the elastic properties, particularly for such a soft material.

The Poisson's ratio, ν_s, was assumed to be 0.5, i.e. the material was assumed incompressible, as is typically done with gelatin [12]. With two elastic moduli known, the remaining elastic properties are determined for a homogeneous, isotropic, linear elastic material. Of particular relevance is the shear modulus, G, which determines the shear or transverse wave speed of the solid, U_s:

$$G = \frac{E}{2(1+\nu_s)} \sim 1.4 \text{ kPa} \tag{2.1}$$

$$U_s = \sqrt{G/\rho_s} \sim 1.2 \text{ m/s}\,, \tag{2.2}$$

where ρ_s is the density of the gelatin (taken to be the same as water due to the mixture ratio). The shear wave speed was several factors higher than the freestream velocity (~0.3 m/s), and thus hydroelastic instability waves were not expected [19]. This provided confidence that most measured deformations would be attributable to the material's response to the dynamic roughness forcing. The shear wave speed was also used to estimate the wave speeds of potential surface waves in the gelatin. Rayleigh waves are surface waves that propagate in a semi-infinite elastic solid. For incompressible materials, the Rayleigh wave speed is 95.5% of the shear wave speed [16], which was 1.15 m/s for the gelatin in consideration. The finite thickness of the gelatin sample (relative to the wavelength of the deformations) can be accounted for through generalized Rayleigh waves [4] and Love waves [18]. For completeness, the generalized Rayleigh and Love wave speeds were calculated to be 1.18 and 1.32 m/s, respectively, assuming the gelatin to be incompressible and incorporating the sample geometry and the observed deformation wavelengths. In general, the semi-infinite-domain Rayleigh wave speed is a lower bound on surface wave speeds for a given material, and as will be shown in Chapter 5, the deformation waves measured in the surface were found to be lower than the Rayleigh wave speed of 1.15 m/s. More discussion will be provided in Chapter 5.

To integrate the gelatin sample into the flat-plate facility, a middle plate section was designed with the same cavity and slot for the roughness element as previous discussed, with the addition of a large, rectangular inset beginning 21.2 mm downstream of the roughness slot. A SolidWorks model is provided in Figure 2.9. The inset dimensions are 305 mm long, 25.4 mm deep, and 343 mm wide, to match the roughness element's spanwise length and reduce edge effects along the centerline of the sample. This plate section was placed on a leveling apparatus, and the liquid gelatin mixture was poured into the inset. The mixture was then covered with a lubricated, acrylic-backed, Teflon-sheet lid to achieve a flatter surface and a smoother transition from the acrylic plate to the gelatin. The mixture was cooled for 12-16 hours, after which the lid was carefully removed to prevent tearing of the surface. Initially, the rounded corners of the inset had 6.4 mm radii. However, a high rate of tearing at the corners was experienced when removing the lid. The cause of the tearing was suspected to be high stress concentrations due to the small corners. The corner radii were increased to 25.4 mm, which essentially eliminated corner-initiated failure. Figure 2.10 shows a photo of a finished, undamaged gelatin sample. Note in the shown sample that white ink was added to the mixture for testing purposes. The final gelatin samples were translucent.

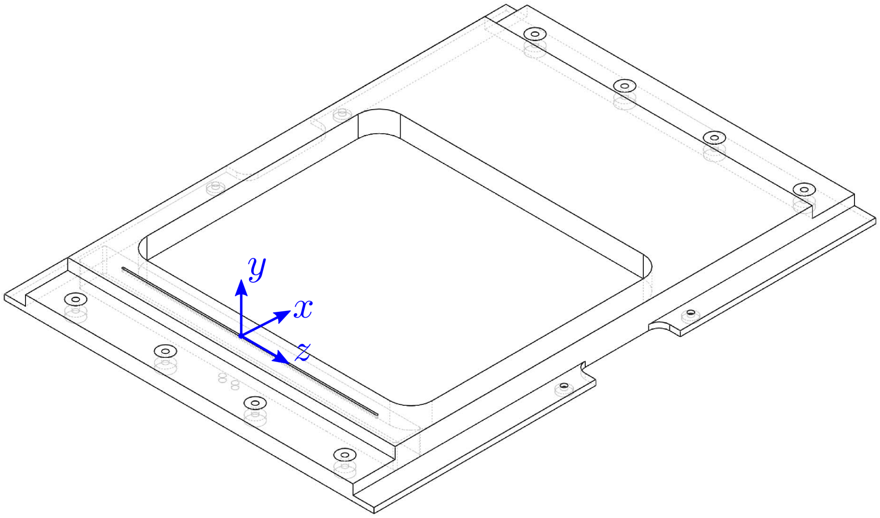

Figure 2.9: Model of middle plate section machined for the gelatin sample

Figure 2.10: A finished gelatin sample. Note the sample pictured was dyed white for a DIC test. The gelatin used in the experiments was translucent.

Once the lid was removed, the sample was left for ~1 hour until the surface was dry enough to receive the speckle pattern, as will be discussed in Section 2.5. After the speckle pattern was applied, the sample was left for another ~1-2 hours for the pattern to dry. The sample-embedded plate section was then integrated with the rest of the flat-plate facility, which would already be suspended above the tunnel test section. This required both a cautious and quick process, as the plate section had to be flipped upside-down such that the gelatin sample faced downward. Once the middle plate section was made flush with the leading and trailing sections, the entire plate was lowered into the tunnel. The dynamic roughness apparatus was then set up and aligned, as discussed in Section 2.2. The gelatin samples had a fairly short lifetime. If left exposed to air for more than a few hours, a sample would begin to evaporate, changing both the surface geometry and material properties. Once submerged, a sample would gradually hydrate and eventually disintegrate into the water, again altering geometry and material properties, as well as degrading the speckle pattern quality. Even with precautions to protect the gelatin from the water, it was estimated that a given sample had a lifetime of one week in the test section before requiring replacement.

As discussed, several measures were taken to make the gelatin surface as level and flat as possible. The surface quality was examined in the PIV images taken for the compliant-wall study. An image, cropped to be near the surface, is given in Figure 2.11. The white pixels for $x \in [0, 21]$ mm are the acrylic plate and for $x > 21$ mm are the gelatin. Clearly the gelatin sample is not level with the plate, as the transition to the surface first rises to about $y \sim 0.6$ mm and gradually falls to below $y = 0$. Not shown in the figure, the surface reaches a minimum height of about $y \sim -0.3$ mm near the sample center and then rises towards the downstream edge. This large bow in the gelatin is well characterized by a parabolic fit, and is likely the result of the material absorbing water and equilibrating to its downward-facing state in the test section. This surface characteristic was addressed in the processing by masking the image below the surface. The varying wall was taken into account in the PIV results by shifting each wall-normal profile to such that the data point nearest to the gelatin surface was moved to the wall-normal location nearest to $y = 0$. This is only a first-order correction, but was chosen to not augment the data more than necessary.

In addition to the bow, the surface also contains a wave-like structure with an approximate wavelength of 18.5 mm and peak-to-peak amplitude of 0.08 mm. After observing this feature, the Teflon lid was inspected for a corresponding signature. Indeed, the lid had small ridges with spacing matching the 18.5 mm. These ridges were caused by the adhesive used to secure the Teflon to the acrylic backing. Though unfortunate, the amplitude of this wavy pattern is much smaller than the bow feature, and so is not expected to be of first-order concern in the analysis. The DIC data later support this, as no energetic content is observed with a matching wavelength.

Both the bow and wave surface traits highlight the difficulty in fabricating 'ideal' compliant surfaces. Given that the bow is likely due to the material hydrating and adjusting to the inverted orientation, there may be few options to prevent it, other than possibly coating the sample with a sealant to lock out the water. This would change the surface properties and would have to be taken into account. The wave feature can likely be avoided by using a smoother adhesive method to bond the Teflon-acrylic lid. Also worth noting is that the surface variation is exaggerated by the aspect ratio in Figure 2.11. Using a true aspect ratio, the variation is barely perceptible. Despite these imperfections in the gelatin sample, a surface deformation is still observed in response to the dynamic roughness forcing, as will be shown in Chapter 6, which demonstrates the utility of targeted forcing in compliant surface research.

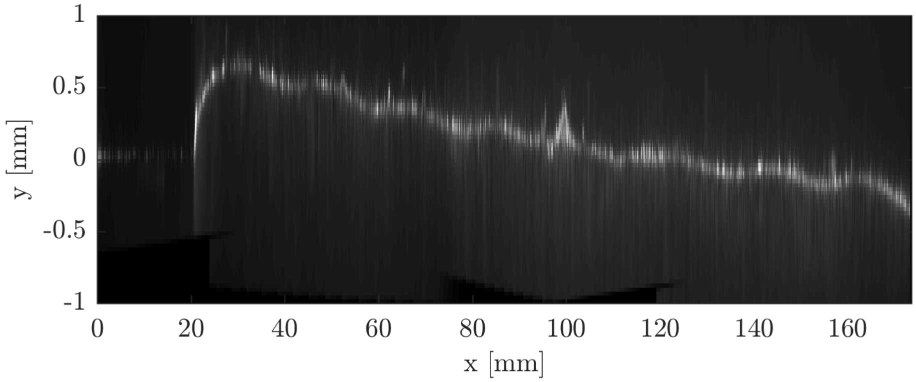

Figure 2.11: Stitched images of the gelatin sample surface from PIV data, highlighting the non-level and non-flat nature of the surface. Note the axes are not in true aspect ratio.

2.4 2D-PIV

2D, planar PIV measurements were made to obtain streamwise and wall-normal velocity fields. These measurements were key to studying the spatio-temporal character of the synthetic structures generated by the dynamic roughness. Two cameras were used to better resolve the anticipated long streamwise extent of these structures, and contribute a novel perspective of this forced system. The flow was seeded with neutrally buoyant, 5 um hollow glass spheres (Vestosint 2070, density: 1.016 g/cm^3) and illuminated using a Photonics DM20-527(nm) dual-head YLF laser, with a laser pulse separation of 1000 us. The laser beam was expanded into a sheet using a -20 mm focal length cylindrical lens, directed up through the bottom of the test section by a 45° mirror, and through the bottom surface of the acrylic plate. The sheet was about 1 mm thick at the acrylic plate. Images were acquired with two Phantom Miro LAB 320 high-speed cameras at full resolution, 1920×1200 px^2, and a frame rate of 100 Hz or varying depending on the roughness actuation frequency. Initially, two AF 180mm f/3.5D Tamron lenses were used with each camera, later to be replaced by two AF Mirco-NIKKOR 200mm f/4D Nikon lenses for improved distortion properties. The laser and cameras were operated and the resulting images processed using LaVision's DaVis software. Unless otherwise specified, vector fields were calculated using a decreasing multi-pass method (1 pass at 64×64 px^2 and 3 passes at 32×32 px^2) with 75% overlap. The region below the plate surface, which will be referred to as 'the wall,' was masked. The calibration target and method will be discussed later in this section.

The optical setup for PIV evolved along with the experiments. For the canonical and preliminary smooth-wall, dynamic-roughness-forced (SW-DRF) turbulent boundary layer studies, a traditional PIV setup was used, with both cameras oriented perpendicular to the desired field of view (FOV), as sketched in Figure 2.12. The size of each camera's FOV was 47×30 mm^2 (streamwise × spanwise), and the minimum distance between each camera's FOV was constrained by the physical size of the cameras. Positioning the cameras side-by-side, the streamwise gap between the FOVs was 61 mm. Data were acquired at one streamwise position (illustrated as the green lines in Figure 2.12), and then both cameras were translated in the streamwise direction to acquire data in the gap (illustrated as the blue lines). However, there remained an average gap of 7 mm between each FOV pair. Flow statistics were calculated for each FOV, and the information in the gap regions was interpolated using Taylor's hypothesis to stitch together all FOVs.

To eliminate the gaps between FOVs and improve the streamwise spectral resolution of the data, a setup was designed to implement a knife-edge, right-angle prism, as illustrated in Figure 2.13. As shown, the prism splits a single, long FOV into two, half-length, horizontally-reflected FOVs. This allows the cameras' FOVs to be adjacent or slightly overlapping, without being constrained by the physical size of the devices. This benefit comes at the cost of increased optical and alignment complexity, as well as a reduction of signal due to losses at the prism. The former concern was addressed through the optomechanical design discussed shortly, and

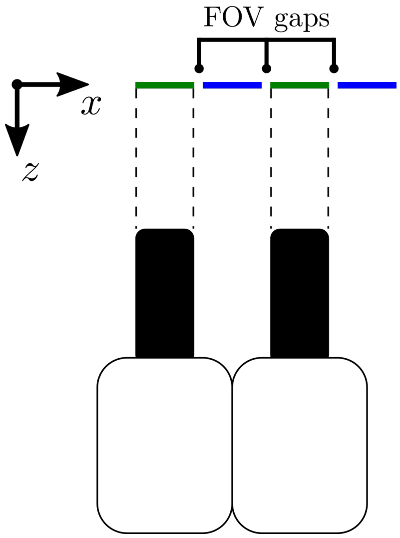

Figure 2.12: Sketch of the camera setup used for PIV for the canonical and preliminary SW-DRF turbulent boundary layer studies (not to scale).

the latter was found to be non-prohibitive as the images acquired in this configuration had sufficient particle intensities for reliable correlations. Thus, this setup was used for the final SW-DRF and compliant-wall, dynamic-roughness-forced (CS-DRF) turbulent boundary layer studies. The camera FOVs in these experiments were 54×34 mm^2, with about a 6 mm overlap between them. As with the traditional PIV setup, data were acquired at one streamwise position, and then the camera-prism system was translated to acquire data at the next position. The streamwise positions were selected to have about a 6 mm overlap between one composite FOV and the next. This way, flow statistics could be stitched with a more reliable blending method, rather than the extrapolation method used in the traditional PIV setup.

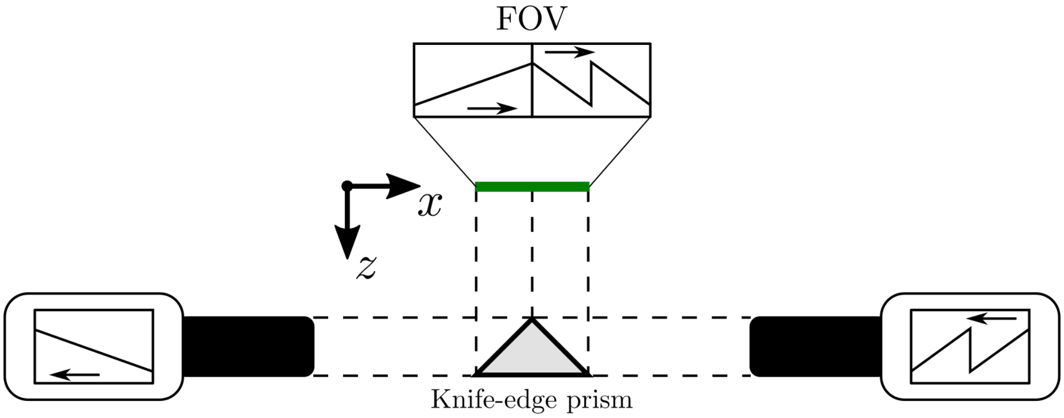

Figure 2.13: Sketch of the knife-edge, right-angle prism camera setup used for PIV for the final SW-DRF and CW-DRF turbulent boundary layer studies (not to scale).

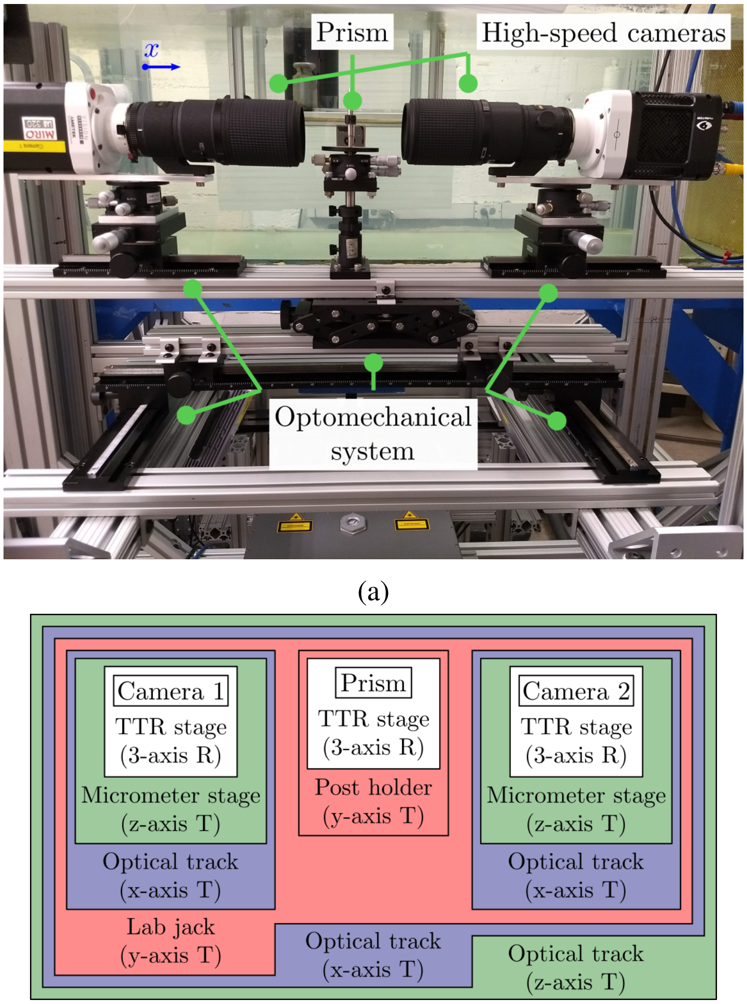

(a)

(b)

Figure 2.14: (a) Photo and (b) diagram of the optomechanical system used to align and translate the PIV camera setup. Each box in the diagram represents an alignment component, with all contained boxes being mounted to that component. The boxes are colored by the adjustment axis of the component: x- (blue), y- (red), z- (green), and rotational (white) axes. The adjustment axes are also given in the parentheses, with "T" and "R" indicating translation and rotation, respectively.

As mentioned, an optomechanical system was designed to meet the alignment and translational needs of the knife-edge prism PIV configuration. A photo of the full system is shown in Figure 2.14a and a diagram of the alignment components is provided in Figure 2.14b. The two cameras and the prism were each mounted to a tip-tilt-rotation (TTR) stage, which enabled adjustment about all three rotational axes. Each camera was also mounted to a micrometer stage and optical track for z- and x-axis translation, respectively, while the prism was mounted to an adjustable post holder for y-axis translation. These components allowed the cameras and prism to be aligned to each other and to the laser sheet/FOV in the test section. The camera and prism modules were supported by an 80/20 frame affixed to a lab jack, which allowed for the composite FOV to be vertically adjusted to best position the wall location in the images. The jack was connected to a streamwise-oriented optical track, used to rigidly translate the entire system to the desired streamwise positions. Finally, spanwise-oriented optical tracks served as the base of the system to facilitate a study of the spanwise-variation of the roughness-forced synthetic structure. This involved acquiring PIV at four equispaced, off-centerline, $x - y$ planes. To adjust the laser sheet alignment, the 45° mirror under the test section was mounted to a single-axis rotational stage (for rotation about the y-axis) and an optical track (for translation in the z-axis). This is not pictured nor included in the diagram in Figure 2.14.

It was important to obtain accurate measurements of the freestream velocity, to scale the data and to note any changes to freestream conditions as the dynamic roughness and compliant surface were added to the experiment. However, it was also important to maintain relatively high spatial resolution to capture any near-wall flow features. To decouple these opposing requirements, separate PIV measurements were made solely to acquire the freestream velocity, and will be referred to as the 'freestream PIV.' These measurements were made in sequence with the aforementioned PIV, using the same laser sheet, with a laser pulse separation of 6900 us. The images were acquired with a FLIR Flea3 USB3 camera at full resolution, 1280×1024 px^2, and a frame rate of 12 Hz, with a 50mm C series TechSpec lens. The Flea3 camera was positioned on the opposite side of the test section to the Phantom cameras, as shown in Figure 2.15, and was operated using FLIR FlyCapture software. The images were then imported to and processed in DaVis, using a multi-pass method (3 passes at 48×48 px^2) with 75% overlap. The FOV for these measurements was 121×97 mm, with the wall in-frame, to have a sufficient number of vectors in the freestream flow.

A robust calibration process and sufficiently resolved target were critical in achieving high-quality PIV, particularly for accurate stitching between FOVs to study very long flow features. The process of calibrating was challenging due to inaccessibility of the measurement location, being on the underside of and midway downstream the acrylic plate. Not only did the calibration target have to be supported on the underside, but the alignment also had to be precisely controlled. Through iterative design, suitable devices were developed, as shown in the SolidWorks model in Figure 2.16. The

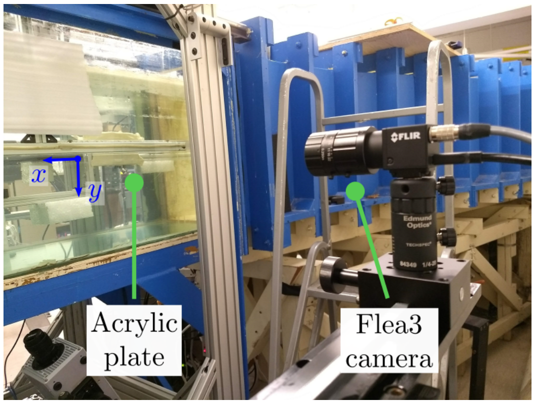

Figure 2.15: Photo of the Flea3 camera setup, used to acquire freestream velocity measurements.

calibration target (red) was held by two threaded plate holders, fixed to an 80/20 arm. The 80/20 was connected to an acrylic block (blue), in which two 38 mm diameter × 13 mm thick neodymium magnets were embedded. This apparatus constituted the calibration support device, and was positioned under the flat plate, with the acrylic block made flush to the plate's bottom surface. A second, magnet-embedded acrylic block was aligned with the first block on the top surface, and the magnetic force between both blocks suspended the support device. By slowly sliding the top block, the support device could be maneuvered along the bottom surface of the plate. Both acrylic blocks were upholstered with a microfiber cloth to prevent scratching of the plate surface. Not visible in the image, the edge of the 80/20 arm was shaved to allow the laser sheet to pass through the calibration target to ensure the two were coplanar.

Figure 2.16 also shows the spacer mechanism used to align the support apparatus. A 6.4 mm thick acrylic sheet (green) was machined to a precise width and such that its long edges were parallel, to act as a spacer. This sheet was attached to an 80/20 arm and positioned under the flat plate, adjacent to the support device. The spacer was butted up against the side wall of the test section, and the magnetic acrylic block was made flush to the other side of the spacer. In this way, the calibration target was brought a fixed distance from and parallel to the test section wall. The support device was free to translate along the spacer, maintaining the calibration target's alignment for all streamwise PIV positions. Pieces of plastic packing foam were attached to the support and alignment devices to provide positive buoyancy and prevent the them from sinking.

The calibration target used in the final stages of this experiment was an Edmund

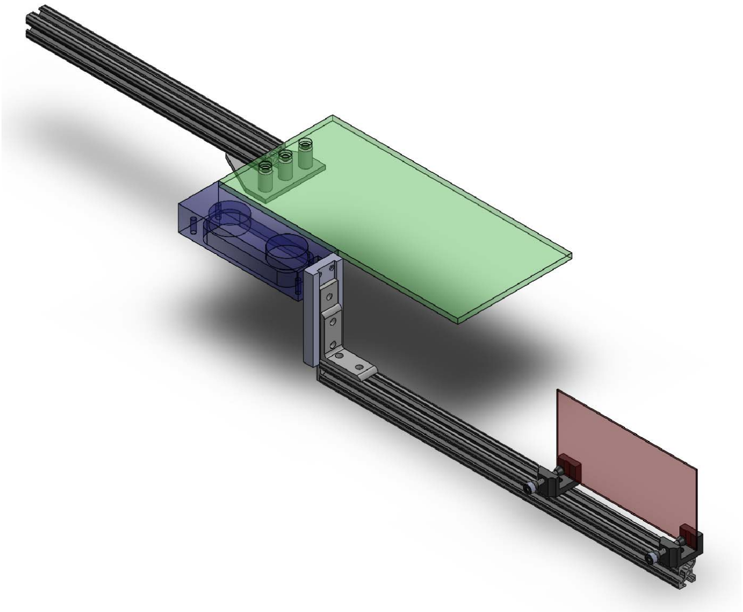

Figure 2.16: Model of the calibration target, support device, and alignment device.

Optics glass distortion target (#62-207), with 0.5 mm diameter dots spaced 1 mm apart. The full 150×150 mm^2 target was cut in half to 150×75 mm^2 to reduce its weight and applied torque on the support device. This target was selected for its size, able to simultaneously span the FOVs of both cameras, and for its high feature density, $\sim$1500 dots per FOV. The need for this unusually high feature density came from an early observation that the streamlines of the mean streamwise velocity appeared to have a pronounced parabolic-type distortion, which occurred in both cameras and for various flow conditions. Upon further investigation, the distortion was found to be radially symmetric and attributed to the change in index of refraction through the test section wall. The initial calibration target (LaVision, type 58-5) had insufficient feature density to adequately correct for this distortion, while the Edmund Optics target yielded a successful correction. The image calibration and correction were done through DaVis, using a 3rd order polynomial fit and having a standard deviation of fit of <0.1 pixels.

An uncertainty analysis was performed on the PIV results using DaVis's uncertainty calculations. The average uncertainties on the streamwise and wall-normal velocities are 2.9 mm/s and 2.8 mm/s, respectively, both about 0.8% of the freestream velocity. For each roughness actuation condition, records of 1837 image pairs were acquired, each yielding a dataset of 1837 velocity fields. 10 records were acquired for the SW-DRF experiments, and 5 records for the CW-DRF experiments (due to limited sample lifetimes). For full ensemble statistics, this equates to 18,370 samples (9185 for the CW-DRF), and for phase-averaged statistics, 910 (455) samples. The factor of ~20 reduction in number of samples for the phase-averaged statistics is due to the sampling rate over the actuation period, as will be discussed in Section 2.6. 2.7 mm/s uncertainty for Flea.

2.5 Stereo-DIC

Stereo-DIC measurements were made to obtain two-dimensional, three-component surface deformations of the gelatin sample. These measurements enabled direct study of the compliant wall response to the roughness-forced synthetic mode. Though these data were not acquired simultaneously with PIV, because both measurements were phase-locked to the roughness actuation, their statistics and phave-averaged quantities could be correlated. A photo of the setup is shown in Figure 2.17. Two Photron Fastcam APS-RS cameras were used, each equipped with an AF NIKKOR 50mm f/1.8D Nikon lens. Images were acquired at full resolution, 1024×1024 px^2, and a frame rate of 100 Hz or varying depending on the roughness actuation frequency. The cameras were positioned under the test section, at a 22° viewing angle from FOV. This angle was selected for sufficient depth information to resolve the wall-normal displacements without requiring prisms to correct the distortion from the refractive index change. The gelatin sample was frontlit via an LED flood lamp. The images were acquired and processed in DaVis, using a least squares matching (LSM) method with 7 seeding points, a subset size of 31×31 px^2 and a step size of 8 px, and built-in ‘medium’ calculation mode.

DIC measurements were acquired in the $x - z$ plane coincident with the gelatin surface. Data were taken in three locations, as illustrated in Figure 2.18:

1. Along the upstream edge of the sample, roughly centered on the centerline, referred to as the leading-edge or LE FOV.
2. In the upstream, $-z$ corner of the sample, referred to as the corner FOV.
3. Along the downstream edge of the sample, roughly centered on the centerline, referred to as the trailing-edge or TE FOV.

The majority of the data were acquired at the LE FOV, since this corresponded with the location of the PIV measurements. The corner and TE data were taken to characterize the surface behavior at the other boundaries of the sample. The

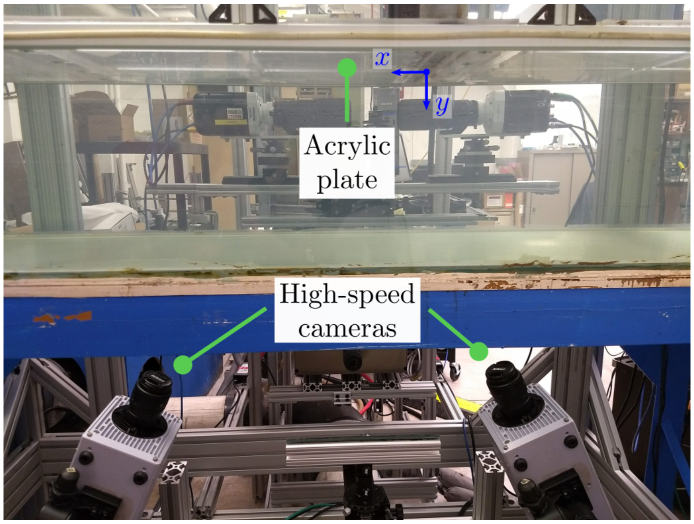

Figure 2.17: Photo of stereo-DIC camera setup. The two cameras were positioned under the test section, at an angle of 22° from the normal.

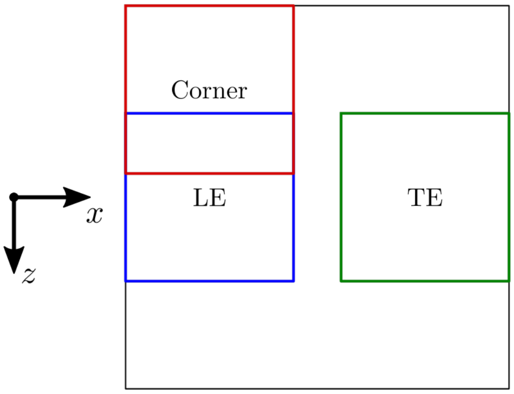

Figure 2.18: Diagram of the three FOV locations for the DIC study: leading-edge (LE), corner, and trailing-edge (TE).

streamwise-spanwise dimensions for the three FOVs were roughly 133×147 mm^2; note these were not square because a portion of the streamwise dimension was masked out for the acrylic plate.

For accurate DIC measurements, an adequate speckle pattern is required. According to Correlated Solutions [56], an optimal speckle pattern should have the following characteristics:

- High contrast
- 50% speckle-to-background ratio
- Speckle features of size 3-5 pixels

- Pattern isotropy and randomness

These qualities are typically achieved by a stamp roller applicator, spray paint, Sharpie marker, or direct printing. However, each of these methods either failed to create a high-contrast mark due to the gelatin's wet surface, damaged the soft sample, or were impractical for the desired spatial resolution. Instead, the speckle pattern was applied using a Flairosol spray bottle and black India ink. The spray bottle created a fine mist from the ink, which settled onto and stained the gelatin surface, forming a pattern such as the one shown in Figure 2.19. This speckle pattern met most of the aforementioned requirements, with a speckle density slightly less than 50%. This was because spraying too much ink led to large droplets to form. Still, this pattern was found to yield good DIC results.

Figure 2.19: Photo of the speckle pattern generated with a fine mist water bottle and black India ink. The photo dimensions are 40×40 mm^2.

The DIC was calibrated using a LaVision, type 58-5 stereo calibration plate. The target was mounted to the end of an 80/20 extrusion and carefully made parallel to the extrusion's faces. This apparatus was positioned in the test section, with the 80/20 flush to the plate's bottom surface. The target was moved into the center of the FOV and the calibration image acquired. This was processed using DaVis, accounting for the wall-normal distance between the calibration and measurement planes.

An uncertainty analysis was performed on the DIC results using DaVis's uncertainty calculations. The average uncertainties on the streamwise, wall-normal, and spanwise displacements are 0.3, 0.3, and 0.2 um, respectively. In addition, the noise floor was estimated by processing a record of the stationary sample. The average noise floor for the streamwise, wall-normal, and spanwise displacements are 0.5, 1.4, and 0.5 um, respectively. For each roughness actuation condition, records of 2048 images were acquired, each yielding a dataset of 2047 displacement fields. 10 records were acquired when operating in the LE FOV, and 5 records in the corner and TE FOVs. For full ensemble statistics, this equates to 20,470 (10,235 for the corner and TE) samples, and for phase-averaged statistics, 1020 (510) samples. The factor of ~20 reduction in number of samples for the phase-averaged statistics is due to the sampling rate over the actuation period, as will be discussed in Section 2.6.

2.6 Phase-locking

A critical element of the smooth- and compliant-wall dynamic roughness experiments was the phase-locking of the PIV and DIC measurements to the roughness actuation. In the previous studies [14, 32], the hotwire data were acquired at sufficiently high rates such that the phase-locking was able to be done in post-processing. In the PIV done by Jacobi [32], phase-locking was done independently of the roughness position by setting the acquisition rate to be a multiple of the actuation frequency. However, this approach did not allow for data from separate records to be averaged as the relative phase information was lost. In these experiments, to preserve the phase information, the roughness motion and image acquisition were phase-locked. The camera frame rates, f_s, were set to a multiple of the roughness actuation frequency, f_f:

$$f_s = SR \cdot f_\mathrm{f}\,, \tag{2.3}$$

where SR is the integer sampling rate or number of samples acquired per actuation period. For these experiments, SR was 20. Take the roughness height, $h(t)$, to be a cosine with amplitude and mean of $h_\mathrm{rms}/\sqrt{2}$, and $h(t) = 0$ indicates that the roughness is flush with the wall. For a record of N images, the jth image corresponds to a roughness height of:

$$\begin{gathered} h(t_j) = h_j = \frac{h_\mathrm{rms}}{\sqrt{2}}\left[-\cos\left(2\pi\frac{j+n_0}{SR}\right)+1\right] \\ j \in [0, N-1],\ n_0 \in [0, SR-1]\,, \end{gathered} \tag{2.4}$$

where n_0 is the integer shift for the first ($j = 0$) image, since it may occur at any of the SR phase positions. The cosine is negated such that when its argument is zero, the roughness is in the wall-flush position. To achieve phase-locking in the experiment, the digital clock signal for the cameras and laser had to be synchronized to the analog encoder signal from the Bose motor. This was done through a National Instruments PCIe-6321 DAQ card and the MATLAB DAQ Toolbox. A timing diagram illustrating this process is provided in Figure 2.20. The analog encoder signal was first acquired for one actuation period (Buffer A). The signal was mean-subracted, and the rising zero-crossing was found (the black dot in Buffer A) and used as the starting phase for the digital clock. During a second actuation period (Buffer B), a clock trigger signal was constructed with a rising-edge pulse aligned to this starting phase. After Buffer B, the trigger was sent and initiated a digital clock signal, with frequency f_s. This clock was sent to the high-speed controller operating the cameras and laser. Once the clock signal was received, a record trigger was manually sent through DaVis to begin (rising-edge) and complete (falling-edge) image acquisition, illustrated as the blue circles on the encoder signal. In order to minimize frequency drift during the record, before image acquisition, a long record of the encoder's signal was taken and the actuation frequency determined to 0.01 mHz using a peak-finding method. This was used to set the clock signal frequency. Over a typical record of ~2000 images, the clock and encoder signal remained synchronized to within 0.015% of the actuation period.

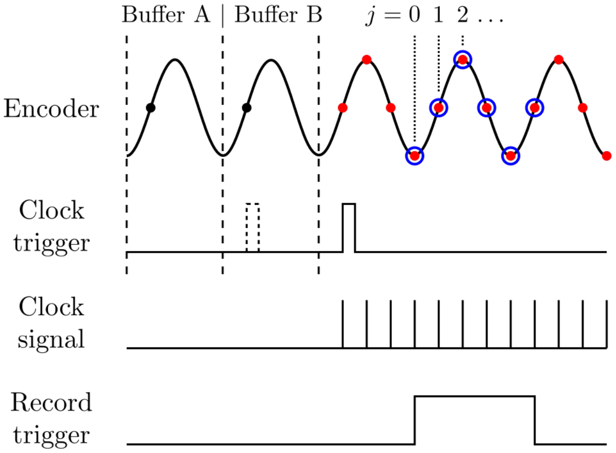

Figure 2.20: Timing diagram for phase-locking process. In this example, $SR = 4$ and $n_0 = 3$.

Chapter 3

FLAT-PLATE BOUNDARY LAYER CHARACTERIZATION AND MEAN FLOW PROPERTIES

A study was performed of the flow over the unmodified, flat plate to ensure that the new facility generated a canonical, turbulent boundary layer. The measurements were made starting near 626 mm downstream of the leading edge, where the roughness slot would be situated in later experiments. As mentioned previously, the streamwise origin ($x = 0$) is located on the downstream edge of the roughness slot. Based on the PIV data at $x = 120$ mm, the freestream velocity, U_∞, was 33.4 cm/s, the boundary layer thickness (based on 99% of U_∞), δ, was 25.4 mm, and the momentum thickness, θ, was 2.6 mm. The Reynolds number based on momentum thickness was then $Re_\theta = 870$. These values are presented in Table 3.1, alongside the values for the SW-DRF and CW-DRF studies for later reference.

The friction velocity, u_τ was estimated using the Clauser chart method discussed in Chapter 1. The constants κ and B were taken to be 0.41 and 5.0 [11, 13], respectively. The points used for the Clauser fit were those that satisfied $y^+ > 40$ and $y/\delta < 0.3$, using an initial guess of $u_\tau = 0.05U_\infty$ and re-selecting the points after the initial fit was performed. u_τ was calculated to be 1.60 cm/s, which gave friction Reynolds number of $Re_\tau = 410$. The Clauser method was not employed for the dynamic-roughness-forced cases, as they are non-equilibrium flows. Alternative methods to estimate u_τ are available, as laid out by Jacobi (2013) [31], but instead, outer scaling is used for the majority of the results. The freestream velocity and boundary layer thickness from the canonical study are used to scale all data to facilitate comparison. Any inner-scaled quantities are calculated using $Re_\tau = 410$ from the canonical study.

	U_∞ [cm/s]	δ [mm]	θ [mm]	u_τ [cm/s]	Re_θ	Re_τ
Canonical	33.6	25.5	2.60	1.60	870	410
SW-DRF	36.4	23.2	2.35	-	860	-
CW-DRF	34.8	25.3	2.64	-	920	-

Table 3.1: Mean flow properties from PIV taken at $x = 120$ mm for the canonical, SW-DRF, and CW-DRF studies. U_∞ is calculated from freestream PIV data when available (SW- and CW-DRF studies).

The mean flow statistics from $x = 120$ mm are plotted in Figure 3.1, alongside turbulent boundary layer DNS data from Wu et al. (2009, 2017) [60, 61] at $Re_\theta = 900$ for comparison. The experimental mean profile (3.1a) shows excellent agreement with the DNS, only deviating slightly for $y/\delta < 0.03$. The streamwise and wall-normal turbulence intensities (3.1b-3.1c) are also in very good correspondence with the DNS data, with the v_{rms} only slightly underestimating the numerical data in the outer part of the flow. The discrepancy in the Reynolds shear stress (3.1d) is more pronounced, but still quite small. Based on these comparisons, the flow over the unmodified flat plate was confirmed to be that of a canonical turbulent boundary layer.

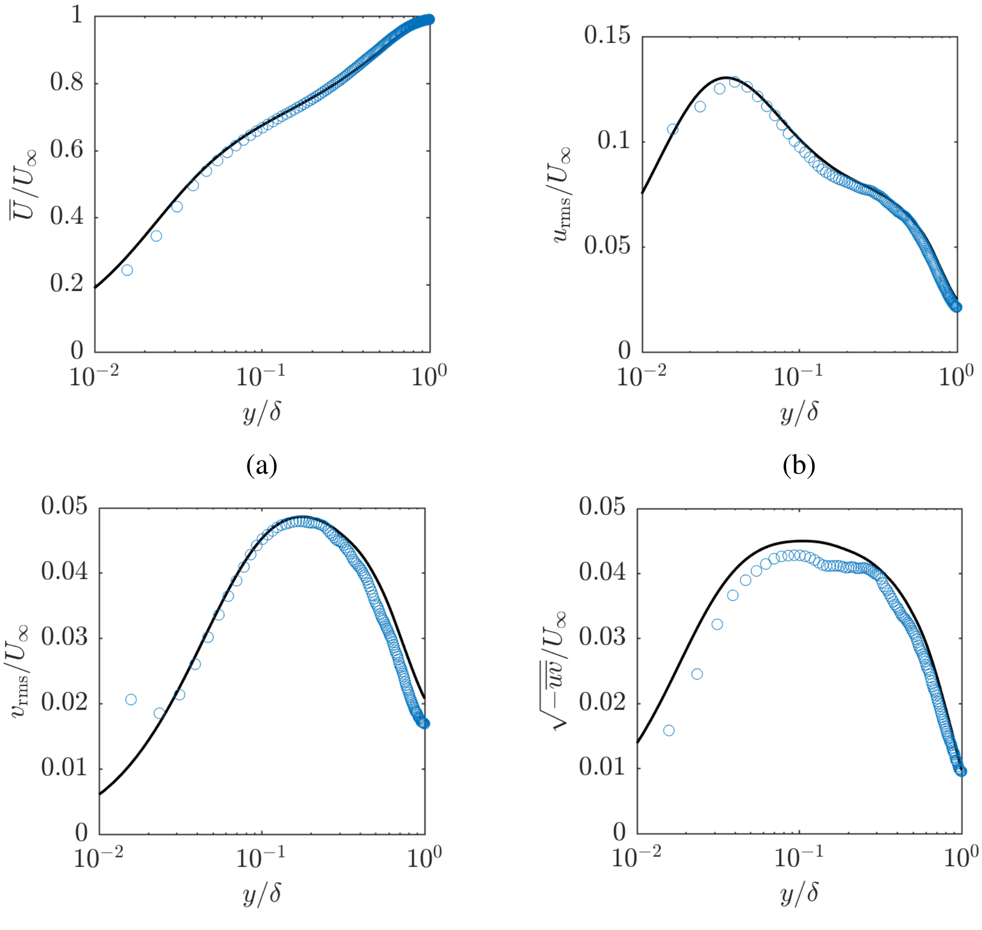

(a) (b)

(c) (d)

Figure 3.1: Profiles of mean flow statistics ($x = 120$ mm): (a) mean streamwise velocity, (b) streamwise turbulence intensity, (c) wall-normal turbulence intensity, (d) Reynolds shear stress. Velocities are scaled by the freestream velocity and plotted in outer scaling, y/δ. ○ PIV data; — Wu et al. (2009, 2017) [60, 61], $Re_\theta = 900$.

To quantify any pressure gradient effects, the acceleration parameter was calculated, defined in previous studies [13, 48] as:

$$K = \frac{\nu}{U_\infty^2} \frac{\mathrm{d}U_\infty}{\mathrm{d}x}. \tag{3.1}$$

The acceleration parameter is very small in all cases, and on average $K = 3 \cdot 10^{-8}$. This is well below the limit of $K > 1.6 \cdot 10^{-6}$, above which deviation from log law occurs. Thus, any pressure gradient effects were deemed negligible.

In the following tables, the relevant dimensions of the experimental design are recapitulated and scaled based on the boundary layer thickness (and δ_ν in some cases). Table 3.2 contains the relevant physical lengths of the experimental apparatus. Tables 3.3, 3.4, and 3.5 have the camera FOVs and processing window sizes for each optical measurement, 2D-PIV, freestream PIV, and stereo-DIC, respectively.

	Flat plate			Roughness element			Gelatin inset		
	x	y	z	x	y	z	x	y	z
[mm]	1280	32	440	2.2	3.2	307	305	25.4	343
$(\cdot)/\delta$	50	1.3	17	0.086	0.13	12	12	1.0	13

Table 3.2: Relevant physical length dimensions of the experiment in dimensional and outer-scaled forms. The coordinate variables indicate which dimension is provided below. Outer scaling is done with δ from the canonical TBL study, listed in Table 3.1.

	2D-PIV		
	[mm]	$(\cdot)/\delta$	$(\cdot)^+$
Single FOV	54×34	2.1×1.3	860×540
Composite FOV (SW-DRF)	282×34	11.0×1.3	4510×540
Composite FOV (CW-DRF)	195×34	7.6×1.3	3120×540
Int. window	0.9	0.035	14

Table 3.3: FOV and interrogation window dimensions for 2D-PIV measurements, in dimensional, outer-, and inner-scaled forms. Because the interrogation windows used were square (32×32 px^2), only one side length is given.

	Freestream PIV		
	[mm]	$(\cdot)/\delta$	$(\cdot)^+$
FOV	121×97	4.7×3.8	1940×1550
Int. window	4.54	0.18	73

Table 3.4: FOV and interrogation window dimensions for freestream PIV measurements, in dimensional, outer-, and inner-scaled forms. Because the interrogation windows used were square (32×32 px^2), only one side length is given.

	Stereo-DIC		
	[mm]	$(\cdot)/\delta$	$(\cdot)^+$
FOV	133×147	5.2×5.8	2130×2350
Subset size	4.6	0.18	74

Table 3.5: FOV and subset dimensions for stereo-DIC measurements, in dimensional, outer-, and inner-scaled forms. Because the interrogation windows used were square (31×31 px^2), only one side length is given.

Chapter 4

SPATIO-TEMPORAL RESPONSE OF A TURBULENT BOUNDARY LAYER TO DYNAMIC ROUGHNESS FORCING

The dynamic roughness setup described in Section 2.1 was used to generate a synthetic flow structure over a smooth wall. This smooth-wall, dynamic-roughness-forced study is abbreviated 'SW-DRF' for conciseness. Similar flows were study by Jacobi & McKeon [32] and Duvvuri & McKeon [14] in a wind tunnel at a lower non-dimensional actuation frequency and higher Reynolds number. These studies relied largely on hot-wire measurements, and thus had limited streamwise resolution and focused primarily on the streamwise velocity. In the present work, a thorough investigation was performed to explore the spatial nature of both velocity components of the synthetic mode, validate the 2D assumption through spanwise measurements, study the parametric behavior of this type of forcing, and investigate its spatial spectral signature. This also provides a base case with which to compare the results of the compliant wall study. The majority of the data presented in this chapter are from the final SW-DRF study, with a comparison made to data from a preliminary SW-DRF study. [1]

The roughness actuation signal was singly-periodic with angular frequency ω_f and rms amplitude h_rms, as shown in Equation 4.1.

$$h(t) = \frac{h_\mathrm{rms}}{\sqrt{2}} \left[-\cos\left(2\pi\omega_\mathrm{f} t\right) + 1 \right] \tag{4.1}$$

Per the description in Section 2.6, the PIV data were phase-locked to the roughness motion and acquired at a sampling rate of $SR = 20$ samples per actuation period. Thus, for data acquired at phase index $j \in [0, SR-1]$, the corresponding height of the roughness is described by Equation 4.2.

$$\begin{gathered} h_j = \frac{h_\mathrm{rms}}{\sqrt{2}} \left[-\cos\left(2\pi \frac{j}{SR}\right) + 1 \right] \\ j \in [0, SR-1] \end{gathered} \tag{4.2}$$

The actuation conditions explored in these experiments are provided in Table 4.1, numbered i-iv for reference. The conditions are given in dimensionless form (and

---

[1] Discussion of the preliminary study and methodologies are given in Huynh & McKeon (2018) [29].

dimensional form parenthetically), with the dimensionless frequency scaled in outer units, $\frac{\omega_\mathrm{f}\delta}{U_\infty}$. From the table, the range of outer-scaled frequencies studied was 1.4−4.8, and the two actuation amplitudes were h_rms/δ=0.042 and 0.069 or h^+_rms=17 and 28. For comparison, the single-frequency oscillation conditions of Duvvuri & McKeon [14] were $\frac{\omega_\mathrm{f}\delta}{U_\infty} = 0.24$ and $h_\mathrm{rms}/\delta = 0.033$. The order-of-magnitude higher frequencies used in this study generated much shorter wavelength flow structures, enabling a more spatially-resolved investigation. Most of the results presented will pertain to case iii, which had the highest amplitude actuation, though comparisons with other conditions will be made when appropriate.

		h_rms/δ [h_rms]	
		0.042 [1.1 mm]	0.069 [1.8 mm]
$\frac{\omega_\mathrm{f}\delta}{U_\infty}$ [f_f]	1.4 [3 Hz]	i	-
	2.4 [5 Hz]	ii	iii
	4.8 [10 Hz]	iv	-

Table 4.1: Roughness actuation conditions explored in these experiments, parameterized by motion rms height and frequency. i-iv indicate conditions that were tested and are labeled for reference; dashed cells indicate those that were excluded.

4.1 Triple decomposition and mean flow statistics

As discussed in Chapter 1, the velocity of a turbulent flow is typically Reynolds decomposed using a ensemble-approximated temporal mean, repeated here in Equation 4.3 for comparison.

$$U = \overline{U} + u \tag{4.3}$$

For a flow with a deterministically periodic component, it is natural to define the phase-average operation, denoted by $\widetilde{(\cdot)}$. A formal definition of this operation is given in Appendix B, but simply, the process computes the ensemble mean of the subset of data corresponding to phase j of the roughness, for all phases $j \in [0, SR-1]$. The resulting phase-averaged quantity is strictly periodic in time with frequencies ω_f and its resolvable harmonics. This allows the velocity to be phase-average decomposed as:

$$U = \widetilde{U} + u' \,, \tag{4.4}$$

where $\widetilde{U}$ is the phase-averaged full velocity (referred to as the phase-averaged mean for convenience), u' is the fluctuation about the phase-averaged full velocity. Substituting equation 4.3 into the $\widetilde{U}$ term of equation 4.4, we arrive at the triple decomposition of Hussain and Reynolds [26]:

$$U = \overline{U} + \widetilde{u} + u' \,, \tag{4.5}$$

where $\widetilde{u}$ is the phase-average of u (referred to as the phase-averaged velocity). Much of the focus of the analysis will be concerned with $\widetilde{u}$ and $\widetilde{v}$, as these are the components temporally coherent with the roughness actuation. Note that by definition, all terms involving the fluctuating velocity, u, have zero temporal mean, $\overline{u} = \overline{\widetilde{u}} = \overline{u'} = 0$, and that the perturbation about the phase-averaged mean has a zero phase-average, $\widetilde{u'} = 0$. This leads to the property that the phase-averaged velocity and the perturbation about the phase-averaged mean are uncorrelated in time, i.e. $\overline{\widetilde{u}_i u'_j} = 0$, as shown in Appendix B. This property will be useful in decomposing the Reynolds stress terms, discussed shortly.

The mean flow statistics for the roughness-forced flow for actuation condition iii are presented as red squares (□) in Figure 4.1, along with the statistics from the canonical flow study as blue circles (○). In Figure 4.1a, the forced mean exhibits a deficit for $0.07 < y/\delta < 0.6$. Figures 4.1b-4.1d show that the turbulence intensities and Reynolds shear stress all have increased value over the canonical case. To determine whether these energetic humps are due to static, blockage-type effects or dynamic, synthetic mode-related effects, we can leverage the aforementioned property that $\overline{\widetilde{u}_i u'_j} = 0$ to decompose the Reynolds stress terms:

$$\begin{aligned} \overline{u_i u_j} &= \overline{(\widetilde{u}_i + u'_i)(\widetilde{u}_j + u'_j)} \\ &= \overline{\widetilde{u}_i \widetilde{u}_j} + \overline{\widetilde{u}_i u'_j} + \overline{u'_i \widetilde{u}_j} + \overline{u'_i u'_j} \\ &= \overline{\widetilde{u}_i \widetilde{u}_j} + \overline{u'_i u'_j}. \end{aligned} \tag{4.6}$$

$\overline{\widetilde{u}_i \widetilde{u}_j}$ is a (co)variance term for the phase-averaged velocities, and $\overline{u'_i u'_j}$ is the Reynolds stress for the rest of the flow that is non-harmonic with the dynamic forcing.

Both $\overline{u_i u_j}$ (□) and $\overline{u'_i u'_j}$ (•) for actuation condition iii are plotted in Figure 4.2, showing that the two are nearly identical. In the streamwise and wall-normal Reynolds stresses, the non-harmonic component is only slightly less than the full component, indicating that relatively little kinetic energy is contained in the phase-averaged terms. In the shear term, the non-harmonic component is slightly larger, indicating that $\widetilde{u}$ and $\widetilde{v}$ are positively correlated in that wall-normal region, and again the covariance of the phase-averaged fields is quite small relative to the rest of the flow. Clearly the majority of the $\overline{u_i u_j}$ Reynolds stresses are carried by the non-harmonic components of the flow, suggesting that the modification to the mean flow properties is largely a static roughness effect and a signature of an internal layer, like those reported by Jacobi & McKeon [32, 33]. Given that the roughness element used here is essentially spatially impulsive, it is anticipated that a single internal layer has developed, rather than the two layers of Jacobi & McKeon.

The turbulence intensities and Reynolds shear stress for actuation condition iii are plotted in Figure 4.3 to illustrate the streamwise behavior of the mean flow properties. The data are plotted as lines rather than symbols for visual clarity. As may be expected, the elevated energetics quickly decay and approach (but do not quite return to) the unforced flow values as the flow moves downstream.

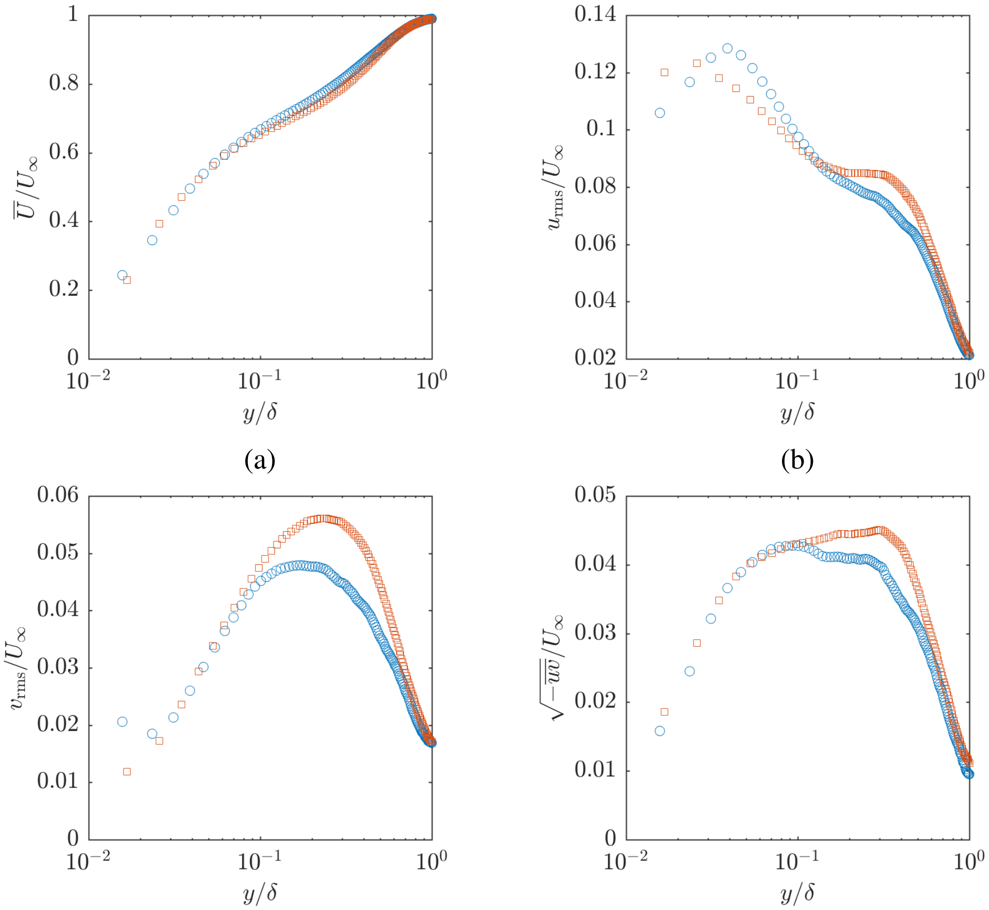

(a)

(b)

(c)

(d)

Figure 4.1: Comparison of canonical and SW-DRF (actuation condition iii) mean flow statistics ($x/\delta = 4.7$): (a) mean streamwise velocity, (b) streamwise turbulence intensity, (c) wall-normal turbulence intensity, (d) Reynolds shear stress. Velocities are scaled by the freestream velocity and plotted in outer scaling, y/δ. ○ canonical; □ SW-DRF.

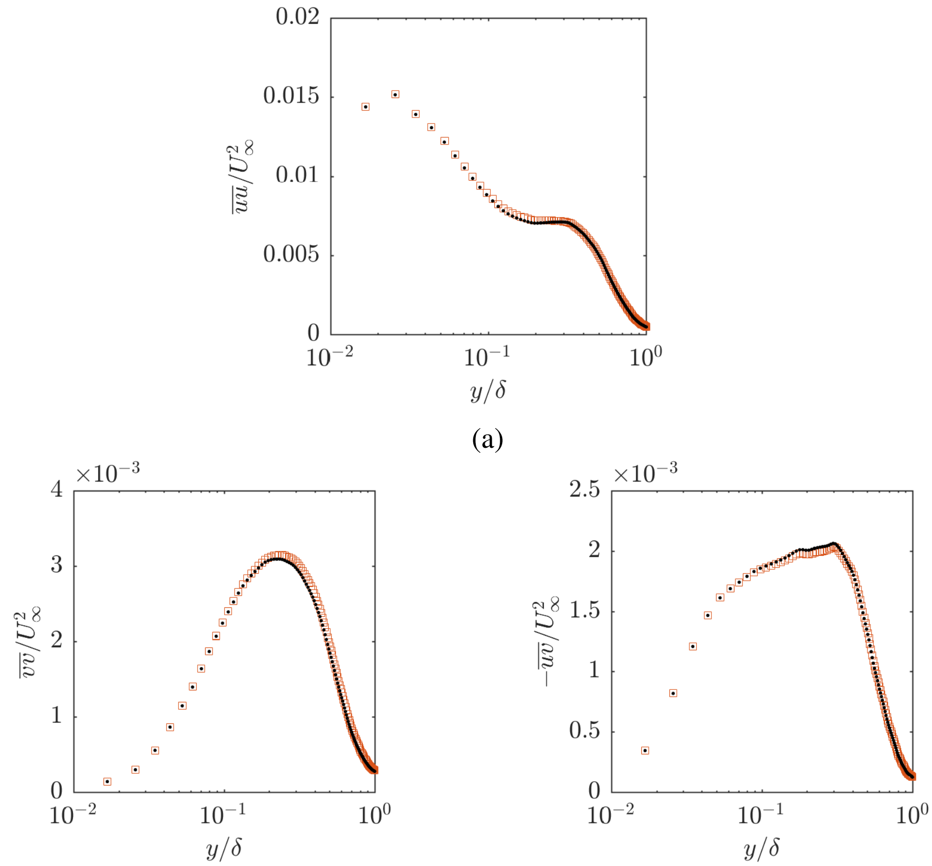

(a)

(b)

(c)

Figure 4.2: Comparison of Reynolds stresses and their corresponding non-harmonic components ($x/\delta = 4.7$), for actuation condition iii: (a) streamwise, (b) wall-normal, and (c) shear Reynolds stresses. Stresses are scaled by the square of the freestream velocity and plotted in outer scaling, y/δ. □ full Reynolds stress; • non-harmonic component.

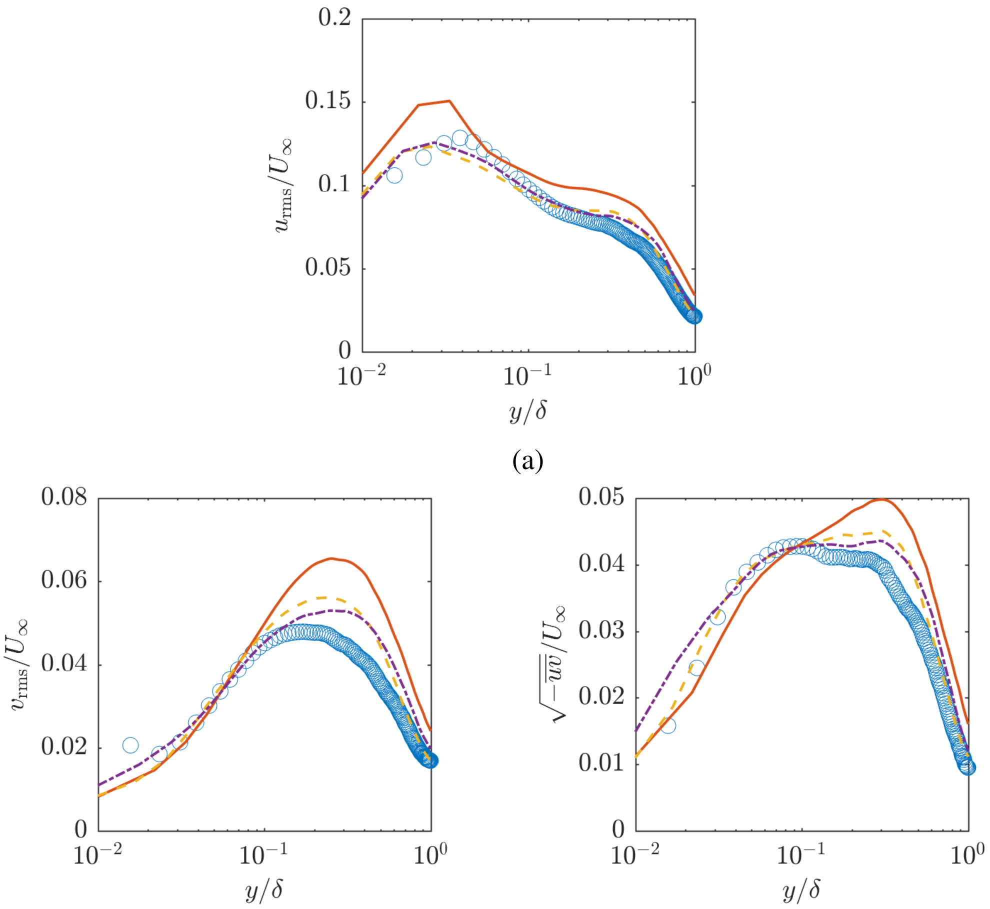

(a)

(b)

(c)

Figure 4.3: Flow statistics (actuation condition iii) at increasing streamwise stations: (a) streamwise turbulence intensity, (b) wall-normal turbulence intensity, (c) Reynolds shear stress. Velocities are scaled by the freestream velocity and plotted in outer scaling, y/δ. — $x/\delta = 2.8$; – – $x/\delta = 4.7$; • – $x/\delta = 6.7$; ○ canonical flow.

4.2 Phase-averaged velocity fields

The phase-averaged velocity fields capture the portion of the flow that is temporally coherent with the actuation frequency. Identically, the phase-averaging process is a Fourier filter that retains only the temporal components that are harmonic with ω_f, without imposing any spatial constraints on the data. Phase snapshots of the streamwise and wall-normal phase-averaged velocities from actuation condition iii are given in Figure 4.4, where red and blue indicate regions of high and low speed, respectively, and the plots top to bottom are increasing in phase index. A white rectangle is drawn to scale at $x = 0$ to indicate the roughness height in each frame. A streamwise-periodic structure is immediately apparent, and is seen to convect downstream. $\widetilde{u}$ exhibits a sharp π phase jump in y, with the near-wall structure leaning downstream and the outer-flow structure slightly leaning upstream. In contrast, $\widetilde{v}$ is very tall and straight in y. $\widetilde{u}$ and $\widetilde{v}$ are also $\pi/2$ phase-shifted with respect to one another, which means $\overline{\widetilde{u}\,\widetilde{v}}$ is expected to be very small. Thus, even if the variances of the phase-averaged flow were a significant portion of the total Reynolds normal stresses, it is expected that Figure 4.2c would look similar due to the phase relationship between $\widetilde{u}$ and $\widetilde{v}$.

In $\widetilde{u}$, there are four structures that form from the motion of the roughness: the high and low speed lobes that reside near the wall, and the high and low speed lobes that sit on top of them. The outer-flow structures form on top of the roughness. The positive lobe forms halfway through the upstroke of the rib ($j = 6$) and pinches off halfway through the downstroke ($j = 15$). Reciprocally, the negative lobe forms halfway through the downstroke ($j = 15$) and pinches off halfway through the upstroke ($j = 6$). Once pinch-off occurs, the lobes convect downstream and gradually drift away from the wall. These top lobes may be generated through the periodic contraction and expansion, and thus acceleration and deceleration, of the flow just above the roughness. The inner-flow structures form just downstream of the rib. The positive lobe forms at the end of the upstroke ($j = 9$) and pinches off at the end of the downstroke ($j = 18$). Again in complementary fashion, the negative lobe forms at the end of the downstroke ($j = 18$) and pinches off at the end of the upstroke ($j = 9$). These bottom structures form as small pockets near the roughness and rapidly broaden downstream, as well gradually become taller while remaining attached to the wall.

In $\widetilde{v}$, there are only two tall structures (high and low velocity lobes) that form from the motion of the roughness. The positive lobe forms at the start of the upstroke

($j = 0$) near the roughness and continues to grow through the stroke. Though slightly difficult to see, the negative lobe does form at the start of the downstroke ($j = 9$) and continues to grow through the stroke. The vertical velocity structures appear to be driven by a blockage mechanism, as the flow is forced to navigate over the roughness.

An interesting observation is that the positive-negative structures in $\widetilde{u}$ and $\widetilde{v}$ are slightly asymmetric in streamwise size. The top negative lobes in $\widetilde{u}$ are slightly broader than the positive lobes, and the reverse is true for the bottom lobes, with positive broader than negative. In $\widetilde{v}$, the positive lobes are quite clearly wider than the negative lobes. As will be shown shortly, these asymmetries are a result of higher frequency content in the phase-averages.

As mentioned, the phase-averaging process is directly related to Fourier analysis. Thus, it is natural to employ a discrete Fourier transform in time to further decompose the flow fields into a fundamental component corresponding to ω_{f} and its harmonics:

$$\widetilde{u}(x, y, t) = \sum_{m=1}^{SR/2} \widehat{u}_{m\omega_{\mathrm{f}}}(x, y) e^{-im\omega_{\mathrm{f}} t} + \text{c.c.}, \tag{4.7}$$

where $\widehat{u}_{m\omega_{\mathrm{f}}}$ are the 2D Fourier modes and ‘c.c.’ stands for complex conjugate to recover a real velocity field. Note that the $m = 1$ mode corresponds to the forcing frequency component, $\widehat{u}_{\omega_{\mathrm{f}}}$. The velocity field reconstructed by $\widehat{u}_{\omega_{\mathrm{f}}}$ is accordingly referred to as $u_{\omega_{\mathrm{f}}}$. Phase snapshots of $u_{\omega_{\mathrm{f}}}$ and $v_{\omega_{\mathrm{f}}}$ are shown in Figure 4.5, in parallel format to Figure 4.4. The forcing frequency components are nearly identical to their full phase-averaged counterparts, but are spatially smoother. The aforementioned asymmetry in the lobes is removed, as it was a manifestation of the higher temporal harmonic content superimposed on the ω_{f} mode. In Figure 4.6, the $j = 0$ snapshot is shown for the full phase-averaged velocities (top), followed by the snapshots for the $m = 1, 2,$ and 3 modes. These plots reinforce the observation in Figure 4.5 that the fundamental component carries the majority of the energy of $\widetilde{\mathbf{u}}$, as the two fields agree quite closely. The higher harmonic content is lower in amplitude and decays more rapidly than the fundamental mode, and is higher in streamwise wavenumber, accounting for the spatial asymmetry and ‘noisiness’ in the full field. The wavenumber increases in lock-step with the frequency, and thus the Fourier modes have the same wave speed. Interestingly, the harmonic modes closely resemble the fundamental mode in wall-normal shape, but are scaled in the streamwise and wall-normal direction. The remaining analysis will focus on the fundamental component of the flow response, but is noted that the harmonic content is readily available as well.

The smoother nature of the forcing component fields provides an opportunity to reevaluate the mechanism behind the synthetic mode structure from a vorticity perspective. The spanwise vorticity was calculated by taking the curl of the 2D velocity field, $\Omega_{\omega_\mathrm{f}} = \frac{\partial v_{\omega_\mathrm{f}}}{\partial x} - \frac{\partial u_{\omega_\mathrm{f}}}{\partial y}$. Phase snapshots of $\Omega_{\omega_\mathrm{f}}$are given in Figure 4.7. As expected, there is a clear streamwise-periodic structure to the fields, taking the form of a series of counter-rotating vortices. Negative vorticity is generated on the roughness upstroke ($j = 0$ to $j = 9$), and positive vorticity generated on the downstroke ($j = 12$ to $j = 18$). These vortices undergo strong shear as they convect downstream, likely due to the lower convection speed near the wall. Similar vortex pairs are observed in studies of synthetic jets in cross flow [3]; however the vortices in Figure 4.7 are more diffuse and have less compact, core structure, likely due to the lesser momentum of the dynamic roughness versus the synthetic jets.

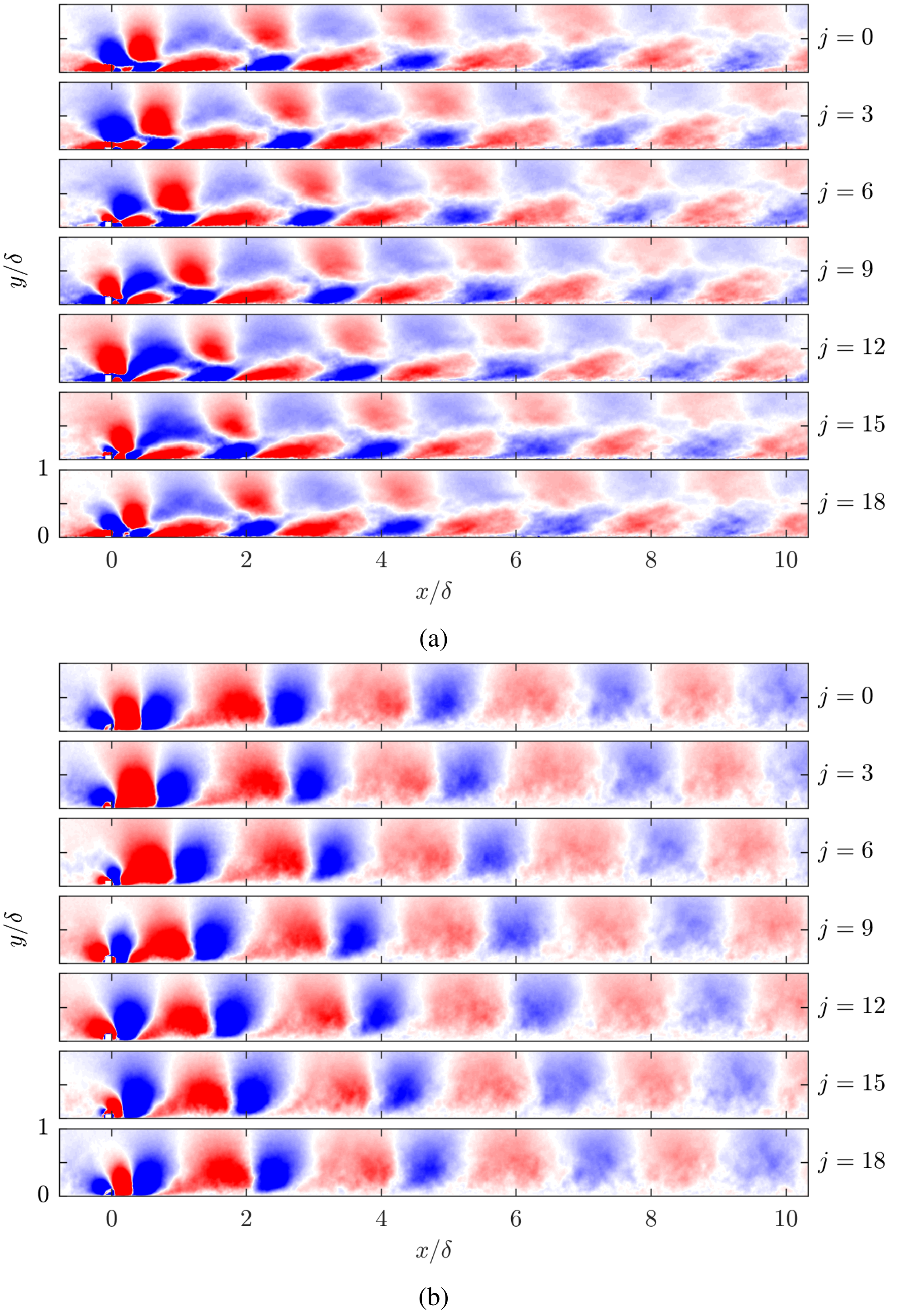

Figure 4.4: Phase snapshots of phase-averaged (a) streamwise ($\widetilde{u}$) and (b) wall-normal ($\widetilde{v}$) fluctuating velocities (actuation condition iii). Phase indices increase from top to bottom, $j = [0, 3, 6, 9, 12, 15, 18]$. The colorbar limits are $[-0.2, 0.2]$.

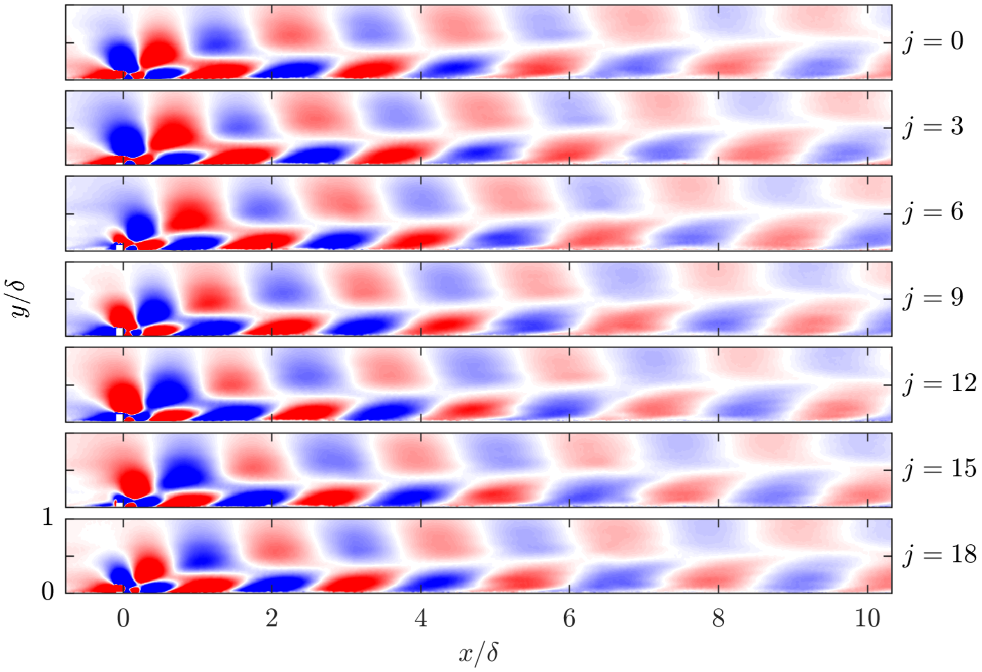

(a)

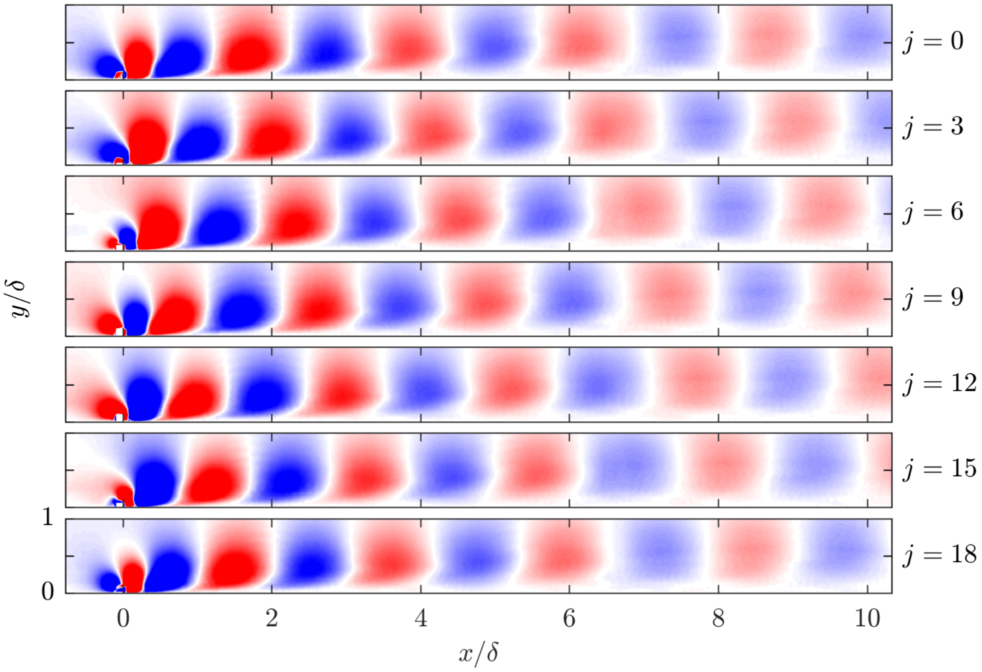

(b)

Figure 4.5: Phase snapshots of (a) u_{ω_f} and (b) v_{ω_f} (actuation condition iii). Phase indices and colorbar follow the same format as Figure 4.4.

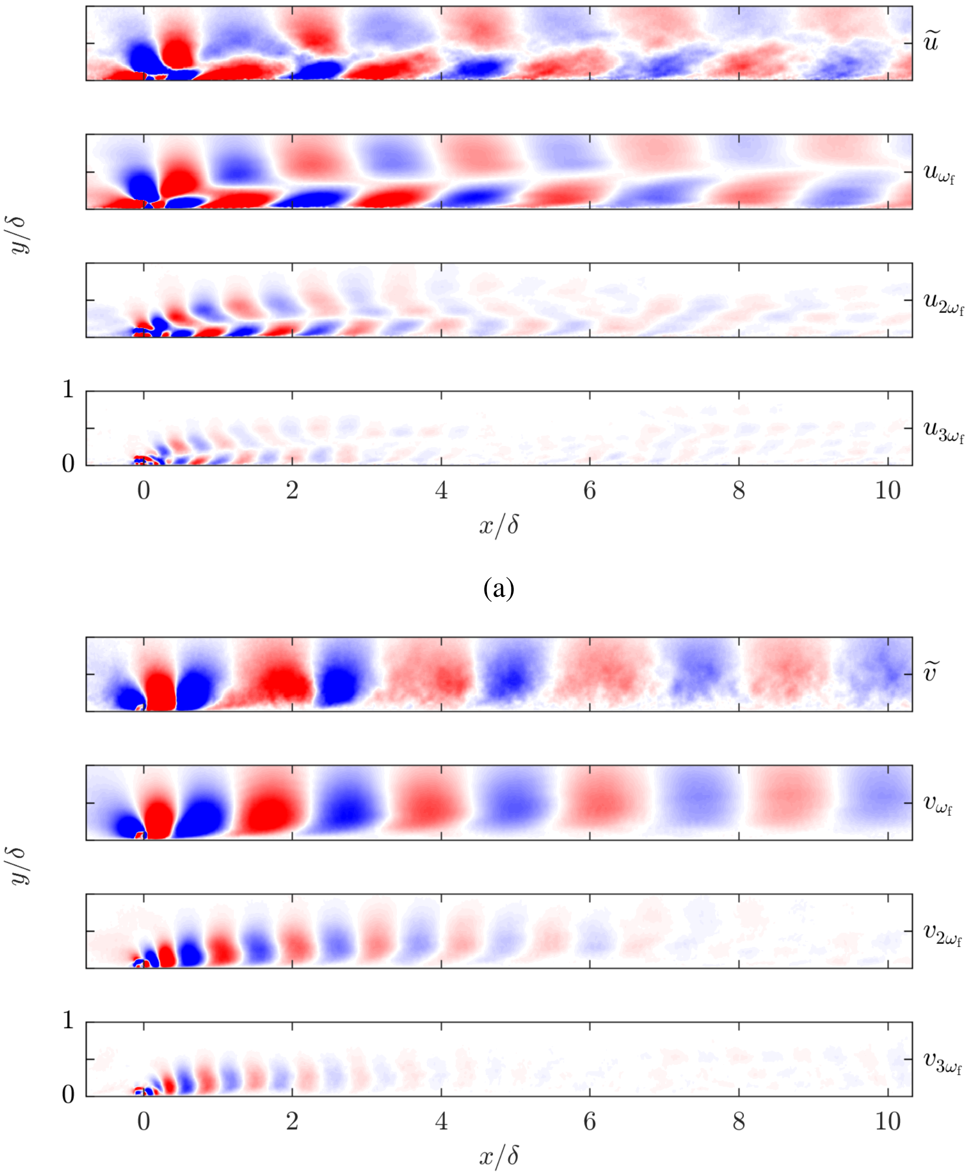

(a)

(b)

Figure 4.6: Temporal Fourier decomposition of the (a) streamwise and (b) wall-normal phase-averaged velocities (actuation condition iii). The top plot is the full, phase-averaged field, followed by the ω_f, $2\omega_\mathrm{f}$, and $3\omega_\mathrm{f}$ modes, respectively. All plots are at phase index $j = 0$. The colorbar limits are $[-0.2, 0.2]$.

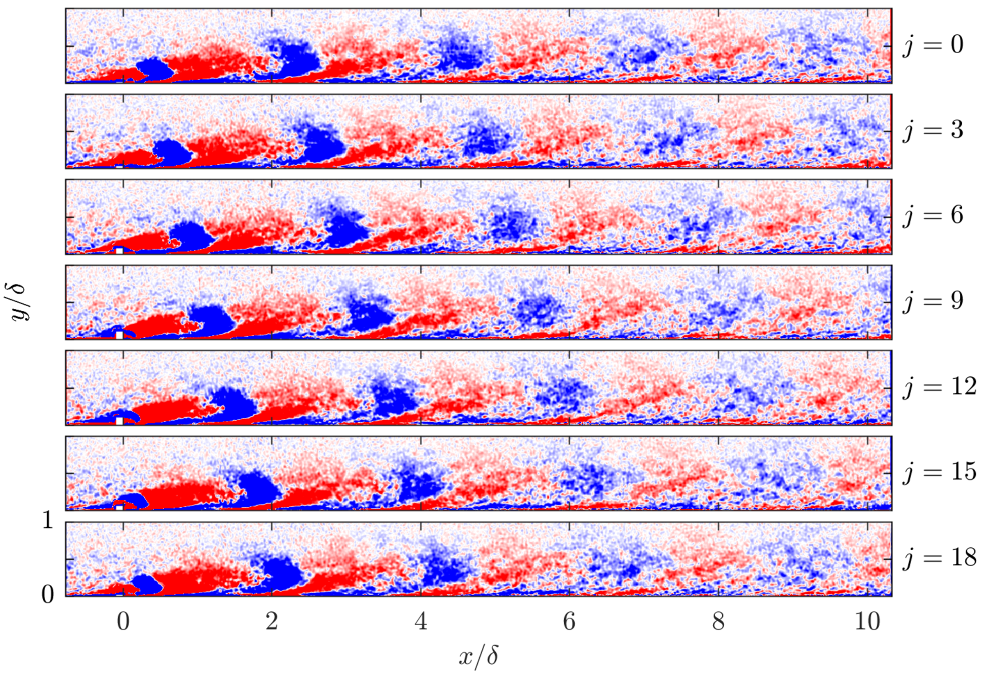

Figure 4.7: Phase snapshots of Ω_{ω_f}(actuation condition iii). Phase indices follow the same format as Figure 4.4. The colorbar limits are $[-0.08, 0.08]$.

4.3 Spanwise variation study

As described in Section 2.4, an investigation was performed for the spanwise variation of the synthetic mode through streamwise-wall-normal PIV measurements at 5 spanwise locations, z_{-1} to z_3, with z_0 corresponding to the centerline. The measurement planes were equispaced 46.6 mm (1.83δ) apart, as given in Table 4.2. The span on the roughness element was $z/\delta \in [-6, 6]$, so these PIV locations were expected to give insight into the three-dimensionality of the flow, or lack thereof. This study was done exclusively for actuation condition iii.

z_{-1}	z_0	z_1	z_2	z_3
-1.83	0	1.83	3.67	5.50

Table 4.2: Locations of the PIV planes for the spanwise study, scaled by δ. For reference, the roughness element spans $z/\delta = [-6, 6]$.

Figure 4.8 shows the $j = 0$ phase snapshots of u_{ω_f} and v_{ω_f} at each of the spanwise locations. Qualitatively, positions z_{-1} through z_2 are very similar and are all consistent with the $j = 0$ snapshots of Figures 4.5a and 4.5b. There is a clear breakdown of the synthetic mode by z_3, as seen in both velocity components. At z_3, u_{ω_f} no longer exhibits the four-lobe structure, as instead the bottom lobes grow more rapidly, convect downstream sooner, and merge with their same-sign top lobe counterparts. The lack of a π phase jump in u_{ω_f} is an indicator of the presence of spanwise flow, or more specifically, $\frac{\partial w_{\omega_\text{f}}}{\partial z}$, based on continuity. The outer region of the synthetic mode at z_3 appears to be reasonably well-aligned with the other spanwise positions, with the deviation growing as the wall is approached. This suggests that the 3D effects of the finite-span roughness impact the near-wall structures first and then percolate outwards.

As in Section 4.2, the vorticity perspective is explored by plotting isosurfaces of Ω_{ω_f}in Figure 4.9, with the axes having a true aspect ratio. The data between the spanwise positions has been linearly interpolated to generate these surfaces, and the z_2 and z_3 data have been reflected across the $z = 0$ centerline to form the full span. The isosurfaces show essentially two-dimensional vortex tubes forming from the roughness and convecting downstream. The view in Figure 4.9b highlights the shearing that occurs in the vortex tubes, as they are deformed into more sheet-like structures downstream. The vortex tubes decay as they convect, but remain mostly 2D. This was anticipated, given the 2D geometry of the roughness element, but is now confirmed through measurement. Certainly along the centerline, where the majority of the data were taken, the synthetic mode remains two-dimensional for a significant streamwise extent, and thus the assumption of 2D flow is validated.

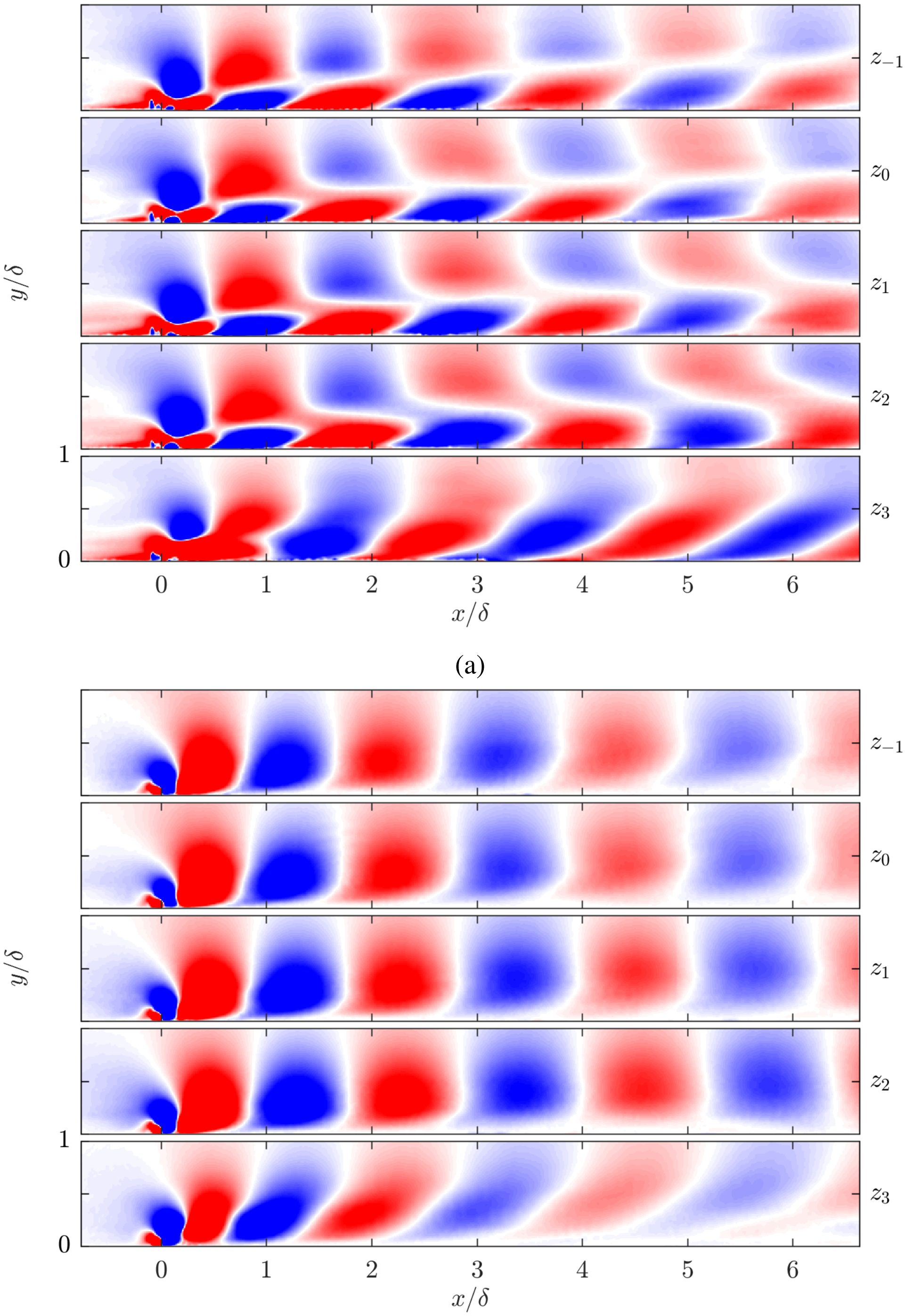

(a)

(b)

Figure 4.8: $j = 0$ phase snapshot of (a) $u_{\omega_{\mathrm{f}}}$ and (b) $v_{\omega_{\mathrm{f}}}$ at each spanwise position (actuation condition iii).

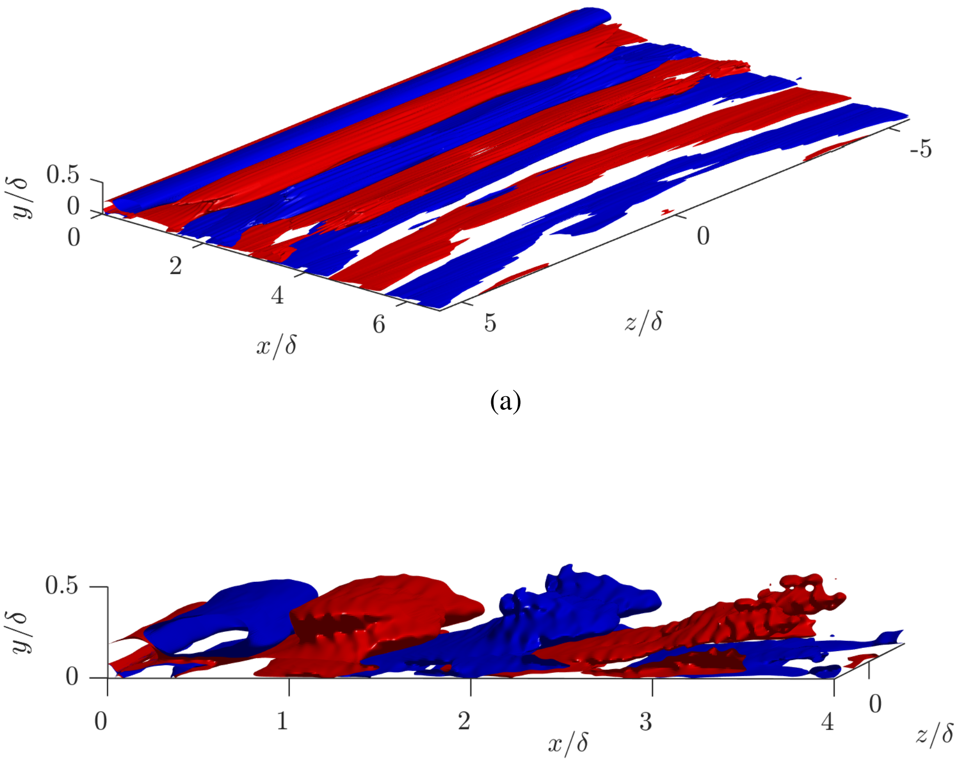

(a)

(b)

Figure 4.9: Isosurfaces (-0.08 and 0.08) of spanwise vorticity ($\Omega_{\omega_f}\delta/U_\infty$) from actuation condition iii, with data linearly interpolated between spanwise positions and z_2 and z_3 reflected across the centerline ($z = 0$) to form the full span. (a) top view, (b) side view.

4.4 Parametric study of the synthetic modes

Figure 4.10 shows the $j = 0$ snapshots for u_{ω_f} and v_{ω_f} at actuation conditions i-iv. There is a clear positive correlation between actuation frequency and synthetic mode wavenumber. The structures also share a general shape, though the structures at the highest frequency (condition iv) depart from this pattern and appear much less distinct than the lower frequency cases. The two middle frames show the cases ii and iii, having the same frequency but different amplitudes. The structures have very similar streamwise wavelengths, with case ii appearing more sheared in shape and losing form more quickly than case iii. Two useful metrics are the maximum and rms values of the velocity fields, which are given in Table 4.3. The u_{ω_f} maxima do not appear to be very sensitive to the actuation conditions, all being within 11% of their mean value, with a slight negative correlation with increasing actuation frequency and amplitude. The v_{ω_f} maxima have much more variation relative to their mean, and a positive correlation with increasing frequency and amplitude. Given that the kinetic energy of the roughness is proportional to the square of the frequency and linearly with amplitude, these trends suggest that the v_{ω_f} structures are more directly coupled to the dynamics of the motion than the u_{ω_f} structures. The rms values tend to decrease with increasing frequency, reflecting the fact that the higher frequency structures decay more rapidly. Case iii shows that the highest amplitude actuation results in the highest rms value by a factor of ~2-3.

	i	ii	iii	iv
max(u_{ω_f})×10	3.6	3.4	3.2	3.2
max(v_{ω_f})×10	0.8	1.1	1.5	1.3
rms(u_{ω_f})×10^3	7.3	6.3	12.2	5.4
rms(v_{ω_f})×10^3	4.4	4.1	11.5	3.2

Table 4.3: Maximum and rms values of u_{ω_f} and v_{ω_f} for each actuation condition, scaled by U_∞.

To characterize the synthetic modes, their streamwise wavenumbers, $k_{x\mathrm{f}}$, were calculated by treating them as simple, downstream-traveling waves. This allowed the wavenumber to be determined by the streamwise derivative of the phase of the Fourier modes:

$$
\begin{aligned}
u_{\omega_\mathrm{f}} &= e^{i(k_{x\mathrm{f}}x-\omega_\mathrm{f}t)} + \text{c.c.}\\
\widehat{u}_{\omega_\mathrm{f}} &= e^{ik_{x\mathrm{f}}x}\\
\angle\widehat{u}_{\omega_\mathrm{f}} &= k_{x\mathrm{f}}x\\
\Rightarrow k_{x\mathrm{f}} &= \frac{\partial\angle\widehat{u}_{\omega_\mathrm{f}}}{\partial x}.
\end{aligned}
\tag{4.8}
$$

This approach was equally valid for the streamwise and wall-normal velocities, and they generally yielded similar results (within 2% of one another). However, the v_{ω_f} fields were typically smoother than u_{ω_f} and did not have any abrupt phase jumps, so v_{ω_f} was used to determine $k_{x\mathrm{f}}$. Figure 4.11a shows the phase of v_{ω_f} at $y/\delta = 0.5$, plotted as a function of x (for actuation condition iii). The phase is essentially linear in x, strengthening the traveling-wave assumption, with only a slight kink at $x/\delta = 6.5$ due to the stitching of the FOVs. The streamwise derivative of $\angle\widehat{v}_{\omega_\mathrm{f}}$ was estimated by calculating the slopes of secant lines whose endpoints were 20 points apart and taking the trimmed mean (excluding the top and bottom 5% values) to reduce the effect of noise. Only points for $x/\delta > 2$ were taken to avoid the transient region immediately downstream of the roughness. This process was performed and a $k_{x\mathrm{f}}$ calculated at every wall-normal location, and the result is shown in Figure 4.11b (for actuation condition iii). For $y/\delta > 0.1$, the estimated $k_{x\mathrm{f}}$ is essentially the constant in y. The average of these values was taken over $0.3 < y/\delta < 1.0$ to avoid near-wall variations, and that value was taken to be the streamwise wavenumber for a given actuation condition. This calculation was done for each dataset except for case iv, and the resulting wavenumbers and wavelengths are given in Table 4.4. The flow field for case iv was found to be much more complex and the single-traveling-wave assumption was not appropriate. This was not explored further, and a rough wavenumber was estimated by hand-selecting a few peaks in the velocity and calculating the distance between them.

Table 4.4 supports the observation from Figure 4.10 that $k_{x\mathrm{f}}$ increases as ω_f increases, and that cases ii and iii have comparable $k_{x\mathrm{f}}$. With $k_{x\mathrm{f}}$ and $\lambda_{x\mathrm{f}}$ determined, the wave speeds of the forced modes were calculated, $c_\mathrm{f} = \omega_\mathrm{f}/k_{x\mathrm{f}} = f_\mathrm{f}\lambda_{x\mathrm{f}}$, and are provided in Table 4.5. Here, the scaling is done with the freestream velocities from the SW-DRF datasets, rather than the canonical flow dataset, for a more accurate sense of wave speed. Though the wave speeds are all fairly similar, within 10% of their mean, there is a trend of increasing wave speed with increasing frequency. To better understand the contents of Tables 4.4 and 4.5, the synthetic mode wavenumber and wave speed are plotted as functions of actuation frequency in Figure 4.12, for cases i, ii, and iv ($h_{\mathrm{rms}}/\delta = 0.042$). The data point from the single-frequency study by Duvvuri & McKeon [14], $\left(\frac{\omega_{\mathrm{f}}\delta}{U_\infty} = 0.24, k_{x\mathrm{f}}\delta = 0.41\right)$, is included to examine the agreement between the experiments, and is a reasonable comparison due to the fairly similar amplitude ($h_{\mathrm{rms}}/\delta = 0.033$). In Figure 4.12a, $k_{x\mathrm{f}}$ appears to be linear in ω_{f}. A simple least-squares linear fit is also plotted and found to agree quite well with the data. The calculated linear fit is:

$$k_{x\mathrm{f}}\delta\left(\frac{\omega_{\mathrm{f}}\delta}{U_\infty}, \frac{h_{\mathrm{rms}}}{\delta} = 0.042\right) = 1.10\,\frac{\omega_{\mathrm{f}}\delta}{U_\infty} + 0.18. \tag{4.9}$$

The non-zero $k_{x\mathrm{f}}$-axis intercept of the fit is likely unphysical, and indicates nonlinear behavior for very small ω_{f}. This could be reasonable, as the dynamic nature of the perturbation would breakdown for very long actuation timescales, i.e. the quasi-static limit. The greater-than-one coefficient on ω_{f} in Equation 4.9 is physically reasonable, as it bounds the wave speed to be less than the freestream velocity in the limit as ω_{f} approaches infinity. The coefficients of this fit may also be functions of the actuation amplitude, though likely weak functions based on the similarity between the wavenumbers/wave speeds of cases ii and iii. Thus, Equation 4.9 may be able to predict the streamwise scale of the synthetic mode for a given frequency of dynamic roughness actuation.

		h_{rms}/δ [h_{rms}]	
		0.042 [1.1 mm]	0.069 [1.8 mm]
$\frac{\omega_{\mathrm{f}}\delta}{U_\infty}$ [f_{f}]	1.4 [3 Hz]	i. 1.69 (3.71)	-
	2.4 [5 Hz]	ii. 2.60 (2.41)	iii. 2.67 (2.36)
	4.8 [10 Hz]	iv. 5.02 (1.25)	-

Table 4.4: Streamwise wavenumbers, $k_{x\mathrm{f}}\delta$, (and wavelengths, $\lambda_{x\mathrm{f}}/\delta$, in parentheses) calculated for each actuation condition.

		h_{rms}/δ [h_{rms}]	
		0.042 [1.1 mm]	0.069 [1.8 mm]
$\frac{\omega_{\mathrm{f}}\delta}{U_\infty}$ [f_{f}]	1.4 [3 Hz]	i. 0.79	-
	2.4 [5 Hz]	ii. 0.85	iii. 0.83
	4.8 [10 Hz]	iv. 0.88	-

Table 4.5: Wave speed, c_{f}/U_∞, for each actuation condition.

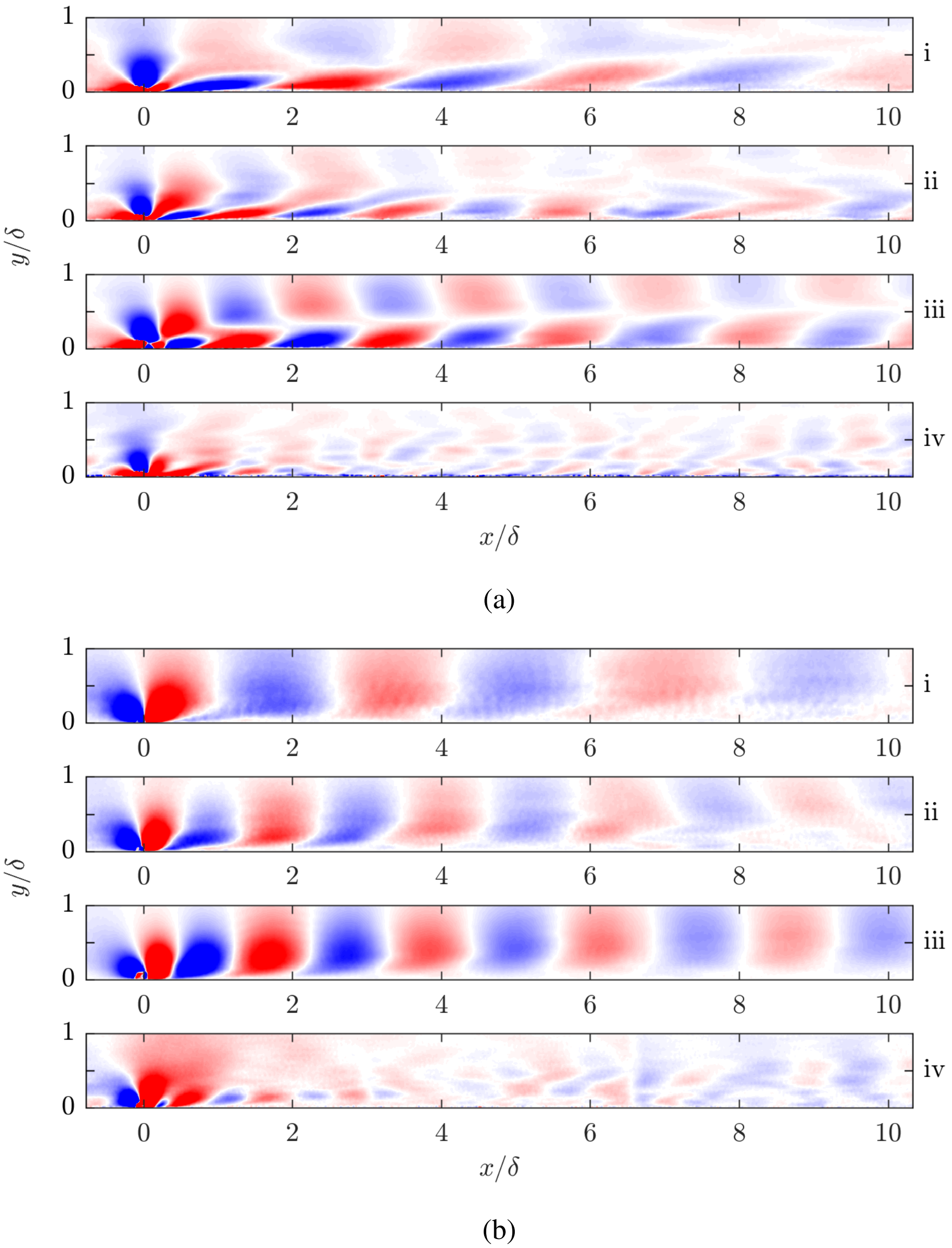

Figure 4.10: Comparison of the (a) u_{ω_f} and (b) v_{ω_f} synthetic structures generated at different roughness actuation conditions, with top to bottom plots corresponding to (i-iv) from Table 4.1. All plots are at phase index $j = 0$. The colorbar limits vary for each plot for visibility.

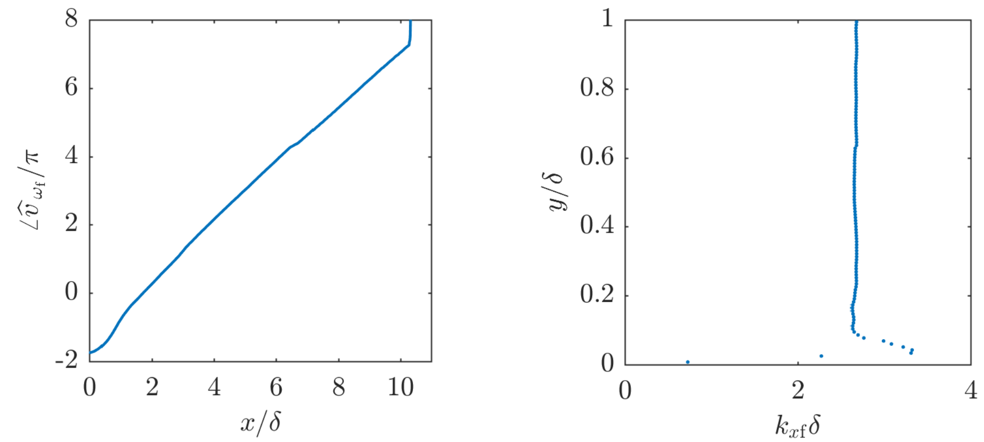

(a) (b)

Figure 4.11: (a) $\angle\widehat{v}_{\omega_\mathrm{f}}(y/\delta = 0.5)$ as a function of x, and (b) $k_{x\mathrm{f}}$ calculated at each wall-normal location. Both plots correspond to actuation condition iii.

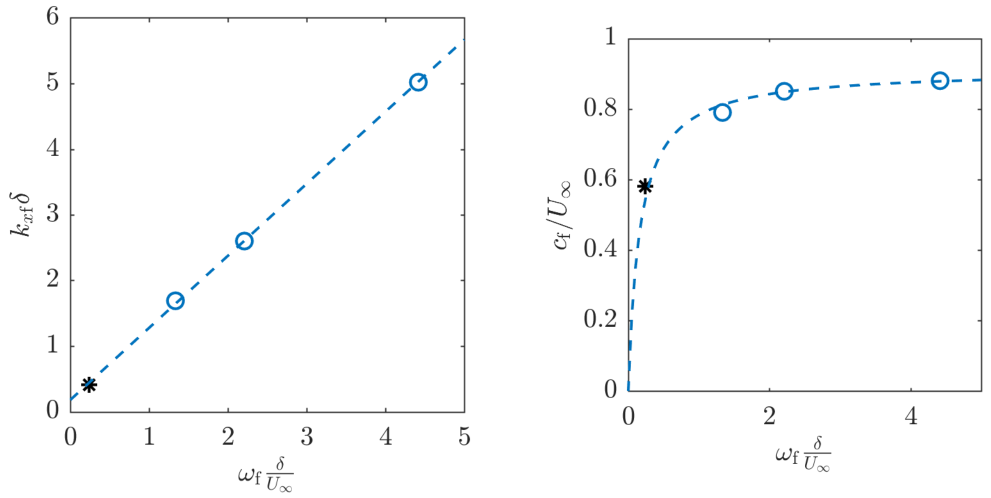

(a) (b)

Figure 4.12: (a) Streamwise wavenumber, $k_{x\mathrm{f}}$, and (b) streamwise wave speed, c_f, of the synthetic mode versus angular forcing frequency, ω_f. ○ SW-DRF data; – – SW-DRF linear fit; $*$ Duvvuri & McKeon (2015) [14].

4.5 Temporal Fourier mode shapes and amplitude modulation

Given the natural Fourier framework for the phase-averaged velocities, the Fourier mode shapes were explored to better understand the flow's dynamic roughness response. The 1D amplitude mode shapes are given in Figure 4.13 at three streamwise locations from actuation condition iii. A clear dual-peak is observed in $|\widehat{u}_{\omega_\mathrm{f}}|$, while $|\widehat{v}_{\omega_\mathrm{f}}|$ is seen to be quite tall, both in agreement with the previously shown 2D snapshots in Figure 4.5. Tracking the maxima supports the previous observation that the modes decay and drift away from the wall downstream, consistent with internal layer structures. The decay rate is estimated by a streamwise decaying exponential fit to the mode amplitude, done for each wall-normal location:

$$|\widehat{u}_{\omega_\mathrm{f}}|(x, y) = Ae^{-\alpha_u x/\delta}. \tag{4.10}$$

The wall-normal profiles of the streamwise and wall-normal velocity decay rates are given in Figure 4.14 for actuation condition iii. The maximum decay rates for $|\widehat{u}_{\omega_\mathrm{f}}|$ and $|\widehat{v}_{\omega_\mathrm{f}}|$ are 0.3 and 0.4, respectively, and the mean decay rate is 0.12 for both. It is clear that the decay is not uniform in y. The decay profiles seem to reflect features of the mode amplitudes in Figure 4.13, with the dual-peak in α_u and a single peak in α_v, though the peak in α_v sits much lower to the wall than the peak in $|\widehat{v}_{\omega_\mathrm{f}}|$, more closely aligned to the near-wall peak of α_u. Both decay rates are negative very near the wall, though this is obviously unphysical and likely due to noise in the data and the lack of exponential behavior. α_u is also negative farther from the wall, around $0.3 < y/\delta < 0.42$. This corresponds to the location of the π phase jump in u_{ω_f}, which gradually shifts away from the wall, and thus is a region where a growth or decay rate is ill-defined. In general, the decay rates observed here are slightly larger than Jacobi & McKeon (2011) [32], who observed a maximum decay rate on the order of 0.07 for the streamwise velocity mode.

Returning to Figure 4.13, it is also evident in that the maxima in $|\widehat{v}_{\omega_\mathrm{f}}|$ correspond well with the (near) zero crossings in $|\widehat{u}_{\omega_\mathrm{f}}|$. This is required by continuity for a 2D flow with a constant-phase wall-normal component, and provides evidence that the present perturbation is indeed two-dimensional. In sum, the mode shapes are reminiscent of 2D Tollmien-Schlichting instability waves. This structure is interesting given that the flow is fully turbulent.

The PIV data also allowed access to the 2D, streamwise-resolved mode shapes, which are shown in Figure 4.15 for actuation condition iii. The (wrapped) phase contours in 4.15b make clear the earlier observation that u_{ω_f} undergoes a sharp, π

phase jump in y, as well as highlight the downstream inclination of the structure near the wall and the subtle upstream inclination away from the wall. $\angle\widehat{v}_{\omega_\mathrm{f}}$ is nearly constant in y except near the wall, where $\frac{\partial \angle\widehat{v}_{\omega_\mathrm{f}}}{\partial y} < 0$. As expected, the amplitude contours in 4.15a are consistent with the plots in Figure 4.13, with the dual-peak structure in $|\widehat{u}_{\omega_\mathrm{f}}|$ seen as the two bright stripes, while $|\widehat{v}_{\omega_\mathrm{f}}|$ has a single, tall band. These contours provide a 2D description of the observations from the 1D profiles, and the internal layer-like drift and decay of the mode amplitudes are well-resolved. To quantify the internal layer shape, a power law fit is applied y-locations of the mode amplitude maxima using MATLAB's non-linear least squares solver:

$$g(x) = A\,(x/\delta)^{\beta}\,. \tag{4.11}$$

The fit is calculated for the inner and outer peaks in $|u_{\omega_\mathrm{f}}|$ and for the single peak in $|v_{\omega_\mathrm{f}}|$. The fits are plotted as the blue dashed lines in Figure 4.15a, and given for actuation condition iii below:

$$\begin{aligned} g_{u,\mathrm{inner}}(x) &= 0.05\,(x/\delta)^{0.60} && (4.12)\\ g_{u,\mathrm{outer}}(x) &= 0.40\,(x/\delta)^{0.35} && (4.13)\\ g_{v}(x) &= 0.23\,(x/\delta)^{0.41}\,. && (4.14) \end{aligned}$$

Visually, the power law fits describe the gradual drift of the maxima well. All of equations 4.12-4.14 indicate that the synthetic structures are gradually detaching from the wall. Jacobi & McKeon (2011) [32] calculated a similar fit to the single peak in their observed roughness-forced u structure to be $0.08(x/\delta)^{0.45}$. The fit coefficients in of equations 4.12-4.14 are of a comparable scale to those calculated by Jacobi & McKeon, and the disparities may be explained by the differences in roughness geometry, flow conditions, and overall synthetic mode shape.

Close inspection of the contours reveals a sinuous pattern oriented in x, and is best seen along the top of the $|\widehat{u}_{\omega_\mathrm{f}}|$ plot. Such a feature indicates amplitude modulation, as the amplitude is not simply decaying, but is beating, albeit weakly. In Figure 4.16, the x-axis is scaled by $\lambda_{x\mathrm{f}}$ instead of δ, which highlights that the modulation length scale is the same as the length scale of the synthetic mode itself. This is a special case of amplitude modulation and can be understood through a simple example.

For a single-wavenumber signal, the amplitude of the Fourier mode is constant, e.g.:

$$\begin{aligned} \widehat{u}_{\omega_\mathrm{f}} &= e^{ik_{x1}x}\\ |\widehat{u}_{\omega_\mathrm{f}}| &= 1. \end{aligned} \tag{4.15}$$

In contrast, for multi-wavenumber signal, the amplitude is a sum of sinusoids with wavenumbers equal to the difference of wavenumber pairs, e.g. for a two-wavenumber signal:

$$\begin{aligned}
\widehat{u}_{\omega_\mathrm{f}} &= e^{ik_{x1}x} + e^{ik_{x2}x} \\
|\widehat{u}_{\omega_\mathrm{f}}| &= \left(e^{ik_{x1}x} + e^{ik_{x2}x}\right)\left(e^{-ik_{x1}x} + e^{-ik_{x2}x}\right) \\
&= e^{i(k_{x1}-k_{x2})x} + e^{i(k_{x2}-k_{x1})x} + 2 \\
&= 2\left(\cos\left((k_1 - k_2)x\right) + 1\right).
\end{aligned} \tag{4.16}$$

From Equation 4.16, it is clear that the amplitude modulation requires multiple scales, as with any amplitude modulation, and for the modulation wavenumber to be the same as the dominant structure in the flow, the interaction must be between two wavenumbers whose difference is equal to $k_{x\mathrm{f}}$. Direct interaction with the dominant $k_{x\mathrm{f}}$ content would require either a DC scale ($k_x = 0$), a first-harmonic scale ($k_x = 2k_{x\mathrm{f}}$), or both. However, any two wavenumbers with sufficient energy and satisfying $k_{x1} - k_{x2} = k_{x\mathrm{f}}$ would contribute to this modulation. Generally, the presence of this modulation suggests a somewhat broad k_x spectral peak around $k_{x\mathrm{f}}$, as will be explored further in the next section.

To better visualize this modulation, the mode amplitudes are plotted along the power law curves from equations 4.12-4.14 in Figure 4.17, corresponding to actuation condition iii. Figure 4.17a shows the data from the final and currently presented SW-DRF study, with very small modulations visible in the $|\widehat{u}_{\omega_\mathrm{f}}|$ peaks. In contrast, Figure 4.17b shows the data from the initial SW-DRF study [29], where a much more pronounced modulation is observed in $|\widehat{u}_{\omega_\mathrm{f}}|$ and possibly in $|\widehat{v}_{\omega_\mathrm{f}}|$ as well. The flow and actuation conditions between the initial and final studies were essentially the same. The primary differences were the removal of the shaft bearing, addition of the PVC-pipe housing around the roughness shaft, and overall improved alignment of the apparatus in the final study, described in Section 2.2. These changes minimized the load on the Bose motor and noticeably improved the actuation signal quality, as shown in Figure 2.6. This suggests a direct connection between the actuation motion and the modulation phenomenon, as opposed to a flow-born interaction. The interpretation of this difference in modulation intensity will be revisited in the next section.

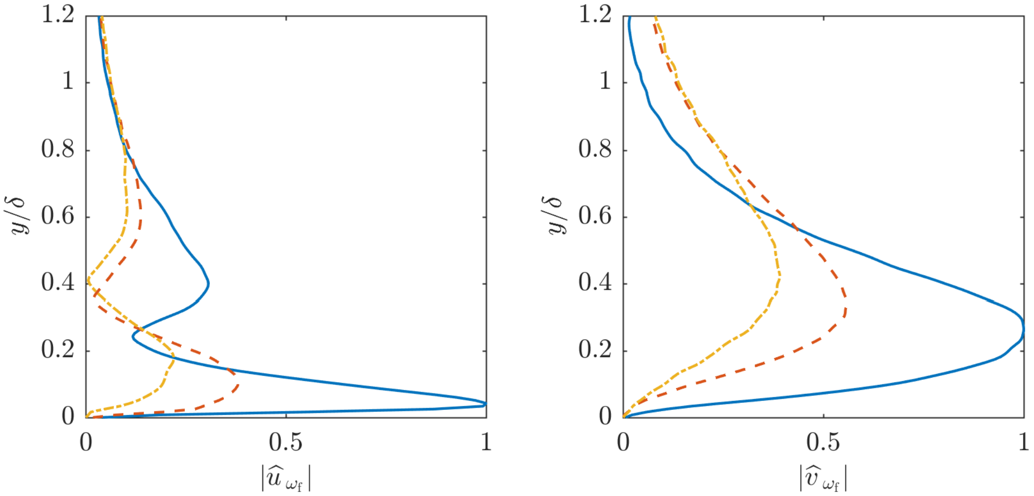

(a)

(b)

Figure 4.13: Mode amplitudes at increasing streamwise stations (actuation condition iii), normalized by the peak amplitude of the upstream-most station: (a) streamwise and (b) wall-normal component. — $x/\delta = 2.8$; – – $x/\delta = 4.7$; ● – $x/\delta = 6.7$.

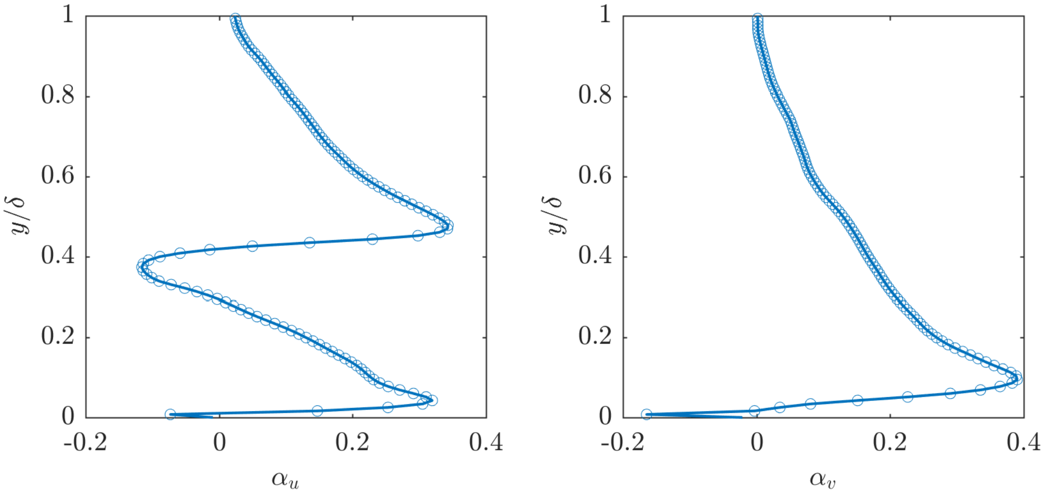

(a)

(b)

Figure 4.14: Wall-normal profiles of the streamwise exponential decay rates for the ω_f mode amplitudes (actuation condition iii): (a) streamwise velocity decay rate, α_u, and (b) wall-normal velocity decay rate, α_v.

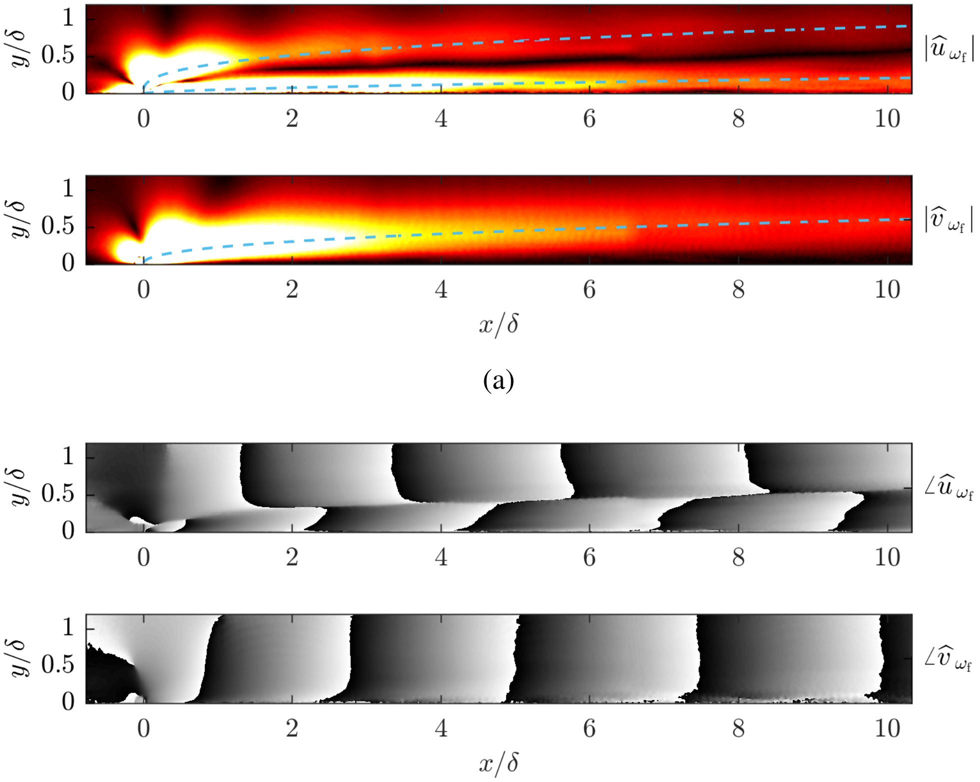

(a)

(b)

Figure 4.15: 2D contours of mode (a) amplitude and (b) phase (wrapped) for actuation condition iii. Top plots are of the streamwise component, $\widehat{u}_{\omega_f}$, bottom plots the wall-normal component, $\widehat{v}_{\omega_f}$.

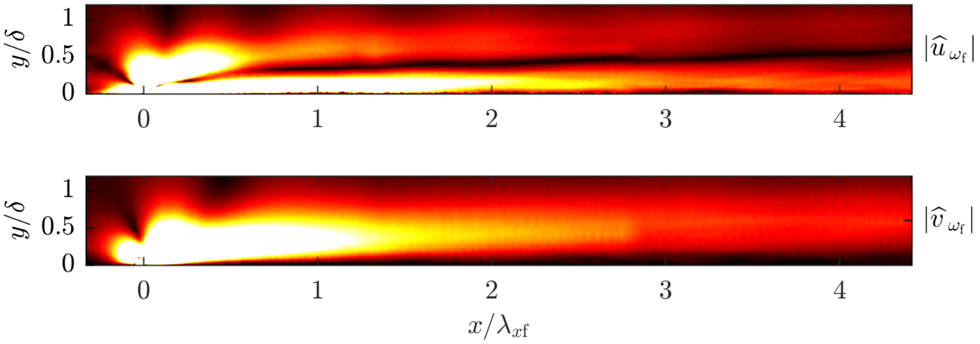

Figure 4.16: 2D contour of mode amplitude (actuation condition iii), with the x-axis scaled by λ_{xf} to highlight the modulation length scale. The top plot is the streamwise component, $\widehat{u}_{\omega_f}$, and bottom plot the wall-normal component, $\widehat{v}_{\omega_f}$.

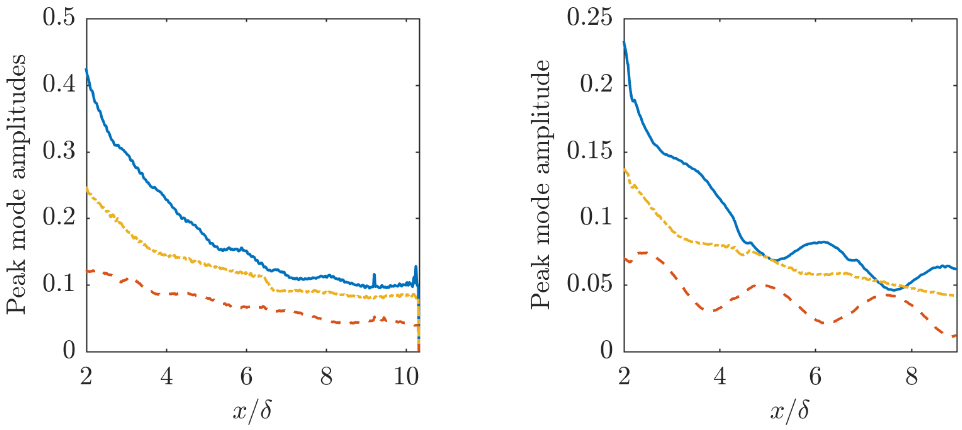

(a) (b)

Figure 4.17: Peak mode amplitude (in y) as a function of x for actuation condition iii. (a) Data from the final and (b) the initial SW-DRF study. — $|\widehat{u}_{\omega_\mathrm{f}}|$, inner peak; – – $|\widehat{u}_{\omega_\mathrm{f}}|$, outer peak; ● – $|\widehat{v}_{\omega_\mathrm{f}}|$.

4.6 Spatio-temporal analysis and spectral signature of the synthetic mode

With the temporal coherence of the synthetic scale given by ω_f and the spatial coherence characterized by $k_{x\mathrm{f}}$, a streamwise-spatio-temporal decomposition is now employed to better understand the spatial spectral content of the synthetic mode. Ideally, this would involve a transformation of the wall-normal coordinate, y, to account for the non-parallel nature of the flow, i.e. $\widehat{u}_{\omega_\mathrm{f}}(x, y) = \widehat{u}_{\omega_\mathrm{f}}(x, \eta(x))$. However, such a coordinate transformation adds other complexities to the analysis, and based on the drift behavior of the flow described in equations 4.12-4.14, a single transformation may not apply to both velocity components or to the whole domain. Instead, a more straightforward approach is taken here by assuming locally parallel flow.

Anticipating the $k_{x\mathrm{f}}$ content, the temporal Fourier modes, $\widehat{u}_{\omega_\mathrm{f}}(x, y)$ and $\widehat{v}_{\omega_\mathrm{f}}(x, y)$, are zero-padded in x to accommodate the next multiple of $\lambda_{x\mathrm{f}} = \frac{2\pi}{k_{x\mathrm{f}}}$, such that the spectral resolution is an optimal fraction of the synthetic mode wavenumber. This zero-padding amounts to a total-energy-preserving spectral interpolation that leverages the knowledge of $k_{x\mathrm{f}}$. For the full procedure, the ω_f velocity field is discrete Fourier transformed in time (equation 4.17), zero-padded in x, and then discrete Fourier transformed in x (equation 4.18):

$$u_{\omega_\mathrm{f}}(x, y, t) = \widehat{u}_{\omega_\mathrm{f}}(x, y)e^{-i\omega_\mathrm{f} t} + \text{c.c.} \tag{4.17}$$

$$= \left[\sum_n \widehat{\widehat{u}}_{\omega_\mathrm{f}}(y; nk_{x\mathrm{f}})e^{i(nk_{x\mathrm{f}}x - \omega_\mathrm{f} t)}\right] + \text{c.c.}, \tag{4.18}$$

where $\widehat{\widehat{(\cdot)}}$ indicates a quantity that has been discrete Fourier transformed in t and x. The (rational, not necessarily integer) values of n are determined by the zero-padding process, and by construction include $n = 1$. The $n = 1$ Fourier coefficient corresponds to the ω_f-$k_{x\mathrm{f}}$ spatio-temporal Fourier component of the velocity and is referred to as $\widehat{\widehat{u}}_{\omega_\mathrm{f} k_{x\mathrm{f}}} = \widehat{\widehat{u}}_{\omega_\mathrm{f}}(y; n = 1)$. Accordingly, the velocity field reconstructed by this Fourier coefficient is referred to as $u_{\omega_\mathrm{f} k_{x\mathrm{f}}}$, and is purely sinusoidal in x and t and varies in y. This procedure was performed for $x/\delta > 2$ (to avoid the transient region just downstream of the roughness) and for all y.

The streamwise and wall-normal ω_f-$k_{x\mathrm{f}}$ mode shapes for actuation condition iii are provided in Figures 4.18 and 4.19, respectively. The mode amplitudes are both normalized by the peak in $|\widehat{\widehat{u}}_{\omega_\mathrm{f} k_{x\mathrm{f}}}|$ for comparison. The overall features are consistent with the mode shapes in Figures 4.13, 4.15, with strong T-S wave features. Despite $\widehat{u}_{\omega_\mathrm{f}}$ and $\widehat{v}_{\omega_\mathrm{f}}$ exhibiting a gradual drift in the wall-normal direction, $\widehat{\widehat{u}}_{\omega_\mathrm{f} k_{x\mathrm{f}}}$ and $\widehat{\widehat{v}}_{\omega_\mathrm{f} k_{x\mathrm{f}}}$ appear well-defined, suggesting that the local-parallel-flow assumption is reasonable. Comparing the normalized amplitudes of the modes, the inner peak of $|\widehat{\widehat{u}}_{\omega_\mathrm{f} k_{x\mathrm{f}}}|$ is the largest at 1.0, followed by the peak of $|\widehat{\widehat{v}}_{\omega_\mathrm{f} k_{x\mathrm{f}}}|$ at 0.7, and the outer peak of $|\widehat{\widehat{u}}_{\omega_\mathrm{f} k_{x\mathrm{f}}}|$ at 0.4. The inner peak of $|\widehat{\widehat{u}}_{\omega_\mathrm{f} k_{x\mathrm{f}}}|$ is notably more narrow than the other peaks. The streamwise mode phase in Figure 4.18b still contains the sharp π jump. The phase difference between $\widehat{\widehat{u}}_{\omega_\mathrm{f} k_{x\mathrm{f}}}$ and $\widehat{\widehat{v}}_{\omega_\mathrm{f} k_{x\mathrm{f}}}$ is nearly constant at $\pi/2$ in the outer portion of the profiles. After the phase jump in $\widehat{\widehat{u}}_{\omega_\mathrm{f} k_{x\mathrm{f}}}$, the phase difference is roughly $\pi/2$ in the opposite sense. Both $\widehat{\widehat{u}}_{\omega_\mathrm{f} k_{x\mathrm{f}}}$ and $\widehat{\widehat{v}}_{\omega_\mathrm{f} k_{x\mathrm{f}}}$ exhibit a slight downstream incline for $0.05 < y/\delta < 0.4$, and both reverse to be upstream inclined for $y/\delta < 0.05$.

The k_x amplitude spectra were calculated for the ω_f Fourier modes and averaged in y, and are given in Figure 4.20 for actuation condition iii. The spectra are normalized by the larger of the two spectral peaks, which is the peak in $|\widehat{\widehat{v}}_{\omega_\mathrm{f}}|$ in this case, though both are very close in value. The two spectra have similar shapes, both with a distinct peak at $n = 1$ or $k_x = k_{x\mathrm{f}}$, as expected. Though the Fourier amplitudes do drop off adjacent to $k_{x\mathrm{f}}$, they maintain non-trivial, $\sim 0.1 - 0.3$ of the peak value. This supports the amplitude modulation phenomenon in Figures 4.15a and 4.16, and agrees with the supposition of the previous section that the spatial spectral peak is at least somewhat broad. It is noted that part of the broad k_x spectrum is expected given the decaying nature of the flow, making it not strictly periodic. However, reconstructing a toy signal based on the $n = [0, 2]$ amplitudes and arbitrary phases captures both the decaying nature and the modulating envelope observed in the data. Thus, the amplitude modulation feature is a reflection of the broadness of the $k_{x\mathrm{f}}$ peak of the synthetic mode.

This spectral analysis provides context for the earlier note that the preliminary SW-DRF study observed more intense amplitude modulation than the final study. A reduction in the modulation phenomenon corresponds to a narrowing of the $k_{x\mathrm{f}}$ spectral peak, in other words, a 'cleaner' synthetic structure. By improving the alignment and actuation quality, the spectral characteristics of the roughness-forced mode must have been improved. Precisely how these additional scales come about remains unclear. One possible explanation is that slight misalignment of the roughness induces a small streamwise component to the nominally wall-normal actuation. This streamwise motion would temporally coherent with ω_f, but may have shifted k_x content from the dominant synthetic mode. By improving the alignment and minimizing the streamwise motion, this spatial harmonic content would be reduced and the amplitude modulation would diminish.

Lastly, the amplitude and phase values of the streamwise and wall-normal ω_f-$k_{x\mathrm{f}}$ modes are given in Table 4.6 for actuation conditions ii and iii. These values are taken from the critical layer location for the modes, y_CL, also provided in the table, and will be used for comparison to the compliant-wall study. As might be expected, the amplitude for both velocity components is notably higher for the larger h_rms condition. The amplitude of $\widehat{\widehat{v}}_{\omega_\mathrm{f} k_{x\mathrm{f}}}$ is larger than the corresponding $\widehat{\widehat{u}}_{\omega_\mathrm{f} k_{x\mathrm{f}}}$, which is also expected given that these data are taken at the critical layer, where $\widehat{\widehat{u}}_{\omega_\mathrm{f} k_{x\mathrm{f}}}$ undergoes a zero crossing. The phase values are consistent for $\widehat{\widehat{v}}_{\omega_\mathrm{f} k_{x\mathrm{f}}}$ between the two cases, and much less consistent for $\widehat{\widehat{u}}_{\omega_\mathrm{f} k_{x\mathrm{f}}}$. This, again, is due to the phase jump in $\widehat{\widehat{u}}_{\omega_\mathrm{f} k_{x\mathrm{f}}}$ around y_CL.

	Case ii			Case iii		
	y_CL/δ	Amplitude	Phase	y_CL/δ	Amplitude	Phase
$\widehat{\widehat{u}}_{\omega_\mathrm{f} k_{x\mathrm{f}}}(y_\mathrm{CL})$	0.34	$0.7 \cdot 10^{-3}$	0.23π	0.35	$3.8 \cdot 10^{-3}$	0.67π
$\widehat{\widehat{v}}_{\omega_\mathrm{f} k_{x\mathrm{f}}}(y_\mathrm{CL})$	0.34	$2.1 \cdot 10^{-3}$	0.31π	0.35	$9.7 \cdot 10^{-3}$	0.39π

Table 4.6: Amplitudes and phases of the ω_f-$k_{x\mathrm{f}}$ velocity modes at the critical layer location, for the SW-DRF study, cases ii and iii. The amplitudes are scaled to reflect the physical velocity and normalized by U_∞.

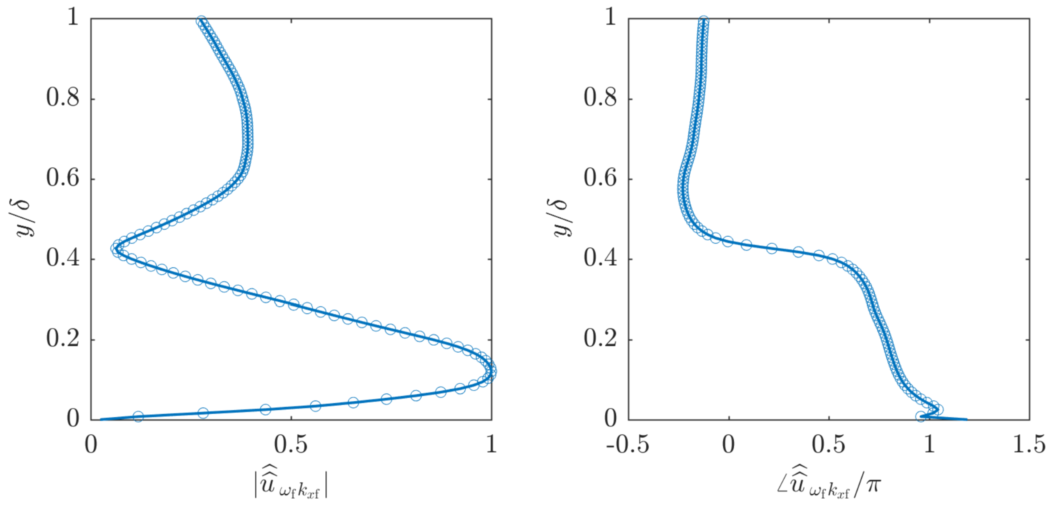

(a) (b)

Figure 4.18: Mode (a) amplitude and (b) phase of the ω_f-$k_{x\mathrm{f}}$ Fourier component of the streamwise velocity, $\widehat{\widehat{u}}_{\omega_\mathrm{f} k_{x\mathrm{f}}}$, from actuation condition iii. The amplitude is normalized by its peak.

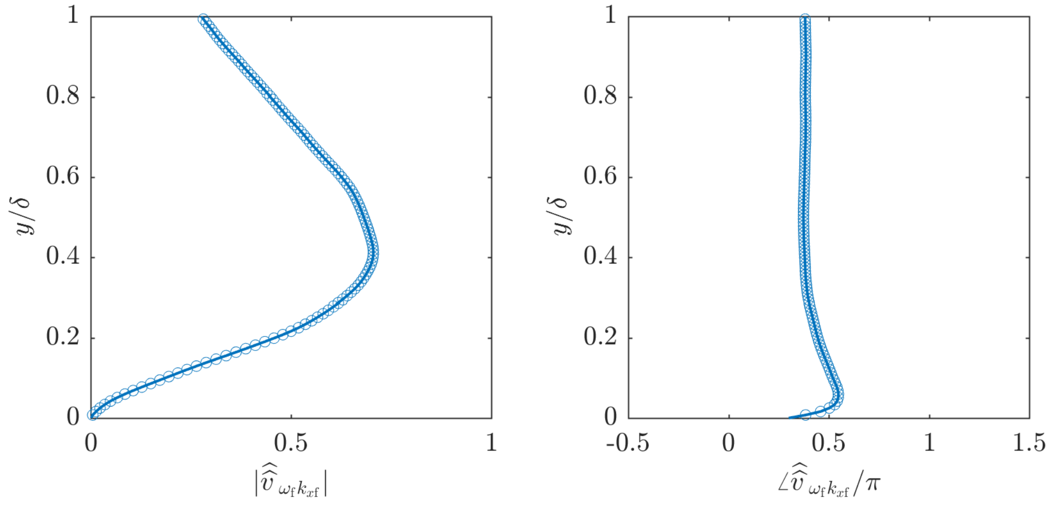

(a) (b)

Figure 4.19: Mode (a) amplitude and (b) phase of the ω_f-$k_{x\mathrm{f}}$ Fourier component of the wall-normal velocity, $\widehat{\widehat{v}}_{\omega_\mathrm{f} k_{x\mathrm{f}}}$, from actuation condition iii. The amplitude is normalized by the peak of $|\widehat{\widehat{u}}_{\omega_\mathrm{f} k_{x\mathrm{f}}}|$ for comparison.

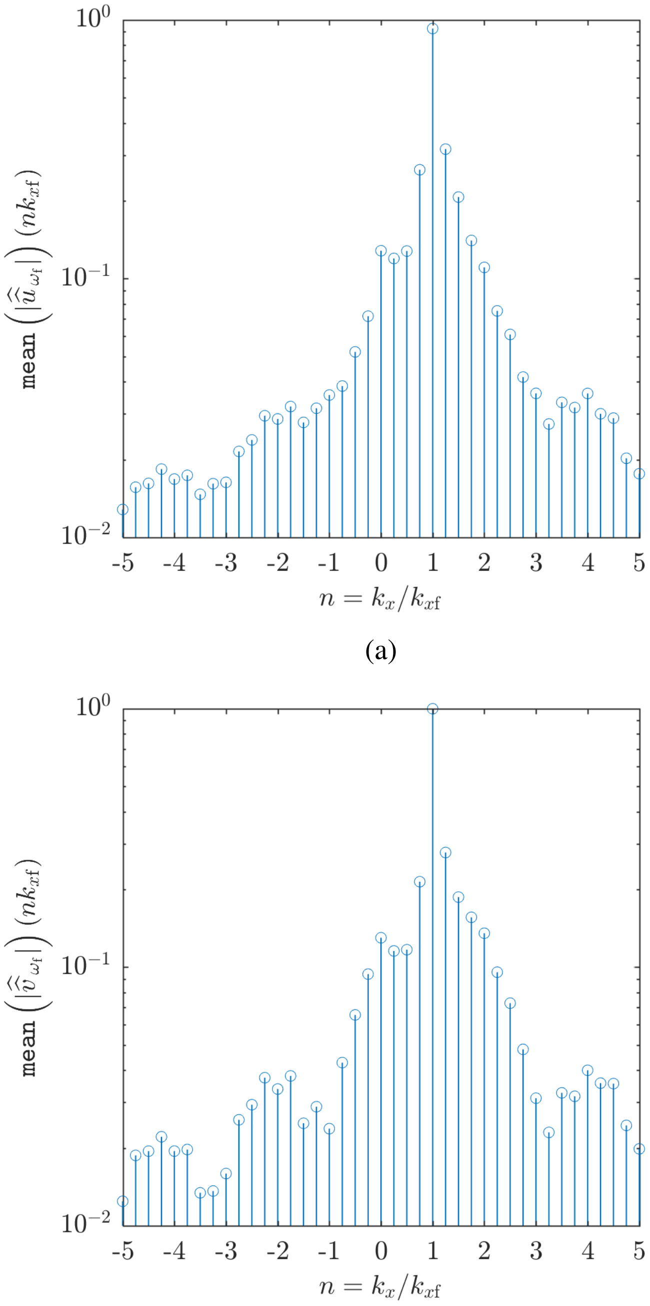

(a)

(b)

Figure 4.20: k_x amplitude spectra (averaged in y) of the ω_f component of the (a) streamwise ($\widehat{\widehat{u}}_{\omega_\mathrm{f}}$) and (b) wall-normal ($\widehat{\widehat{v}}_{\omega_\mathrm{f}}$) velocities, from actuation condition iii. The spectra are normalized by the peak in $|\widehat{\widehat{v}}_{\omega_\mathrm{f}}|$, larger of the two spectral peaks.

4.7 Chapter summary

A smooth-wall, turbulent boundary layer was forced by dynamic roughness in a water tunnel, generating a synthetic flow structure that was measured using phase-locked PIV. The prior dynamic roughness studies by Jacobi & McKeon (2011) [32] and Duvvuri & McKeon (2015) [14] were done in a wind tunnel and relied primarily on hot-wire measurements. As such, they mostly considered temporal analyses of the streamwise velocity, or spatial analyses by invoking Taylor's hypothesis. Though PIV measurements were made by Jacobi & McKeon (2011), Jacobi & McKeon (2013) [34] later discussed that the finite camera FOV essentially acted as an implicit, spatial highpass filter, limiting the spatial analysis available on the incredibly large, $\sim 15 - 18\delta$ length scale of the synthetic mode. In this work, the multi-FOV, phase-locked PIV measurements enabled resolved spatial and spatio-temporal investigations of both u and v signatures of the synthetic mode. The longer timescales of water granted access to higher non-dimensional frequencies, resulting in shorter synthetic structures.

The mean flow statistics were modified primarily by the static roughness component of the forcing, with signatures of internal layer development consistent with observations of Jacobi & McKeon (2011) [32, 33]. The streamwise and wall-normal velocity fields were phase-averaged and revealed a coherent traveling wave associated with the forcing. The forcing frequency (ω_f) component of the flow response was isolated using a discrete Fourier decomposition, and found to account for the majority of the structure's energy. The harmonic frequency content contained correspondingly harmonic wavenumber content, which acted to slightly distort the dominant ω_f mode. A study of $x - y$ plane PIV measurements at various spanwise locations was performed to vet the assumption of two-dimensionality of the synthetic mode. Significant deviations in the velocity fields were only observed near the spanwise edge of the roughness. Thus, the 2D assumption was confirmed along the centerline for the synthetic structure. Isosurfaces of spanwise vorticity also highlighted the alternating vortex tubes that make up the flow structure and illustrated the shearing that takes place as these tubes convect downstream.

A parametric study was done by altering the forcing frequency and roughness amplitude for actuation conditions i-iv. The streamwise wavenumber of the synthetic scale, $k_{x\mathrm{f}}$, was calculated by estimating the streamwise derivative of the phase of the wall-normal velocity mode, $\widehat{v}_{\omega_\mathrm{f}}$. $k_{x\mathrm{f}}$ ranged from $[1.69 - 5.02]/\delta$ ($\lambda_{x\mathrm{f}}$ from $[3.71 - 1.25]\delta$), and was found to increase with ω_f in an approximately linear fashion, though coherence of the synthetic structure departs dramatically for the highest frequency tested (actuation condition iv). This linear relationship agreed well with the data of Duvvuri & McKeon (2015) [14], and the resulting empirical linear fit may be used to select a forcing frequency to achieve a particular streamwise length scale of synthetic mode.

The 1D and 2D ω_f Fourier mode shapes were investigated and found to resemble T-S instability modes, with $\widehat{u}_{\omega_\mathrm{f}}$ being dual-peaked and undergoing a π phase jump, and $\widehat{v}_{\omega_\mathrm{f}}$ being single-peaked and tall, with nearly constant phase. The mode features gradually decayed and drifted away from the wall in x, in a manner again consistent with an internal layer structure. Careful examination of the 2D mode amplitudes revealed an amplitude modulation feature, with the modulation envelope having the same streamwise wavenumber as the synthetic structure itself, $k_{x\mathrm{f}}$. This indicated a somewhat broad peak around $k_x = k_{x\mathrm{f}}$, and was able to be tested directly by a (zero-padded) discrete Fourier decomposition in x. The now ω_f-$k_{x\mathrm{f}}$ mode shapes remained reminiscent of T-S waves and were well-defined despite the flow not being strictly parallel in x. The k_x spectra displayed a peak at $k_{x\mathrm{f}}$ with non-trivial adjacent spectral content, confirming the interpretation of the amplitude modulation phenomenon. Comparison with the initial SW-DRF study, which observed a more notable modulation feature, highlighted the importance of careful alignment and equipment isolation in the experiment for a clean synthetic mode.

The analysis laid out in this chapter provides a framework with which to process and analyze the data from the subsequent compliant-wall studies. The SW-DRF study also provides a base case for comparison with the CW-DRF study. The judicious design and construction of the experiment and the novel experimental technologies enabled the precision actuation of the dynamic roughness element and the phase-locked PIV measurements. These measurements allowed for a thorough spatio-temporal treatment of the streamwise and wall-normal velocity components, and the subsequent analysis contributed to our understanding of dynamic roughness forcing of a turbulent boundary layer.

Chapter 5

RESPONSE OF AN ELASTIC, COMPLIANT-WALL TO A CANONICAL, TURBULENT BOUNDARY LAYER

Before analyzing the compliant-wall's response to the dynamic roughness forcing, the response of the gelatin sample to the unforced turbulent boundary layer flow was studied. This was done by submerging the compliant sample in the test section, fixing the roughness element to be flush with the wall, and running the water tunnel. The non-dynamic-roughness-forced, compliant-wall system is referred to as 'CW-unforced' for conciseness, though it is recognized that the flow-surface system is indeed being driven by the flow. The characterization of the unforced system is important to determine whether the synthetic mode directly causes a surface response, or simply amplifies a naturally occurring mode. Stereo-DIC data were acquired in three FOVs as discussed in Section 2.5 and illustrated in Figure 2.18, referred to as: leading-edge (LE), corner, and trailing-edge (TE). The streamwise, wall-normal, and spanwise deformation fields (temporally mean subtracted) are denoted by d_x, d_y, and d_z, respectively, and are each functions of x, z, and t.

For a sense of scale, the rms values for the LE FOV deformations are given in Table 5.1. The deformation distributions are essentially Gaussian, with the vast majority of the displacements within 3 times the rms value for a given component. From Chapter 2, the average uncertainty values of the stereo-DIC processing are 0.3, 0.3, and 0.2 um and the estimated noise floor is 0.5, 1.4, and 0.5 um for d_x, d_y, and d_z, respectively. Thus, the instantaneous displacements are generally resolvable.

	d_x	d_y	d_z
rms($\cdot$) [um]	4.2	4.0	2.6
rms($\cdot$)/$\delta \cdot 10^{-4}$	1.6	1.6	1.0
rms($\cdot$)$^+$	0.07	0.06	0.04

Table 5.1: Rms values of each deformation component for the LE FOV of the CW-unforced study, provided in dimensional, outer-scaled, and inner-scaled forms. For reference, the uncertainty values on the stereo-DIC calculation were 0.3, 0.3, and 0.2 um for d_x, d_y, and d_z, respectively.

5.1 Features of the unforced deformation power spectra

To identify energetic features in the deformations, the temporal power spectral densities (PSDs) are calculated from single DIC records, using Welch's method in MATLAB, with 10 windows and 50% overlap. The DIC records were 2047 samples long and acquired at 100 Hz, and the FOVs dimensions were roughly 133×147 mm^2 (946×1024 px^2). The PSDs are calculated for each deformation component, at each x and z spatial position in the data. The spectra are then averaged over x and z (removing the top and bottom 5% values) to arrive at a representative PSD for a given deformation component in a given FOV. The power spectra are plotted in Figure 5.1, with the spectra of d_x, d_y, and d_z plotted together for a single FOV. There are several features highlighted by the power spectra, and a brief discussion of five select frequencies bands will be given. For reference, each frequency band/feature will be named A-E in order of increasing frequency content, per Table 5.2 and the labels in Figure 5.1. In addition to observations from the PSDs in Figure 5.1, the spatial structure of each feature will be explored by discrete Fourier bandpass filtering the deformation signal over the corresponding frequency band. This is performed on the same 2047-sample-length, 100 Hz DIC records as the PSDs. A Fourier bandpass filtered signal is denoted with a subscript $\omega_{(\cdot)}$, with $(\cdot)$ replaced by the feature name; for example, the wall-normal deformation, Fourier filtered for feature A is denoted $d_{y|\omega_A}$. An amplitude is defined for each filtered field at each $x - z$ location by calculating the rms value in time. This amplitude is referred to as the rms-amplitude and denoted by $\text{rmsa}(\cdot)$ to distinguish from taking an rms along other dimensions.

Feature	A	B	C	D	E
f band [Hz]	0-3	4.5-5.5	11-16	18.3-19.3	41-45

Table 5.2: Names and corresponding frequency bands for the spectral features in the CW-unforced deformations from Figure 5.1.

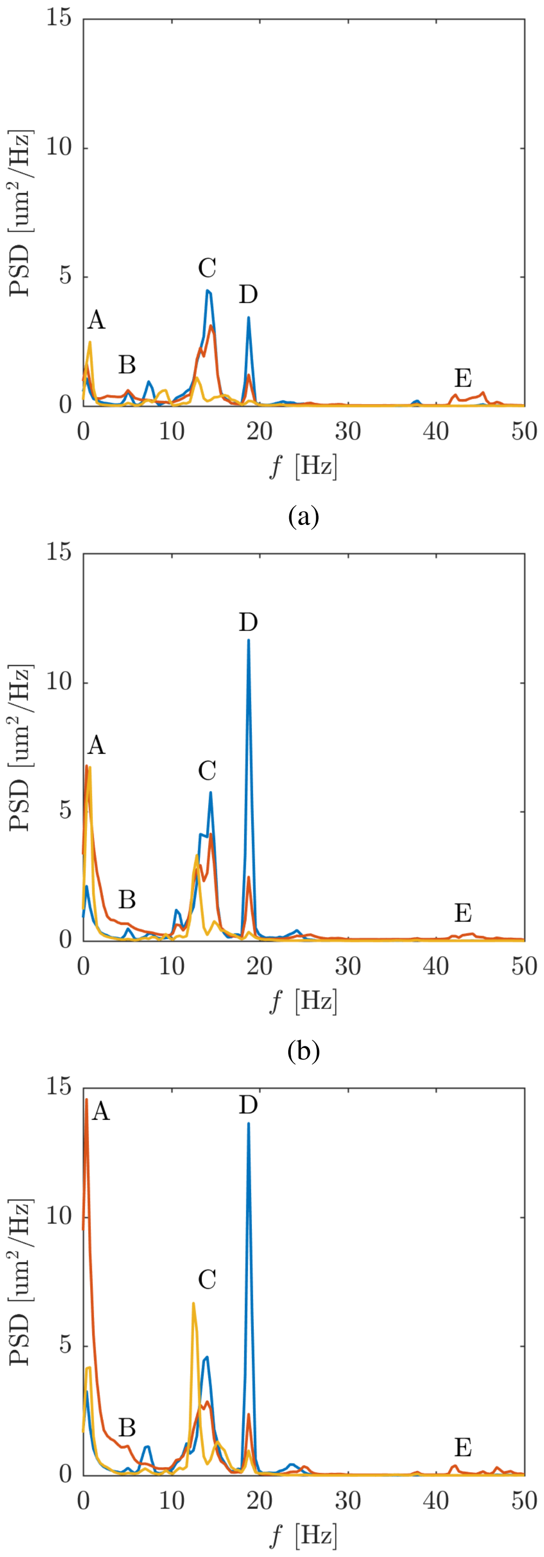

(a)

(b)

(c)

Figure 5.1: Power spectra of the deformations from the CW-unforced study: (a) LE, (b) corner, and (c) TE FOV. — d_x; — d_y; — d_z.

Feature A sits in a low, 0-3 Hz frequency band and is visible in all three deformation components in all three FOVs. The amplitude of the peaks for d_x and d_z are fairly uniform in the FOVs, but is significantly higher in the TE for d_y. A snapshot of the Fourier bandpass filtered deformation fields for feature A is given in Figure 5.2, for each of the FOVs (columns) and each deformation component (rows). Large spatial structures are observable in $d_{x|\omega_A}$ and $d_{y|\omega_A}$, and somewhat less so in $d_{z|\omega_A}$. The $d_{y|\omega_A}$ deformations are the highest amplitude of the three components. These large structures are observed to convect downstream very slowly. Because of its very low frequency content, it is possible that this feature is driven by the mean shear, with the surface slowly deforming and restoring. Another possible driver may be the near-wall cycle (NWC), which is often characterized by the inner scaled wavelength and wave speed of (λ_x^+, c^+)=(1000, 10). This converts to an inner scaled frequency of f^+=0.01, which equates to f=2.6 Hz for these flow conditions. However, while this does fall within the frequency range for feature A, the structures in Figure 5.2 appear more spanwise/obliquely aligned than the quasi-streamwise vortices typical of the NWC.

Feature B is a small peak near 5 Hz (taken to be the band 4.5-5.5 Hz) that is not immediately apparent in the power spectra of Figure 5.1. It is examined not because of its energetic content, but because it resides near the 5 Hz forcing frequency for actuation conditions ii and iii, which are the focus of the compliant-wall studies. The peak of feature B is present in all three deformation components and all three FOVs, as is slightly higher for d_y. Though the peak is made broad in Figure 5.1 by the window averaging process, taking the windows to be the full record length to maximize the spectral resolution resolves the peak location at 5.18 Hz, well outside the range of the precise 5 Hz forcing frequency. A snapshot of the Fourier filtered deformations for feature B is provided in Figure 5.3. $d_{x|\omega_B}$ is fairly uniform and does not exhibit a great deal of structure in any of the FOVs. $d_{z|\omega_B}$ is similar, with some weak streamwise-aligned features in the corner FOV. In contrast, $d_{y|\omega_B}$ contains well-defined structures that are nearly spanwise-aligned, and the wall-normal deformation is slightly higher in amplitude than the other components, consistent with the power spectra in Figure 5.3. These $d_{y|\omega_B}$ structures are seen to convect downstream, occasionally organizing into distinct spanwise-constant, streamwise-traveling waves, and then quickly breaking up. Given the downstream directionality of these structures, it is likely that they are somehow flow driven. Their semi-spanwise alignment may indicate origins from the smooth-to-compliant transition at the upstream edge of the sample.

Feature C is the broadband spectral content observed for 11-16 Hz in Figure 5.1. It is present in all three deformation components and all three FOVs, and appears to be stronger in d_x and d_y, though in the TE FOV, d_z has comparable magnitude as well. A snapshot of the Fourier filtered deformations for feature C is provided in Figure 5.3. Here, we see strong coherent structures in $d_{x|\omega_C}$, $d_{y|\omega_C}$, $d_{z|\omega_C}$ for all FOVs. $d_{x|\omega_C}$ appears to contain predominantly spanwise waves, while $d_{y|\omega_C}$ and $d_{z|\omega_C}$ exhibit primarily streamwise waves, with a distinct spanwise modulation. Strikingly, all waves tend to travel towards the compliant sample's center, i.e. spanwise waves move towards $z = 0$ and streamwise waves towards $x/\delta = 7$. The streamwise and spanwise nature of the deformation waves suggests that a geometry-dependent mechanism is involved, imprinting the sample's rectangular geometry into the surface response. This is in contrast to feature B, that exhibits only streamwise waves that travel strictly downstream. $d_{x|\omega_C}$ and $d_{y|\omega_C}$ dominate the deformations of feature C near the upstream edge of the sample (LE and corner FOV), while all three components are comparable at the TE. The energy for this frequency content may come from natural vibration modes of the plate/support structure. This feature will be discussed in more detail later in the chapter.

Feature D is a large peak centered at f=18.8 Hz in Figure 5.1. The peak amplitude is highest for d_x in all of the FOVs, and is strongest at the TE. A snapshot of the Fourier filtered deformations for feature D is provided in Figure 5.5. There are very strong similarities between the structures in Figures 5.5 and 5.4, both containing distinct streamwise and spanwise waves. Notably, feature D appears to contain slightly higher wavenumber content than C. Given the slightly higher frequency band of D, this is consistent with the two features having similar wave speeds. The structural similarity suggests that features C and D may share a geometry-dependent mechanism that dictates their spatial coherence. The 18.8 Hz frequency of feature D matches very well with the tunnel pump frequency of 18.94 Hz, so it is likely that the energy for this feature is derived from oscillations induced by the pump. However, it is not obvious the medium through which these oscillations transmit to the gelatin, whether through the water, by flow-driven vibrations of the plate structure, or by structural vibrations directly from the pump.

Feature E resides in the 41-46 Hz frequency band, nearer to the 50 Hz Nyquist limit than the other features. Though not as apparent as some of the other features, there is some broadband content appearing in this frequency range. Looking at the associated Fourier bandpass filtered deformations in Figure 5.6, the fields are uniformly incoherent and appear noise-like. Thus, this content may be the result of some source of noise in high-speed cameras.

The mean rms-amplitude for each deformation component of each feature is given in Table 5.3. The deformation magnitude was estimated using the rms-amplitudes of the components, and the mean (d_μ) and standard deviation (d_σ) of the deformation magnitudes are also provided in the table. These values allow for the features to be compared in a general sense and for trends to be observed. Looking at the d_μ values, features A and C contain higher deformations than the others. This is due to the features' strong and broad spectral peaks, integrating to a relatively large deformation contribution. In contrast, features B and E are quite weak, and sit close to or below the estimated noise floor. This coupled with the lack of spatial incoherence of feature E further supports that E is signal noise. Also noteworthy is the prominence of the wall-normal deformation. Indeed, the mean rms-amplitude of $d_{y|\omega}$ is $0.6d_\sigma$, $1.0d_\sigma$, and $2.0d_\sigma$ greater than the next highest deformation for features A, B, and E, and is within $0.2d_\sigma$ and $1.0d_\sigma$ of the highest deformation ($d_{x|\omega}$) for features C and D, respectively. Given that d_y is such a significant deformation component, and in anticipation of a strong relationship to the wall-normal velocity near the wall, d_y will be the focus of the analysis in the next section and all of Chapter 6. This also serves to narrow the otherwise very broad scope of the data. A summary of the observations for each feature is provided in Table 5.4 for reference.

Feature	A	B	C	D	E
mean(rmsa($d_{x\|\omega}$))	1.5	0.6	3.1	2.2	0.2
mean(rmsa($d_{y\|\omega}$))	3.0	0.9	2.9	1.1	2.0
mean(rmsa($d_{z\|\omega}$))	2.1	0.3	2.2	0.6	0.2
d_μ	4.0	1.1	4.9	2.7	1.0
d_σ	1.4	0.3	1.1	1.2	0.4

Table 5.3: The mean rms-amplitude for each deformation component, as well as the mean (d_μ) and standard deviation (d_σ) of the deformation magnitudes, for each feature from the power spectra in Figure 5.1 from the CW-unforced study. All quantities are in um.

Feature	A	B	C
f band [Hz]	0-3	4.5-5.5 (5.2 peak)	11-16
Mean deformation magnitude	4.0 um $1.6 \cdot 10^{-4}\delta$ $0.06\delta_v$	1.1 um $0.4 \cdot 10^{-4}\delta$ $0.02\delta_v$	4.9 um $1.9 \cdot 10^{-4}\delta$ $0.08\delta_v$
Strongest component	d_y	d_y	d_x, d_y
Spatial structure	Large-scale, slow traveling	Semi-coherent streamwise waves	Coherent streamwise & spanwise waves; geometry-dependent
Potential driver	Mean shear, NWC	Flow interaction w/upstream edge	Plate/support vibrations

Feature	D	E
f band [Hz]	18.3-19.3 (18.8 peak)	41-45
Mean deformation magnitude	2.7 um $1.1 \cdot 10^{-4}\delta$ $0.04\delta_v$	1.0 um $0.4 \cdot 10^{-4}\delta$ $0.02\delta_v$
Strongest component	d_x	d_y
Spatial structure	Same as C, scaled for higher f	Incoherent
Potential driver	Tunnel pump	Noise

Table 5.4: Summary of the discussed features from the power spectra in Figure 5.1 from the CW-unforced study. The mean deformation magnitude values are computed over all x and z, and all three FOVs, and are provided in dimensional, outer-scaled, and inner-scaled forms.

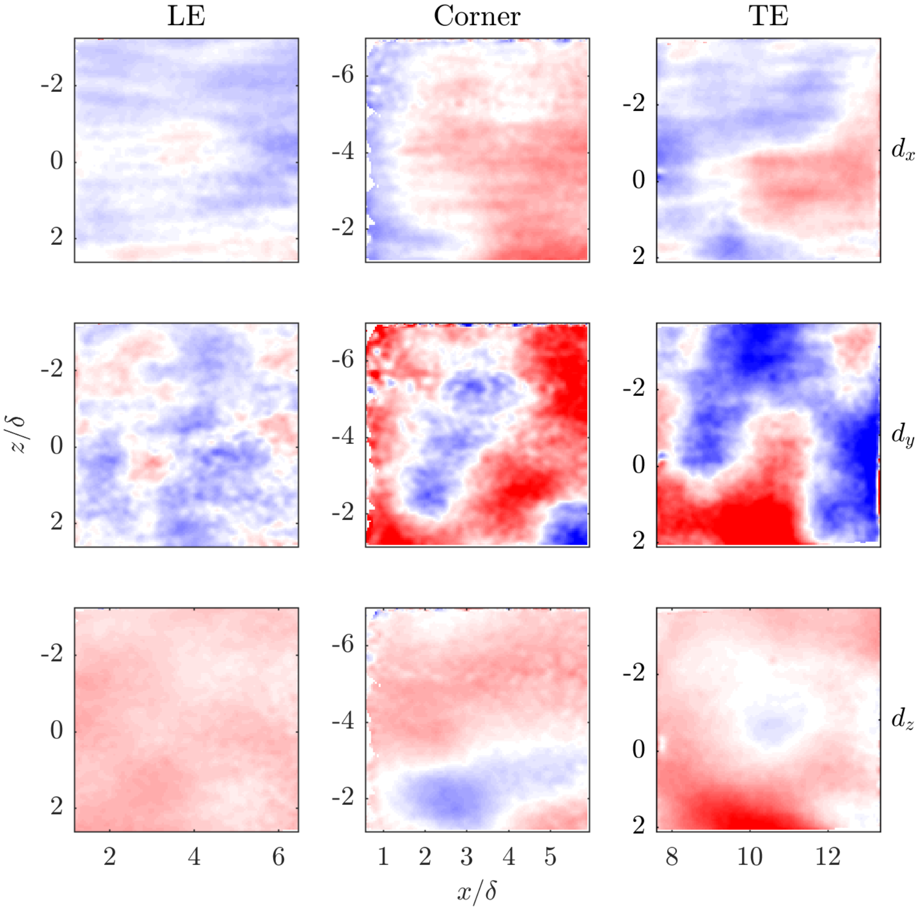

Figure 5.2: A snapshot of the Fourier bandpass filtered deformation fields for feature A. Columns: (left) LE, (center) corner, (right) TE FOVs. Rows: (top) $d_{x|\omega_A}$, (middle) $d_{y|\omega_A}$, (bottom) $d_{z|\omega_A}$. Colorbar limits are [-6.0, 6.0] um.

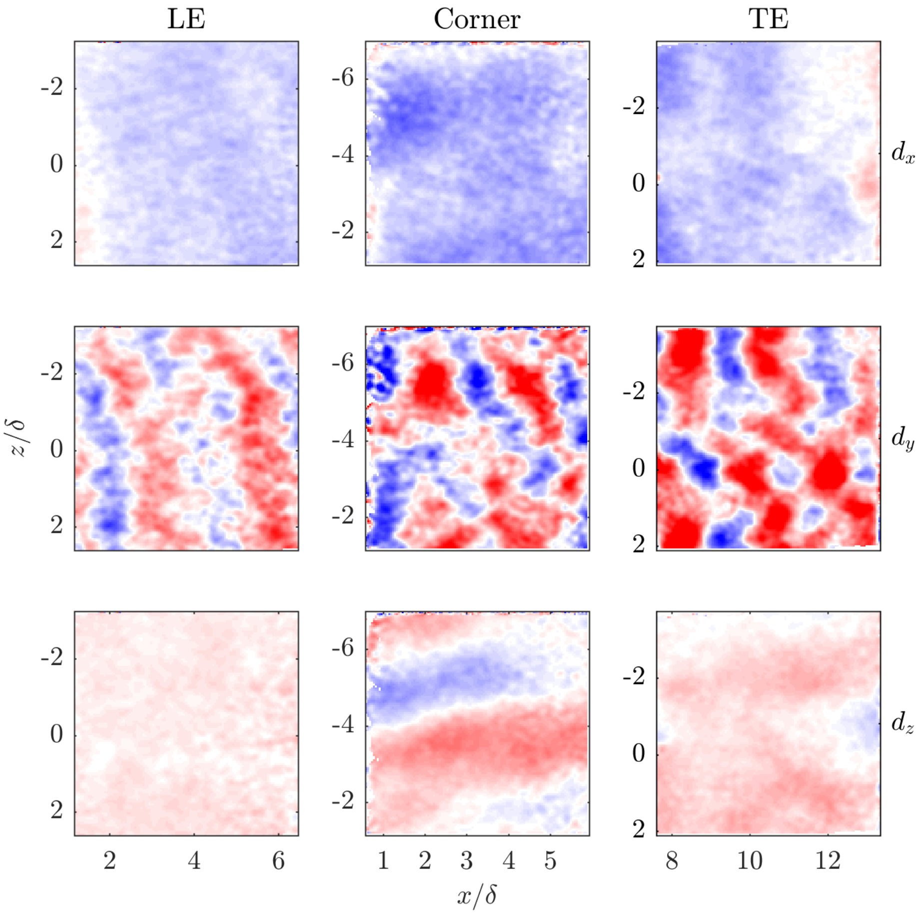

Figure 5.3: A snapshot of the Fourier bandpass filtered deformation fields for feature B. Same plot format as Figure 5.2. Note the different colorbar limits of [-2.0, 2.0] um.

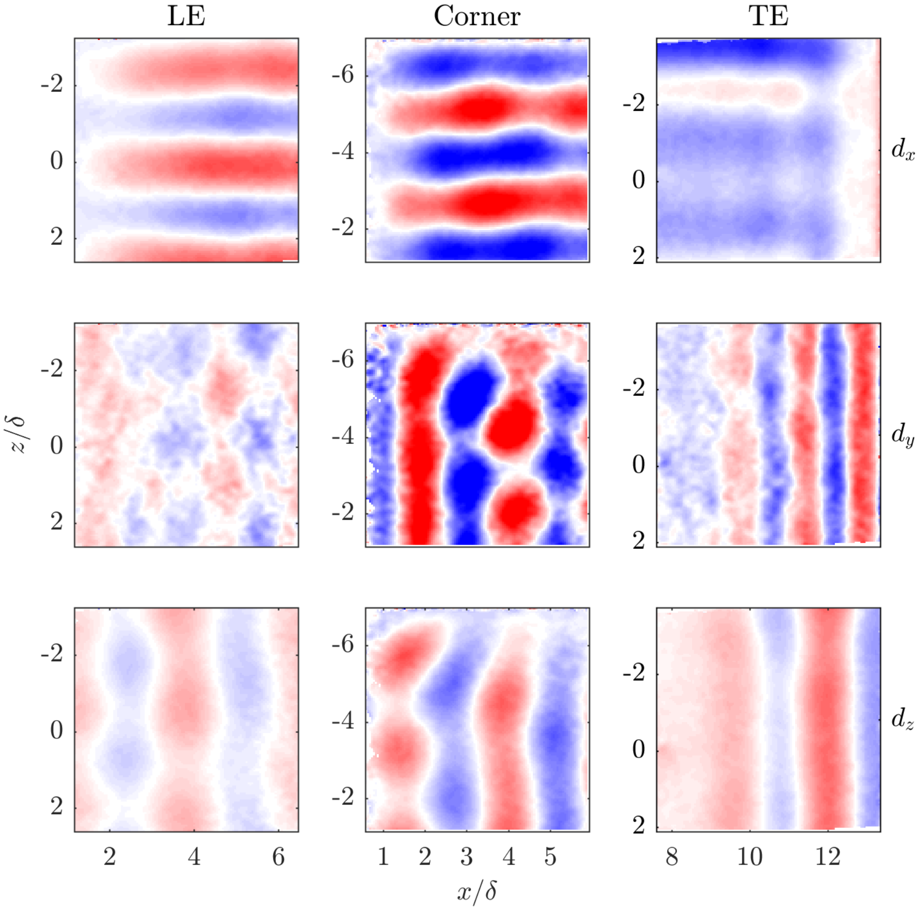

Figure 5.4: A snapshot of the Fourier bandpass filtered deformation fields for feature C. Same plot format as Figure 5.2. Note the different colorbar limits of [-9.0, 9.0] um.

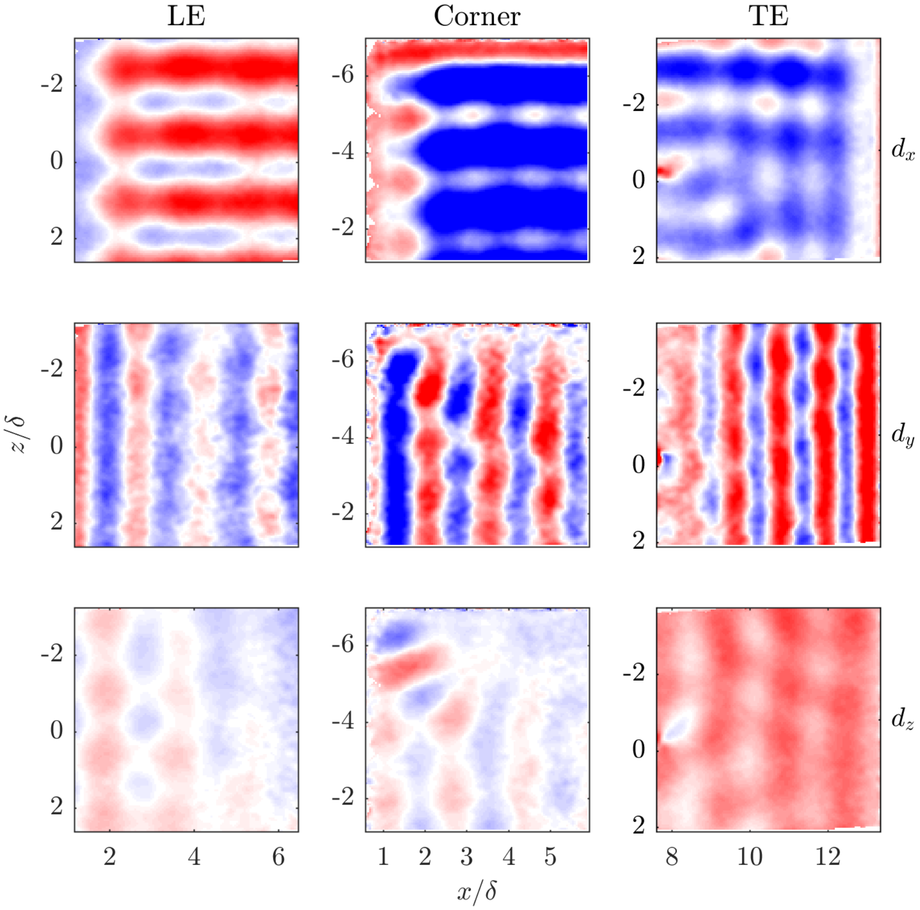

Figure 5.5: A snapshot of the Fourier bandpass filtered deformation fields for feature D. Same plot format as Figure 5.2. Note the different colorbar limits of [-3.0, 3.0] um.

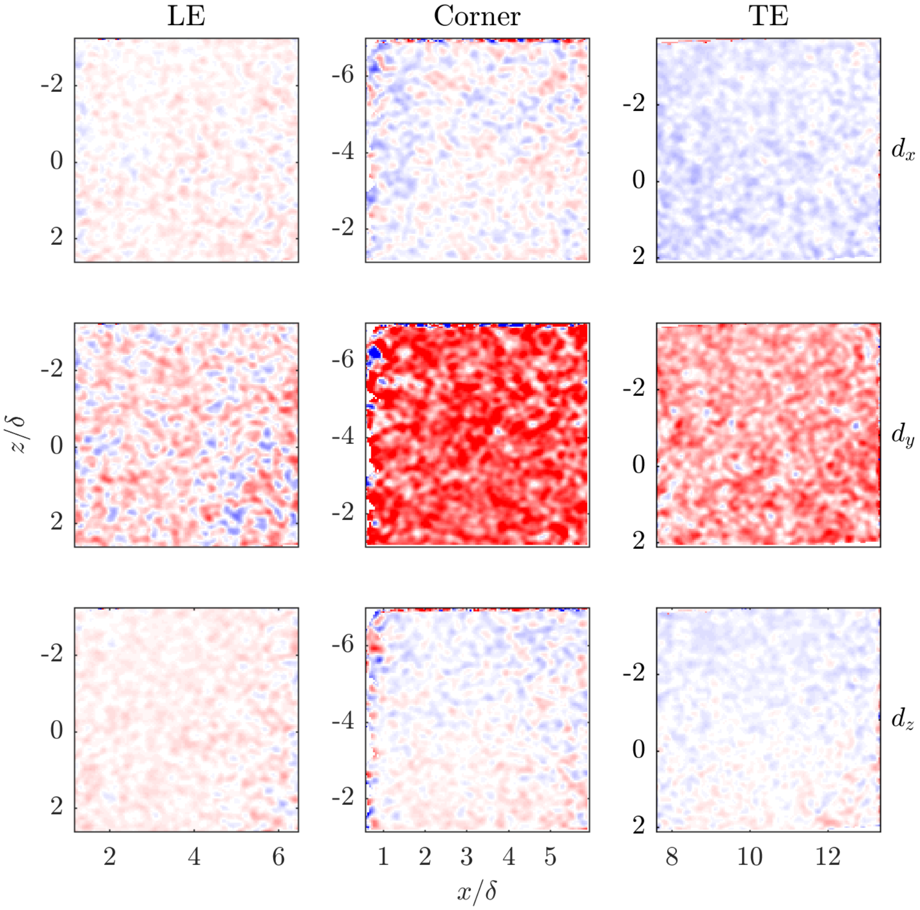

Figure 5.6: A snapshot of the Fourier bandpass filtered deformation fields for feature E. Same plot format as Figure 5.2. Note the different colorbar limits of $[-2.0, 2.0]$ um.

5.2 Spatio-temporal analysis of dynamic, broadband content

As mentioned at the beginning of this chapter, the characterization of the unforced compliant-wall system is important to identifying and attributing the deformation response to the synthetic mode in the roughness-forced system. The synthetic mode in the flow has been shown to be strongly coherent in space and time and have a 2D, streamwise-traveling-wave structure, and so a corresponding surface response is expected to have similar properties. From the summary of the spectral features in the unforced system in Table 5.4, only features C and D exhibit strongly coherent, traveling-wave structures, and so their content is explored further for comparison with the roughness-forced surface response in Chapter 6. Because features C and D are so similar in nature, feature C is taken to be representative of both and will be discussed. Again, only the d_y component will be considered, given its prevalence and for a more manageable analysis.

To better understand the spatial content of the wave system in feature C, a single frequency is selected to enable a full spatio-temporal discrete Fourier analysis. 14.65 Hz is chosen from the 11-16 Hz band, but all the mode shapes within the frequency band have nearly identical characteristics. The temporal Fourier mode corresponding to this frequency is extracted and denoted by $\widehat{d_{y|\omega_0}}$. As mentioned previously, the spatial content of these waves appears to consist of streamwise ($k_z = 0$) and spanwise ($k_x = 0$) waves, and so for comparison, $\widehat{d_{y|\omega_0}}$ is additionally discrete Fourier filtered in x and z, retaining only the $k_z = 0$ and $k_x = 0$ modes, denoted by $\widehat{d_{y|\omega_0 k_{x0} k_{z0}}}$.

The mode shapes of $\widehat{d_{y|\omega_0}}$ and $\widehat{d_{y|\omega_0 k_{x0} k_{z0}}}$ for the LE, corner, and TE FOVs are given in Figures 5.7, 5.8, and 5.9, respectively. The figures provide the (a) amplitude and (b) wrapped phase contours of the full 14.65 Hz mode ($\widehat{d_{y|\omega_0}}$), as well as the (c) amplitude and (d) wrapped phase contours of the mode reconstructed with only k_z=0 and k_x=0 modes ($\widehat{d_{y|\omega_0 k_{x0} k_{z0}}}$). Figure 5.7a displays streamwise and spanwise amplitude modulation, creating oblique rays that are symmetric about the centerline. These ray features can be understood as the interaction of streamwise waves corresponding to a broad k_x peak and positive/negative spanwise waves corresponding to broad k_z peaks. The phase in Figure 5.7b is predominantly streamwise-oriented, with spanwise variation on top, indicating that the streamwise waves are higher in amplitude than the spanwise. The mode amplitude and phase in Figures 5.7c and 5.7d match closely, with the streamwise structure captured very well and the spanwise modulation reasonably represented too. This highlights the fact that the dominant content of $\widehat{d_{y|\omega_0}}$ is indeed streamwise and spanwise waves.

Figure 5.8 is consistent with Figure 5.7, having streamwise and spanwise modulations that form rays directed towards the centerline. The phase is also similar to the LE data, exhibiting a spanwise variation on an otherwise streamwise-oriented structure, except for very near the spanwise edge of the sample. Once again, the k_z=0 and k_x=0 modes accurately represent the mode features, deviating only near the spanwise edge of the sample. The data from the LE and corner FOVs strongly suggest a system of waves generated at the boundaries of the sample, propagating inwards towards the sample's center. Streamwise waves emanate from the upstream edge of the sample, while spanwise waves radiate from the spanwise edge, and these waves appear to be generated in-phase rather than in alternating fashion, since the corner, where the edges meet, is an amplitude antinode rather than a node.

Figure 5.9 reveals that the structures in the TE FOV are noticeably weaker and less distinct than their upstream counterparts. The mode amplitude is less interpretable, while the phase still appears relatively streamwise coherent, but horizontally reflected relative to the LE and corner FOVs, indicative of upstream traveling waves. Looking at the streamwise/spanwise wave reconstruction, the amplitude in Figure 5.9c is quite different than what is seen in the upstream FOVs, much more resembling a standing wave system. As the ray features in Figures 5.7 and 5.8 could be explained by waves with broad k_x and k_z spectral peaks, the transition to standing waves downstream may indicate waves with narrower spectral peaks near the trailing edge. The mechanism for this change in behavior is not clear, but its presence is evident in the data.

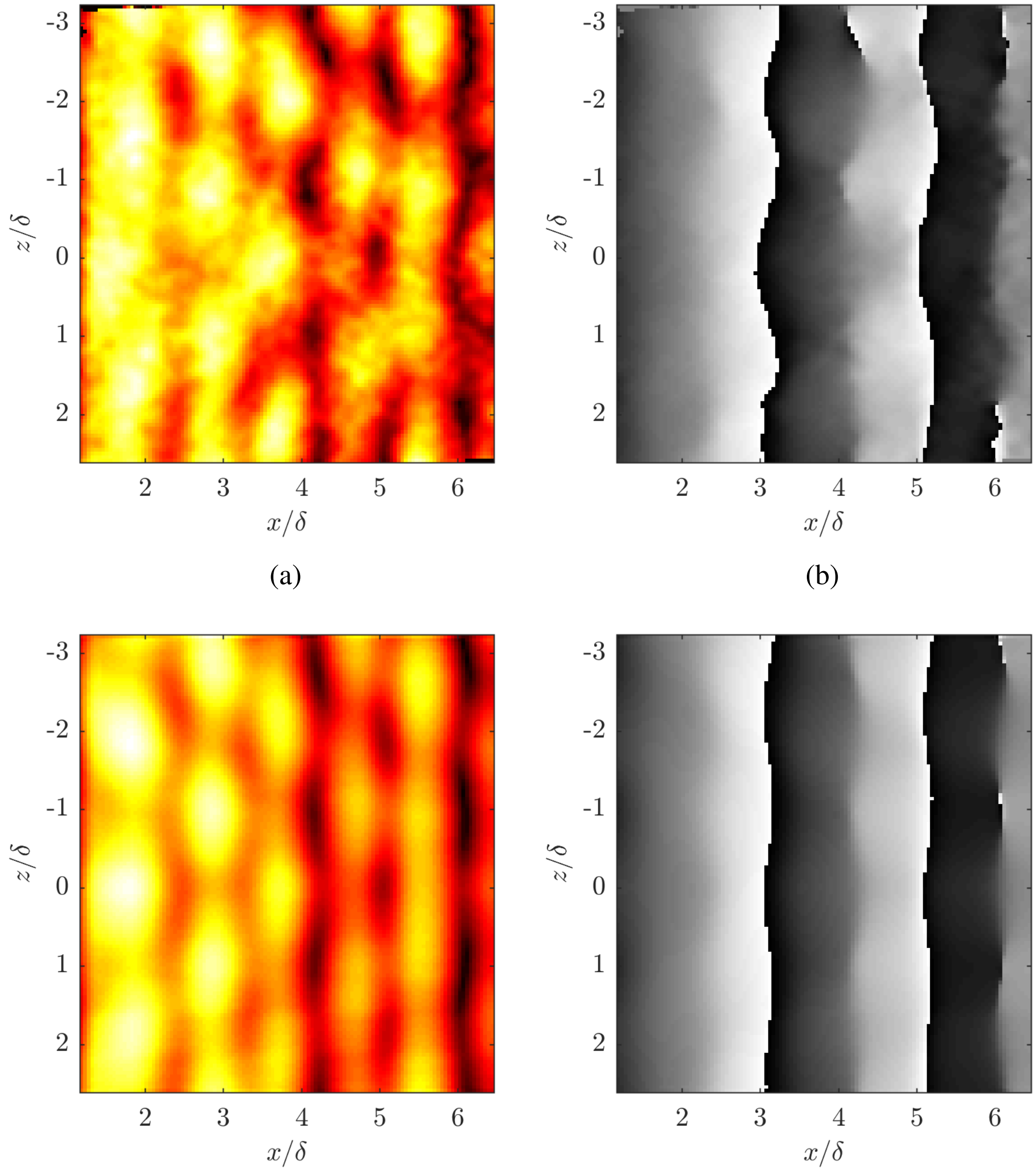

(a) (b) (c) (d)

Figure 5.7: Mode shapes of the LE FOV 14.65 Hz Fourier mode from the CW-unforced study: (a) amplitude and (b) wrapped phase of the full Fourier mode; (c) amplitude and (d) wrapped phase of the k_z=0 and k_x=0 reconstructed Fourier mode.

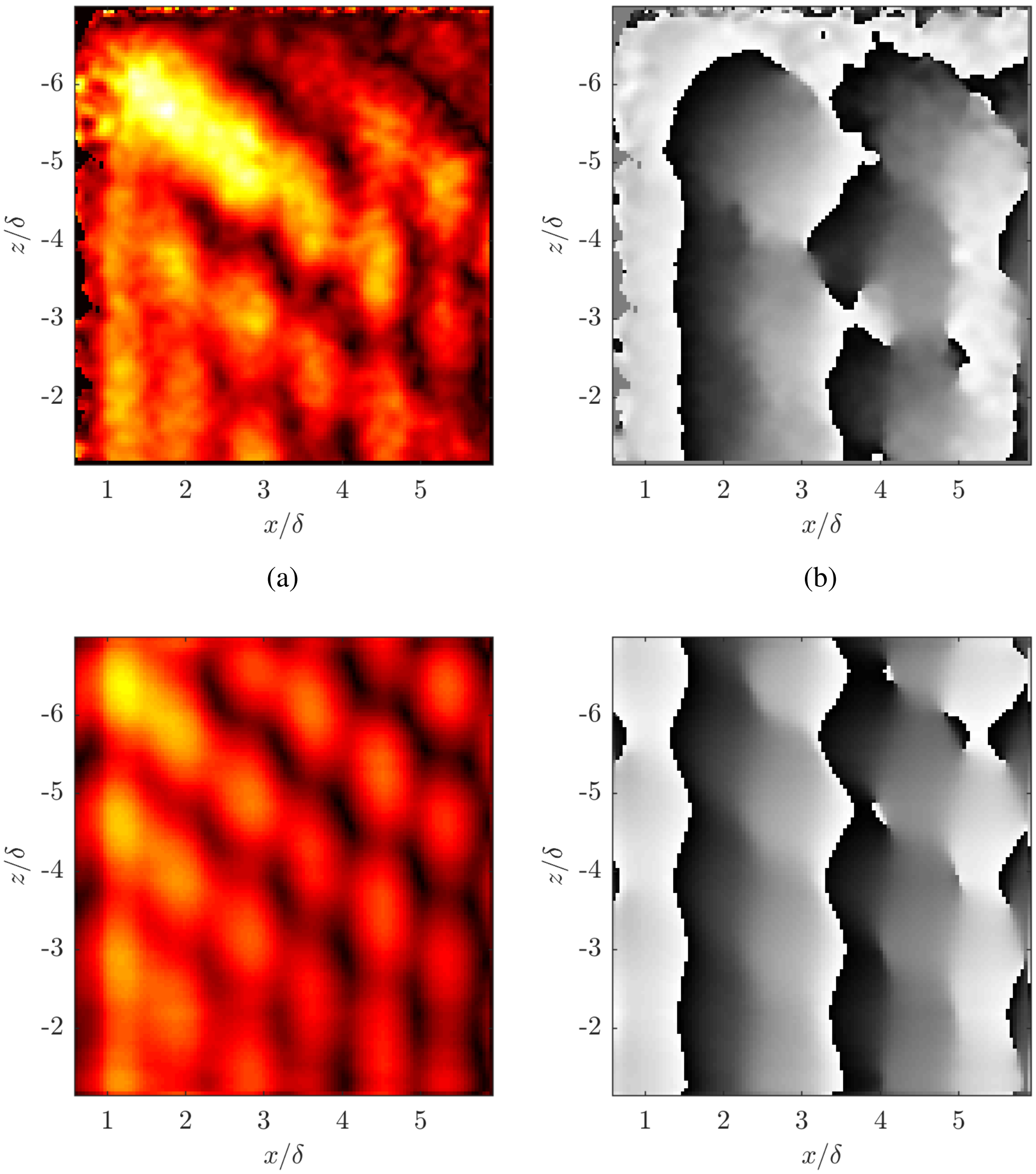

(a) (b) (c) (d)

Figure 5.8: Mode shapes of the corner FOV 14.65 Hz Fourier mode from the CW-unforced study, following the same format as Figure 5.7.

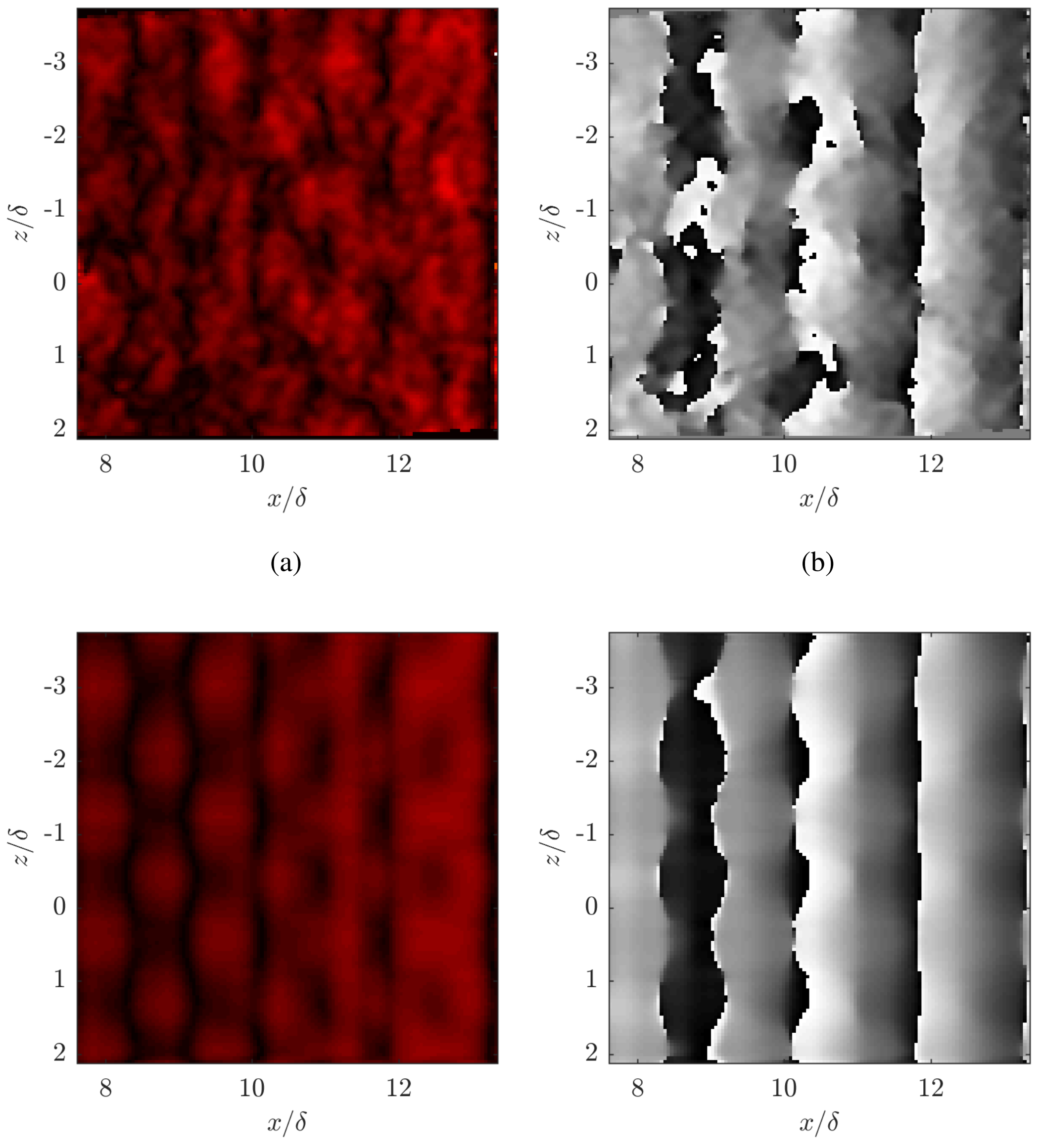

(a) (b)

(c) (d)

Figure 5.9: Mode shapes of the TE FOV 14.65 Hz Fourier mode from the CW-unforced study, following the same format as Figure 5.7.

The wave speeds of the streamwise waves were computed for comparison with the dynamic roughness-forced structures. This was done in a similar manner to Section 4.4, by assuming a simple traveling wave and estimating the streamwise derivative of the phase of the temporal Fourier mode. Plots of $\angle\widehat{d}_{y|\omega_0}$ versus x are given in Figure 5.10 for each FOV, with data taken from the spanwise center of the FOV. The phases are primarily linear, with some modulation which is expected based on the previously discussed spanwise content. The streamwise derivative and thus streamwise wavenumber were estimated by a linear fit to the data. The method of secant lines was not employed because the DIC data are single FOV and thus do not have the issue of stitched regions. This process was performed for each frequency in the 11-16 Hz band, and the resulting k_x values plotted in Figure 5.11. As expected, the k_x for the LE and corner FOVs agree very well, both with positive values that increase linearly with f. In the TE data, the k_x are more scattered, reflective of the less smooth phase observed in Figure 5.9b. However, the k_x are primarily negative, as expected of upstream traveling waves, and roughly exhibit a similar linear trend as the LE and corner data. The linearity of the k_x values with f suggests a common wave speed among the Fourier modes, which is evidence for the modes sharing a governing mechanism, as might be expected for a broadband spectral peak signature. A trimmed mean was computed across the frequency band (excluding the top and bottom 5% values) to determine a representative wavenumber, and used with the average frequency of 13.5 Hz to compute a wave speed for each FOV, provided in Table 5.5. The wave speeds are ~80 cm/s, and are higher than the freestream velocity of 33-36 cm/s, yet lower than the gelatin's estimated shear wave speed of 120 cm/s and Rayleigh wave speed of 115 cm/s. As mentioned in Chapter 2, the generalized Rayleigh and Love wave speeds that take into account the finite thickness of the gelatin layer are higher than the semi-infinite-domain Rayleigh wave speed, and are a poorer match to the measured wave speeds. It is possible and perhaps likely that the material's shear wave speed was not estimated with sufficient accuracy given the extreme softness of the material and simple compression tests performed. Additionally, it is almost certain that the material's properties would have changed after being submerged in the water tunnel for multiple days, likely further softening it and reducing its shear wave speed. Given the phase relationship between the streamwise and spanwise waves, it is proposed that these waves occur as the flat plate structure vibrates along the y-axis. These vibrations would translate into shear deformation waves, emanating from the sample boundaries simultaneously and propagating inwards to the sample's center, and in this way, the sample geometry is embedded in the shape of the deformation waves. Were the geometry altered, one would expect the response shape to change accordingly.

	LE	Corner	TE
$k_x\delta$	2.48	2.64	-2.78
c [cm/s]	86.9	81.6	-77.5

Table 5.5: Streamwise wavenumbers and wave speeds computed for each FOV for the 11-16 Hz wave system observed in the CW-unforced study.

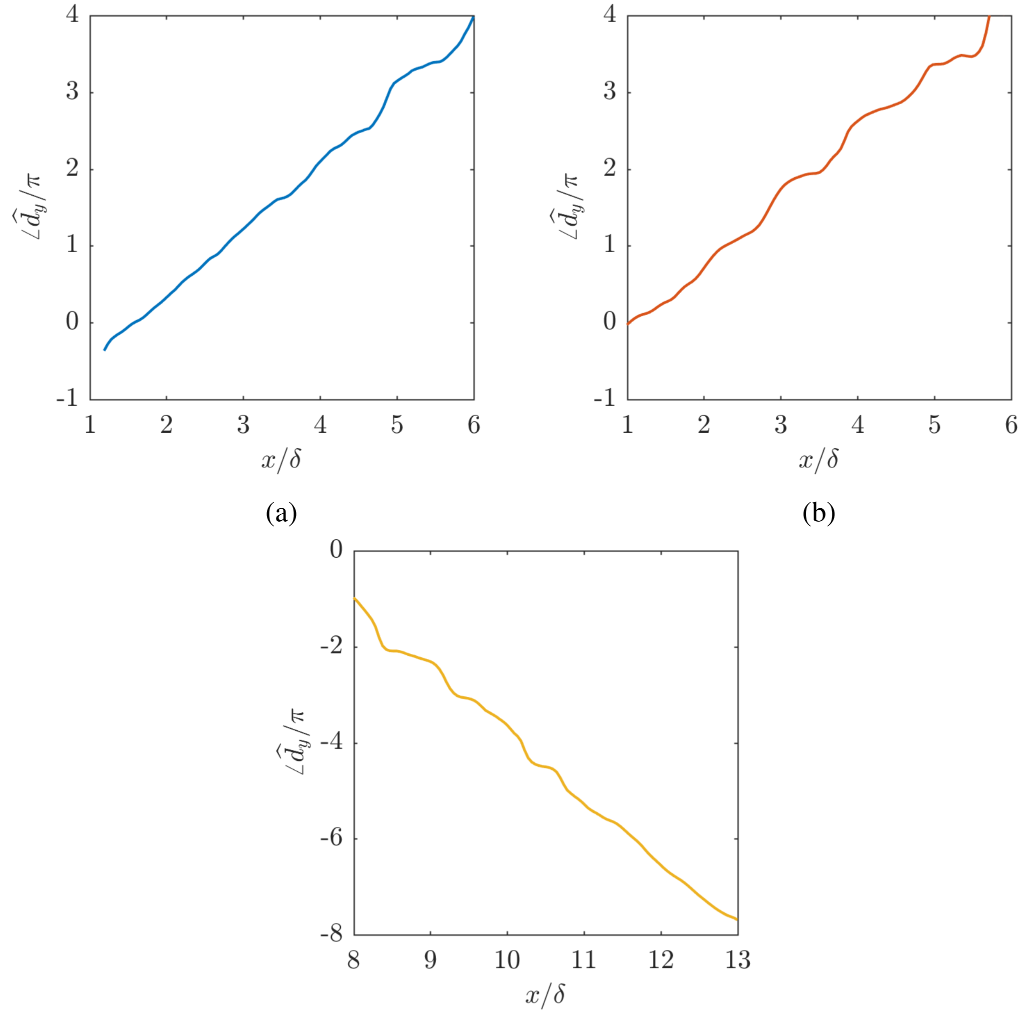

(a)

(b)

(c)

Figure 5.10: Phase of the d_y Fourier mode (14.65 Hz) as a function of x for the (a) LE, (b) corner, and (c) TE FOVs, from the CW-unforced study.

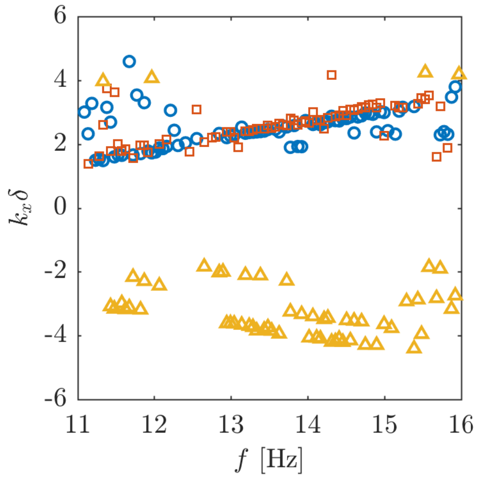

Figure 5.11: Streamwise wavenumbers versus frequency, computed for each frequency in the 11-16 Hz band and for each FOV in the CW-unforced study: ○ LE; □ corner; △ TE FOV.

5.3 Chapter summary

The surface response of the unforced, compliant-wall system studied. From the power spectra of the deformations, several features (A-E) were observed and explored, and are summarized in Table 5.4. Feature A (0-3 Hz) consisted of large-scale, slow moving structures that may be connected to the mean shear or NWC. Feature B (5.2 Hz peak) showed semi-coherent streamwise-traveling waves and may be due to a flow interaction with the smooth-to-compliant wall transition at the upstream sample edge. Feature E (41-45 Hz) was spatially incoherent and likely a noise-related signal. Features C (11-16 Hz) and D (18.8 Hz peak) contained very similar structures, both with strongly coherent streamwise and spanwise waves. Feature C was proposed to stem from flow-driven plate or support structure vibrations, while the frequency of D corresponded closely to the tunnel pump frequency. The spatial content of C and D was investigated by considering the 14.65 Hz Fourier mode, $\widehat{d}_{y|\omega_0}$, in detail, taken to represent the general characteristics of the two features. $\widehat{d}_{y|\omega_0}$ was found to be well-captured by streamwise ($k_z = 0$) and spanwise ($k_x = 0$) deformation waves, which appeared to emanate from the sample's edges and propagate towards the sample's center. The wave speeds of these deformations were estimated to be ~80 cm/s. This thorough characterization of the CW-unforced system provides a basis from which to attribute the deformation response of the CW-DRF discussed in the next chapter.

Chapter 6

SURFACE AND FLOW RESPONSE OF A COMPLIANT-WALL, TURBULENT-BOUNDARY-LAYER SYSTEM UNDER DYNAMIC ROUGHNESS FORCING

With the response of the unforced compliant-wall system characterized, the compliant-wall, dynamic-roughness-forced (CW-DRF) system is now analyzed. The surface response will first be compared to the CW-unforced study of the previous chapter to confirm the direct relationship between the synthetic mode in the flow and the phase-averaged deformations. The mean flow properties and synthetic mode characteristics will then be described. Knowledge of the synthetic mode will be leveraged to extract the ω_f-$k_{x\mathrm{f}}$ component of the surface response. The data presented in this chapter will be from actuation conditions ii and iii, with h_rms/δ of 0.042 and 0.069, respectively, and both at $f_\mathrm{f} = 5$ Hz. As mentioned in Chapter 5, this analysis will focus on the wall-normal deformation, d_y.

6.1 Attribution of the forced surface deformation

In the previous chapter, several features were identified in the power spectra of the deformations and their spatial structures were explored. To leverage that analysis, the power spectra are calculated for the roughness-forced deformation fields. Using the same process as in Chapter 5, the PSDs of the wall-normal deformation are calculated from single DIC records, using Welch's method in MATLAB, with 10 windows and 50% overlap. The PSDs are calculated at each x and z spatial position in the data, and then averaged over x and z (removing the top and bottom 5% values) to arrive at a representative PSD for a given FOV.

Figure 6.1 shows the temporal power spectra of d_y from actuation condition ii for each FOV. Many of the spectral features from the CW-unforced study are present, with the addition of a pronounced peak at the 5 Hz forcing frequency. While the location of the f_f peak is the same for all FOVs, this peak is strongest in the TE FOV, the reason for which will be explained later. The spectra of Figure 6.1 also differ in the magnitude of the low frequency peak, corresponding to feature A (0-3 Hz) from the CW-unforced study. The amplitude of the low frequency peak increases from LE, to corner, to TE, which is the same FOV trend for feature A of the unforced surface. Other than the low frequency peaks, the spectra are very similar across the

FOVs.

A direct comparison between the roughness-forced and unforced spectra is given in Figure 6.2 for the LE FOV. The two agree well for features/frequency bands C (11-16 Hz), D (18.8 Hz peak), and E (41-46 Hz), though there is a slightly more amplified high frequency peak in CW-DRF. The low frequency peaks (feature A) are co-located in f, with the forced case exhibiting a higher peak. As a note, feature A is roughly equal between the CW-unforced and CW-DRF cases for the corner FOV, and the CW-unforced peak is higher in the TE FOV, so the difference in the low frequency peak is not strictly biased towards the forced or unforced data. The most obvious difference between the two spectra in Figure 6.2 is the 5 Hz forcing frequency peak. As mentioned, though feature B (5.2 Hz peak) from the CW-unforced data resides near f_{f}, it is at a resolvably distinct frequency, and is quite small in amplitude compared to the other features. This comparison strongly suggests that the energy injected into the system by the roughness acts primarily at the forcing frequency and does not significantly alter the energy content of the other surface modes. There does seem to be a modification of the low frequency content, but in a non-straightforward manner. Additionally, the forcing appears to be at frequency that is otherwise relatively inactive in the surface.

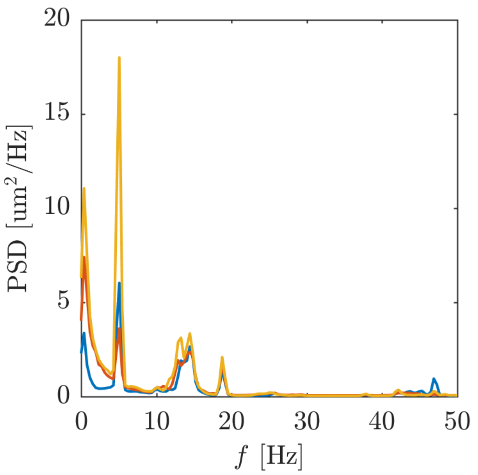

Figure 6.1: Power spectra of d_y from all three FOVs of the CW-DRF study (actuation condition ii): — LE; — corner; — TE.

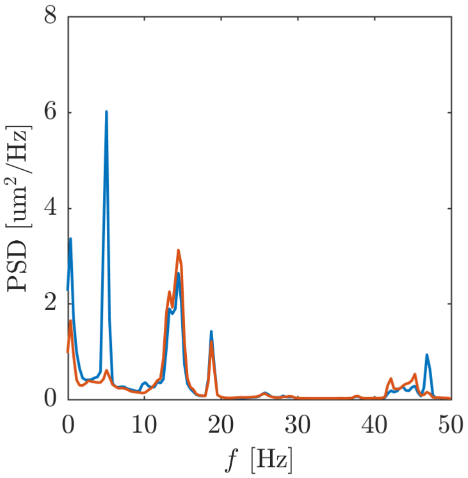

Figure 6.2: Power spectra of d_y from the LE FOV of the CW-DRF study (actuation condition ii): — CW-DRF; — CW-unforced.

Now that the energy of the roughness-forcing has been identified at the forcing frequency, the spatial structure of this content is explored to compare with unforced deformation features. To do this, the DIC data are phase-averaged and the forcing frequency component extracted in the same manner as the PIV velocity fields in Chapter 4, yielding $d_{y|\omega_\mathrm{f}}$. While an interaction with the synthetic mode was anticipated, preliminary laser displacement measurements indicated that the compliant surface responded to the roughness actuation even when the water tunnel remained off. Such a response indicated that oscillations from the roughness apparatus were somehow transmitted to the compliant surface, even with no flow. Great care was taken to completely isolate the roughness element/motor apparatus, the acrylic plate/support structure, and the camera/laser/optics from one another. In addition, the forcing frequency signature was still observed in the gelatin surface in the preliminary laser displacement data when the roughness was actuated far from the plate, with no possibility of direct contact or direct vibration transmission. Thus, quite surprisingly, it is likely that this signature is due to pressure fluctuations from the roughness element, transmitted through the water, into the acrylic, and finally to the gelatin. To characterize and possibly separate this response, DIC data were acquired with the roughness actuation on and the tunnel off. These data were also phase-averaged and the forcing component extracted, and are denoted by an additional subscript 'TO' for 'tunnel-off', i.e. $d_{y,\mathrm{TO}|\omega_\mathrm{f}}$.

Phase snapshots of the phase-averaged deformation fields are given in Figures 6.3, 6.4, and 6.5, where j is the phase index variable defined in equation 4.2, with

$j = 0$ corresponding to the roughness-flush position. The left column plots are the data with the tunnel on, $d_{y|\omega_\mathrm{f}}$, and the center column plots the data with the tunnel off, $d_{y,\mathrm{TO}|\omega_\mathrm{f}}$. As a simple attempt to remove the signature of the latter from the former, the tunnel-off data are uniformly scaled and subtracted from the tunnel-on data. This scaling factor, γ, is determined as the minimizer of the square difference, $\left(d_{y|\omega_\mathrm{f}} - \gamma d_{y,\mathrm{TO}|\omega_\mathrm{f}}\right)^2$. Additional consideration could have been taken to account for a slight phase difference in the two signals; however, as this is primarily a visual aid, the simple scaling factor is used. This scaled difference is plotted in the right column of the figures.

In the left column of Figure 6.3 (LE FOV), nearly spanwise-constant waves are observed to convect downstream, where they are slightly obscured by a low-wavenumber, high-amplitude component. This low-wavenumber content in $d_{y|\omega_\mathrm{f}}$ correlates very well with the $d_{y,\mathrm{TO}|\omega_\mathrm{f}}$ field in the center column, where the streamwise waves are absent. $d_{y,\mathrm{TO}|\omega_\mathrm{f}}$ appears to be similar to the first normal mode of a vibrating membrane, and is the signature of the pressure waves from the roughness oscillation. In contrast, the traveling-wave structure observed in $d_{y|\omega_\mathrm{f}}$ is best attributed to interaction with the synthetic mode in the flow. The scaled difference in the right column better highlights the streamwise waves, though the vibration signal is still somewhat present.

Figure 6.4 is consistent with 6.3, showing clear streamwise traveling waves in $d_{y|\omega_\mathrm{f}}$ and signs of the vibration mode in both $d_{y|\omega_\mathrm{f}}$ and $d_{y,\mathrm{TO}|\omega_\mathrm{f}}$. Notably, there are no spanwise waves emanating from the side edge of the sample, as is the case in features C and D from the CW-unforced data. Once again, the scaled difference in the right plot is able to highlight the streamwise wave component of the deformation. In the TE data given in Figure 6.5, the traveling waves even more obscured by the now more pronounced vibration mode. The scaled difference is less successful in drawing out the waves. However, the $k_z = 0$ waves are present and do convect downstream. Despite the traveling waves being more obscured, the vibration mode is notably stronger at the TE, and this is the reason for the f_f peak being highest for the TE FOV in Figure 6.1. The TE also contains the largest low frequency (feature A) peak in Figure 6.1, as well as for the CW-unforced data in Figure 5.1 from the previous chapter. Feature A appeared to consist of large-scale, low wavenumber structures. It may be that some asymmetry in the geometry or properties of the gelatin sample leads to the TE area being more sensitive to large-scale deformation modes. It may also have to do with the interaction with the mean flow, biasing the surface's response.

In all, the data from the three FOVs in Figures 6.3, 6.4, and 6.5 describe streamwise-traveling waves, with a wavelength of ~2δ, convecting strictly downstream with a wave speed of ~25 cm/s or ~$0.7U_\infty$. Comparing to the observations of the CW-unforced study, these waves are decidedly not consistent with features A (large-scale, slowly convecting) or E (noise signal). There are some similarities to B (semi-coherent streamwise waves), but $d_{y|\omega_\mathrm{f}}$ is significantly more coherent. Features C and D do contain distinct streamwise and spanwise traveling waves. However, these waves propagate towards the sample's center at a speed of ~80 cm/s, in contrast with the $d_{y|\omega_\mathrm{f}}$ waves traveling strictly downstream and with a much lower wave speed. In conclusion, the traveling-wave component of the roughness-forced surface response is best attributed to direct interaction with the synthetic mode. Thus, the experiment has successfully elicited a detectable surface response to the flow structure generated by the dynamic roughness.

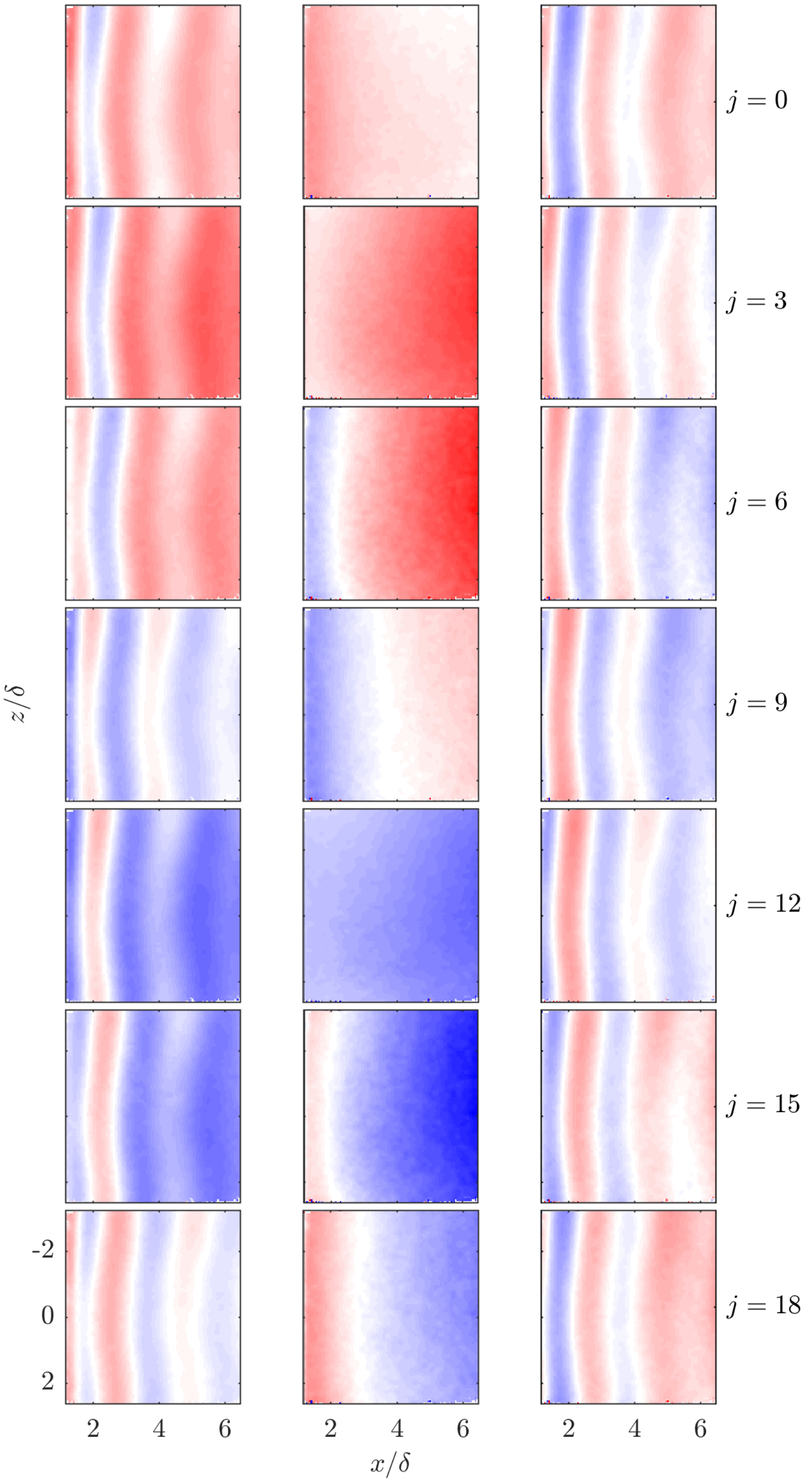

Figure 6.3: Phase snapshots of LE FOV from the CW-DRF study (actuation condition ii) of (left column) $d_{y|\omega_\mathrm{f}}$, (center) $d_{y,\mathrm{TO}|\omega_\mathrm{f}}$, and (right) $d_{y|\omega_\mathrm{f}} - \gamma d_{y,\mathrm{TO}|\omega_\mathrm{f}}$. The colorbar limits are $[-6, 6]$ um.

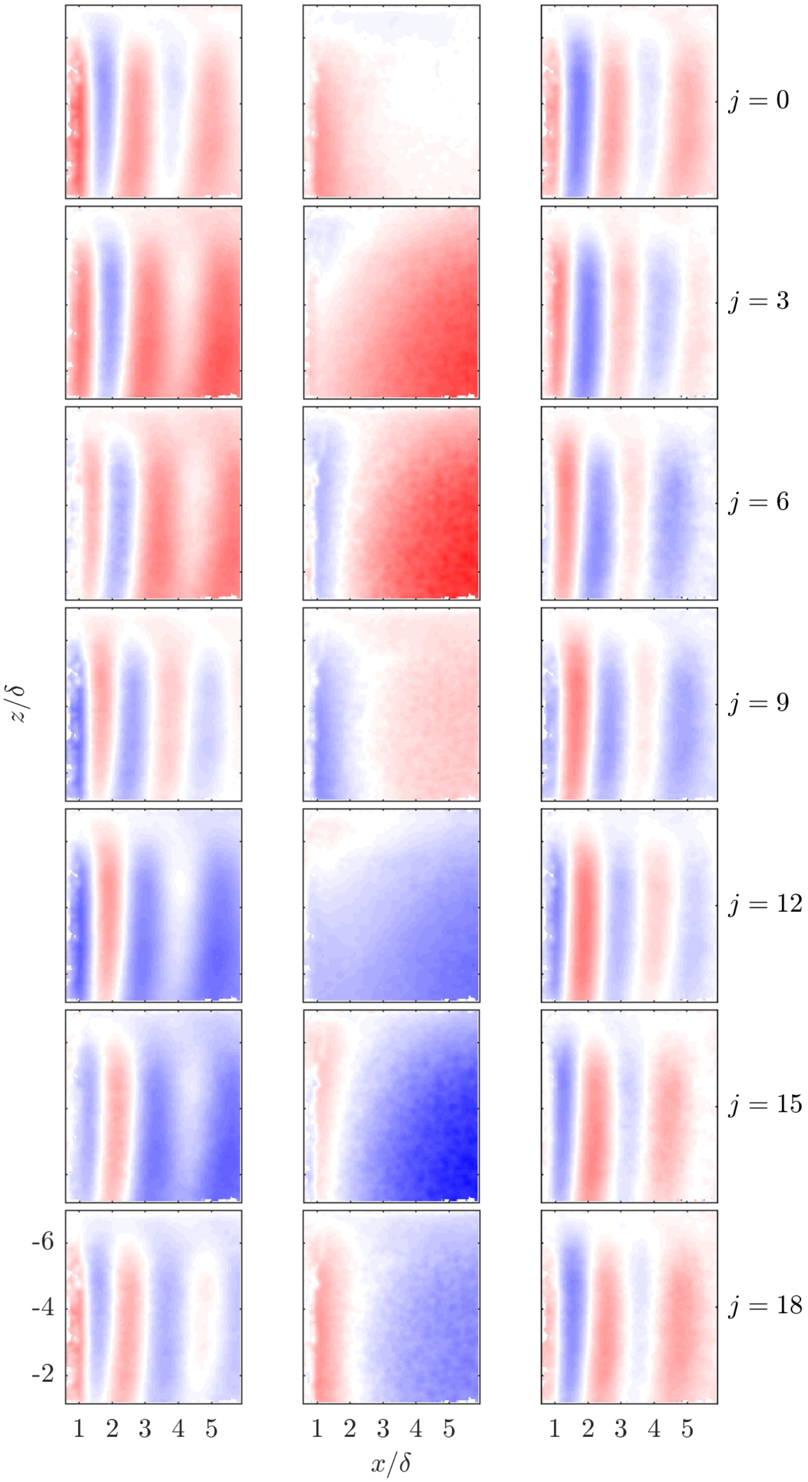

Figure 6.4: Phase snapshots of corner FOV from the CW-DRF study (actuation condition ii), following the same column format as Figure 6.3. The colorbar limits are $[-6, 6]$ um.

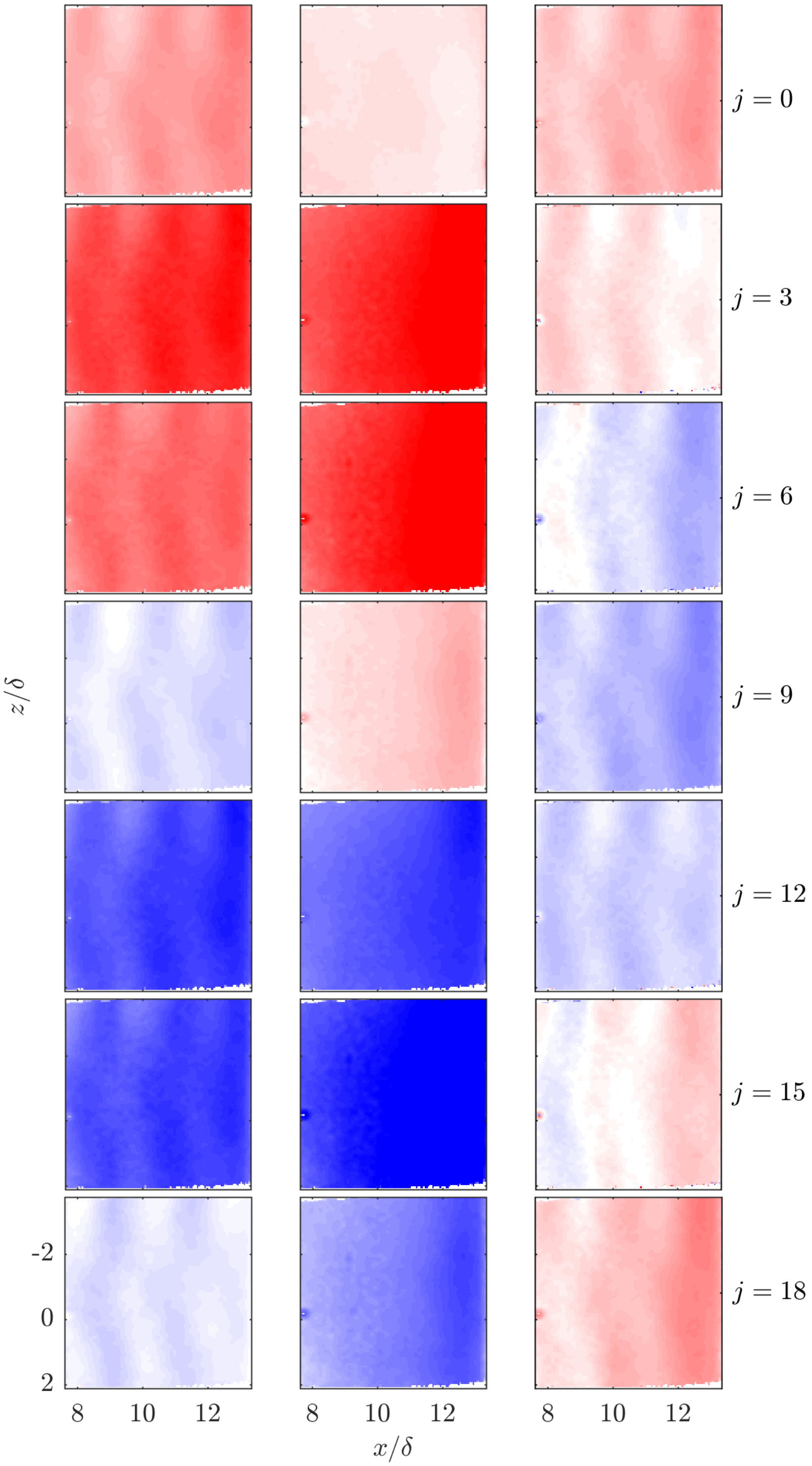

Figure 6.5: Phase snapshots of TE FOV from the CW-DRF study (actuation condition ii), following the same column format as Figure 6.3. The colorbar limits are [−6, 6] um.

6.2 Extracting the spatial component of the forced deformation (part 1)

As with the velocity data of the synthetic mode, a method was developed to extract the spatial component of the deformation data that is directly correlated to the dynamic roughness forcing. In the case of the flow measurements, this was accomplished by temporally phase-averaging the data and estimating the streamwise derivative of the phase of the resulting Fourier mode, yielding the synthetic mode wavenumbers, $k_{x\mathrm{f}}$. This method was applicable because the velocity response is well approximated by a single (decaying) traveling wave and has a nearly linear streamwise phase. As already discussed, the surface deformations contain at least one traveling wave and a vibration mode, and possibly other spatial scales. This is readily observable in the streamwise mode shapes of $\widehat{d}_{y|\omega_\mathrm{f}}$, as shown in Figure 6.6 for the LE data and actuation condition ii. Figure 6.6a gives the amplitude of $\widehat{d}_{y|\omega_\mathrm{f}}$ as a function of x, displaying strong modulation due to interacting spatial scales. Figure 6.6b gives the streamwise phase, which is clearly nonlinear, again due to multiple scales interacting, and thus the previous method of calculating $k_{x\mathrm{f}}$ is not valid. However, it has already been shown that the traveling-wave component of the surface response is directly attributable to interaction with the synthetic mode. Thus, rather than independently identifying $k_{x\mathrm{f}}$ from the deformation data, the well-defined $k_{x\mathrm{f}}$ of the synthetic mode in the flow will be leveraged to extract the $k_{x\mathrm{f}}$-coherent spatial component of the surface response. This is the same process as was used to isolate the ω_f-$k_{x\mathrm{f}}$ component of the velocity fields in Chapter 4. Before applying this procedure, the velocity measurements for the CW-DRF study will be briefly discussed.

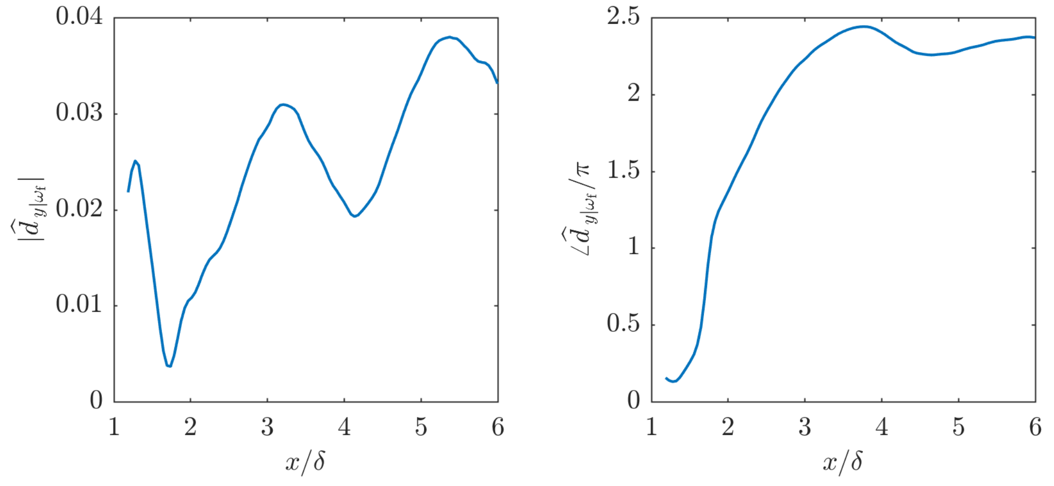

(a) (b)

Figure 6.6: (a) amplitude and (b) phase of $\widehat{d}_{y|\omega_\mathrm{f}}$ as functions of x, taken from the LE FOV of the CW-DRF study for actuation condition ii.

6.3 Mean properties and spatio-temporal signature of the CW-DRF flow

The mean flow statistics for the compliant-wall, dynamic-roughness-forced flow (△) are presented in Figure 6.7, along with the statistics from the SW-DRF (□) and canonical (○) flow studies. The forced data are for actuation condition iii, and each data set is scaled using the freestream velocity and boundary layer thickness from the corresponding SW- and CW-unforced data sets (values given in Table 3.1). All profiles are taken from the $x/\delta = 4.7$ station in the PIV. In Figure 6.7a, the compliant-wall mean profile closely resembles the smooth-wall profile, exhibiting the same deficit for $0.07 < y/\delta < 0.6$. Likewise, Figures 6.7b-6.7d show close agreement in the turbulence intensities and Reynolds shear stress, having increased values over the canonical case, again indicative of internal layers. Some deviation can be seen in the streamwise turbulence intensity near the wall, as the u_{rms} peak in the compliant-wall profile has shifted nearer to the wall to an unresolved y location.

The $j = 0$ (roughness-flush) phase snapshots of the ω_{f} velocity components are shown in Figure 6.8 for the SW- and CW-DRF data (actuation condition iii). The smooth-wall data have been truncated in x to match the compliant-wall FOV. Both the streamwise and wall-normal structures are very similar between the two studies, containing T-S wave traits. Close inspection of the downstream region shows that the compliant-wall synthetic mode begins to lag slightly behind the smooth-wall mode. This is a result of the compliant-wall structure having a slightly shorter wavelength, as will be quantified shortly. Nearly all the observations of the SW-DRF study discussed in Chapter 4 apply to the CW-DRF data, including broad $k_{x\mathrm{f}}$ spectral peak and resulting the amplitude modulation, and will not be repeated here.

The method to estimate the streamwise wavenumber of the synthetic mode employed in Chapter 4 (calculating the streamwise derivative of $\angle\widehat{v}_{\omega_{\mathrm{f}}}$) is applied to the compliant-wall PIV data here. The resulting wavenumbers and wave speeds are given in Tables 6.1 and 6.2. $k_{x\mathrm{f}}$ for the smooth- and compliant-wall studies are plotted together in Figure 6.9. As in the smooth-wall case, the compliant-wall $k_{x\mathrm{f}}$ is a nearly linear function of ω_{f}. The least-squares linear fit to the compliant-wall data (not including the Duvvuri & McKeon (2015) [14] data point) is also plotted and is calculated to be:

$$k_{x\mathrm{f}}\delta\left(\frac{\omega_{\mathrm{f}}\delta}{U_\infty}, \frac{h_{\mathrm{rms}}}{\delta} = 0.042\right) = 1.20\,\frac{\omega_{\mathrm{f}}\delta}{U_\infty} + 0.17. \tag{6.1}$$

The coefficient on ω_{f} in Equation 6.1 is 9% larger than the coefficient for the smooth-wall case (Equation 4.9), indicating that the compliant-wall system supports shorter synthetic structures. The $k_{x\mathrm{f}}$-axis intercepts appear similar in Figure 6.9, with the compliant-wall value being 5.5% lower than the smooth-wall value. As discussed in Chapter 4, the non-zero $k_{x\mathrm{f}}$-axis intercept is unphysical and suggests nonlinear behavior for very small ω_f.

		h_rms/δ $[h_\mathrm{rms}]$	
		0.042 [1.1 mm]	0.069 [1.8 mm]
$\frac{\omega_\mathrm{f}\delta}{U_\infty}$ $[f_\mathrm{f}]$	1.4 [3 Hz]	i. 1.99 (3.17)	-
	2.4 [5 Hz]	ii. 2.88 (2.19)	iii. 2.78 (2.26)
	4.8 [10 Hz]	iv. 5.93 (1.06)	-

Table 6.1: Streamwise wavenumbers, $k_{x\mathrm{f}}\delta$, (and wavelengths, $\lambda_{x\mathrm{f}}/\delta$, in parentheses) calculated for each actuation condition for the CW-DRF study.

		h_rms/δ $[h_\mathrm{rms}]$	
		0.042 [1.1 mm]	0.069 [1.8 mm]
$\frac{\omega_\mathrm{f}\delta}{U_\infty}$ $[f_\mathrm{f}]$	1.4 [3 Hz]	i. 0.67	-
	2.4 [5 Hz]	ii. 0.77	iii. 0.80
	4.8 [10 Hz]	iv. 0.74	-

Table 6.2: Wave speed, c_f/U_∞, for each actuation condition for the CW-DRF study.

The method to isolate the ω_f-$k_{x\mathrm{f}}$ component of the velocity fields employed in Chapter 4 (DFT in t and x, zero-padding in x to match $k_{x\mathrm{f}}$) is applied to the compliant-wall PIV data. Following the analysis of Chapter 4, the amplitude and phase values of the streamwise and wall-normal modes are given in Table 6.3. Comparing to the values of Table 4.6, the amplitudes between the two studies are comparable. As in the smooth-wall case, the amplitude of $\widehat{\widehat{v}}_{\omega_\mathrm{f} k_{x\mathrm{f}}}$ is noticeably higher for the higher actuation condition, while the phases are both $\pi/2$ from the phase of the roughness. A more detailed comparison and analysis of the ω_f-$k_{x\mathrm{f}}$ velocity mode shapes in these studies will be presented in Chapter 7.

	Case ii			Case iii		
	y_CL/δ	Amplitude	Phase	y_CL/δ	Amplitude	Phase
$\widehat{\widehat{u}}_{\omega_\mathrm{f} k_{x\mathrm{f}}}(y_\mathrm{CL})$	0.27	$3.3 \cdot 10^{-3}$	0.46π	0.31	$3.0 \cdot 10^{-3}$	0.84π
$\widehat{\widehat{v}}_{\omega_\mathrm{f} k_{x\mathrm{f}}}(y_\mathrm{CL})$	0.27	$3.0 \cdot 10^{-3}$	0.50π	0.31	$11.1 \cdot 10^{-3}$	0.52π

Table 6.3: Amplitudes and phases of the ω_f-$k_{x\mathrm{f}}$ velocity modes at the critical layer location, for the CW-DRF study, actuation conditions ii and iii. The amplitudes are scaled to reflect the physical velocity and normalized by U_∞.

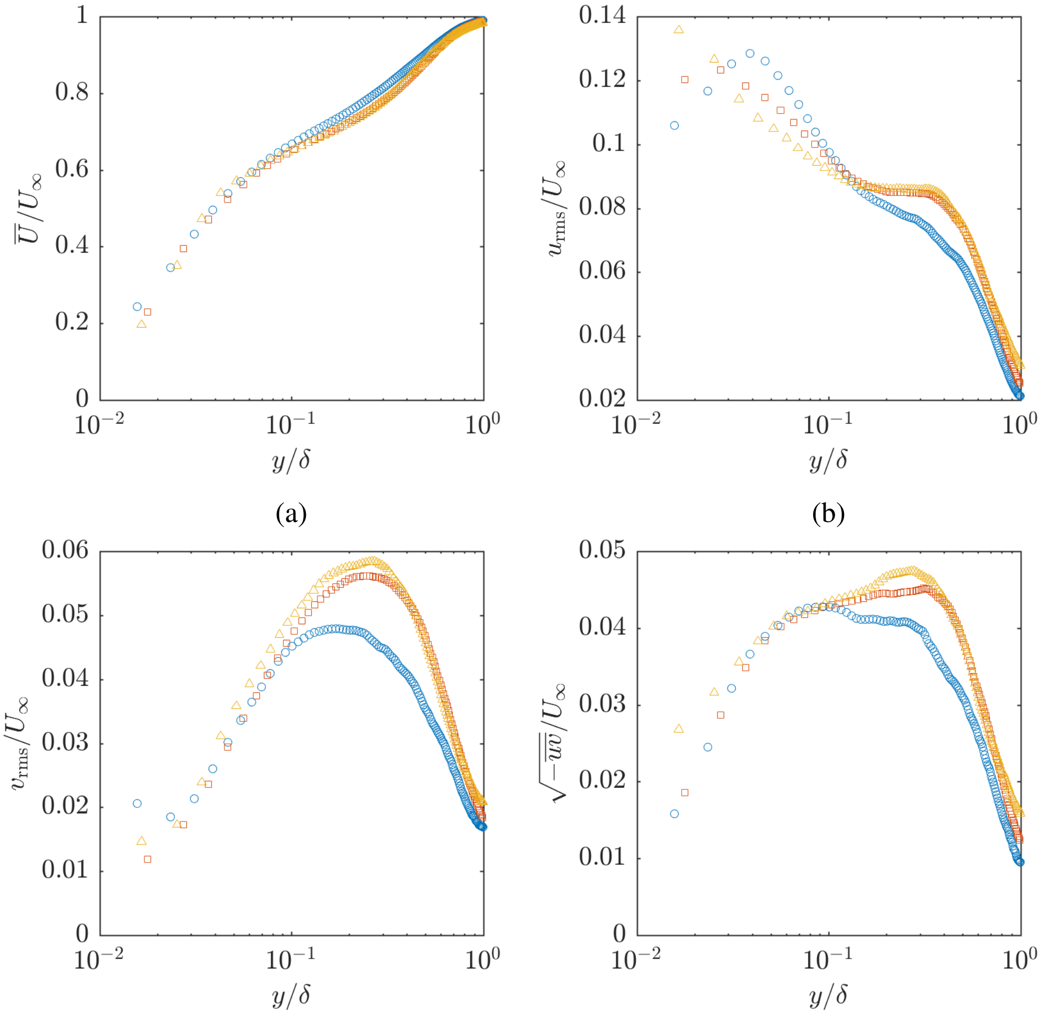

(a) (b)

(c) (d)

Figure 6.7: Comparison of canonical, SW-DRF, and CW-DRF mean flow statistic, taken from $x/\delta = 4.7$ and for actuation condition iii for the forced data: (a) mean streamwise velocity, (b) streamwise turbulence intensity, (c) wall-normal turbulence intensity, (d) Reynolds shear stress. Velocities are scaled by the freestream velocity and plotted in outer scaling, y/δ. ○ canonical; □ SW-DRF; △ CW-DRF.

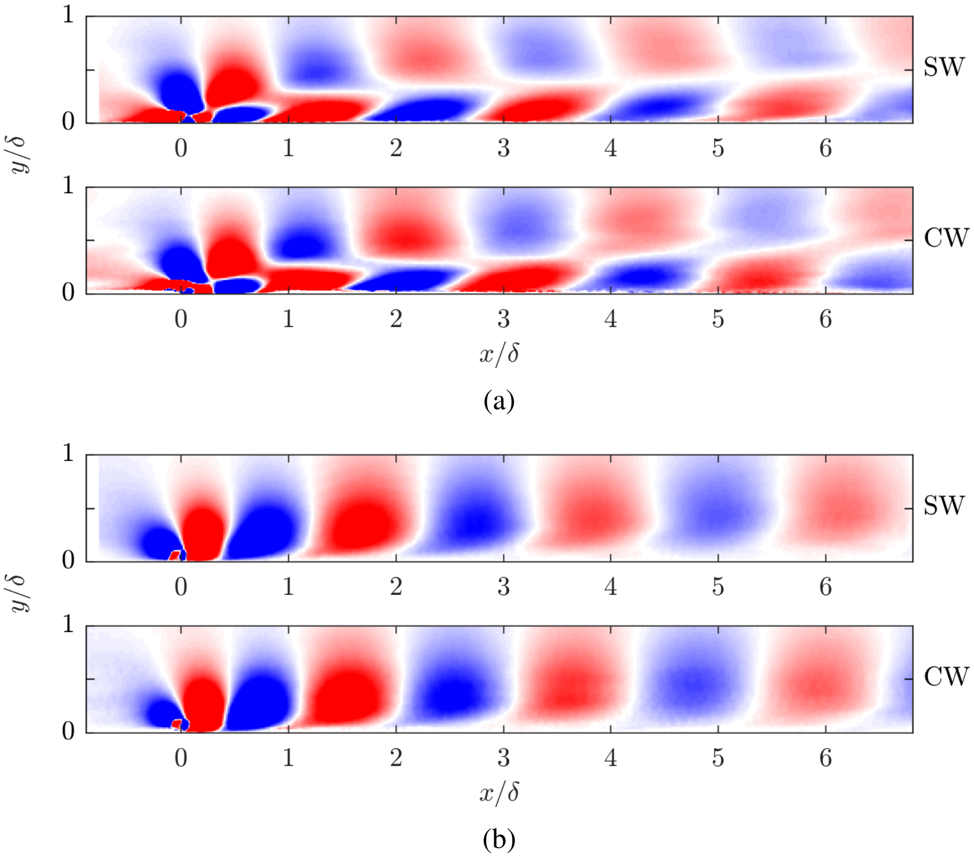

(a)

(b)

Figure 6.8: $j = 1$ phase snapshot of (a) u_{ω_f} and (b) v_{ω_f} for the SW-DRF (top) and CW-DRF (bottom) studies, both at actuation condition iii. The colorbar limits are [−0.2, 0.2].

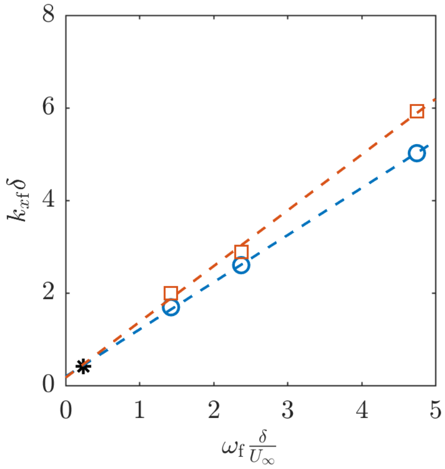

Figure 6.9: Streamwise wavenumber of the synthetic mode, $k_{x\mathrm{f}}$, versus angular forcing frequency, ω_f, for the actuation amplitude h_rms=0.042. ○ SW-DRF data; – – SW-DRF linear fit; □ CW-DRF; – – CW-DRF linear fit; ∗ Duvvuri & McKeon (2015) [14].

6.4 Extracting the spatial component of the forced deformation (part 2)

The wavenumbers calculated for the CW-DRF synthetic flow mode are now used to inform the extraction of the synthetic mode-forced component of the surface response. The method is identical to the one used to isolate the ω_f-$k_{x\mathrm{f}}$ component of the velocity fields: the DIC data are zero-padded in x for the optimal spectral resolution that is a fraction of $k_{x\mathrm{f}}$. This procedure was performed for $x/\delta > 2$ (to avoid the transient region just downstream of the roughness) and for all z.

The phase-averaged, ω_f component of the wall-normal deformation is discrete Fourier transformed in time, and then zero-padded and transformed in the streamwise direction, as shown in Equations 6.2 and 6.3, respectively:

$$
\begin{aligned}
d_{y|\omega_\mathrm{f}}(x,z,t) &= \widehat{d}_{y|\omega_\mathrm{f}}(x,z)e^{-i\omega_\mathrm{f}t} + \text{c.c.} && (6.2)\\
&= \left[\sum_n \widehat{\widehat{d}}_{y|\omega_\mathrm{f}}(z;nk_{x\mathrm{f}})e^{i(nk_{x\mathrm{f}}x-\omega_\mathrm{f}t)}\right] + \text{c.c.}, && (6.3)
\end{aligned}
$$

where, again, $\widehat{\widehat{(\cdot)}}$ indicates a quantity that has been discrete Fourier transformed in t and x. As with the velocity data, the ω_f-$k_{x\mathrm{f}}$ Fourier component of the deformations is referred to as $\widehat{\widehat{d}}_{y|\omega_\mathrm{f}k_{x\mathrm{f}}} = \widehat{\widehat{d}}_{y|\omega_\mathrm{f}}(z;n=1)$ and the reconstructed deformation field referred to as $d_{y|\omega_\mathrm{f}k_{x\mathrm{f}}}$. The phase snapshots of $d_{y|\omega_\mathrm{f}k_{x\mathrm{f}}}$ from the LE are given on the right in Figure 6.10. Qualitatively, the ω_f-$k_{x\mathrm{f}}$ component captures the traveling wave deformations well.

The amplitudes of the ω_f-$k_{x\mathrm{f}}$ Fourier coefficient for the LE (○) and corner (□) FOVs are plotted as a function of z in Figure 6.11 to investigate any spanwise variation. The data from the two FOVs agree well in the region of overlap, and both indicate that the amplitude of the ω_f-$k_{x\mathrm{f}}$ response is slightly weaker along the centerline, increases towards the spanwise edge, plateaus between $-4.5 < z/\delta < -2.5$, and then decays to the edge ($z/\delta = 6$). To explore a possible reason for the convex bowing in $|\widehat{\widehat{d}}_{y|\omega_\mathrm{f}k_{x\mathrm{f}}}|$, the k_x-amplitude spectrum is plotted in Figure 6.12 for two spanwise locations, $z/\delta = 0$ and -2.8δ. The k_x-axis is scaled by $k_{x\mathrm{f}}$. For both locations, a local peak is seen at $k_x = k_{x\mathrm{f}}$, but the peak is notably higher in the off-center location, while the $k_x = 0$ content, related to the vibration mode, is higher in the centerline location. The synthetic mode in the flow has already been shown to be 2D, so this variation is unlikely to be due to a variation in the flow forcing. The inverse relationship between the $k_x = k_{x\mathrm{f}}$ and $k_x = 0$ peaks suggests that the presence of the vibration mode reduces the signature of the traveling-wave mode. This could be a dynamical interaction, with the vibration mode altering the compliant surface and reducing its receptivity to the synthetic mode forcing. Alternatively, it could be a kinematical interaction, if the vibration mode is sufficiently broadband in k_x and has a $k_x = k_{x\mathrm{f}}$ component out of phase with the synthetic mode forcing, resulting in destructive interference.

Even with the decreased amplitude, the ω_f-$k_{x\mathrm{f}}$ component of the deformation is still discernible along the centerline, and allows for an amplitude and phase of the surface response mode to be defined. The amplitude and phase of the wall-normal deformation can be related to the amplitude and phase of the wall-normal velocity at the wall (v_w) by the Fourier transformed no-through flow boundary condition:

$$\widehat{\widehat{v}}_{w|\omega_\mathrm{f}k_{x\mathrm{f}}} = -i\omega_\mathrm{f}\widehat{\widehat{d}}_{y|\omega_\mathrm{f}k_{x\mathrm{f}}} \tag{6.4}$$

$$\Rightarrow \left|\widehat{\widehat{v}}_{w|\omega_\mathrm{f}k_{x\mathrm{f}}}\right| = \omega_\mathrm{f}\left|\widehat{\widehat{d}}_{y|\omega_\mathrm{f}k_{x\mathrm{f}}}\right| \tag{6.5}$$

$$\Rightarrow \angle\widehat{\widehat{v}}_{w|\omega_\mathrm{f}k_{x\mathrm{f}}} = \angle\widehat{\widehat{d}}_{y|\omega_\mathrm{f}k_{x\mathrm{f}}} - \frac{\pi}{2}. \tag{6.6}$$

The amplitudes and phases of the ω_f-$k_{x\mathrm{f}}$ wall-normal deformation and wall velocity were computed for actuation conditions ii and iii, and are given in Table 6.4. In both cases ii and iii, the deformation amplitude is very small, $\sim$1 um or $\sim 10^{-4}\delta$. Though the amplitudes are comparable to those measured in the unforced study, it is expected that these deformations are more reliably measured due to the phase-averaging process. Taking the uncertainty or noise floor of the DIC processing to be a standard error of the measurement, the phase-averaging process reduces the propagated error by a factor of $\sqrt{N}$, where N is the number of samples. In this case, the error is reduced by a factor of 30 by the phase-averaging procedure. While the wall velocity magnitudes are also small relative to U_∞, they are on the order of 1% of the critical layer values in Table 6.3. The phase difference between the wall velocity and critical layer values is difficult to interpret using only two points. This ambiguity will be resolved in Chapter 7 using the full mode shape.

	Case ii		Case iii	
	Amplitude	Phase	Amplitude	Phase
$\widehat{\widehat{d}}_{y\vert\omega_\mathrm{f}k_{x\mathrm{f}}}$	0.61 um $0.2 \cdot 10^{-4}\delta$ $0.01\delta_\nu$	1.37π	1.81 um $0.7 \cdot 10^{-4}\delta$ $0.03\delta_\nu$	1.46π
$\widehat{\widehat{v}}_{w\vert\omega_\mathrm{f}k_{x\mathrm{f}}}$	$5.3 \cdot 10^{-5}$	0.87π	$1.6 \cdot 10^{-4}$	0.96π

Table 6.4: Amplitudes and phases of the ω_f-$k_{x\mathrm{f}}$ wall-normal surface deformation mode and corresponding wall velocity mode for the CW-DRF study, actuation conditions ii and iii. $\widehat{\widehat{d}}_{y|\omega_\mathrm{f}k_{x\mathrm{f}}}$ amplitudes are scaled to reflect the physical deformations and are provided in dimensional, outer-scaled, and inner-scaled forms. $\widehat{\widehat{v}}_{w|\omega_\mathrm{f}k_{x\mathrm{f}}}$ amplitudes are scaled to reflect the physical velocity and normalized by U_∞.

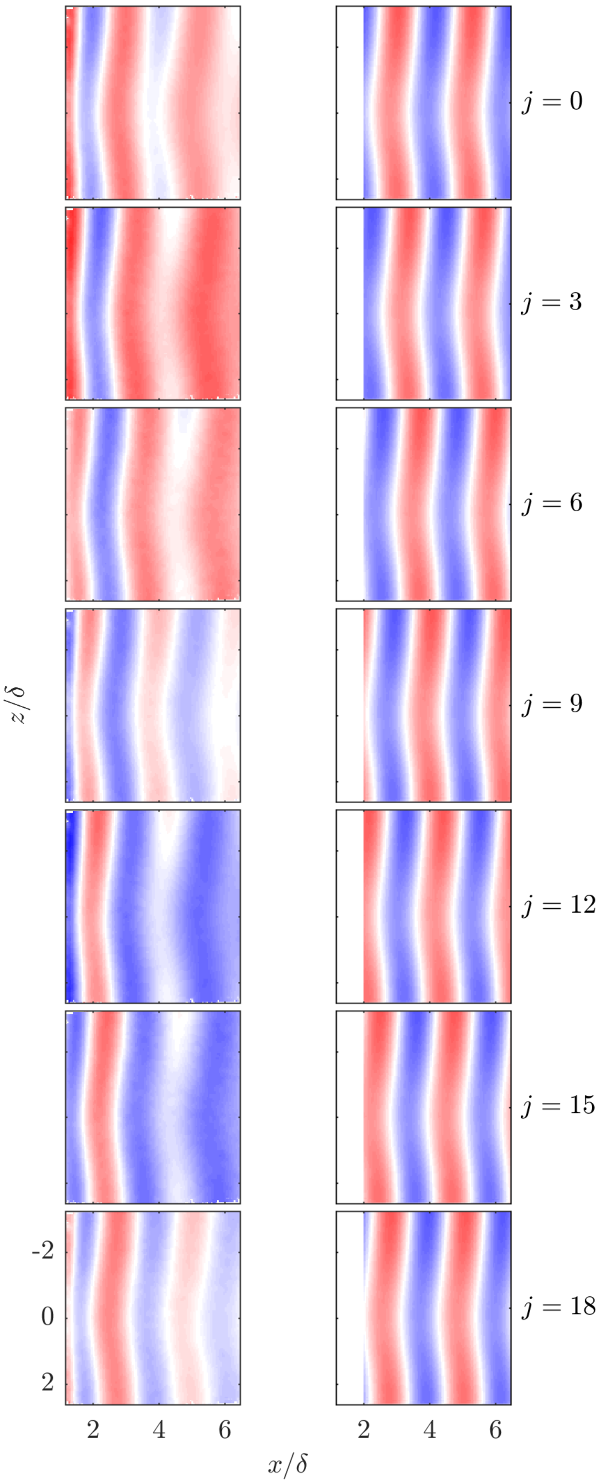

Figure 6.10: Phase snapshots from the LE FOV (actuation condition iii) of the (a) forcing frequency deformations, $d_{y|\omega_\mathrm{f}}$ and (b) ω_f-$k_{x\mathrm{f}}$ component, $d_{y|\omega_\mathrm{f} k_{x\mathrm{f}}}$. Phase indices increase from top to bottom, $j = [1, 3, 7, 10, 13, 16, 19]$. The colorbar limits are $[-5.5, 5.5]$ um. The colorbar limits are $[-1.5, 1.5]$ um.

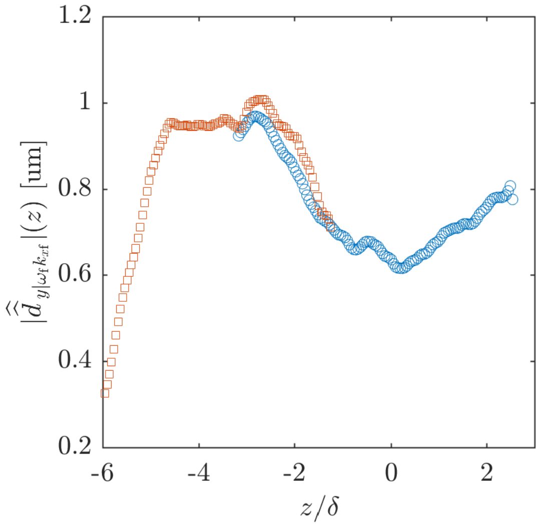

Figure 6.11: Amplitudes of the of the ω_f-$k_{x\mathrm{f}}$ deformation versus z for actuation condition ii. The amplitudes are scaled to reflect the corresponding physical surface displacements in um. ○ LE FOV; □ corner FOV.

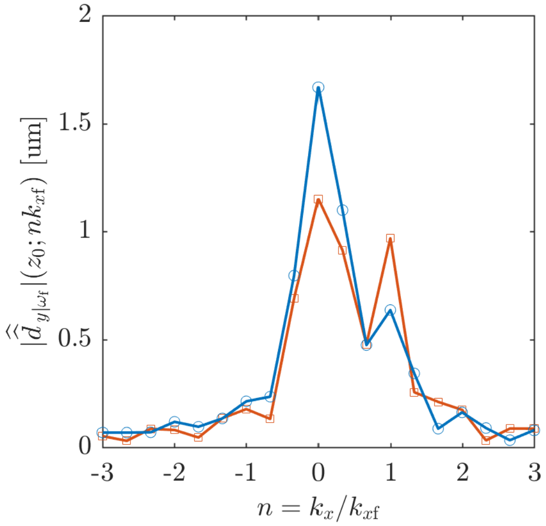

Figure 6.12: k_x-amplitude spectrum of the of the wall-normal deformation at two spanwise locations. The k_x-axis is normalized by $k_{x\mathrm{f}}$, and the amplitudes are scaled to reflect the corresponding physical surface displacements in um. ○ — $z/\delta = 0$; □ — $z/\delta = -2.8$.

6.5 Chapter summary

The deformation response of the CW-DRF system was studied. Comparing the d_y power spectra between the CW-unforced and CW-DRF cases, the forced data appeared very similar to the unforced, with slightly modified low frequency content and the addition of a prominent peak at the forcing frequency. The spatial structure of the f_f content was examined and found to contain a large amplitude, low wavenumber, vibration-type component, and a nearly-spanwise constant, streamwise traveling wave. The vibration-type deformation was present even when there was no flow, and was attributed to the pressure waves emanating from the roughness as it oscillated, which transmitted indirectly to the gelatin, through the water and the acrylic plate. The traveling wave was best attributed to the surface's response to the synthetic mode in the flow, as it was not consistent with any of the unforced deformation modes from the CW-unforced study. Thus, the experiment successfully elicited a surface response from the roughness-generated synthetic mode.

The flow response of the CW-DRF was then characterized. The mean flow properties were found to be very similar to the SW-DRF case, with evidence of internal layer development. Phase snapshots from the SW and CW studies were compared and found to share dominant, T-S-like structure, with the CW data having a slightly higher streamwise wavenumber. $k_{x\mathrm{f}}$ values were calculated for the CW data and exhibited a similar linear relationship with ω_f as the SW study, though with a higher slope such that the CW $k_{x\mathrm{f}}$ were higher than the SW for a given ω_f.

The $k_{x\mathrm{f}}$ values were then used to extract the spatial component of the forced surface deformation using an identical zero-padded DFT process as the velocity fields in Chapter 4. $d_{y|\omega_\mathrm{f} k_{x\mathrm{f}}}$ captured the traveling-wave component of the phase-averaged deformations well. The LE and corner data for the $|\widehat{\widehat{d}}_{y|\omega_\mathrm{f} k_{x\mathrm{f}}}|(z)$ revealed that the amplitude of the ω_f-$k_{x\mathrm{f}}$ deformation mode has a convex bow-shape centered at $z = 0$. As $|\widehat{\widehat{d}}_{y|\omega_\mathrm{f} k_{x\mathrm{f}}}|$ increases towards the spanwise edge, the $k_x = 0$ (vibration-type) mode amplitude, $|\widehat{\widehat{d}}_{y|\omega_\mathrm{f}}|(z; n = 0)$, decreases. This may suggest an interaction between the vibration and traveling-wave modes, whereby the vibration acts to reduce the amplitude of the synthetic mode surface response. The $\widehat{\widehat{d}}_{y|\omega_\mathrm{f} k_{x\mathrm{f}}}$ component was used to estimate the wall-normal velocity of the surface, $\widehat{\widehat{v}}_{w|\omega_\mathrm{f} k_{x\mathrm{f}}}$, which in turn allowed for a $\widehat{\widehat{v}}_{\omega_\mathrm{f} k_{x\mathrm{f}}}$ amplitude ratio and phase difference to be defined between the critical layer and wall locations.

Chapter 7

COMPARISON OF SMOOTH- AND COMPLIANT-WALL RESPONSES TO DYNAMIC ROUGHNESS FORCING THROUGH THE LENS OF RESOLVENT ANALYSIS

As mentioned in Chapter 6, the flows in the SW- and CW-DRF studies share many features. The structure of the synthetic mode is certainly visually similar in both cases. One notable difference is in the streamwise wave numbers of the synthetic modes, with the compliant-wall $k_{x\mathrm{f}}$ being measurably shorter than the smooth-wall values. To explore other, possibly more nuanced effects of the compliant wall on the synthetic mode, the resolvent framework will be used to provide a guiding perspective. In this chapter, the resolvent methodology will be briefly outlined, resolvent modes will be computed to predict flow features, and the ω_f-$k_{x\mathrm{f}}$ velocity modes will be compared to the predictions in addition to conditionally averaged modes.

7.1 Resolvent formulation

The resolvent framework was applied by McKeon & Sharma (2010) [45] as an approach to study problems turbulent flows in a low-rank manner by investigating the preferentially amplified modes of the resolvent operator. Here, the formulation by Luhar et al. (2015) [43] will be considered, for a fully developed channel flow, with x, y, and z corresponding to the streamwise, wall-normal, and spanwise directions, walls at y=0 and y=2, the channel half-height denoted h. All terms in the following methodology have been non-dimensionalized using h and u_τ. A Fourier decomposition is employed in the homogeneous directions, x, z, and t:

$$g(x, y, z, t) = \iiint_{-\infty}^{\infty} \breve{g}_\mathbf{k}(y) e^{i(k_x x + k_z z - \omega t)} \, \mathrm{d}k_x \mathrm{d}k_z \mathrm{d}\omega \,, \tag{7.1}$$

where $\mathbf{k} = (k_x, k_z, \omega)$ is the Fourier wavenumber vector and $\breve{(\cdot)}$ indicates a Fourier-transformed quantity in all three homogeneous directions, to avoid confusion with the $\widehat{(\cdot)}$ notation for a 1D-DFT used up until this point.

The Navier-Stokes equations (NSEs) are written in primitive-variable form, with pressure explicitly retained to later solve for the boundary condition. The NSEs are then Fourier-transformed and written in an input-output form:

$$\begin{bmatrix} \check{\mathbf{u}}_{\mathbf{k}} \\ \check{p}_{\mathbf{k}} \end{bmatrix} = \left(-i\omega \begin{bmatrix} \mathbf{I} & \\ & 0 \end{bmatrix} - \begin{bmatrix} \mathcal{L}_{\mathbf{k}} & -\nabla_{\mathbf{k}} \\ \nabla_{\mathbf{k}}^{\mathrm{T}} & 0 \end{bmatrix} \right)^{-1} \begin{bmatrix} \mathbf{I} \\ 0 \end{bmatrix} \check{\mathbf{f}}_{\mathbf{k}} \tag{7.2}$$

$$= \mathcal{H}_{\mathbf{k}}\, \check{\mathbf{f}}_{\mathbf{k}} \,, \tag{7.3}$$

where $\check{\mathbf{u}}_{\mathbf{k}}$ and $\check{p}_{\mathbf{k}}$ are the Fourier-transformed velocity and pressure fields and $\check{\mathbf{f}}_{\mathbf{k}}$ is the Fourier-transformed nonlinear term:

$$\check{\mathbf{f}}_{\mathbf{k}} = \widecheck{(-\mathbf{u} \cdot \nabla \mathbf{u})}_{\mathbf{k}} \,, \tag{7.4}$$

all corresponding to the wavenumber vector $\mathbf{k}$. $\nabla_{\mathbf{k}} = [ik_x, \partial/\partial y, ik_x]^{\mathrm{T}}$ and $\nabla_{\mathbf{k}}^{\mathrm{T}}$ represent the Fourier-transformed gradient and divergence operators, respectively. In this framework, the nonlinear term acts as an endogenous forcing to the velocity and pressure through the resolvent operator, $\mathcal{H}_{\mathbf{k}}$, which depends on the linear component of the NSEs:

$$\mathcal{L}_{\mathbf{k}} = \begin{bmatrix} -ik_x\overline{U} + Re_\tau^{-1}\nabla_{\mathbf{k}}^2 & -\partial\overline{U}/\partial y & 0 \\ 0 & -ik_x\overline{U} + Re_\tau^{-1}\nabla_{\mathbf{k}}^2 & 0 \\ 0 & 0 & -ik_x\overline{U} + Re_\tau^{-1}\nabla_{\mathbf{k}}^2 \end{bmatrix} , \tag{7.5}$$

where $\nabla_{\mathbf{k}}^2$ is the Fourier-transformed Laplacian. Note that $\mathcal{H}_{\mathbf{k}}$ contains terms with the mean velocity, $\overline{U}(y)$, which is assumed to be known *a priori*.

The problem is discretized in y using N Chebyshev collocation points, then the discrete resolvent operator $\mathcal{H}_{\mathbf{k}}$ is constructed, and a singular value decomposition (SVD) is performed:

$$\mathcal{H}_{\mathbf{k}}(y) = \sum_{q=1}^{N} \psi_{\mathbf{k}q}(y)\, \sigma_{\mathbf{k}q}\, \phi_{\mathbf{k}q}^{*}(y) \,, \tag{7.6}$$

where $\psi_{\mathbf{k}q}$ are the singular response modes (henceforth referred to as resolvent modes), $\sigma_{\mathbf{k}q}$ are the (ordered) singular values, and $\phi_{\mathbf{k}q}$ are the singular forcing modes. Velocity and pressure can then be expressed as:

$$\begin{bmatrix} \check{\mathbf{u}}_{\mathbf{k}}(y) \\ \check{p}_{\mathbf{k}}(y) \end{bmatrix} = \sum_{q=1}^{N} \psi_{\mathbf{k}q}(y)\, \sigma_{\mathbf{k}q} \left(\phi_{\mathbf{k}q} \,,\, \check{\mathbf{f}}_{\mathbf{k}} \right) \tag{7.7}$$

$$= \sum_{q=1}^{N} \psi_{\mathbf{k}q}(y)\, \sigma_{\mathbf{k}q}\, \chi_{\mathbf{k}q} \,, \tag{7.8}$$

where $(\cdot\,,\cdot)$ indicates an inner product and $\chi_{\mathbf{k}q}$ are the weights formed by projecting the nonlinear forcing onto the singular forcing modes.

At this point, the rank-1 approximation discussed in Chapter 1 is invoked to approximate the resolvent operator by the first resolvent mode, singular value, and singular forcing mode:

$$\mathcal{H}_{\mathbf{k}}(y) \approx \psi_{\mathbf{k}1}(y)\,\sigma_{\mathbf{k}1}\,\phi^{*}_{\mathbf{k}1}(y). \tag{7.9}$$

This then allows the velocity and pressure to be approximated by:

$$\begin{bmatrix} \check{\mathbf{u}}_{\mathbf{k}}(y) \\ \check{p}_{\mathbf{k}}(y) \end{bmatrix} \approx \sigma_{\mathbf{k}1}\,\psi_{\mathbf{k}1}(y) \tag{7.10}$$

with the additional assumption of broadband forcing, discussed in McKeon & Sharma (2010) [45]. In this analysis, the shapes of the resolvent modes, $\psi_{\mathbf{k}1}$, are used to predict features of the SW- and CW-DRF data. In the discussion, the subscript '$\mathbf{k}1$' will be suppressed and will indicate the response component, i.e. ψ_x, ψ_y, and ψ_p for the streamwise, wall-normal, and pressure resolvent modes.

The framework by Luhar et al. (2015) [43] models the effect of a compliant-wall by modifying the otherwise rigid, smooth-wall boundary condition. The compliant wall is considered by introducing a wall displacement term at the boundaries, $\eta(x,z,t)$, constrained to be in the wall-normal direction. Along the boundary, the no-slip and no-through flow conditions are applied and a Taylor's expansion performed about the undeformed wall location. These boundary conditions can be made for an arbitrarily large wall deformation by retaining higher-order terms in the expansion, at the cost of a more complex, nonlinear set of equations. Instead, following Luhar et al. (2015) [43], the deformations are assumed small and the boundary conditions are linearized to enable a more computationally tractable analysis. Given the small deformations observed in the DIC data, $O\left(10^{-4}\right)\delta$, this assumption is at least somewhat justified and will be considered when interpreting the results. Thus, the linearized, Fourier-transformed velocity boundary conditions can be written as:

$$\check{u}_{\mathbf{k}}(0) = -\check{\eta}_{\mathbf{k}}\,\left.\frac{\mathrm{d}\overline{U}}{\mathrm{d}y}\right|_{0} \tag{7.11}$$

$$\check{v}_{\mathbf{k}}(0) = -i\omega\check{\eta}_{\mathbf{k}} \tag{7.12}$$

$$\check{w}_{\mathbf{k}}(0) = 0. \tag{7.13}$$

A derivation of the compliant-wall boundary conditions is provided in Appendix C. Note that $\check{u}_{\mathbf{k}}(0)$ is required to balance a mean shear term introduced by the wall deformation, and that $\check{v}_{\mathbf{k}}(0)$ is related to the deformation by the no-through flow boundary condition. Also, equations 7.11 and 7.12 together require that $\check{u}_{\mathbf{k}}(0)$ has a $\pi/2$ phase lead with respect to $\check{v}_{\mathbf{k}}(0)$ at the wall.

The pressure boundary condition is determined by the dynamic coupling between pressure and the wall motion. Here, this coupling is modeled as a spring-mass-damper system [62], for which the wall pressure and wall deformation are connected by:

$$\left[C_m(-\omega^2) + C_d(-i\omega) + C_k\right]\check{\eta}_{\mathbf{k}} = -\check{p}_{\mathbf{k}}(0)\,, \tag{7.14}$$

where C_m, C_d, and C_k are the dimensionless mass, damping, and spring coefficients. These coefficients are defined as:

$$C_m = \frac{\rho_w b_w}{\rho h} \tag{7.15}$$

$$C_d = \frac{d_w}{\rho u_\tau} \tag{7.16}$$

$$C_k = \frac{k'_{sw} h}{\rho u_\tau^2}\,, \tag{7.17}$$

where the following are all plate properties with subscript 'w' for 'wall': ρ_w is the density, b_w the thickness, d_w the damping coefficient, and k'_{sw} the area-spring stiffness. Though not considered in this analysis, additional tension and stiffness coefficients can be included to account for the effects of tension and flexural rigidity (stiffness) of the plate.

A complex wall admittance term, Y, is defined that connects the pressure and the wall-normal velocity at the wall, and using equations 7.12 and 7.14 is written as:

$$Y = \frac{\check{v}_{\mathbf{k}}(0)}{\check{p}_{\mathbf{k}}(0)} \tag{7.18}$$

$$= \frac{i\omega}{-\omega^2 C_m - i\omega C_d + C_k}. \tag{7.19}$$

This complex admittance is used to account for the material properties of the wall. Thus, equations 7.11-7.13 and 7.18-7.19 are used as the boundary conditions for the velocities and pressure at y=0 and y=2, with the sign of Y flipped between the two walls due to centerline symmetry.

The value of Y was calculated for the gelatin material used in this study, using the canonical flow values of δ and u_τ from Table 3.1. As discussed in Chapter 2, the viscoelastic effects in the gelatin were found to be minimal, and so the material is considered linearly elastic. Accordingly, the damping coefficient was assumed zero, and thus Y was guaranteed to be purely imaginary. Taking the channel half-height to be the boundary layer thickness and taking the gelatin's density to be the same as water, the mass coefficient was calculated to be $C_m = 1$. An effective area-spring stiffness was related to the gelatin's Young's modulus, E, by considering the material to be in uniaxial tension/compression:

$$k'_{sw} = \frac{k_{sw}}{A_w} = \frac{E}{b_w}\,, \tag{7.20}$$

where k_{sw} is the typical spring stiffness and A_w is the $(x{-}z)$ area of the gelatin sample. Thus, the spring coefficient was calculated to be $C_k = 1.7 \cdot 10^4$. The frequency was taken to be the forcing frequency from actuation condition iii and non-dimensionalized by h and u_τ, yielding $\omega = 50$. This gave an admittance of $Y = 0.003i$. The purely imaginary nature of Y indicates that the wall-normal velocity leads the pressure at the wall by $\pi/2$. The boundary condition in equation 7.12 implies that the wall deformation, in turn, leads the velocity by $\pi/2$. This is precisely the expected behavior of the damping-less spring-mass model being used. The amplitude of Y is low relative to values explored by Luhar et al. [43], indicating that the material is relatively rigid, despite the gelatin being fabricated as soft as possible. This may provide perspective on the level of compliance required by a physical material to achieve a modeled performance, or suggest that other coefficient terms need to be exploited. Note that though arriving at this value of Y required a number of assumptions, the results are fairly insensitive to the precise value of Y, with key features only being scaled in magnitude and wall-normal location for $10^{-4} < Y < 10^{-2}$.

The MATLAB code for channel flow resolvent analysis with a compliant-wall boundary condition [43] was used to generate the results discussed in this chapter. A study was done with code for a boundary layer flow as well [32, 52], with identical results near the wall and only slight differences in the outer part of the flow, as expected. The mean velocity profile is generated using the eddy viscosity model of Reynolds & Tiederman (1967) [51], with more description provided in Luhar et al. (2015) [43]. An experimental mean profile could have been used to account for the modification from the dynamic roughness, but this would have required a choice of interpolation scheme and would have become difficult near the wall, where the averaging effect of PIV is more pronounced. Therefore, the following analysis considers an uncontrolled, numerically-generated mean, which is an additional simplification. Note that the same mean profile is used for both the smooth-wall and compliant-wall resolvent modes. The grid resolution used was $N = 200$, and the friction Reynolds number was matched to the canonical flow value of $Re_\tau = 410$ from Table 3.1. The code was executed on a single-core laptop and took about 0.5 s to compute one set of singular values and resolvent modes.

7.2 Prediction of compliant-wall flow features from resolvent modes

Resolvent modes were computed for smooth-wall (Y=0) and compliant-wall ($Y = 0.003i$) boundary conditions, using wavenumber vectors $\mathbf{k}=[k_x, k_z, \omega]^\mathrm{T}$ that corresponded to the synthetic mode from the experiments, $\mathbf{k}_\mathrm{f} = [k_{x\mathrm{f}}, 0, \omega_\mathrm{f}]^\mathrm{T}$, for actuation condition iii. As $k_{x\mathrm{f}}$ differs between the SW- and CW-DRF studies, k_x=2.67 and k_x=2.78 are used for the smooth-wall and compliant-wall resolvent modes, respectively. The mode shapes are plotted in outer scaling, y/h, to facilitate comparison with the experimental data. All amplitudes are normalized by the peaks of $|\psi_x|$ to preserve the relative amplitude information between ψ_x and ψ_y. The phase of the smooth-wall ψ_y mode is matched to the phase of the compliant-wall ψ_y mode at y=h, and all other mode phases are shifted accordingly. This normalization and phase matching are done for all comparisons of smooth- and compliant-wall modes.

Figures 7.1 and 7.2 show the amplitudes and phases for both the SW and CW ψ_x and ψ_y. The streamwise modes in Figure 7.1 are dual-peaked in amplitude and undergo a π phase jump at the wall-normal location corresponding to the amplitude zero-crossing, with the jump indicative of a downstream inclination of the modes. The wall-normal modes in Figure 7.2 are single-peaked and tall, with a nearly constant phase except very near the wall. The amplitude of ψ_x is notably higher than ψ_y. Comparing the SW and CW cases, there is a clear difference in where the modes are centered; the compliant-wall mode is shifted more towards the wall. This can be understood from a critical layer perspective, since the CW mode has a larger k_x with the same ω, and thus has a lower wave speed and lower critical layer location than the SW mode. If the CW modes were scaled in y to match the SW y_CL location, the two would still not match identically. In $|\psi_x|$, the second peak is slightly more amplified (relative to the first peak) for the CW mode than the SW mode. Looking at $|\psi_y|$, the CW mode is distinctly less amplified than the SW mode, again relative to the peak in $|\psi_x|$. The phases of ψ_x and ψ_y between the two sets have nearly identical shape and shift, with the shifted critical layer clearly evident in $\angle\psi_x$. The phases deviate between the SW and CW modes very near the wall, which is explored next.

The same amplitude and phase plots are shown in Figures 7.3 and 7.4 for $0 < y/\delta < 0.1$ to examine the near-wall behavior. In Figure 7.3a, the CW streamwise mode amplitude appears higher compared to the SW, though it is difficult to discern if this is an effect of the boundary condition or simply the difference in y_{CL}. Note that the CW amplitude does not go to zero at $y = 0$, as expected for the modified boundary condition. The phases in Figure 7.3b show a more distinct feature in ψ_x, with the CW phase deviating from the SW around $y/h = 0.016$ and going from a positive to negative gradient as the wall is approached. In Figure 7.4a, the CW $|\psi_y|$ has a minimum at $y/h = 0.016$, while $\angle\psi_y$ in Figure 7.4b undergoes a $-\pi$ phase jump at the same location. Both of these details are absent in the SW modes. The local minimum or cusp in $|\psi_y|$ and $-\pi$ phase jump in $\angle\psi_y$ are similar to the features observed in the resolvent-based opposition control study by Luhar et al. (2014) [41], who drew comparison with the 'virtual wall' described by DNS opposition control studies [10, 25]. In these opposition control studies, wall jets were simulated and induced vertical blowing/sucking to oppose the vertical velocity measured at a selected wall-normal measurement plane. From a mode phase perspective, this opposition requires that $\angle\psi_y$ undergoes a π jump near the wall. This control scheme developed a virtual wall above the actual wall, limiting momentum transfer in the near-wall region.

The fact that spring-mass-modeled, compliant-wall resolvent modes act in a similar way to the opposition control can be understood by considering the phase behavior of ψ_y and ψ_p, which are plotted for the SW and CW case in Figure 7.5. Outside of the near-wall region, ψ_y and ψ_p have a nearly constant $\pi/2$ phase difference, $\angle\psi_y - \angle\psi_p = -\pi/2$. As explained by Luhar et al. (2014) [42], this constant $\pi/2$ phase difference stems from the fact that, for the resolvent modes, the primary contribution to the pressure term is from the so-called 'fast pressure' term in the Poisson equation for pressure. Within the scope of the mode phases, this implies $\psi_p \sim -i\psi_y$ to within a real-valued scaling, leading to $\angle\psi_y - \angle\psi_p = -\pi/2$. However, the purely imaginary complex admittance, Y, in the resolvent boundary condition requires that the velocity leads pressure by $\pi/2$ at the wall, $\angle\psi_y(0) - \angle\psi_p(0) = \pi/2$, per equation 7.18. As also observed by Luhar et al., the pressure modes in Figure 7.5 have essentially constant phase through the entire domain, down to the wall. With $\angle\psi_p$ constant, $\angle\psi_y$ is required to undergo a π phase jump to satisfy the phase boundary condition, just as in the case with opposition control. Thus, from the resolvent perspective, a purely elastic (and relatively rigid) wall mimics the action of the wall jets in opposition control, and yields the familiar virtual wall. This feature provides a lens through which the experimental mode shapes can be examined.

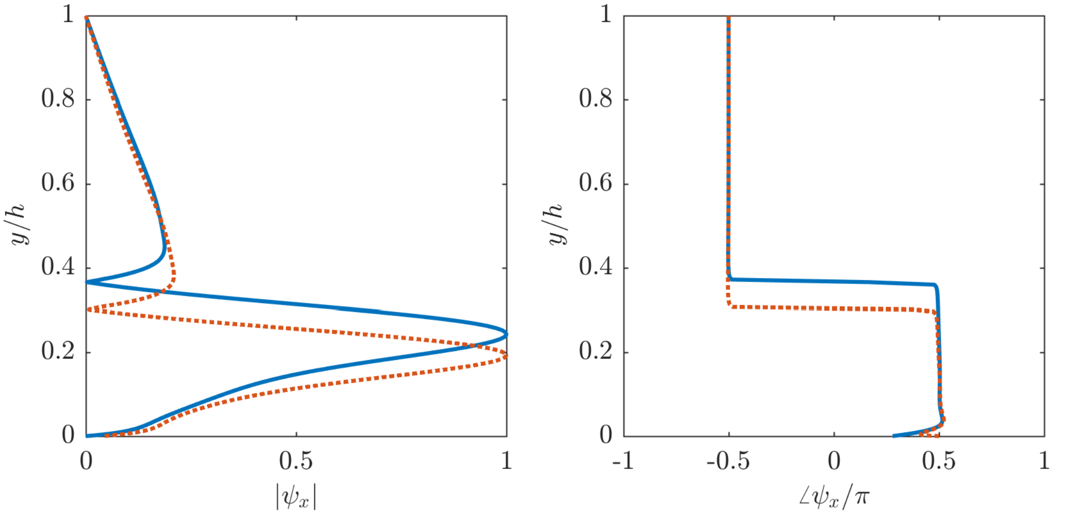

(a) (b)

Figure 7.1: Comparison of the (a) amplitudes and (b) phases of the streamwise resolvent response mode, ψ_x, with the smooth- and compliant-wall k_x values matching those of the experiment. Mode amplitudes are normalized by their peaks, and the smooth-wall mode phase is matched to the compliant-wall phase at $y = h$. — smooth-wall ($k_x = 2.67$); – – compliant-wall ($Y = 0.003i,\ k_x = 2.78$)

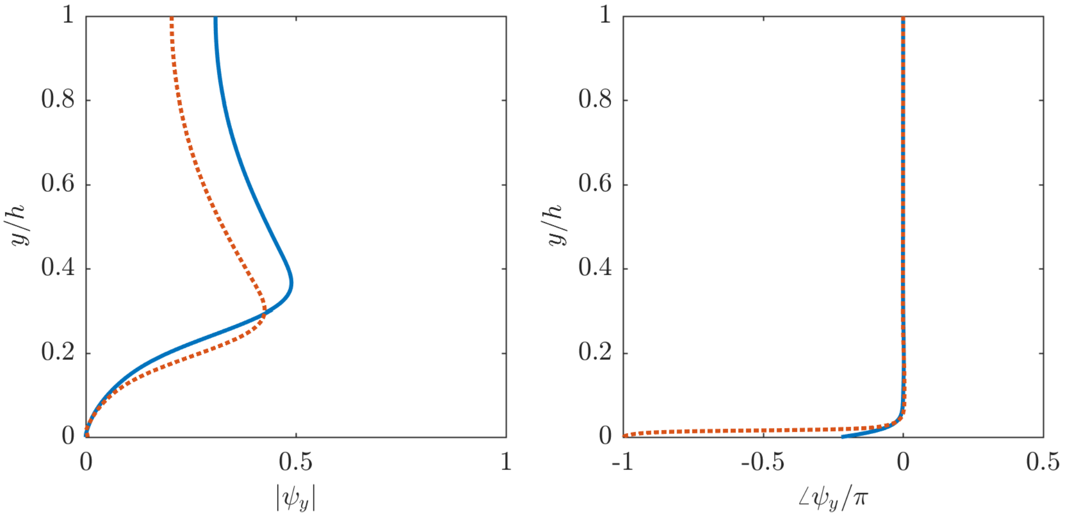

(a) (b)

Figure 7.2: Comparison of the (a) amplitudes and (b) phases of the wall-normal resolvent response mode, ψ_y, with the smooth- and compliant-wall k_x values matching those of the experiment. Mode amplitudes are normalized by the peak in $|\psi_x|$, and the smooth-wall mode phase is matched to the compliant-wall phase at $y = h$. — smooth-wall ($k_x = 2.67$); – – compliant-wall ($Y = 0.003i,\ k_x = 2.78$)

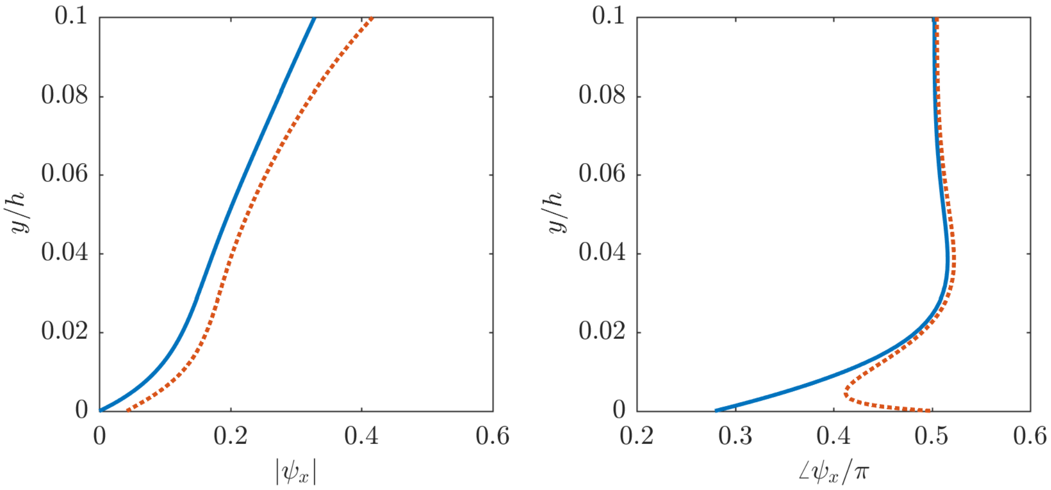

(a) (b)

Figure 7.3: Comparison of the (a) amplitudes and (b) phases of the streamwise resolvent response mode, ψ_x, with the smooth- and compliant-wall k_x values matching those of the experiment. Mode amplitudes are normalized by their peaks, and the smooth-wall mode phase is matched to the compliant-wall phase at $y = h$. — smooth-wall ($k_x = 2.67$); – – compliant-wall ($Y = 0.003i,\ k_x = 2.78$)

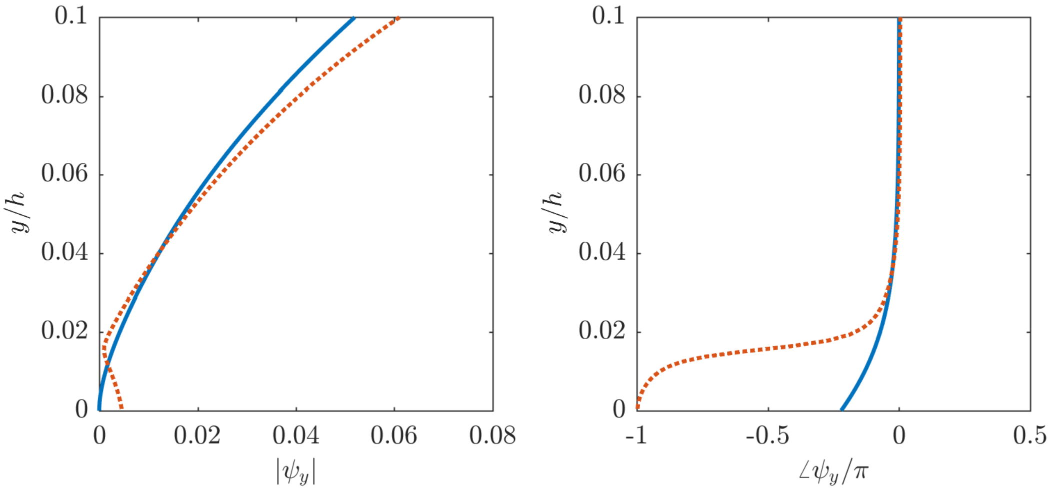

(a) (b)

Figure 7.4: Comparison of the (a) amplitudes and (b) phases of the wall-normal resolvent response mode, ψ_y, with the smooth- and compliant-wall k_x values matching those of the experiment. Mode amplitudes are normalized by the peak in $|\psi_x|$, and the smooth-wall mode phase is matched to the compliant-wall phase at $y = h$. — smooth-wall ($k_x = 2.67$); – – compliant-wall ($Y = 0.003i,\ k_x = 2.78$)

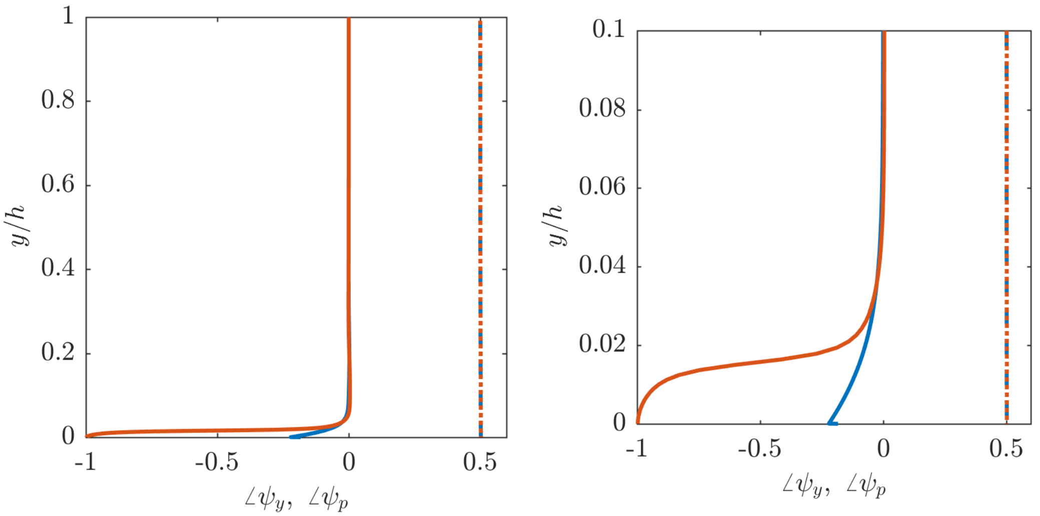

(a) (b)

Figure 7.5: Comparison of the phases of the wall-normal (ψ_y, solid lines) and pressure (ψ_p, dashed lines) resolvent response modes, with k_x values matching those of the experiment.: (a) full view, $0 < y/\delta < 1$, (b) near-wall view, $0 < y/\delta < 0.1$. — SW ψ_y; — CW ψ_y; – – SW ψ_p; · · · CW ψ_p.

7.3 Comparison of smooth- and compliant-wall experimental mode shapes

The streamwise and wall-normal ω_f-$k_{x\mathrm{f}}$ Fourier mode shapes from the SW- and CW-DRF studies (actuation condition iii) are given in Figures 7.6 and 7.7, with the corresponding resolvent modes from Figures 7.1 and 7.2 plotted for comparison. The amplitudes are normalized and phases shifted in the same manner as the previous section. The SW and CW mode shapes look structurally similar in amplitude and phase, and have several striking resemblances to the resolvent modes. The T-S characteristics remain present, with a dual-peaked amplitude and (downstream inclined) π phase jump in $\widehat{\widehat{u}}_{\omega_\mathrm{f} k_{x\mathrm{f}}}$ and a single-peaked, tall amplitude and nearly constant phase in $\widehat{\widehat{u}}_{\omega_\mathrm{f} k_{x\mathrm{f}}}$. The CW $|\widehat{\widehat{u}}_{\omega_\mathrm{f} k_{x\mathrm{f}}}|$, $|\widehat{\widehat{v}}_{\omega_\mathrm{f} k_{x\mathrm{f}}}|$, and $\angle\widehat{\widehat{u}}_{\omega_\mathrm{f} k_{x\mathrm{f}}}$ exhibit a shift towards the wall relative to the corresponding SW modes. This is in agreement with the resolvent modes, and again, is consistent with a y_CL mechanism due to the lesser wave speed of the CW synthetic mode. The second peak in $|\widehat{\widehat{u}}_{\omega_\mathrm{f} k_{x\mathrm{f}}}|$ is more amplified for the CW mode than the SW mode, as is observed for the resolvent modes. The peaks in $|\widehat{\widehat{v}}_{\omega_\mathrm{f} k_{x\mathrm{f}}}|$ are both less amplified than the peak in $|\widehat{\widehat{u}}_{\omega_\mathrm{f} k_{x\mathrm{f}}}|$, as was the case for $|\psi_y|$. However, the SW and CW $|\widehat{\widehat{v}}_{\omega_\mathrm{f} k_{x\mathrm{f}}}|$ match much more closely in amplitude than the SW and CW $|\psi_y|$, for which the SW mode is discernibly more amplified. A noticeable deviation occurs in the $\angle\widehat{\widehat{v}}_{\omega_\mathrm{f} k_{x\mathrm{f}}}$ between the SW and CW near the wall, as the CW phase shifts in the positive direction.

As done with the resolvent modes, a closer inspection is made of the $0 < y/\delta < 0.1$ near-wall region in Figures 7.8 and 7.9. There are no discernible aspects of $\widehat{\widehat{u}}_{\omega_\mathrm{f} k_{x\mathrm{f}}}$ akin to the aforementioned virtual wall feature. In Figure 7.9a with the amplitude of $\widehat{\widehat{v}}_{\omega_\mathrm{f} k_{x\mathrm{f}}}$, there does appear to be a knee in the CW profile around $y/\delta \sim 0.03$, but is modest at best in comparison to the cusp in Figure 7.9b. As noted, the CW phase of $\widehat{\widehat{v}}_{\omega_\mathrm{f} k_{x\mathrm{f}}}$ in Figure 7.9c does diverge from the SW phase by over $\pi/2$. It seems plausible that the phase may continue to a full π phase difference if the measurement extended closer to the wall, which would agree with the required π phase jump of ψ_y in Figure 7.9d for the resolvent prediction. However, the sense of this jump is flipped, with the CW $\widehat{\widehat{v}}_{\omega_\mathrm{f} k_{x\mathrm{f}}}$ structure leaning downstream, while the CW ψ_y mode leaned upstream.

The overall structure of the SW and CW ω_f-$k_{x\mathrm{f}}$ modes is similar, with a relative wall-normal shift consistent with the different critical layer locations. There is a substantial deviation in $\angle\widehat{\widehat{v}}_{\omega_\mathrm{f} k_{x\mathrm{f}}}$ near the wall between the two cases, but this is in the opposite sense as the prediction based on the resolvent modes. The cusp feature in $|\widehat{\widehat{v}}_{\omega_\mathrm{f} k_{x\mathrm{f}}}|$, one of the clear signatures of a virtual wall, is notably absent in the CW mode. Certainly, several assumptions have been made in the resolvent analysis, not the least of which is the linearized boundary condition, which has an immediate impact on the region of interest. However, even if a virtual wall phenomenon is present in the experimental data, there are several reasons that a Fourier analysis may not be unable to capture it. First, the signature is expected to be very near the wall, for which the resolution of the data has not been optimized. For example, the potential ‘knee’ feature in Figure 7.9a is contained in the 4-5 points nearest the wall. Second, as mentioned in Chapter 2, the gelatin surface is not perfectly smooth nor flat. This has been addressed to first order, but the surface geometry certainly effects the DFT analysis. Third and relatedly, as discussed in Chapters 5 and 6, there are other deformation modes present in the surface besides the response to the synthetic mode. Though the energy of these other deformations are removed by the phase-averaging and DFT processes, their imprint on the ω_f-$k_{x\mathrm{f}}$ modes percolates through via a changing of the wall location and nonlinear interactions. Even neglecting the nonlinear contributions, the compounding effects of surface geometry and non-harmonic deformations on the wall location would distort an existing, near-wall, streamwise structure, and require a nontrivial coordinate transformation to capture the structure by Fourier decomposition. Thus, despite not appearing as expected in the ω_f-$k_{x\mathrm{f}}$ modes, the virtual wall feature is not yet ruled out. Instead, an alternative analysis based on conditional averaging will be done in an attempt to circumvent the above listed challenges in the data.

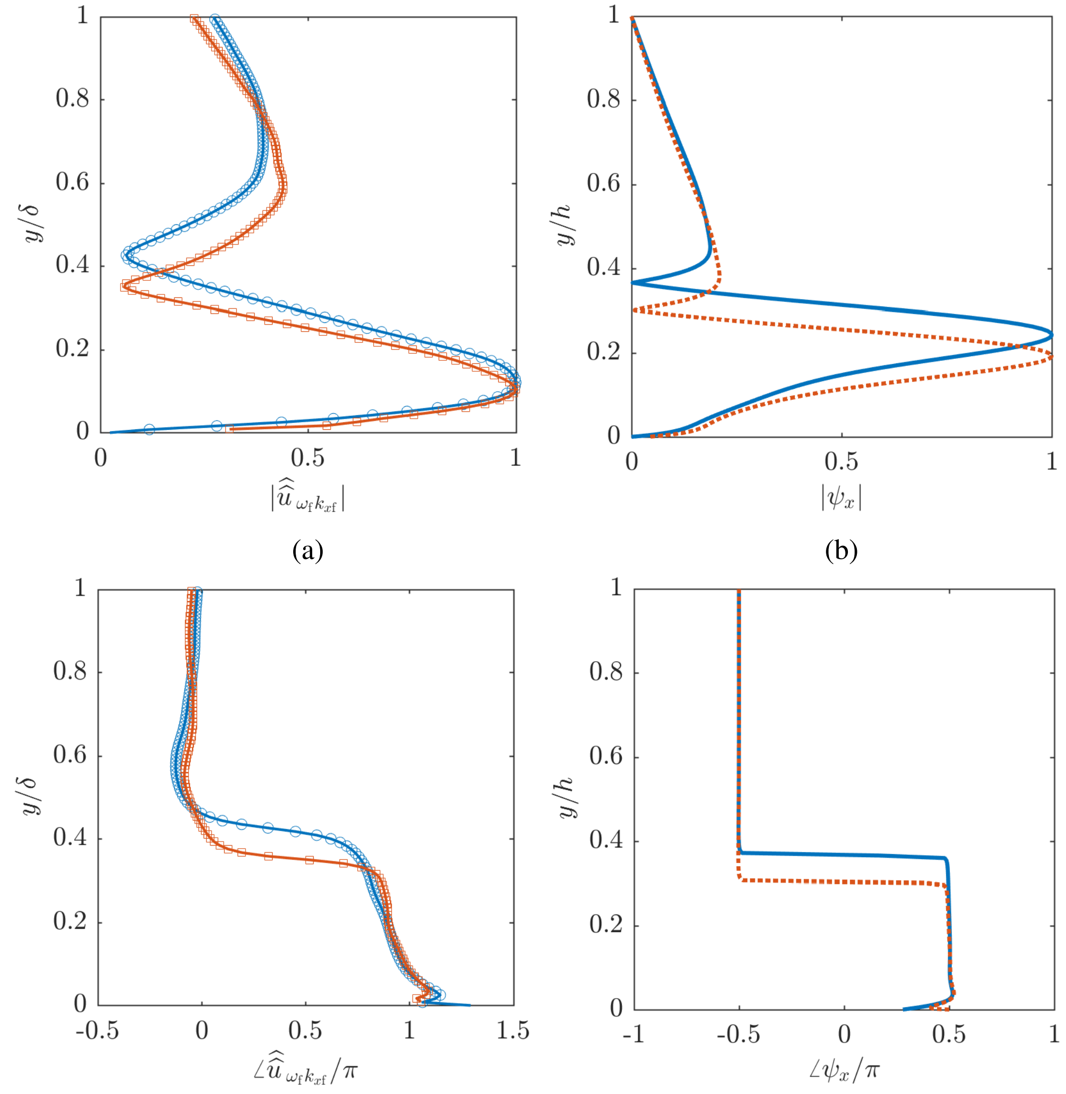

(a) (b)

(c) (d)

Figure 7.6: The smooth-wall and compliant-wall (a) amplitudes and (c) phases of the $\widehat{\widehat{u}}_{\omega_f k_{xf}}$ Fourier modes for actuation condition iii, with the (b) amplitudes and (d) phases of the streamwise resolvent modes, ψ_x, plotted for comparison. Mode amplitudes are normalized by their peaks, and the smooth-wall mode phase is matched to the compliant-wall phase at $y{=}\delta$ ($y{=}h$ for the resolvent modes). ○ — SW-DRF; □ — CW-DRF; — smooth-wall resolvent mode ($k_x = 2.67$); – – compliant-wall resolvent mode ($Y = 0.003i,\ k_x = 2.78$).

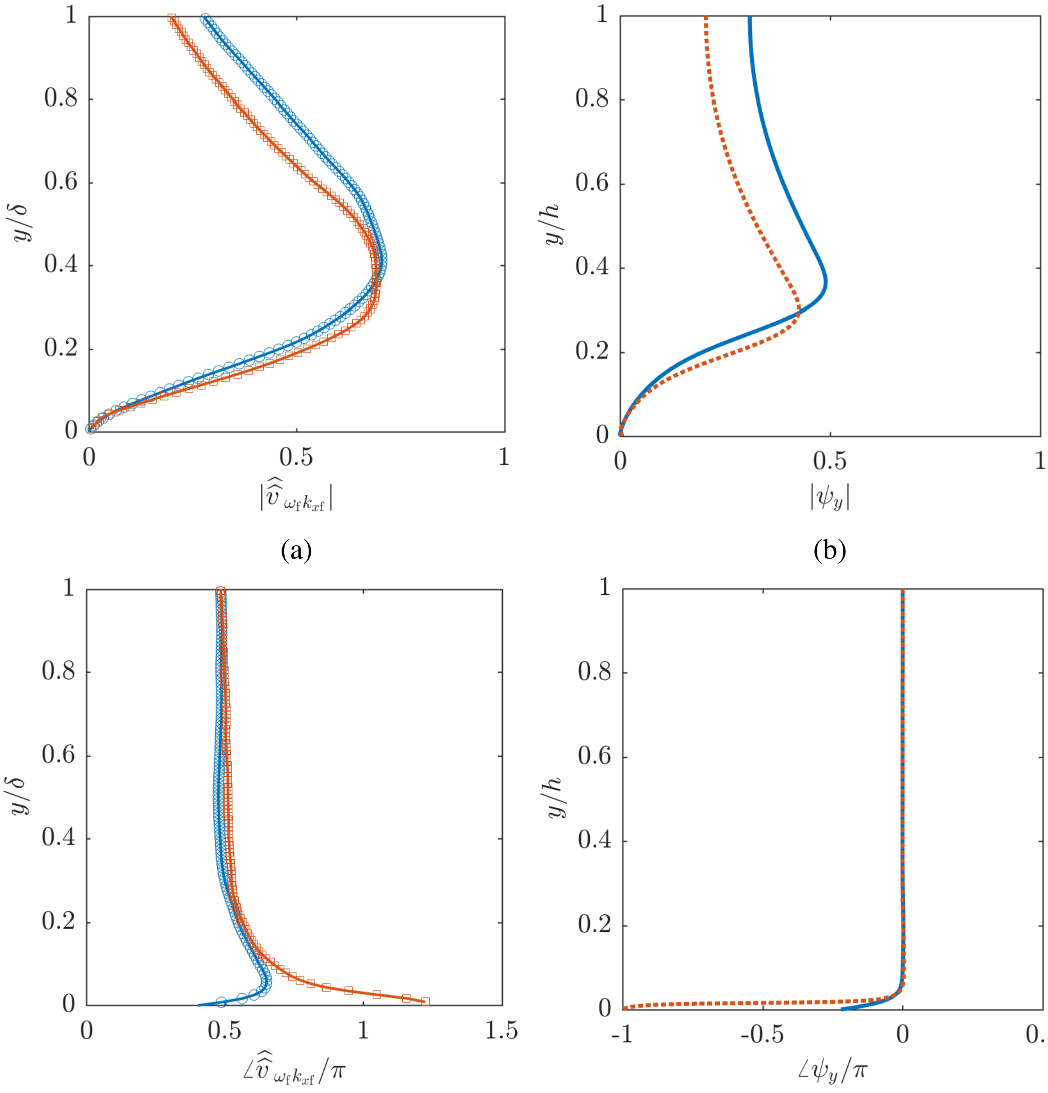

(a) (b)

(c) (d)

Figure 7.7: The smooth-wall and compliant-wall (a) amplitudes and (c) phases of the $\widehat{\widehat{v}}_{\omega_{\rm f}k_{x\rm f}}$ Fourier modes for actuation condition iii, with the (b) amplitudes and (d) phases of the wall-normal resolvent modes, ψ_y, plotted for comparison. Mode amplitudes are normalized by the peaks in $|\widehat{\widehat{u}}_{\omega_{\rm f}k_{x\rm f}}|$ ($|\psi_x|$ for the resolvent modes), and the smooth-wall mode phase is matched to the compliant-wall phase at $y{=}\delta$ ($y{=}h$ for the resolvent modes). ○ — SW-DRF; □ — CW-DRF; — smooth-wall resolvent mode ($k_x = 2.67$); – – compliant-wall resolvent mode ($Y = 0.003i,\ k_x = 2.78$).

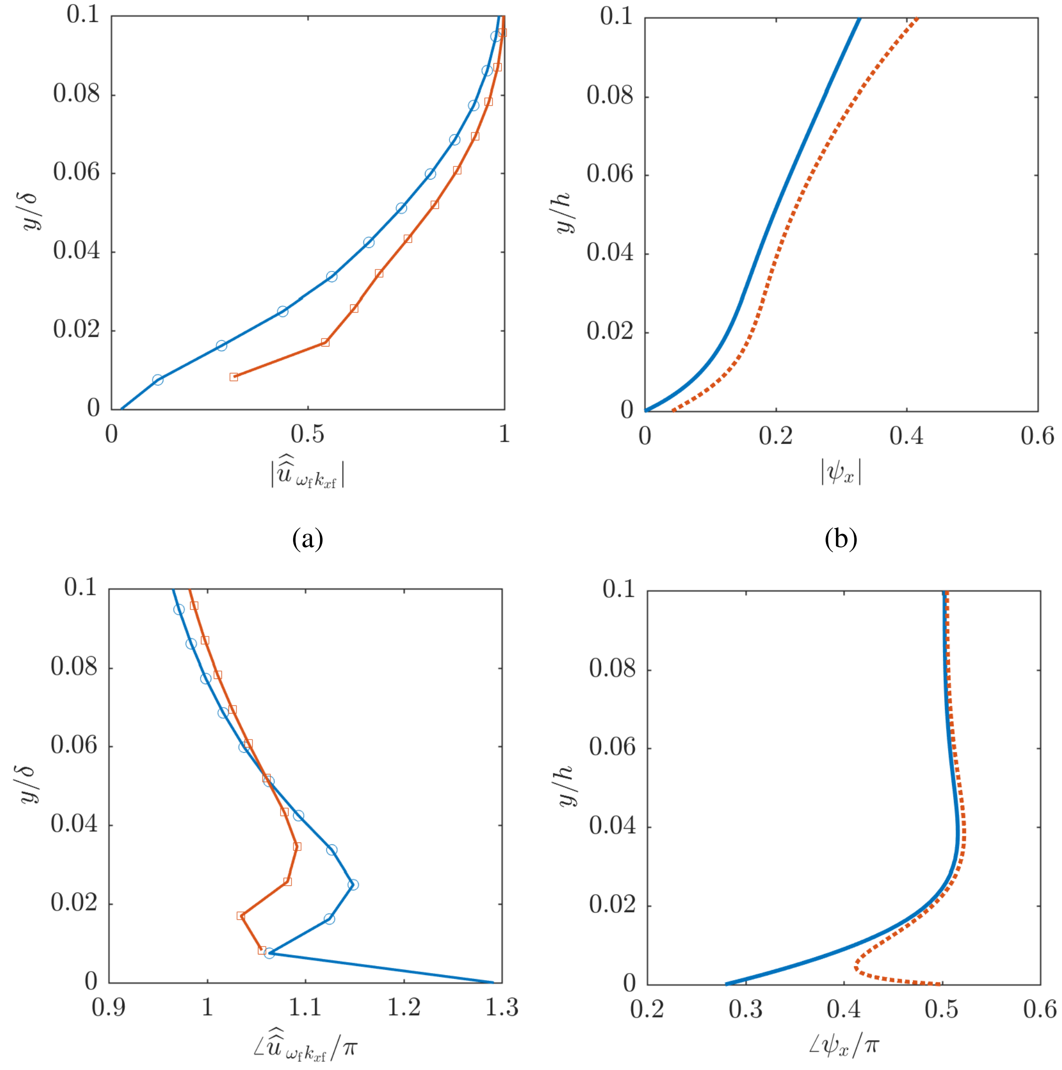

(a) (b)

(c) (d)

Figure 7.8: Near-wall close-up of the smooth-wall and compliant-wall (a) amplitudes and (c) phases of the $\widehat{\widehat{u}}_{\omega_\mathrm{f} k_{x\mathrm{f}}}$ Fourier modes for actuation condition iii, with the (b) amplitudes and (d) phases of the streamwise resolvent modes, ψ_x, plotted for comparison. Mode amplitudes are normalized by their peaks, and the smooth-wall mode phase is matched to the compliant-wall phase at $y{=}\delta$ ($y{=}h$ for the resolvent modes). ○ — SW-DRF; □ — CW-DRF; — smooth-wall resolvent mode ($k_x = 2.67$); – – compliant-wall resolvent mode ($Y = 0.003i,\ k_x = 2.78$).

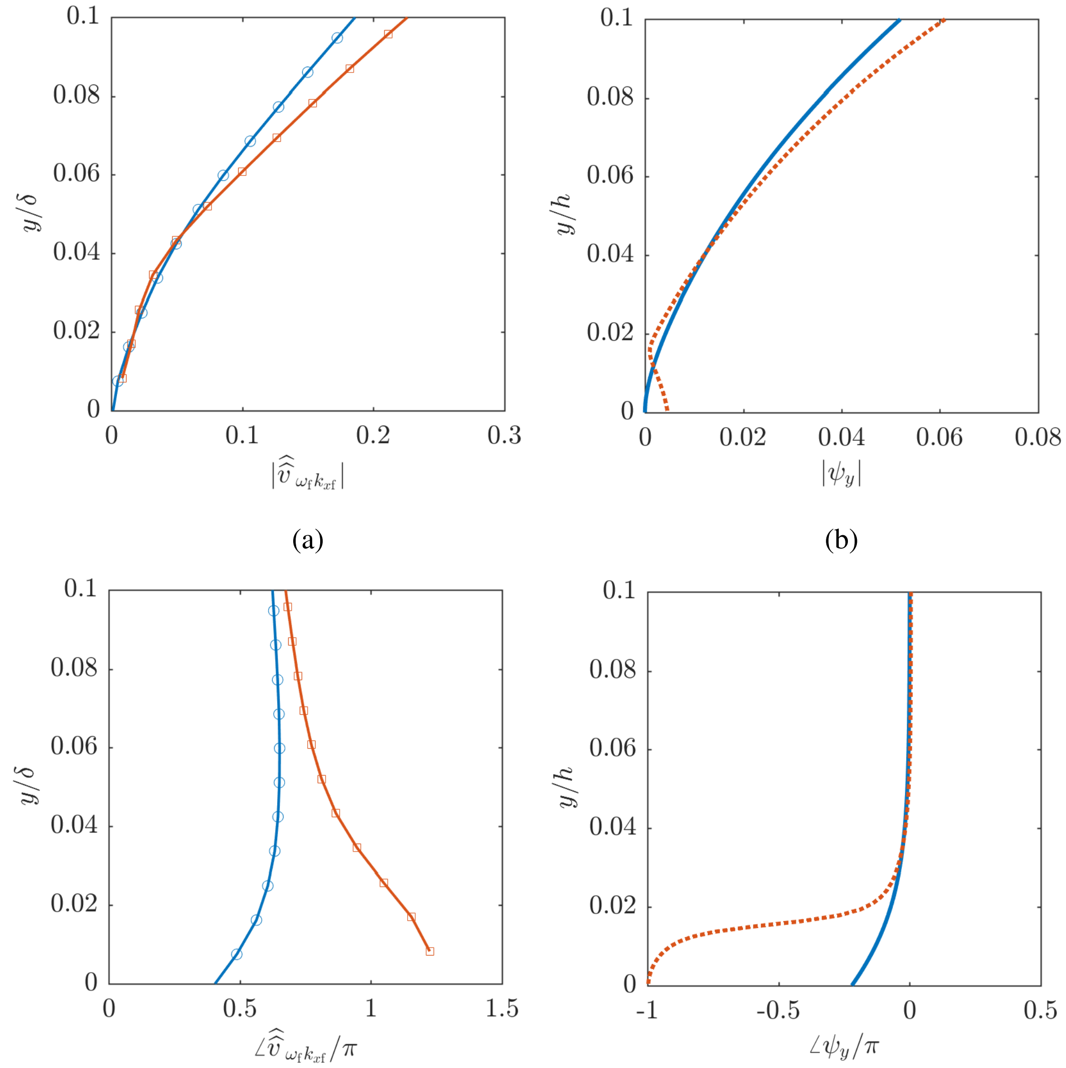

(a) (b)

(c) (d)

Figure 7.9: Near-wall close-up of the smooth-wall and compliant-wall (a) amplitudes and (c) phases of the $\widehat{\widehat{v}}_{\omega_f k_{xf}}$ Fourier modes for actuation condition iii, with the (b) amplitudes and (d) phases of the wall-normal resolvent modes, ψ_y, plotted for comparison. Mode amplitudes are normalized by the peaks in $|\widehat{\widehat{u}}_{\omega_f k_{xf}}|$ ($|\psi_x|$ for the resolvent modes), and the smooth-wall mode phase is matched to the compliant-wall phase at $y=\delta$ ($y=h$ for the resolvent modes). ○ — SW-DRF; □ — CW-DRF; — smooth-wall resolvent mode ($k_x = 2.67$); – – compliant-wall resolvent mode ($Y = 0.003i,\ k_x = 2.78$).

7.4 Conditional averaging

To avoid the limitations in the data brought on by a nontrivial wall location, a condition is devised that can be applied to each streamwise position in the data to search for the anticipated virtual wall feature. From the resolvent modes in Figure 7.4a, the virtual wall's most identifying aspect is the cusp in $|\psi_y|$. Because of this, the condition is based on the wall-normal gradient of $|\widehat{v}_{\omega_\mathrm{f}}(x, y)|$. The gradient, $\frac{\partial |\widehat{v}_{\omega_\mathrm{f}}|}{\partial y}$, is generally positive near the wall, as the mode amplitude increases to its peak value. However, with a virtual wall, the gradient would be negative nearest to the wall and change signs at a cusp point away from the wall. Accordingly, $\frac{\partial |\widehat{v}_{\omega_\mathrm{f}}|}{\partial y}$ is calculated using a one-sided difference scheme, and each streamwise station is conditioned on whether $\frac{\partial |\widehat{v}_{\omega_\mathrm{f}}|}{\partial y} < 0$ for the first, second, or third points from the wall. A profile meeting this condition from the CW data (actuation condition iii) is plotted in Figure 7.10. In this profile, a clear cusp feature is observed around $y/\delta = 0.3$ and resembles the resolvent mode shape in Figure 7.4a.

Proceeding cautiously, the statistical significance of this type of profile is examined. The conditioning is performed on $|\widehat{v}_{\omega_\mathrm{f}}|$ for both the smooth- and compliant-wall data, to determine if this feature is present in both data sets and is possibly an artifact of the PIV processing. This is done for $2 < x/\delta < 7$ to match the smaller FOV of the CW study. 10% of the SW data meets the gradient condition, while 64% of the CW data satisfy the criterion. This is a statistically significant increase and suggestive of a change to a physical mechanism. The locations where the condition is met, x_c, are visualized for both data sets in Figure 7.11, where it is seen that the SW locations are spread and sparse, while the CW locations indeed occupy the majority of the domain and form relatively cohesive regions.

The conditioned streamwise locations, x_c, provide a subset of data where a change in sign of $\frac{\partial |\widehat{v}_{\omega_\mathrm{f}}|}{\partial y}$ occurs and over which an average can be taken. However, any cusp-like features may vary in wall-normal location across x_c and would be diminished by a blind average. Thus, before averaging, the cusp location, y_c, is estimated by the near-wall zero-crossing of $\frac{\partial |\widehat{v}_{\omega_\mathrm{f}}|}{\partial y}$ for each x_c. Then, the profiles $|\widehat{u}_{\omega_\mathrm{f}}|(x_c, y)$ and $|\widehat{v}_{\omega_\mathrm{f}}|(x_c, y)$ are shifted in y such that the cusp point occurs at the same wall-normal location, y_0, for each x_c station. Finally, the shifted profiles are averaged together, yielding $|\widehat{u}_{\omega_\mathrm{f}}|_\mathrm{cond}$ and $|\widehat{v}_{\omega_\mathrm{f}}|_\mathrm{cond}$, both of which are functions of y. Note that phase information is not considered in this process and would require special treatment due to the profiles no longer being equispaced in x. Also, because each of the x_c profiles are shifted in y to move the cusp locations to y_0, y_0 is somewhat arbitrary and must be chosen. Here, y_0 is selected to be the average of the cusp locations, y_c, which for this data was the 4^{th} point from the wall. The conditionally averaged profiles of the CW amplitudes are compared to the fully streamwise averaged SW amplitudes, as conditionally averaging the SW data is not appropriate.

The averaged mode amplitudes are given in Figure 7.12 with the resolvent modes for comparison. Plots of the near-wall region are given in Figure 7.13. As in previous sections, the amplitudes are normalized by the peak in $|\widehat{u}_{\omega_\mathrm{f}}|$ to preserve the relative difference between the streamwise and wall-normal velocities. As expected, the overall characteristics of the mode amplitudes remain in agreement, with T-S wave-like characteristics. However, in the near-wall region in Figure 7.13c, a distinct cusp can be seen in $|\widehat{v}_{\omega_\mathrm{f}}|$ around $y/\delta = 0.35$, and the SW-CW comparison quite closely resembles the ψ_y resolvent modes in Figure 7.13d. As mentioned, the cusp has been selected to sit at the average cusp location, 4 points from the wall, allowing the feature to be resolved. There does not appear to be a corresponding feature in $|\widehat{u}_{\omega_\mathrm{f}}|$ in Figure 7.13a, though there is also a lack of distinguishable difference in the ψ_x resolvent modes in Figure 7.13b. The CW $|\widehat{u}_{\omega_\mathrm{f}}|$ profile is more amplified than the SW profile near the wall, which is consistent with the $|\psi_x|$ behavior. These conditionally averaged mode shapes are consistent with the observations of previous opposition control studies [10, 25, 41] and suggest the formation of a virtual wall.

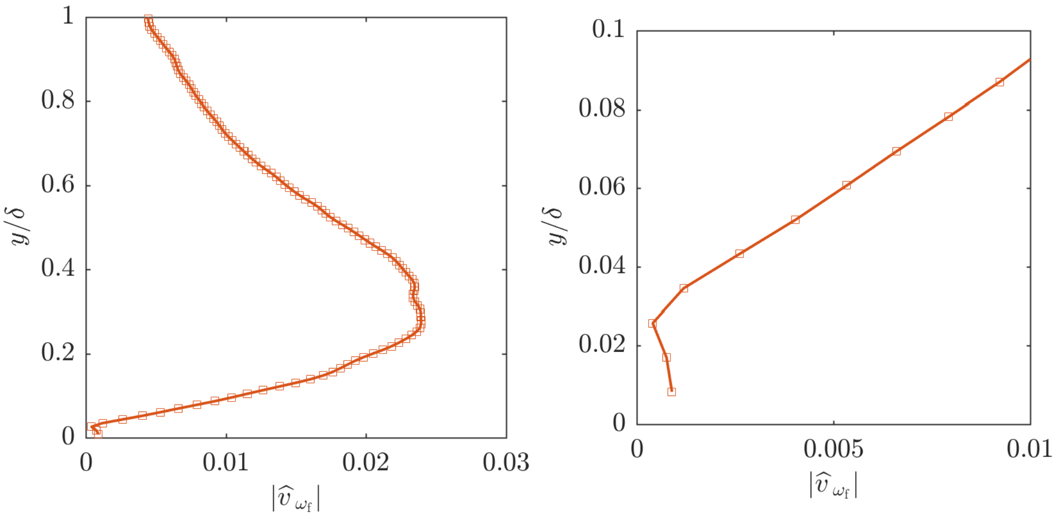

(a) (b)

Figure 7.10: A sample of a $|\widehat{v}_{\omega_\mathrm{f}}|$ profile from the CW-DRF study (actuation condition iii) satisfying the near-wall $\frac{\partial|\widehat{v}_{\omega_\mathrm{f}}|}{\partial y} < 0$ condition. (a) The full mode shape and (b) a near-wall close-up. The mode amplitudes is normalized by its peak.

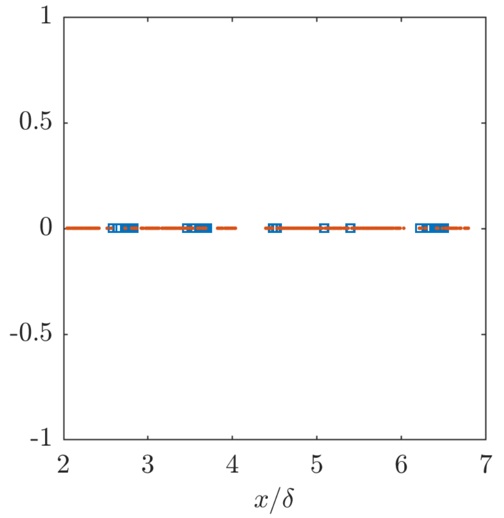

Figure 7.11: A visualization of the streamwise locations where the near-wall $\frac{\partial|\widehat{v}_{\omega_\mathrm{f}}|}{\partial y} < 0$ condition is met in the by the data from actuation condition iii: □ SW-DRF; ● CW-DRF.

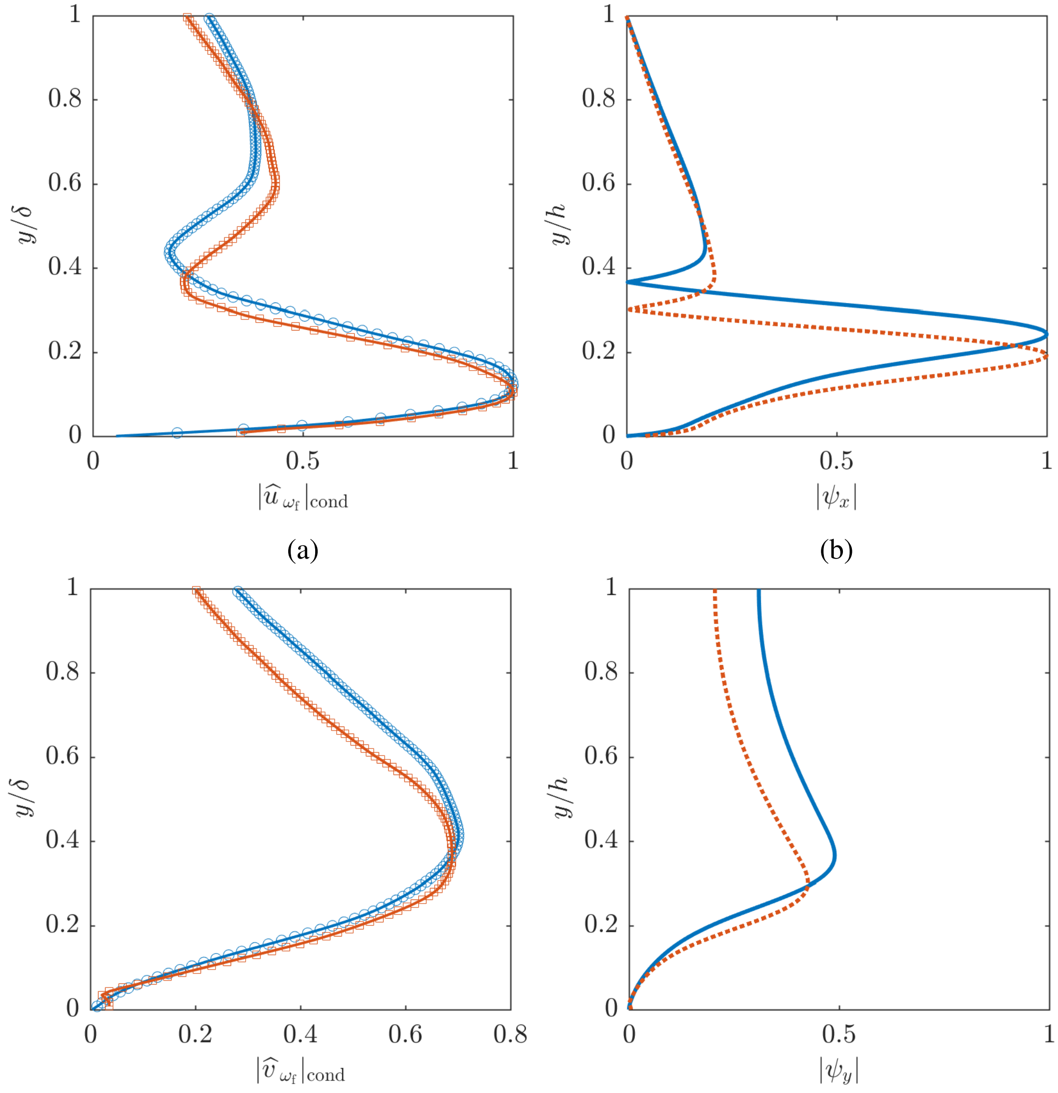

(a) (b)

(c) (d)

Figure 7.12: Comparison of the (a) streamwise, $|\widehat{u}_{\omega_\mathrm{f}}|$, and (c) wall-normal, $|\widehat{v}_{\omega_\mathrm{f}}|$, spatially averaged ω_f Fourier modes from actuation condition iii The smooth-wall data are fully spatially averaged, while the compliant-wall data are conditionally averaged on $\frac{\partial|\widehat{v}_{\omega_\mathrm{f}}|}{\partial y} < 0$ events near the wall. The amplitudes of the (b) ψ_x and (d) ψ_y resolvent modes are plotted for comparison. Mode amplitudes are normalized by the peak in $|\widehat{u}_{\omega_\mathrm{f}}|$. ◯ — SW-DRF; □ — CW-DRF; — smooth-wall resolvent mode ($k_x = 2.67$); – – compliant-wall resolvent mode ($Y = 0.003i,\ k_x = 2.78$).

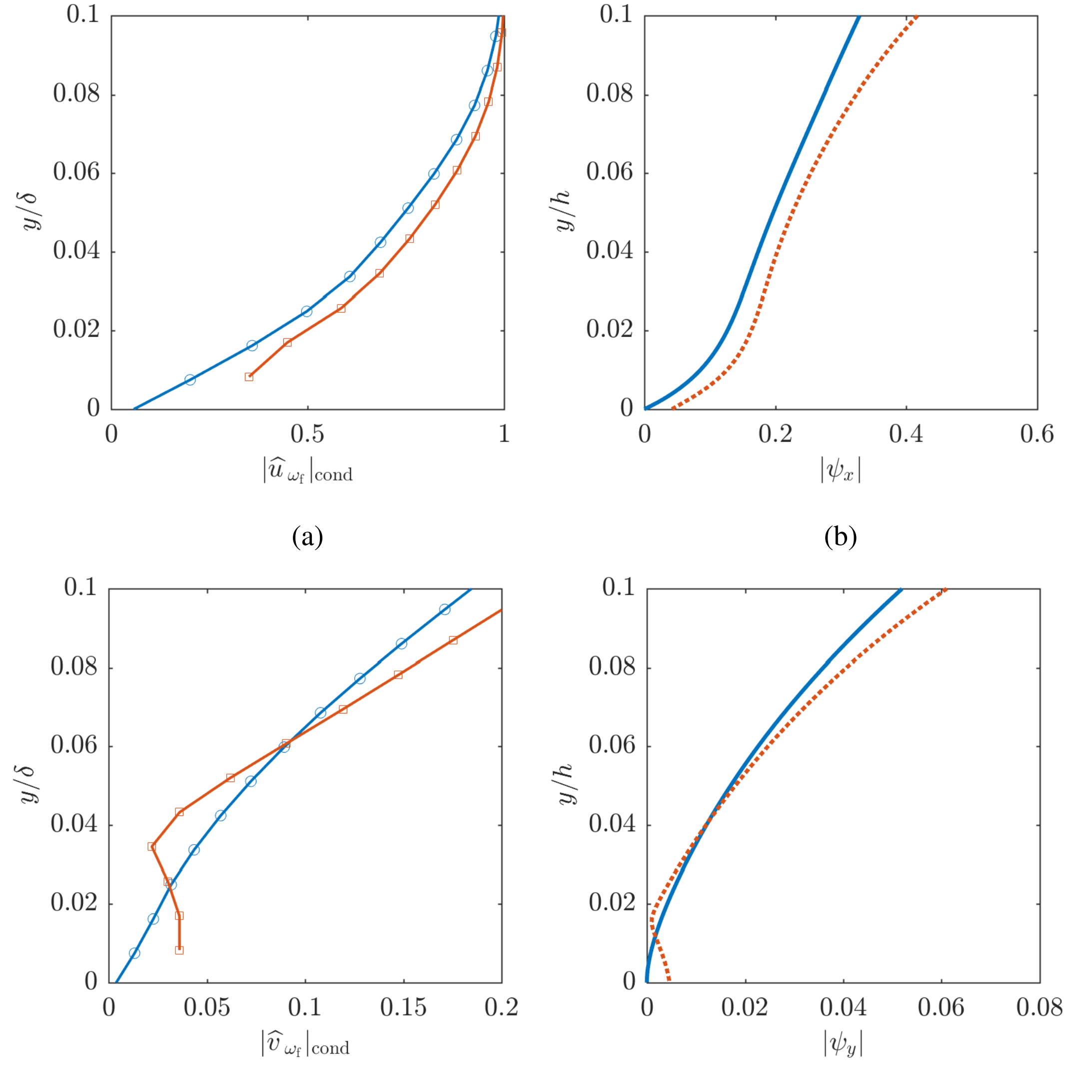

(a) (b)

(c) (d)

Figure 7.13: Near-wall close-up of the (a) streamwise, $|\widehat{u}_{\omega_\mathrm{f}}|$, and (c) wall-normal, $|\widehat{v}_{\omega_\mathrm{f}}|$, spatially averaged ω_f Fourier modes from actuation condition iii The smooth-wall data are fully spatially averaged, while the compliant-wall data are conditionally averaged on $\frac{\partial|\widehat{v}_{\omega_\mathrm{f}}|}{\partial y} < 0$ events near the wall. The amplitudes of the (b) ψ_x and (d) ψ_y resolvent modes are plotted for comparison. Mode amplitudes are normalized by the peak in $|\widehat{u}_{\omega_\mathrm{f}}|$. ○ — SW-DRF; □ — CW-DRF; — smooth-wall resolvent mode ($k_x = 2.67$); – – compliant-wall resolvent mode ($Y = 0.003i,\ k_x = 2.78$).

7.5 Chapter summary

The compliant-wall resolvent analysis developed by Luhar et al. (2015) [43] was used to predict differences in the smooth- and (purely elastic) compliant-wall mode shapes with wavenumber vectors matching those of the roughness-forced synthetic modes from the experiments. In this analysis, both mode shapes exhibited T-S wave characteristics. The CW mode was expected to be shifted towards the wall relative to the SW mode, explained by the lower wave speed and thus lower y_{CL} location in the CW case. The resolvent modes also showed a zero-crossing, cusp feature in $|\psi_y|$ and accompanying π phase shift in $\angle\psi_y$. Both of these traits were consistent with observations from previous resolvent and DNS studies of opposition control [10, 25, 41], where a virtual wall structure developed above the physical wall location. The presence of a virtual wall in the compliant-wall resolvent was explained by the π phase jump in $\angle\psi_y$, required by the purely imaginary wall admittance (Y) corresponding to a purely elastic wall, which mimics the phase jump imposed by the wall jets in opposition control. The critical layer shift and virtual wall features were used as context for the comparison of the experimental SW-CW spatio-temporal mode shapes.

The SW-CW ω_{f}-$k_{x\mathrm{f}}$ Fourier mode shapes were compared and indeed had T-S wave qualities, as observed in the earlier chapters and anticipated by the resolvent analysis. The CW mode was shifted towards the wall relative to the SW mode, congruent with a critical layer mechanism. The relative amplitudes of the second peaks in the SW-CW $|\widehat{\widehat{u}}_{\omega_{\mathrm{f}} k_{x\mathrm{f}}}|$ profiles was in agreement with the resolvent modes, while in contrast the peaks in SW-CW $|\widehat{\widehat{v}}_{\omega_{\mathrm{f}} k_{x\mathrm{f}}}|$ were more comparable. Notably, the resolvent-predicted, near-wall cusp was absent in $|\widehat{\widehat{v}}_{\omega_{\mathrm{f}} k_{x\mathrm{f}}}|$, and though a significant phase shift was seen in $\angle\widehat{\widehat{v}}_{\omega_{\mathrm{f}} k_{x\mathrm{f}}}$, it was in the opposite sense as what was seen in $\angle\psi_y$. The expected agreement between the resolvent and experimental modes is certainly limited, as the resolvent analysis uses several assumptions, such as the linearized, compliant-wall boundary condition. However, the existence of the virtual wall in the experimental data was not ruled out, as several factors may have masked it out in the DFT analysis, namely a streamwise varying wall location.

In an attempt to avoid the limitations in the data, an alternative analysis was developed using on conditional averaging. Anticipating a near-wall cusp feature in $|\widehat{v}_{\omega_{\mathrm{f}}}|$, the condition was chosen to be $\partial|\widehat{v}_{\omega_{\mathrm{f}}}|/\partial y < 0$ for the first, second, or third points from the wall. This condition was applied at each streamwise position to the SW and CW data, and 10% of the SW profiles met the condition, while 64% of the CW profiles satisfied the criterion. This was a statistically significant increase, and so the CW $|\widehat{u}_{\omega_\mathrm{f}}|$ and $|\widehat{v}_{\omega_\mathrm{f}}|$ were conditionally averaged (shifting the profiles for a consistent cusp location) and compared to the fully streamwise averaged SW profiles. A distinct cusp feature emerged in $|\widehat{v}_{\omega_\mathrm{f}}|$ from the conditional averaging, and was quite similar to the feature in the resolvent modes. This suggests the presence of a virtual wall-type structure forming due to the elastic, compliant surface acting to oppose the v velocity above it.

Chapter 8

CONCLUSIONS AND FUTURE WORK

In the present work, an elastic gelatin sample was exposed to a turbulent boundary layer flow, and the fluid-structural system was forced by a dynamic roughness element. This approach to studying the interaction between a compliant surface and a turbulent flow was unique due to the narrow-band forcing enabled by dynamic roughness, as opposed to considering the full broad-band flow-surface interaction. The synthetic, traveling-wave structure induced by the roughness was strongly coherent and readily characterized. The surface, in turn, exhibited a traveling-wave deformation response. By studying the interaction between the roughness-forced flow and surface structures, the complex multiscale nature of the full fluid-structural problem was simplified for a more tractable analysis. The velocity mode shapes for smooth- and compliant-wall conditions were compared, and the effect of the compliant-wall understood by leveraging a resolvent-based perspective.

In the context of dynamic roughness forcing, this work has contributed to a better understanding of the spatial nature of the synthetic mode, as well as the behavior of the v velocity component. This was enabled by the nontraditional knife-edge-prism PIV setup and the naturally shorter length scale of the synthetic mode in water, which allowed for a large, structure-resolved streamwise measurement domain. Through 2D measurements at various spanwise locations, the three-dimensional structure of the synthetic mode was studied and confirmed to be two-dimensional along the z=0 centerline to good approximation. An amplitude modulation phenomenon was observed whereby the synthetic mode would beat as it convected downstream. This was investigated through a simple, quasi-parallel analysis of the flow, and in particular the k_x spectrum of the flow, where a slightly broad spectral peak centered at k_x=$k_{x\mathrm{f}}$ was observed. The broadness of the peak was found to reflect the quality of the dynamic roughness alignment. A parametric study lead to an empirical linear relationship between the synthetic mode wavenumber and the forcing frequency. This empirical fit may allow future studies to determine the actuation frequency to target a desired flow length scale, further developing the capabilities of dynamic roughness as an experimental tool.

Several of the challenges in designing the compliant surface component of these experiments were identified and many were addressed. A fabrication and molding process were developed for the gelatin and a speckle-generation technique was created to enable stereo-DIC surface measurements. Phase-locked surface and flow measurements were made to correlate the synthetic velocity structure and the deformation response. The phase-averaged deformation measurements revealed surface waves in the roughness-forced case that were distinct in frequency and spatial coherence from the structures in the unforced case, and were consistent with the structure of the synthetic mode in the flow. This confirmed that a surface response to the roughness-forced synthetic scale had been achieved.

With the roughness-forced flow-surface interaction confirmed, a comparison was made between the smooth- and compliant-wall velocity modes to study the impact of the compliant surface. The resolvent analysis was used as a lens through which to examine the experimental data by predicting features introduced by the compliant-wall boundary condition, namely a virtual wall signature. The virtual wall was a result of the π phase jump in the wall-normal velocity mode required by the purely elastic surface boundary condition. The experimental mode shapes generated through a discrete Fourier decomposition showed the CW mode shifted closer to the wall than the SW mode, consistent with a critical layer mechanism and with the resolvent mode prediction. However, the virtual wall feature was not observed in the compliant-wall data, and the near-wall differences between the SW and CW modes were difficult to interpret and nondefinitive. This may have been at least partly due to some limitations in the data, the primary one being a non-flat and non-harmonically varying wall position. As an attempt to circumvent these limitations, an alternative, conditional averaging process was devised based on the wall-normal gradient of the amplitude of v, in anticipation of the virtual wall signature from the resolvent modes. Indeed, the condition was met for 64% of the CW profiles, a statistically significant increase over the 10% of the SW data. Executing the conditional averaging, the v modes exhibited a distinct zero-crossing cusp that agreed well with the resolvent prediction. This strongly suggests that the elastic, gelatin surface acted to oppose the v velocity near the wall, forming a feature that resembles the virtual wall of wall-jet opposition control studies, which is known to lead to drag reduction under some conditions.

As with any study, there are limitations to these experiments and opportunities for improvement. The PIV was not optimized for near-wall measurements, which was the region of most significant flow modification. Performing a dedicated near-wall study could reveal more aspects of the compliant-wall effects. In a similar vein, the gelatin surface was neither completely flat nor smooth, despite best efforts. An improved molding process (as was suggested in Chapter 2) could make the analysis more robust and allow for subtle features to be detected more readily. Also enabled by near-wall PIV and smoother surface conditions are modern image-based shear stress estimation methods [59], which could add a novel dimension to both dynamic roughness understanding and compliant surface effects. In terms of the resolvent analysis, an uncontrolled mean profile generated by an eddy viscosity model was used. This is a significant simplification and does not incorporate the modification to the mean by the dynamic roughness nor the compliant surface. Finding a method to appropriately interpolate the experimental mean profiles could provide resolvent modes that are more faithful to the data.

Also worth consideration for future work is that the dynamic roughness disturbance employed here was 2D and primarily a single spatio-temporal scale. Though this made for a more tractable experiment and analysis, turbulence is inherently three-dimensional and multiscaled. As such, a 3D dynamic roughness could lead to results more directly applicable to fully turbulent flows, though the measurement technique would become more complex as well. Likewise, a two-frequency roughness signal could be implemented, as done by Duvvuri & McKeon (2015) [14], which would lead to multiscale synthetic flow structures and possibly allow for the study of nonlinear interactions in the flow, surface, and between the two. In pursuing these more complex disturbances, it would be wise to have in hand a modeling framework with which to navigate the results, as the amount of information and data for the 2D, single-scale case was already quite large and complex.

Naturally, a more complex, viscoelastic material could be considered, as done in other studies. This would require a more complete material characterization to reasonably model the surface behavior. In the context of the resolvent analysis, a viscoelastic material would correspond to a non-zero damping coefficient, leading to a complex wall admittance as opposed to the purely imaginary admittance for an elastic material. This in turn changes the phase difference between the wall-normal velocity and pressure at the wall and would alter the near-wall behavior, weakening or eliminating the virtual wall and establishing a different feature. Studies of such materials could contribute to the understanding of how different material properties impact this fluid-structural interaction and work towards a means to rationally design compliant surfaces to achieve a desired performance goal.

The utility of the resolvent model in this study is worth remark given its numerous assumptions and limited inputs. In the compliant-wall framework employed here, the wall deformations were constrained to be in the wall-normal direction, the wall dynamics were modeled as a spring-damper-backed plate boundary condition, the kinematic boundary condition was linearized, and the material was assumed to be purely elastic, i.e. damping was neglected and the wall admittance term, Y, was constrained to be purely imaginary. In addition, a channel geometry formulation was used, which assumes a parallel flow and does not consider the streamwise development in a boundary layer flow. By using a Fourier analysis in the homogeneous directions, it was inherently assumed that the domain was infinite in x and z. Lastly, the mean velocity profile used was generated through an eddy viscosity model and thus did not account for modifications to the mean due to the dynamic roughness nor the compliant surface. Besides these assumptions, the model also had limit inputs from the experimental data. The only inputs to the compliant-wall resolvent analysis were the wavenumber vector of interest, the wall admittance, and the mean profile, with only the first two coming from the experiment. Despite the many assumptions and restricted inputs, the resolvent modes predicted the general T-S characteristics of the synthetic velocity modes quite well. What's more, the model provided physical insight into the effect of the compliant wall, drawing a connection to opposition control and predicting the virtual wall signature. This guided the conditional averaging process and allowed for the subtle virtual wall feature to be revealed in the data, which would have been difficult to identify otherwise. In this way, this work serves as an experimental demonstration of the efficacy of a compliant-wall resolvent framework.

Future work may consider addressing some of the underlying assumptions in the resolvent analysis. The wall-normal constraint on the surface deformations could be loosened to consider streamwise and spanwise deformations. This would require additional dynamic boundary conditions that relate the fluctuating streamwise and spanwise wall-shear terms to the surface deformations. However, it is anticipated that these additional terms would be quite small, especially relatively to the mean shear for the streamwise deformation, and may not offer significant benefits. The linearized compliant-wall boundary condition restricts the analysis to small deformations and may not apply to more performance-optimized compliant surfaces, requiring higher-order terms to be considered. Naturally, this would increase the complexity of the analysis. The spring-mass-damper model of the wall dynamics may also be exchanged for a viscoelastic wall model, which could better predict the material's behavior. Ultimately, to translate compliant-wall modified mode shapes to an effect on the mean flow properties and the turbulent drag will require modeling of the nonlinear interactions in the flow, i.e. closing the loop with the nonlinear forcing. Work in extending the boundary condition and developing the resolvent model will help build the framework towards its ultimate goal of being a practical, efficient, and widely-used flow control design tool.

BIBLIOGRAPHY

[1] R. Adrian. Hairpin vortex organization in wall turbulence. *Physics of Fluids*, 19(4):041301, 2007.

[2] J. Andreopoulos and D. Wood. The response of a turbulent boundary layer to a short length of surface roughness. *Journal of Fluid Mechanics*, 118:143–164, 1982.

[3] T. Berk, G. Gomit, and B. Ganapathisubramani. Vectoring of parallel synthetic jets: a parametric study. *Journal of Fluid Mechanics*, 804:467–489, 2016.

[4] B. Bolt and J. Butcher. Rayleigh wave dispersion for a single layer on an elastic half space. *Australian Journal of Physics*, 13(3):498–504, 1960.

[5] P. Carpenter. The optimization of compliant surfaces for transition delay. In *Turbulence Management and Relaminarisation*, pages 305–313. Springer, 1988.

[6] P. Carpenter. Optimization of multiple-panel compliant walls for delay of laminar-turbulent transition. *AIAA Journal*, 31(7):1187–1188, 1993.

[7] P. Carpenter and A. c. The hydrodynamic stability of flow over Kramer-type compliant surfaces. Part 1. Tollmien-Schlichting instabilities. *Journal of Fluid Mechanics*, 155:465–510, 1985.

[8] P. Carpenter, C. Davies, and A. Lucey. Hydrodynamics and compliant walls: Does the dolphin have a secret? *Current Science*, 79(6):758–765, 2000.

[9] K. Choi, X. Yang, B. Clayton, E. Glover, M. Atlar, B. Semenov, and V. Kulik. Turbulent drag reduction using compliant surfaces. *Proceedings of the Royal Society of London. Series A: Mathematical, Physical and Engineering Sciences*, 453(1965):2229–2240, 1997.

[10] Y. Chung and T. Talha. Effectiveness of active flow control for turbulent skin friction drag reduction. *Physics of Fluids*, 23(2):025102, 2011.

[11] D. Coles. The law of the wake in the turbulent boundary layer. *Journal of Fluid Mechanics*, 1(2):191–226, 1956.

[12] M. Czerner, L. Fellay, M. Suárez, P. Frontini, and L. Fasce. Determination of elastic modulus of gelatin gels by indentation experiments. *Procedia Materials Science*, 8:287–296, 2015.

[13] D. De Graaff and J. Eaton. Reynolds-number scaling of the flat-plate turbulent boundary layer. *Journal of Fluid Mechanics*, 422:319–346, 2000.

[14] S. Duvvuri and B. McKeon. Triadic scale interactions in a turbulent boundary layer. *Journal of Fluid Mechanics*, 767, 2015.

[15] H. Fernholz and P. Finley. The incompressible zero-pressure-gradient turbulent boundary layer: an assessment of the data. *Progress in Aerospace Sciences*, 32(4):245–311, 1996.

[16] L. Freund. *Dynamic fracture mechanics*. Cambridge University Press, 1998.

[17] K. Fukagata, S. Kern, P. Chatelain, P. Koumoutsakos, and N. Kasagi. Evolutionary optimization of an anisotropic compliant surface for turbulent friction drag reduction. *Journal of Turbulence*, 35(9):1–17, 2008.

[18] Y. Fung. *Foundations of solid mechanics*. Prentice Hall, 1965.

[19] M. Gad-el Hak. The response of elastic and viscoelastic surfaces to a turbulent boundary layer. *Journal of Applied Mechanics*, 53(1):206–212, 1986.

[20] M. Gad-el Hak. Compliant coatings research: a guide to the experimentalist. *Journal of Fluids, Structures*, 1(1):55–70, 1987.

[21] M. Gad-el Hak. Compliant coatings for drag reduction. *Progress in Aerospace Sciences*, 38(1):77–99, 2002.

[22] B. Ganapathisubramani, N. Hutchins, J. Monty, D. Chung, and I. Marusic. Amplitude and frequency modulation in wall turbulence. *Journal of Fluid Mechanics*, 712:61–91, 2012.

[23] M. Gaster. Is the dolphin a red herring? In *Turbulence Management and Relaminarisation*, pages 285–304. Springer, 1988.

[24] M. Guala, S. Hommema, and R. Adrian. Large-scale and very-large-scale motions in turbulent pipe flow. *Journal of Fluid Mechanics*, 554:521–542, 2006.

[25] E. Hammond, T. Bewley, and P. Moin. Observed mechanisms for turbulence attenuation and enhancement in opposition-controlled wall-bounded flows. *Physics of Fluids*, 10(9):2421–2423, 1998.

[26] A. Hussain and W. Reynolds. The mechanics of an organized wave in turbulent shear flow. *Journal of Fluid Mechanics*, 41(2):241–258, 1970.

[27] A. Hussain and W. Reynolds. The mechanics of an organized wave in turbulent shear flow. Part 2. Experimental results. *Journal of Fluid Mechanics*, 54(2): 241–261, 1972.

[28] N. Hutchins and I. Marusic. Large-scale influences in near-wall turbulence. *Philosophical Transactions of the Royal Society of London A: Mathematical, Physical, Engineering Sciences*, 365(1852):647–664, 2007.

[29] D. Huynh and B. McKeon. Characterization of the spatio-temporal response of a turbulent boundary layer to dynamic roughness. *Flow, Turbulence and Combustion*, Submitted.

[30] Y. Hwang and C. Cossu. Linear non-normal energy amplification of harmonic and stochastic forcing in the turbulent channel flow. *Journal of Fluid Mechanics*, 664:51–73, 2010.

[31] I. Jacobi. *Structure of the turbulent boundary layer under static and dynamic impulsive roughness perturbation*. PhD thesis, California Institute of Technology, 2013.

[32] I. Jacobi and B. McKeon. Dynamic roughness perturbation of a turbulent boundary layer. *Journal of Fluid Mechanics*, 688:258–296, 2011.

[33] I. Jacobi and B. McKeon. New perspectives on the impulsive roughness-perturbation of a turbulent boundary layer. *Journal of Fluid Mechanics*, 677: 179–203, 2011.

[34] I. Jacobi and B. McKeon. Phase relationships between large and small scales in the turbulent boundary layer. *Experiments in Fluids*, 54(3):1481, 2013.

[35] M. Jovanovic and B. Bamieh. The spatio-temporal impulse response of the linearized Navier-Stokes equations. In *Proceedings of the 2001 American Control Conference.(Cat. No. 01CH37148)*, volume 3, pages 1948–1953. IEEE, 2001.

[36] E. Kim and H. Choi. Space–time characteristics of a compliant wall in a turbulent channel flow. *Journal of Fluid Mechanics*, 756:30–53, 2014.

[37] M. Kramer. Boundary layer stabilization by distributed damping. *J. Aerosol. Sci.*, 24:459, 1957.

[38] M. Kramer. Boundary layer stabilization by distributed damping. *Journal of the American Society for Naval Engineers*, 72(1):25–34, 1960.

[39] M. Kramer. The dolphin's secret. *New Sci*, 7:1118, 1960.

[40] T. Lee, M. Fisher, and W. Schwarz. Investigation of the stable interaction of a passive compliant surface with a turbulent boundary layer. *Journal of Fluid Mechanics*, 257:373–401, 1993.

[41] M. Luhar, A. Sharma, and B. McKeon. Opposition control within the resolvent analysis framework. *Journal of Fluid Mechanics*, 749:597–626, 2014.

[42] M. Luhar, A. Sharma, and B. McKeon. On the structure and origin of pressure fluctuations in wall turbulence: predictions based on the resolvent analysis. *Journal of Fluid Mechanics*, 751:38–70, 2014.

[43] M. Luhar, A. Sharma, and B. McKeon. A framework for studying the effect of compliant surfaces on wall turbulence. *Journal of Fluid Mechanics*, 768: 415–441, 2015.

[44] S. Maslowe. Critical layers in shear flows. *Annual review of fluid mechanics*, 18(1):405–432, 1986.

[45] B. McKeon and A. Sharma. A critical-layer framework for turbulent pipe flow. *Journal of Fluid Mechanics*, 658:336–382, 2010.

[46] B. McKeon, I. Jacobi, and S. Duvvuri. Dynamic roughness for manipulation, control of turbulent boundary layers: an overview. *AIAA Journal*, 56(6): 2178–2193, 2018.

[47] R. Moarref, A. Sharma, J. Tropp, and B. McKeon. Model-based scaling of the streamwise energy density in high-Reynolds-number turbulent channels. *Journal of Fluid Mechanics*, 734:275–316, 2013.

[48] V. Patel. Calibration of the Preston tube, limitations on its use in pressure gradients. *Journal of Fluid Mechanics*, 23(1):185–208, 1965.

[49] S. Pope. Turbulent flows, 2001.

[50] Electronic Instrument Research. EIR: Laser Extensometers. `https://www.e-i-r.com`. Accessed: 2019-02-07.

[51] W. Reynolds and W. Tiederman. Stability of turbulent channel flow, with application to Malkus's theory. *Journal of Fluid Mechanics*, 27(2):253–272, 1967.

[52] T. Saxton-Fox and B. McKeon. Coherent structures, uniform momentum zones and the streamwise energy spectrum in wall-bounded turbulent flows. *Journal of Fluid Mechanics*, 826, 2017.

[53] H. Schlichting and K. Gersten. *Boundary-layer theory*. Springer Berlin Heidelberg, 2016. ISBN 9783662529195. URL `https://books.google.com/books?id=bOUyDQAAQBAJ`.

[54] P. Schmid and D. Henningson. *Stability and transition in shear flows*. Springer Science & Business Media, 2001.

[55] A. Sharma and B. McKeon. On coherent structure in wall turbulence. *Journal of Fluid Mechanics*, 728:196–238, 2013.

[56] Correlated Solutions. Correlated Solutions: Application Note AN-1701: Speckle Pattern Fundamentals. `http://www.correlatedsolutions.com/support/index.php?/Knowledgebase/Article/GetAttachment/80/14750`. Accessed: 2018-06-15.

[57] H. Tennekes, J. Lumley, J. Lumley, et al. *A first course in turbulence*. MIT press, 1972.

[58] A. Townsend. *The structure of turbulent shear flow*. Cambridge University Press, 1980.

[59] C. Willert. High-speed particle image velocimetry for the efficient measurement of turbulence statistics. *Experiments in Fluids*, 56(1):17, 2015.

[60] X. Wu and P. Moin. Direct numerical simulation of turbulence in a nominally zero-pressure-gradient flat-plate boundary layer. *Journal of Fluid Mechanics*, 630:5–41, 2009.

[61] X. Wu, P. Moin, J. Wallace, J. Skarda, A. Lozano-Durán, and J.P. Hickey. Transitional–turbulent spots, turbulent–turbulent spots in boundary layers. *Proceedings of the National Academy of Sciences*, 114(27):E5292–E5299, 2017.

[62] S. Xu, D. Rempfer, and J. Lumley. Turbulence over a compliant surface: numerical simulation and analysis. *Journal of Fluid Mechanics*, 478:11–34, 2003.

[63] C. Zhang, R. Miorini, and J. Katz. Integrating Mach–Zehnder interferometry with TPIV to measure the time-resolved deformation of a compliant wall along with the 3D velocity field in a turbulent channel flow. *Experiments in Fluids*, 56(11):203, 2015.

[64] C. Zhang, J. Wang, W. Blake, and J. Katz. Deformation of a compliant wall in a turbulent channel flow. *Journal of Fluid Mechanics*, 823:345–390, 2017.

Appendix A

GELATIN FABRICATION PROCESS

Equipment

- Heatable container: large beakers, pot
- Blending container (preferably transparent/translucent): large beaker, bowl
- Heating unit: microwave, stovetop, hot pad
- Heat-resistant gloves
- Emulsion blender
- Weighing scale
- Weigh boats
- Mold for sample
  - Preferably transparent material (see step 9)
  - Any corners in mold should be generously rounded (R>0.5 inches). Sharp corners may lead to fissuring sites when uncovering sample.
- Cover plate, non-stick face with rigid backing, e.g.:
  - Teflon sheet (non-stick face)
  - 1/4” acrylic plate (rigid backing)

Note: The most dilute mixture tested was 3:100, gelatin to water. More dilute mixtures did not fully solidify at room temperature, though it may be possible with refrigeration. Higher gelatin concentrations should make the fabrication process easier and more robust, but will naturally yield more rigid samples. For these experiments, a ratio of 4:100 was used.

Instructions:

1. Fill beakers with measured water, leaving space for blending process.
    - Make sure to have slightly more mixture than the mold volume in order to be able to overfill the mold and avoid surface bubbles.
2. Microwave water to a rolling boil, ~5 minutes.
3. While water is heating, measure appropriate amount of gelatin powder and pour into blending container.
4. Once water is boiling, add to blending container.
5. Immediately blend with emulsion blender.
    - Blend for ~30 seconds at a time, then check for remaining chunks of gelatin.
    - Continue until no gelatin chunks remain.
    - Mixture will froth (Figure A.1); these bubbles will be allowed to dissipate before pouring the solution.
6. Allow mixture to cool and bubbles to pop (~10-20 minutes).
    - To expedite process, slowly and gently transfer mixture to clean beaker, so as to not introduce new bubbles.
    - Rinse empty beaker to remove froth, and repeat.
7. Once bubbles have popped (figure 2), carefully pour mixture into mold (avoiding introduction of bubbles) and allow to cool for another ~10 minutes.
8. Once mixture has cooled (minimal steam), coat Teflon cover plate with thin layer of oil.
9. Slowly cover mold with cover plate .
    - Lay one edge of cover plate down, just off to the side of the mold. This edge will act as the hinge. Keep the rest of the plate elevated at an angle.
    - Gradually lower the rest of the cover plate until the mold is covered.

- Tip: if mold material is transparent (e.g. acrylic) and cover plate material is sufficiently translucent, place a strong light source underneath and pointing up through the mold. This will make the regions of contact between the gelatin mixture and the cover plate visible. User may check real-time for poor contact or bubbles.

10. Apply weights to cover plate if desired, avoiding excessive weight as it may cause rapid delamination upon removal.
11. Allow gelatin to solidify for ~12 hours (will vary depending on mixture ratio).
12. Very carefully remove cover, starting with one corner and gently prying cover off.
    - This is the most sensitive step of the process. Aggressive or early cover removal may cause fissuring and rupturing of sample surface.
    - User is encouraged to practice cover removal on smaller samples.

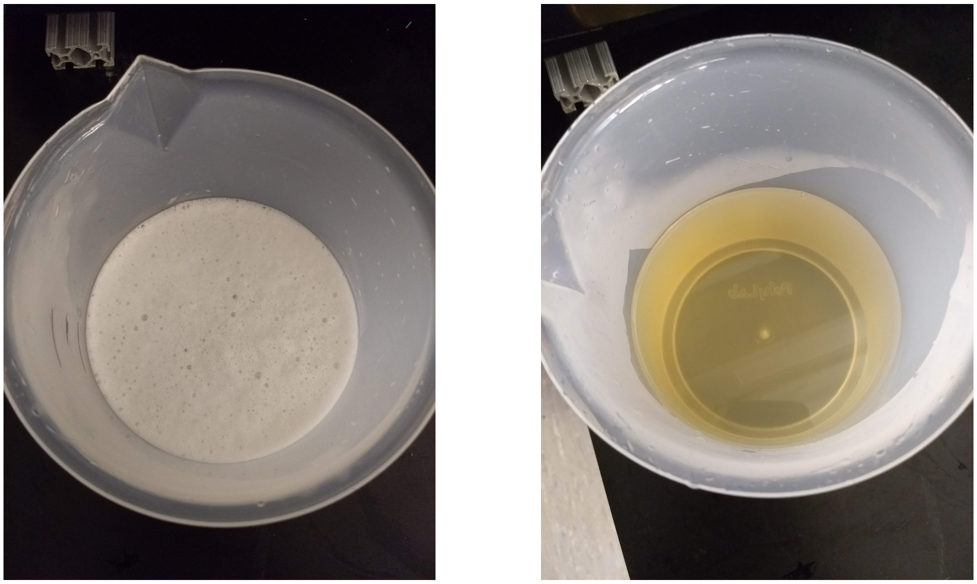
(a) (b)

Figure A.1: Water-gelatin mixture, (a) with bubbles, soon after blending, and (b) without bubbles.

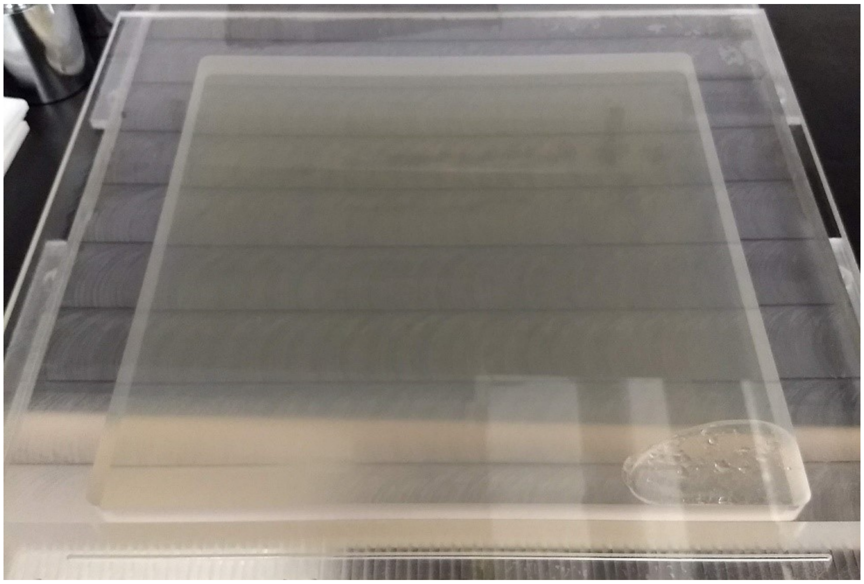

Figure A.2: Gelatin sample with non-Teflon cover on, bubble formed in corner due to curvature of cover plate.

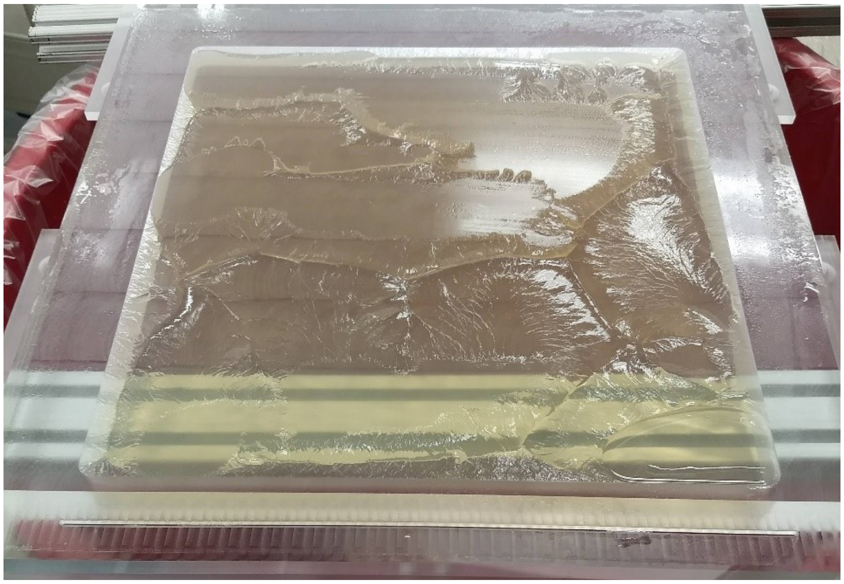

Figure A.3: Gelatin sample with cover removed. Several surface fissures and tears have developed from the lid removal.

Figure A.4: Successfully fabricated gelatin sample, dyed white for a DIC test.

Appendix B

PHASE-AVERAGING

B.1 Definition of the phase-averaging operation

Consider a discrete, finite-time signal, g_k, with record length N and sampling frequency f_s. Let ω_f be an angular frequency of interest with a per-period sampling rate of SR, which requires the full sampling rate to be $f_s = \frac{\omega_\mathrm{f}}{2\pi} \cdot SR$. Let M be the integer number of periods, $\frac{2\pi}{\omega_\mathrm{f}}$, contained in the record, $M = \frac{N}{SR}$. We can then define the ω_f phase-average of g_k as:

$$\widetilde{g}_j = \frac{1}{M}\sum_{m=0}^{M-1} g_{(m\cdot SR+j)} \qquad j \in [0, SR-1], \tag{B.1}$$

where $\widetilde{g}_j$ is the phase-average of g_k. We can periodically tile $\widetilde{g}_j$ to construct the phase-averaged signal $\widetilde{g}_k$ of length N:

$$\widetilde{g}_k = \frac{1}{M}\sum_{m=0}^{M-1} g_{(m\cdot SR+k \bmod SR)} \qquad k \in [0, N-1]. \tag{B.2}$$

Note that $\widetilde{g}_k$ is SR-periodic or ω_f-periodic by construction, i.e. $\widetilde{g}_k = \widetilde{g}_{m\cdot SR+k}$ for integer m.

B.2 Effect of phase-averaging on frequency content

It is clear that the frequency content of $\widetilde{g}_k$ has been modified from g_k by the phase-averaging operation. To show what this modification is, define the discrete Fourier transform (DFT) and inverse discrete Fourier transform (IDFT) pair:

$$G_n = \sum_{k=0}^{N-1} g_k e^{-i2\pi nk/N}, \quad n \in [0, N-1] \tag{B.3}$$

$$g_k = \frac{1}{N}\sum_{n=0}^{N-1} G_n e^{i2\pi nk/N}, \quad k \in [0, N-1]. \tag{B.4}$$

We apply a DFT to $\widetilde{g}_k$:

$$\widetilde{G}_n = \sum_{k=0}^{N-1} \widetilde{g}_k e^{-i2\pi nk/N} \qquad n \in [0, N-1]. \tag{B.5}$$

Writing out the summation terms:

$$\begin{aligned}
\widetilde{G}_n = & \widetilde{g}_0 e^{(-i2\pi n/N)0} && + \widetilde{g}_1 e^{(-i2\pi n/N)1} && + \dots \\
& \widetilde{g}_{SR} e^{(-i2\pi n/N)SR} && + \widetilde{g}_{SR+1} e^{(-i2\pi n/N)(SR+1)} && + \dots \\
& \vdots \\
& \widetilde{g}_{(M-1)SR} e^{(-i2\pi n/N)(M-1)SR} && + \widetilde{g}_{(M-1)SR+1} e^{(-i2\pi n/N)((M-1)SR+1)} && + \dots
\end{aligned} \tag{B.6}$$

Because $\widetilde{g}_k$ is SR-periodic, the column-aligned terms can be grouped and written as:

$$\widetilde{G}_n = \widetilde{g}_0 \sum_{m=0}^{M-1} e^{-i2\pi nm/M} + \widetilde{g}_1 \sum_{m=0}^{M-1} e^{-i2\pi n\left(\frac{m}{M}+\frac{1}{N}\right)} + \dots \tag{B.7}$$

This can then be written as an additional summation over the SR period:

$$\begin{aligned}
\widetilde{G}_n &= \sum_{j=0}^{SR-1} \widetilde{g}_j \sum_{m=0}^{M-1} e^{-i2\pi n\left(\frac{m}{M}+\frac{j}{N}\right)} \\
&= \sum_{j=0}^{SR-1} \widetilde{g}_j e^{-i2\pi n\frac{j}{N}} \sum_{m=0}^{M-1} e^{-i2\pi nm/M}.
\end{aligned} \tag{B.8}$$

Focusing on the m summation, let $n = pM + q$, where p and q are integers, $p \in [0, SR-1]$ and $q \in [0, M-1]$, such that $n \in [0, N-1]$. The m summation then becomes:

$$\begin{aligned}
\sum_{m=0}^{M-1} e^{-i2\pi nm/M} &= \sum_{m=0}^{M-1} e^{-i2\pi(pM+q)m/M} \\
&= \sum_{m=0}^{M-1} \cancelto{1}{e^{-i2\pi pm}} e^{-i2\pi qm/M} \\
&= \sum_{m=0}^{M-1} e^{-i2\pi qm/M}.
\end{aligned} \tag{B.9}$$

Note that $e^{-i2\pi qm/M}$, $m \in [0, M-1]$ represents M equispaced points on the unit circle in the complex plane, and thus the m summation equals zero unless $q = 0$:

$$\sum_{m=0}^{M-1} e^{-i2\pi nm/M} = \begin{cases} M & \forall n = pM + q,\ q = 0 \\ 0 & \text{otherwise.} \end{cases} \tag{B.10}$$

This leads to the Fourier coefficients of $\widetilde{g}_k$ to take the form:

$$\widetilde{G}_n = \begin{cases} M \sum\limits_{j=0}^{SR-1} \widetilde{g}_j e^{-i2\pi pj/SR} & \forall n = pM,\ p \in [0, SR-1] \\ 0 & \text{otherwise.} \end{cases} \tag{B.11}$$

It is clear from equation B.11 that the phase-averaging process acts as a discrete Fourier filter, retaining the $n = pM$ terms, i.e. only the frequencies harmonic with ω_f.

For comparison, applying a DFT to the single-period-length $\widetilde{g}_j$, we have:

$$\begin{gathered}\widetilde{G}_{n'} = \sum_{j=0}^{SR-1} \widetilde{g}_j e^{-i2\pi n' j/SR} \\ n' \in [0, SR-1].\end{gathered} \tag{B.12}$$

We see that equation B.12 is identical to the non-trivial case in equation B.11, except for the prefactor M in equation B.11, which is incurred because the DFT was done on the full, length-N record, and so the transform pair has a $\frac{1}{N}$ factor, as opposed to the $\frac{1}{SR} = \frac{M}{N}$ factor for the transform pair associated with equation B.12.

B.3 Interpretations of phase-averaging

Equation B.11 shows that phase-averaging is identical to a discrete Fourier filter for the ω_f harmonic frequencies in a signal. Indeed, phase-averaging and discrete Fourier transforming are intimately related. A sketch proof is given here to illustrate this fact. Construct an $M \times SR$ matrix, g_{mj}, by reorganizing the signal g_k:

$$g_{mj} = \begin{bmatrix} g_0 & g_1 & \cdots & g_{SR-1} \\ g_{SR} & g_{SR+1} & \cdots & g_{2SR-1} \\ \vdots & & & \\ g_{(M-1)SR} & g_{(M-1)SR+1} & \cdots & g_{N-1} \end{bmatrix}. \tag{B.13}$$

Phase-averaging g_k amounts to averaging along the columns of g_{mj}, yielding a $1 \times SR$ row vector, $\widetilde{g}_{1j}$:

$$\widetilde{g}_{1j} = \begin{bmatrix} \widetilde{g}_0 & \widetilde{g}_1 & \ldots & \widetilde{g}_{SR-1} \end{bmatrix}. \tag{B.14}$$

$\widetilde{g}_{1j}$ can then be discrete Fourier transformed along its row to arrive at $\widetilde{G}_{1n'}$:

$$\widetilde{G}_{1n'} = \begin{bmatrix} \widetilde{G}_0 & \widetilde{G}_1 & \ldots & \widetilde{G}_{SR-1} \end{bmatrix}. \tag{B.15}$$

Alternatively, we could have applied a DFT along the rows of g_{mj} first, to get $G_{mn'}$. Note that this is a equivalent to performing a DFT on consecutive SR-length windows of g_k and stacking the results into $G_{n,\mathrm{tr}}$, with ‘tr’ for ‘truncated’:

$$G_{mn'} = \begin{bmatrix} G_{0,\mathrm{tr}} & G_{1,\mathrm{tr}} & \dots & G_{SR-1,\mathrm{tr}} \\ G_{SR,\mathrm{tr}} & G_{SR+1,\mathrm{tr}} & \dots & G_{2SR-1,\mathrm{tr}} \\ \vdots & & & \\ G_{(M-1)SR,\mathrm{tr}} & G_{(M-1)SR+1,\mathrm{tr}} & \dots & G_{N-1,\mathrm{tr}} \end{bmatrix}. \tag{B.16}$$

We can then average $G_{mn'}$ along its columns to arrive at the same $\widetilde{G}_{1n'}$ in equation B.15. This exercise highlights the fact that, because the DFT and phase-averaging (simply reorganized averaging) are both linear operations, they commute with one another. Thus, phase-averaging can be accomplished by phase-locked averaging in time as defined in equation B.1, or equivalently by discrete Fourier transforming consecutive SR-length windows, averaging the result, and inverse transforming back to time. The latter description draws a parallel to Welch’s method of averaging periodogram spectra, except that in this case, the full Fourier coefficients are averaged because the relative phases of the Fourier coefficient sets are consistent.

Note that the above procedure required no knowledge of the phase of the periodic content of interest, only the frequency, ω_f. This means that phase-averaging can be done for a given record without actually phase-locking the measurement to the reference signal. However, by phase-locking, multiple records can be phase-shifted to be consistent with one another, and thus more samples can be used to calculate the phase-averaged fields.

B.4 Summary and remarks on the phase-averaging operation

1. Phase-averaging is identical to discrete Fourier filtering at the resolvable, ω_f-harmonics.
2. Phase-averaging can be achieved through phase-locked averaging, per equation B.1, or by dividing the data into SR-length ($2\pi/\omega_\mathrm{f}$-length) windows, applying a DFT to each, averaging the resulting Fourier coefficient sets, and applying an IDFT. This is a consequence of the discrete Fourier transform and phase-averaging being linear operations.
3. Phase-averaging operates strictly on one dimension of a signal, like a DFT. A phase-average in time applies no constraints on spatial information, only separates it into components with ω_f-harmonic temporal coherence.

4. The definition of phase-averaging in equation B.1 can be extended to continuous-time functions by taking the phase index, j, to be a continuous variable, phi, and on an infinite or semi-infinite time horizon by taking the limit as $M \to \infty$. Consider a continuous-time variable, $g(t)$, defined for $t \geq 0$. The ω_f phase-average, $\widetilde{g}(\phi)$, is defined as:

$$\begin{gathered}\widetilde{g}(\phi) = \lim_{M \to \infty} \frac{1}{M} \sum_{m=0}^{M-1} g\left(m \frac{2\pi}{\omega_\mathrm{f}} + \phi\right) \\ \phi \in [0, 2\pi).\end{gathered} \tag{B.17}$$

B.5 Proof of $\overline{\widetilde{u}_i u'_j} = 0$

In Section 4.1, it is stated that the phase-averaged velocity and the perturbation about the phase-averaged mean are uncorrelated in time, i.e. $\overline{\widetilde{u}_i u'_j} = 0$. To show this, consider two arbitrary discrete time signals of length N, a_k and b_k, triple decomposed following Equation 4.5. It follows that:

$$\begin{aligned}\overline{\widetilde{a} b'} &= \frac{1}{N} \sum_{k=0}^{N-1} \widetilde{a}_k b'_k \\ &= \frac{1}{N} \left[\widetilde{a}_0 b'_0 + \ldots + \widetilde{a}_{SR} b'_{SR} + \ldots + \widetilde{a}_{2SR} b'_{2SR} + \ldots\right] \\ &= \frac{1}{N} \left[\widetilde{a}_0 b'_0 + \ldots + \widetilde{a}_0 b'_{SR} + \ldots + \widetilde{a}_0 b'_{2SR} + \ldots\right] \\ &= \frac{1}{N} \left[\widetilde{a}_0 \left(b'_0 + b'_{SR} + b'_{2SR} + \ldots\right) + \ldots\right] \\ &= \frac{1}{N} \left[SR\, \widetilde{a}_0 \widetilde{b'}_0 + SR\, \widetilde{a}_1 \widetilde{b'}_1 + \ldots\right] \\ &= \frac{SR}{N} \sum_{k=0}^{SR-1} \widetilde{a}_k \widetilde{b'}_k\,, \quad \widetilde{b'}_k \overset{!}{=} 0 \\ \Rightarrow \overline{\widetilde{a} b'} &= 0.\end{aligned} \tag{B.18}$$

Appendix C

DERIVATION OF COMPLIANT-WALL BOUNDARY CONDITION FOR RESOLVENT ANALYSIS

Start by considering the full, streamwise velocity. Perform a Reynolds decomposition and Taylor series expansion about the wall location, y=0:

$$U(y,t) = \overline{U}(y) + u(y,t) \tag{C.1}$$

$$= \overline{U}(0) + y \left.\frac{\mathrm{d}\overline{U}}{\mathrm{d}y}\right|_0 + u(0,t) + y \left.\frac{\partial u}{\partial y}\right|_0 + \text{H.O.T.}\,, \tag{C.2}$$

where the x and z dependence has been suppressed for conciseness.

Allow for a wall deformation $\eta(t)$ constrained to be in the wall-normal direction (in full notation, η is a function of x, z, and t). Thus, along the wall:

$$U(\eta,t) = \overline{U}(0) + \eta(t) \left.\frac{\mathrm{d}\overline{U}}{\mathrm{d}y}\right|_0 + u(0,t) + \eta(t) \left.\frac{\partial u}{\partial y}\right|_0 + \text{H.O.T.} \tag{C.3}$$

$$= \overline{U}(0) + \eta(t) \left.\frac{\mathrm{d}\overline{U}}{\mathrm{d}y}\right|_0 + u(0,t) + \eta(t) \left.\frac{\partial u}{\partial y}\right|_0 + \text{H.O.T.} \tag{C.4}$$

Assume that the wall deformation is small, $\eta \ll 1$, and that near the boundary, u shrinks to be the same order as η:

$$\left.\begin{aligned} \eta &= \epsilon \eta_\epsilon \\ u &= \epsilon u_\epsilon \end{aligned}\right\} \eta_\epsilon, u_\epsilon \sim \mathcal{O}(1)\,,\ \epsilon \ll 1 \tag{C.5}$$

$$\Rightarrow U(\eta,t) = \overline{U}(0) + \epsilon \left(\eta_\epsilon(t) \left.\frac{\mathrm{d}\overline{U}}{\mathrm{d}y}\right|_0 + u_\epsilon(0,t) \right) + \mathcal{O}\left(\epsilon^2\right). \tag{C.6}$$

With the wall deformations constrained to be in wall-normal direction, there is a no-slip boundary condition on U for all orders of ϵ. Retaining only up to the $\mathcal{O}(\epsilon)$ terms and applying the boundary conditions (i.e. a linearized boundary condition) yields:

$$\mathcal{O}(1): \quad \overline{U}(0) = 0 \tag{C.7}$$

$$\mathcal{O}(\epsilon): \quad \epsilon\left(\eta_\epsilon(t)\,\left.\frac{\mathrm{d}\overline{U}}{\mathrm{d}y}\right|_0 + u_\epsilon(0,t)\right) = \eta(t)\,\left.\frac{\mathrm{d}\overline{U}}{\mathrm{d}y}\right|_0 + u(0,t) = 0 \tag{C.8}$$

$$\boxed{u(0,t) = -\eta(t)\,\left.\frac{\mathrm{d}\overline{U}}{\mathrm{d}y}\right|_0 .} \tag{C.9}$$

The same procedure is applied to the wall-normal velocity:

$$V(y,t) = \cancelto{0}{\overline{V}(y)} + v(y,t) \tag{C.10}$$

$$= v(0,t) + y\,\left.\frac{\partial v}{\partial y}\right|_0 + \text{H.O.T.} \tag{C.11}$$

$$V(\eta,t) = v(0,t) + \eta(t)\,\left.\frac{\partial v}{\partial y}\right|_0 + \text{H.O.T.} \tag{C.12}$$

$$= \epsilon v_\epsilon(0,t) + \mathcal{O}\left(\epsilon^2\right). \tag{C.13}$$

Applying the no-through flow boundary condition at the wall kinematically relates v to η:

$$\epsilon v_\epsilon(0,t) = \boxed{v(0,t) = \frac{\partial \eta}{\partial t}.} \tag{C.14}$$

The same procedure and the no-slip boundary condition are applied to the spanwise velocity:

$$\boxed{w(0,t) = 0.} \tag{C.15}$$

These boundary conditions are then Fourier transformed in x, z, and t:

$$\boxed{\begin{aligned} \check{u}_{\mathbf{k}}(0) &= -\check{\eta}_{\mathbf{k}}\,\left.\frac{\mathrm{d}\overline{U}}{\mathrm{d}y}\right|_0 && \text{(C.16)}\\ \check{v}_{\mathbf{k}}(0) &= -i\omega\check{\eta}_{\mathbf{k}} && \text{(C.17)}\\ \check{w}_{\mathbf{k}}(0) &= 0. && \text{(C.18)} \end{aligned}}$$